OPTICAL COOLING OF MAGNETICALLY TRAPPED ATOMIC HYDROGEN

ACADEMISCH PROEFSCHRIFT

ter verkrijging van de graad van doctor
aan de Universiteit van Amsterdam,
op gezag van de Rector Magnificus
prof. dr. P.W.M. de Meijer
in het openbaar te verdedigen in de Aula der Universiteit
(Oude Lutherse Kerk, ingang Singel 411, hoek Spui),
op dinsdag 21 februari 1995 te 13.30 uur

door

Irwan Dani Setija

geboren te Hong Kong

Amsterdam MCMXCIV

Promotor:	prof. dr. J.T.M. Walraven
Co-promotor:	dr. T.W. Hijmans

Commissie:	prof. dr. A. Lagendijk
	prof. dr. ir. H.B. van Linden van den Heuvell
	prof. dr. G. Nienhuis
	dr. L.G. Suttorp
	prof. dr. B.J. Verhaar

Paranimfen:	Into Goudsmit
	Willem Vos

Faculteit der Natuur- en Sterrenkunde

The work described in this thesis was part of the research program of the
Stichting voor Fundamenteel Onderzoek der Materie (FOM),
which is financially supported by the
Nederlandse Organisatie voor Wetenschappelijk Onderzoek (NWO),
and was carried out at the

Van der Waals-Zeeman Laboratorium
Universiteit van Amsterdam
Valckenierstraat 65
1018 XE Amsterdam
The Netherlands

Contents

Chapter 1

Introduction

1.1 Trapped atomic hydrogen

Atomic hydrogen (H) is the first and best documented quantum gas [1, 2]. Due to its small mass and weak interaction, it is predicted to remain gaseous down to 0 K [3], which makes it a very suitable candidate for the study of ultra-cold gases. A number of interesting phenomena can be studied in ultra-cold atomic hydrogen. The reduction of Doppler broadening enables performing high-resolution spectroscopy which yields accurate values for the fundamental constants and constitutes a test for basic theories such as QED. A very challenging test in this respect would be the comparison between hydrogen and anti-hydrogen in their interaction with the electromagnetic field. With ultra-cold H, the fundamental properties can be studied of low-energy collisions of the atoms with surfaces. In the experiments with hydrogen, the surfaces of the cell are usually covered with liquid He, which supports only one bound state for H, with a small energy of physisorption $\varepsilon_a = 1.011(10)\,\mathrm{K}$ [4]. The He-film presents a flat, translationally invariant surface where the elementary excitations, the ripplons, interact with the atoms [5, 6].

One of the most intriguing features of a three-dimensional gas of H is the prediction to undergo a phase transition to a state displaying macroscopic quantum behaviour. This phase transition, called the Bose-Einstein condensation (BEC), occurs when the thermal de Broglie wavelength $\lambda_{th} = h/\sqrt{2\pi m k_B T}$, becomes of the same order as the interparticle distance, $\lambda_{th} \sim n^{-1/3}$. Here T is the temperature and n the density of the gas and m is the atomic mass. BEC in atomic hydrogen would be a realization of macroscopic quantum behaviour in a well understood system which can increase our understanding of macroscopic quantum phenomena such as superfluidity and superconductivity. It is for this reason that the realization of BEC is one of the most important goals in experiments with ultra-cold gases.

H was first stabilized by Silvera and Walraven [7] by spin-polarizing the atoms in a high magnetic field thus suppressing the recombination to the molecular state. By covering the walls of their cell with liquid He, they prevented a massive surface adsorption and a subsequent recombination of the spin-polarized atoms. The first experiments towards reaching BEC were aimed at increasing the density at constant temperature in a gas of high-field-seeking, electron-spin-down-polarized H$\downarrow$ [8, 9]. The maximum attainable density in these gases turned out to be limited by three-body recombination on the liquid He film. The highest volume density up to this moment has been reached by compression of H$\downarrow$ in a highly inhomogeneous magnetic field [10]. The density $n = 2 \times 10^{19}\,\mathrm{cm}^{-3}$ at a temperature $T = 650\,\mathrm{mK}$ reached in this experiment is approximately an order of magnitude below the critical density for BEC at this temperature.

When it was realized that three-body recombination presented a severe limitation to achieving the conditions for BEC, new experiments were set up aimed at reaching as low a temperature as possible at constant (or increasing) density. An important step in achieving this goal was the wall-free confinement of low-field-seeking, electron-spin-up-polarized H$\uparrow$ in magnetostatic traps [11, 12]. Since Maxwell's equations do not allow the creation of a magnetic field maximum in free space, the trapping experiments are performed with H$\uparrow$ which, unfortunately, is a less stable gas than H$\downarrow$. H$\uparrow$ decays by spin relaxational processes to the untrapped H$\downarrow$ state which has the lowest energy in a magnetic field.

A wall-free confined gas requires non-invasive methods for the determination of the central density n_0 and temperature T of the gas. In the first experiments on trapped H$\uparrow$, information on n_0 and T of the trapped gas was obtained by way of destructive or indirect methods. With absorption spectroscopy on the Lyman-α transition ($1S \rightarrow 2P$, $\lambda = 121.56\,\mathrm{nm}$) a very powerful tool was introduced to characterize and manipulate the gas. By measuring the absorption spectrum of trapped H$\uparrow$ and comparing it to a calculated spectrum, Luiten *et al.* [13] have been able to perform an *in situ* determination of n_0 and T with an accuracy of $\sim 25\,\%$, mainly determined by an imprecise knowledge of the shape of the laser beam.

The densities in trapped H$\uparrow$ are the highest densities ($\leq 3 \times 10^{14}\,\mathrm{cm}^{-3}$) so far attained in trapped gases. H$\uparrow$ is loaded in the magnetostatic trap by a cryogenic filling method. Energetic atoms that enter the trapping region thermalize with the He film that covers every cell surface. In this way densities around the trapping region can be built up which are sufficiently high to scatter atoms to states with energies that remain trapped. Due to the high densities in trapped H$\uparrow$, the system quickly reaches a state of thermal equilibrium through interatomic elastic collisions. Knowledge of the thermal distribution function enables the calculation of the statis-

tical properties of the gas and the absorption spectrum. Moreover, it enables the use of evaporative cooling, a cooling method that is based on the preferential removal of the most energetic atoms from the distribution and subsequent rethermalization to a new distribution with a lower temperature [14]. Atoms can be removed by letting the atoms with sufficient energy escape over the trap barrier. By actively lowering the trap barrier, the gas can be cooled even further. By this method, called "forced evaporative cooling", temperatures as low as $\sim 100\,\mu$K have been reached at a density of $\sim 8 \times 10^{13}\,\mathrm{cm}^{-3}$, an order of magnitude above the criterion for BEC [15]. Up until now evaporative cooling has been the only method to cool a gas of trapped H$\uparrow$. Using the interaction between the atoms and the resonant Lyman-α (L_α) light, the gas can also be cooled by way of optical methods.

1.2 Optical cooling

In recent years, ultra-low temperatures have also been achieved in gases of neutral atoms other than H using the techniques of optical cooling and trapping. Trapping of neutral atoms (except H) and ions is closely related to optical cooling. To be trapped, a beam of atoms must first be slowed down to energies sufficiently low that the atoms remain trapped. The first successful experiments to slow down and cool atoms by optical means were based on Doppler cooling, the preferential deceleration of atoms by an opposing laser beam with a frequency tuned slightly below the resonance frequency of an atom at rest. Because of the Doppler effect, atoms with a velocity opposing the beam scatter the light more strongly than atoms at rest or with a velocity parallel to the beam. By irradiating a gas of neutral atoms with 6 cw beams, all three degrees of freedom are cooled. At the intersection of the six beams, Cs atoms have been cooled to temperatures of several μK [16]. A very recent result is the report of a temperature of 700 nK in Cs [17].

Since the first Doppler cooling experiments, there has been an enormous development in the field of optical cooling and trapping [18, 19]. The reason that H has been largely excluded from these developments is the absence of a narrowband, cw light source generating L_α at sufficient intensity. L_α radiation can only be generated using non-linear optical techniques and pulsed lasers. Due to the collisional nature of a gas of trapped H$\uparrow$, however, Doppler cooling can also be performed with pulsed light. Irradiating the trapped gas with a *single, pulsed* beam of L_α radiation results in Doppler cooling of the whole gas since all degrees of freedom are coupled through elastic collisions. The high densities also result in optically thick samples which enables a study of the influence of optical thickness on the Doppler cooling mechanism. The lowest temperature that can be reached with Doppler cooling is

called the Doppler limit, T_D. For H, $T_D = 2.99\,\mathrm{mK}$. To reach lower temperatures, the collisional nature of trapped H$\uparrow$ has been exploited in a new cooling method based on an optical analogue of ordinary evaporative cooling, light-induced evaporative cooling (LIE). In this method, H$\uparrow$ is optically pumped to non-trapped H$\downarrow$ in regions of high potential energy thereby decreasing the average energy of the remaining trapped atoms and hence the temperature.

1.3 Outline of this thesis

The major part of this thesis is devoted to a discussion of the optical cooling methods that have been employed to cool a gas of magnetically trapped H$\uparrow$. Emphasis will be put on the physical mechanisms that underlie Doppler cooling and LIE in inhomogeneous magnetic fields and the limits of both cooling methods. Due to the optical thickness of the samples the light is attenuated as it propagates through the gas. This plays a crucial role in Doppler cooling and LIE.

In all calculations we assume the gas to have a thermal distribution. Since this is such an important assumption, we discuss in chapter 2 the statistical properties of a trapped thermal gas. These properties will be used in a calculation of the evolution of an H$\uparrow$ gas towards an equilibrium temperature when it is subject to intrinsic heating mechanisms and ordinary evaporative cooling. For this calculation the evaporative cooling rate is used as derived by Luiten *et al.* [20].

In chapter 3, a brief discussion is given of the experimental set-up. The optical set-up to generate narrowband Lyman-α (bandwidth $\sim 150\,\mathrm{MHz}$) is based on third-harmonic generation of pulsed UV light with a wavelength of 364.8 nm in gas mixtures of Kr and Ar. The experimental cell is located in the bore of a set of coils that generate the magnetic trapping field. The whole set-up is connected to a dilution refrigerator that keeps the cell temperature at $\sim 80\,\mathrm{mK}$. The cell contains cryogenic detectors to measure the total L_α absorption and the fluorescence from the sample. The optical access to the cell is designed such to minimize the heat load from room temperature radiation.

In the first half of chapter 4, the equations for the propagation of electromagnetic radiation in a spin-polarized gas of neutral atoms are derived. The calculation of the transmission spectrum, broadened by the Zeeman and Doppler shift, will be briefly discussed. In the second half, a simpler equation for the propagation of the light, neglecting effects due to polarization and dispersion, will be discussed. The physical picture that emerges for the attenuation of a light beam will be important for the understanding of the optical cooling experiments.

Chapter 5 deals with the first Doppler cooling experiments on atomic hydrogen.

A detailed analysis is given of Doppler cooling of a thermal gas of neutral atoms in an inhomogeneous magnetic field. It is first discussed for the optically thin limit and then for the optically thick limit to show the strong influence the optical thickness has on the Doppler cooling mechanism. Although the sample is optically thick, the effects of multiple scattering do not lead to a significant heating of the sample for the experimental range of densities and temperatures. The calculated Doppler cooling rate is then used to compute the evolution of n_0 and T of a thermal gas under irradiation at a constant frequency. These evolutions are compared to the experiments and turn out to give an accurate description of the observed phenomena.

Chapter 6 describes the LIE experiments. It begins with a derivation of the general equations for the change in internal energy of a thermal gas if a fraction of the atoms is optically pumped to non-trapped states. A condition is derived for the gas to stay in quasi-equilibrium during optical pumping. These equations are then applied to the optically thin case where, for the case of H, the cooling limit for LIE is shown to be close to the Doppler limit. In the optically thick case, the LIE cooling mechanism changes and the cooling limit is lowered. Finally, the evolution of n_0 and T for a thermal gas is calculated and compared to the experimental results. There is shown to be a reasonable agreement. Based on the theoretical analysis of LIE it is shown that the conditions for BEC cannot be realized with this optical cooling method.

Chapter 7 is a summary of the preliminary results of a study on the decay kinetics of trapped H$\uparrow$. These experiments show that apart from the intrinsic decay processes in a H$\uparrow$ gas, other decay mechanisms play a role in these experiments. Remarkable was the observation in nearly all experiments that the gas spontaneously cooled to a temperature significantly below the cell temperature after loading. The rest of this chapter is devoted to an explanation of this observation by a surface-related recombination mechanism that evaporatively cools the gas.

The Doppler cooling and LIE described in this thesis are the first optical cooling experiments performed on magnetically trapped H$\uparrow$. Rather than being aimed at reaching the lowest possible temperatures, they were aimed at demonstrating the feasibility of both methods for cooling a trapped hydrogen gas. At the time of the experiments, the models for Doppler cooling and LIE were not as extensively developed as in this thesis. With the better understanding we now have of both cooling methods, the experiments can be substantially improved. With the present knowledge of the frequency at which LIE optimally cools the gas, the μK regime should be within reach. Due to the decreasing dimensions of the trapped sample with decreasing temperature, the utmost will be required from the Lyman-α light source and detectors. At present, improvements to the optical set-up are in progress.

References

[1] T.J. Greytak and D. Kleppner, in *New Trends in Atomic Physics*, edited by G. Grynberg and R. Stora (North-Holland, Amsterdam 1984), p. 1125.

[2] I.F. Silvera and J.T.M. Walraven, in *Progress in Low Temperature Physics*, edited by D.F. Brewer (North-Holland, Amsterdam 1986), vol. 10, p. 139.

[3] C.E. Hecht, Physica **25**, 1159 (1959).

[4] W.N. Hardy, M.D. Hürlimann, and R.W. Cline, Jap. J. Appl. Phys. **26**, Suppl. 26-3, 2065 (1987).

[5] J.J. Berkhout, Ph.D. thesis, University of Amsterdam (1994).

[6] J.T.M. Walraven, in *Fundamental Systems in Quantum Optics*, edited by J. Dalibard, J.M. Raimond and J. Zinn-Justin (Elsevier, Amsterdam 1992) p.485.

[7] I.F. Silvera and J.T.M. Walraven, Phys. Rev. Lett. **44**, 164 (1980).

[8] R. Sprik, J.T.M. Walraven, and I.F. Silvera, Phys. Rev. Lett. **51**, 479 (1983).

[9] H.F. Hess, D.A. Bell, G.P. Kochanski, R.W. Cline, D. Kleppner, and T.J. Greytak, Phys. Rev. Lett. **51**, 483 (1983).

[10] P. Arvela, A.V. Frolov, S. Jaakkola, A.Ya. Katunin, I.I. Lukashevich, M. Mertig, A.I. Safonov, and E. Tjukanov, Physica B **194-196** (1994), 441.

[11] H.F. Hess, G.P. Kochanski, J.M. Doyle, N. Masuhara, D. Kleppner, and T.J. Greytak, Phys. Rev. Lett. **59**, 672 (1987).

[12] R. van Roijen, J.J. Berkhout, S. Jaakkola, and J.T.M. Walraven, Phys. Rev. Lett. **61**, 931 (1988).

[13] O.J. Luiten, H.G.C. Werij, I.D. Setija, M.W. Reynolds, T.W. Hijmans, and J.T.M. Walraven, Phys. Rev. Lett. **70**, 544 (1993).

[14] Harald F. Hess, Phys. Rev. B **34**, 3476 (1986).

[15] J.M. Doyle, J.C. Sandberg, I.A. Yu, C.L. Cesar, D. Kleppner, and T.J. Greytak, Phys. Rev. Lett. **67**, 603 (1991).

[16] C. Salomon, J. Dalibard, W.D. Phillips, A. Clairon, and S. Guellati, Europhys. Lett. **12**, 683 (1990).

[17] As reported by the National Institute of Standards and Technology in *The New York Times*, Science supplement, p. B5 (august 23, 1994).

[18] For an overview up to 1989, see the special issue on laser cooling and trapping of neutral atoms, edited by S. Chu and C. Wieman, J. Opt. Soc. Am. B **6**, No. 11 (1989).

[19] Les Houches 1990, *Fundamental Systems in Quantum optics*, edited by J. Dalibard, J.-M. Raimond, and J. Zinn-Justin (Elseviers, Amsterdam 1992).

[20] O.J. Luiten, Ph. D. thesis, University of Amsterdam (1993).

Chapter 2

Magnetostatically trapped H

The essential assumption in describing the optical cooling experiments on magnetically trapped atomic hydrogen is the assumption of a thermal (quasi-)equilibrium. It will be the subject of this chapter in which I will discuss the properties of a gas of magnetically trapped atomic hydrogen in thermal equilibrium, not irradiated by resonant light, and derive the equations describing the evolution of temperature T and central density n_0 under the influence of heating and cooling processes. In order to obtain the thermal distribution function, the potential energy of the trapped atoms must be known. For this purpose, first the ground state energy of H in a magnetic field and expressions for the magnetic field as a function of position will be given for the field configurations that were used for the Doppler cooling experiments and the LIE experiments. With the potential energy, the Boltzmann distribution function for trapped H can be obtained and several important properties, like the density distribution, the size of the sample and the average potential energy, can be calculated. The approach to thermal equilibrium is a non-trivial matter. As the atoms are loaded into the trap, they are expected to thermalize with the superfluid He-film, covering the cell walls. This behaviour was observed in the experiments of Luiten *et al.* [1]. In the present experiments, it was observed that the trapped gas cooled to a temperature substantially below the wall temperature. The main difference in the experimental conditions as compared to the work of Luiten *et al.* was a lower cell temperature ($T_w = 80\,\mathrm{mK}$) resulting from a reduction in spurious radiation from room temperature entering the cell. In chapter 7, a mechanism is discussed in which a sufficiently low cell wall temperature T_w results in evaporative cooling of a trapped H$\uparrow$ gas by recombination with H$\downarrow$ atoms adsorbed on the liquid He film covering the walls surrounding the gas. The thermal quasi-equilibrium that is then attained in the gas is determined by a balance between intrinsic heating and cooling mechanisms. I will discuss the intrinsic decay mechanisms of H and calculate their heating rate. After a brief outline of the evaporation model of Luiten

et al. [2], we give expressions for the evaporation rate and the evaporative cooling rate. If we assume that the gas stays close to internal thermal equilibrium, we can calculate the evolution of the T and n_0 under the influence of these heating and cooling mechanisms and obtain the equilibrium temperature T_{min}. These evolution equations will also play an important role in the calculation of T and n_0 during optical cooling.

2.1 Hyperfine energies and spin states

The energy of a single hydrogen atom in its ground state in a magnetic field $\vec{B}$ can be obtained from the following Hamiltonian

$$H_{hyp} = (g_e \mu_B \vec{s} - g_n \mu_n \vec{i}) \cdot \vec{B} + a_h \vec{i} \cdot \vec{s}, \tag{2.1}$$

where $\vec{i}$ and $\vec{s}$ are the proton spin and the electron spin respectively, μ_B and μ_n are the Bohr magneton and the nuclear magneton and g_e and g_n the corresponding g-factors. The strength of the interaction between $\vec{i}$ and $\vec{s}$ is given by the hyperfine splitting in zero field a_h, where $a_h/k_B = 0.068\,\mathrm{K}$. Diagonalizing H_{hyp} with respect to the $|m_s, m_i\rangle$-basis gives four hyperfine states, labeled a, b, c and d in order of increasing energy (see Fig. 2.1)

$$\begin{aligned} E_a &= -\tfrac{1}{4}a_h - \tfrac{1}{2}a_h[1 + (\mu^+ B/a_h)^2]^{1/2} \\ E_b &= \tfrac{1}{4}a_h - \tfrac{1}{2}\mu^- B \\ E_c &= -\tfrac{1}{4}a_h + \tfrac{1}{2}a_h[1 + (\mu^+ B/a_h)^2]^{1/2} \\ E_d &= \tfrac{1}{4}a_h + \tfrac{1}{2}\mu^- B, \end{aligned} \tag{2.2}$$

where $\mu^{\pm} = g_e \mu_B \pm g_n \mu_n$. The corresponding eigenstates are

$$\begin{aligned} |a\rangle &= \sin\theta|\uparrow\downarrow\rangle - \cos\theta|\downarrow\uparrow\rangle \\ |b\rangle &= |\downarrow\downarrow\rangle \\ |c\rangle &= \cos\theta|\uparrow\downarrow\rangle + \sin\theta|\downarrow\uparrow\rangle \\ |d\rangle &= |\uparrow\uparrow\rangle, \end{aligned} \tag{2.3}$$

where $\uparrow$, $\downarrow$, $\uparrow$ and $\downarrow$ denote $m_s = \frac{1}{2}$, $m_s = -\frac{1}{2}$, $m_i = \frac{1}{2}$ and $m_i = -\frac{1}{2}$ respectively. In this basis there are two mixed states, a and c, where the mixing angle

$$\tan 2\theta \equiv \frac{a_h}{\mu^+ B} \simeq \frac{a_h}{2\mu_B B}. \tag{2.4}$$

In a magnetic field minimum, only the low-field-seeking spin states $|c\rangle$ and $|d\rangle$ are trapped. When atoms in the high-field-seeking spin states $|a\rangle$ and $|b\rangle$ are generated in the trap by intrinsic decay mechanisms or by optical pumping, they are attracted

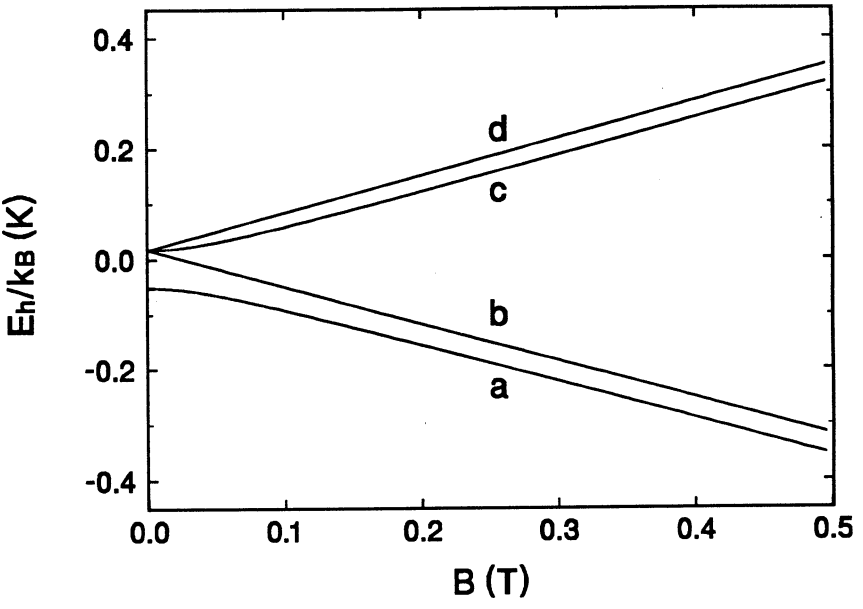

Figure 2.1: Hyperfine energies of atomic hydrogen in units of $k_B T$ as a function of magnetic field.

towards the walls of the cell where the magnetic field is highest. The potential energy of the atoms is measured with respect to the energy at the trap center

$$U_p(\vec{r}) = E_h(\vec{r}) - E_h(\vec{r}_0), \tag{2.5}$$

where h denotes one of the four possible hyperfine states.

2.2 The trapping field

To obtain the potential energy as a function of position, the magnetic field $\vec{B}(\vec{r})$ must be known. The trap that was used in the optical cooling experiments was built and used by Van Roijen *et al.* [3] and first used for spectroscopic experiments by Luiten *et al.* [1]. Trapping takes place in a local magnetic field minimum created by four parallel conductors and two dipole coils, the so-called Ioffe configuration [4]. The Ioffe trap was first proposed for neutral atom trapping by Pritchard [5]. It has a number of properties which are very well suited for trapping of hydrogen. Firstly, it enables the creation of a relatively large trapping depth (maximally 1.5 T for our trap), comparable to the binding energy $\varepsilon_a/k_B = 1.011(10)$ K of H on liquid ^{4}He [6], which

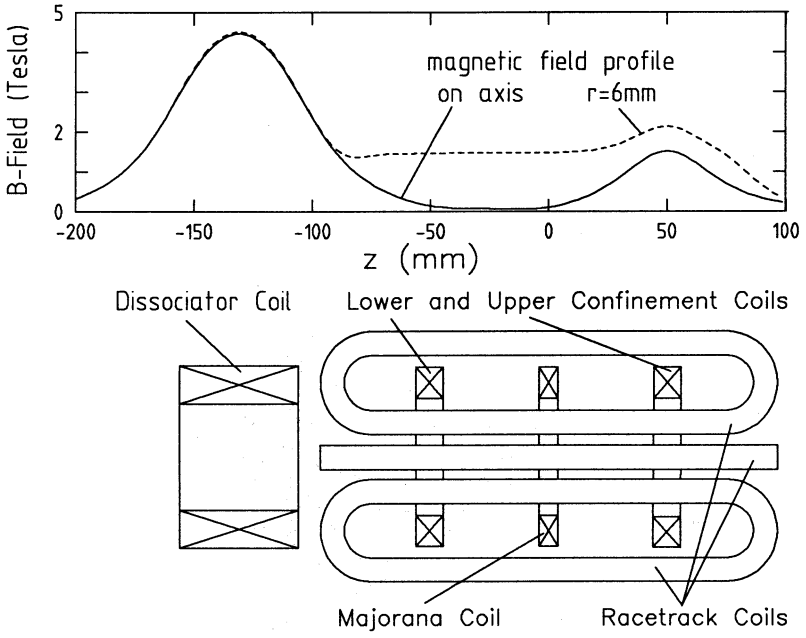

Figure 2.2: Cross section of the trapping magnet coils. The upper part of the figure shows the magnetic field for the "long trap" configuration.

covers the walls of the experimental cell. In thermal equilibrium the surface density σ of H in the presence of a trap with depth ε_{tr} is $\sigma = n_0 \lambda_{th} \exp[(\varepsilon_a - \varepsilon_{tr})/k_B T]$ where n_0 is the bulk density in the field minimum and λ_{th} is the thermal de Broglie wavelength. The magnetic field minimum greatly reduces the surface occupation which enhances the lifetime of the gas and enables one to cool to temperatures $T \ll \varepsilon_a/k_B$. Secondly, the magnitude of the magnetic field in the minimum ($|\vec{B}(\vec{r}_0)| = B_0$) of the Ioffe trap can be non-zero. For $B_0 \simeq 0$, the motion of the atom through the varying magnetic field can induce non-adiabatic spin-flips to non-trapped states, the so-called Majorana transitions [7]. Furthermore, a non-zero field minimum will spectrally separate the transitions which will be essential for the optical cooling experiments. Finally, the Ioffe trap with $B_0 > 0$ has only one central minimum which results in maximum localization of the atoms. As the gas cools down, it contracts around the field minimum. This effect plays a crucial role in determining n_0 and T of the gas.

Fig. 2.2 shows a cross section of the magnetic trap. The inner straight part of the four racetrack shaped coils constitute the four Ioffe bars. These are arranged symmetrically around the symmetry axis of the dipole coils at equal radial distances

with equal currents in alternating directions. Four dipole coils determine the axial field profile and provide axial confinement. The Majorana coil at $z = 0$ is used to adjust the value of B_0. The dissociator coil creates a high field ($\simeq 4.5$ T) in the region where H is produced. This field drives the H$\uparrow$-atoms towards the trapping region and separates them from the H$\downarrow$-atoms. The currents for the four dipole coils can be set independently. The four Ioffe bars create a quadrupole field which is zero on the symmetry axis and the magnitude of which increases linearly with radial distance ρ. Neglecting end-effects, the quadrupole field is everywhere perpendicular to the axis. The dipole coils produce a field which has a minimum near $z = 0$ along the axial direction, but a maximum in the radial direction. If the quadrupole field is strong enough, the sum of the two fields will have a minimum in the centre. From Maxwell's equations for a static, magnetic field in free space, the expression for $\vec{B}(\vec{r})$ in a Ioffe trap can be obtained as a power series in ρ and z [2, 8]. For low temperatures, when the gas resides near the field minimum ($\rho = 0, z = z_0$), it suffices to take into account only the leading terms in the expansion of the field around the trap center

$$\begin{aligned} B_\rho &= -\alpha\rho \sin 2\phi \\ B_\phi &= -\alpha\rho \cos 2\phi \\ B_z &= B_0 + \beta(z - z_0)^2, \end{aligned} \tag{2.6}$$

where $\beta = \frac{1}{2}(\partial^2 B_z(0,0,z)/\partial z^2)_{z=z_0}$ and α is the radial field gradient due to the quadrupole coils. The magnetic field strength is

$$B = |\vec{B}(\vec{r})| = \sqrt{(B_0 + \beta(z - z_0)^2)^2 + \alpha^2\rho^2}. \tag{2.7}$$

For positions so close to the minimum that $(B - B_0) \ll B_0$, the field can be approximated to lowest order in ρ and z by

$$B = B_0 + \beta(z - z_0)^2 + \frac{\alpha^2}{2B_0}\rho^2. \tag{2.8}$$

This so-called "harmonic" approximation is only valid if the temperature of the gas $T \ll T_0 \equiv \mu_B B_0/k_B$. For the trap configurations used in the optical cooling experiments $B_0 \simeq 0.1$ T, which means that the harmonic approximation can be used for $T \ll 67$ mK.

In the optical cooling experiments, two trap configurations were used which we will refer to as the "long trap" and the LIE trap. The so-called "long trap" was used for the Doppler cooling experiments. This trapping geometry was used for the first time in the experiments of Luiten *et al.* [2]. The elongated shape of the "long trap" maximizes the number of trapped atoms and, therefore the light absorption, for a given n_0 and T. The field profile for this configuration is drawn in the upper part of

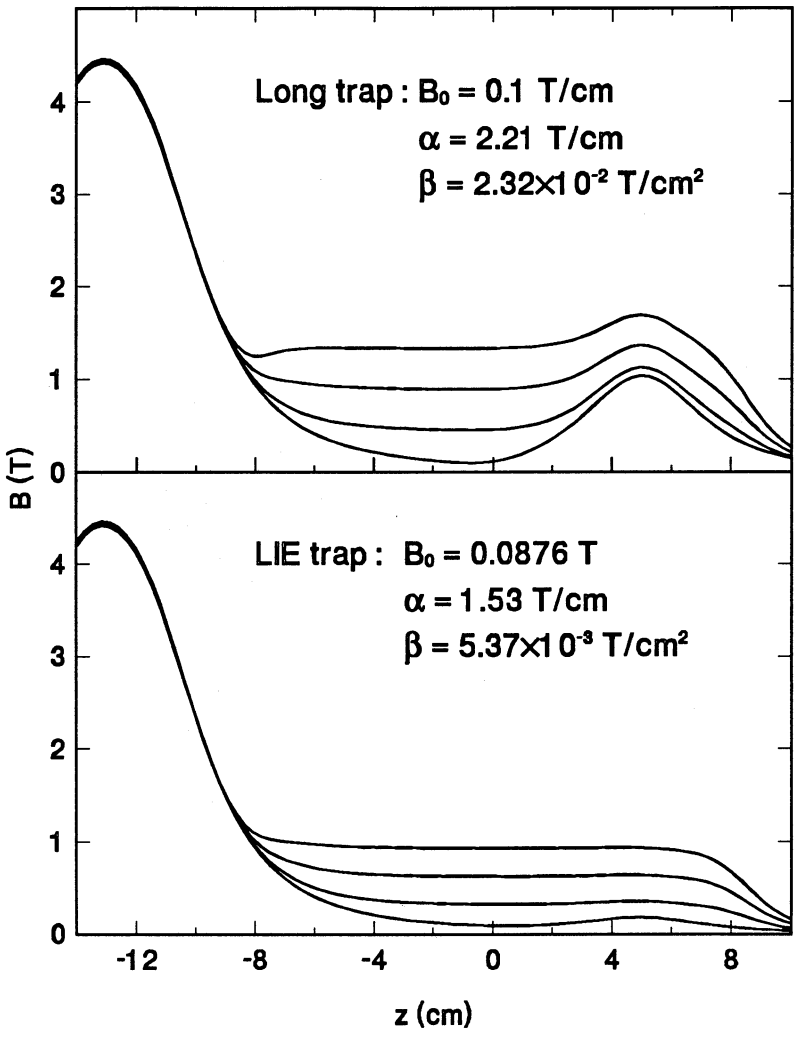

Figure 2.3: Trapping field for (a): the Doppler cooling experiments and (b): the LIE experiments. The field is plotted parallel to the z axis for $\rho = 0$, 2, 4 and 6 mm.

Fig. 2.2 and in more detail in Fig. 2.3(a). The magnetic field parameters of the "long trap" are $B_0 = 0.1\,\mathrm{T}$, $z_0 = -7.5\,\mathrm{mm}$, $\alpha = 2.21\,\mathrm{T/cm}$ and $\beta = 0.0232\,\mathrm{T/cm^2}$. The lowest field on the wall surrounding the trapping region is 1.33 T, giving a trapping depth of $\varepsilon_{tr}/k_B = 0.83\,\mathrm{K}$. The "long trap" has the nice feature that near the walls of the cell the equipotential lines almost run parallel to the wall. This feature is used in the description of evaporative cooling [2].

The shape of the LIE trap, used in the LIE experiments, resembles the shape of the "long trap" but with a smaller trap depth, $\varepsilon_{tr} = 60.4\,\mathrm{mK}$. This has two reasons: (a) after first loading a deeper trap, the gas is cooled by ordinary evaporative cooling and compressed to a density sufficiently high to apply LIE (see chapter 6) and (b) energetic H$\downarrow$ atoms, produced by dipolar decay (e.g. $dd \rightarrow ad$, see Sect. 2.4) with an energy $\varepsilon \simeq \mu_B B_0$ can escape from the trap. In Fig. 2.3(b), the magnetic field for the LIE trap is plotted. The magnetic field parameters are $B_0 = 0.0876\,\mathrm{T}$, $z_0 = 6.35\,\mathrm{mm}$, $\alpha = 1.53\,\mathrm{T/cm}$ and $\beta = 5.37 \times 10^{-3}\,\mathrm{T/cm^2}$.

2.3 Thermal equilibrium

2.3.1 Loading of the trap

Atomic hydrogen is produced by dissociation of H_2 in a cryogenic microwave discharge. The walls of the dissociator (see Sect. 3.3) are covered with a layer of solid H_2 covered by a liquid He-film. The process by which H is produced is not exactly known, but it is believed that a discharge is struck in the He vapour producing energetic free electrons and ions. These charges penetrate the He-film and dissociate H_2 molecules. The temperature of the dissociator during dissociation is $\simeq 0.6\,\mathrm{K}$. The discharge produces H in all four hyperfine states. Due to the strong magnetic field gradient, the H$\uparrow$ states are separated from the H$\downarrow$ states and driven through a narrow tube towards the trapping region.

All surfaces in the experimental cell are covered with a superfluid helium film. It is the low binding energy of H on a liquid He-film that enables loading of the trap. By inelastic collisions with the He-film the H atoms thermalize to the cell wall temperature T_w at which they can, in principle, be magnetically trapped. The minimum energy of the atoms, immediately after they have thermalized with the He-film, is ε_{tr}. To become trapped, the atoms must experience a decelerating collision, while crossing the trapping region, which reduces their total energy to $\varepsilon < \varepsilon_{tr}$. As soon as atoms are trapped, this loading process will be enhanced by elastic collisions with trapped atoms.

2.3.2 Distribution function

Trapped atomic hydrogen under the conditions of the experiments presented in this thesis can be described with the velocity-distribution function of a classical, ideal gas. Classical, because the interparticle distance is much larger than the thermal de Broglie-wavelength and ideal, because the interatomic distance is much larger than the range of the interaction between spin-polarized hydrogen atoms. In thermal

equilibrium the phase space distribution function of atoms in an external potential $U_p(\vec{r})$ is

$$f(\vec{r},\vec{p}) = n_0(2\pi m k_B T)^{-3/2}\exp[-(U_p(\vec{r}) + p^2/2m)/k_B T]. \tag{2.9}$$

The normalization constant n_0 is chosen in such a way that the total number of atoms $N = \int f(\vec{r},\vec{p})\, d^3r d^3p$. By integrating over the entire momentum space, the density distribution is obtained

$$n(\vec{r}) = n_0 \exp[-U_p(\vec{r})/k_B T], \tag{2.10}$$

where n_0 is the density at the potential energy minimum. For d state atoms $U_p(\vec{r}) = \mu_B(\vec{B}(\vec{r}) - B_0)$. For c state atoms, the potential energy has a more complicated B-dependence, but for $B_0 \geq 0.1$ T, which is the case for most experiments described in this thesis, $U_p(\vec{r})$ can be very well approximated by the same expression as for the d state atoms.

In Eq. 2.10, we have assumed the gas to be in an infinite space. In this case, the density of atoms at the position of the surrounding walls would be $n(B_w) = n_0 \exp[-\varepsilon_{tr}/k_B T_g]$, where T_g is the gas temperature. For the parameters of the "long trap" and $T_g \simeq 60$ mK (a typical temperature after loading of the trap), $n(B_w)/n_0 = 10^{-6}$. The density of atoms at the wall under these conditions is neglegible. For increasing T_g, the density at the wall will exponentially increase. For $T_g = 200$ mK (a typical temperature in the experiments of Luiten *et al.*), $n(B_w)$ is still small but, depending on the particular effect the wall has on the density distribution, quantities like the effective volume and the average internal energy of the gas can be strongly influenced. In the thesis of Luiten [2], these quantities were calculated for two extreme cases: a perfectly reflective wall and a perfectly absorptive wall. From this analysis, it can be concluded that for $T < 100$ mK the influence of the wall on $n(\vec{r})$, the effective volume and the internal energy is neglegibly small. The actual mechanism by which the wall will interact with the trapped gas is a complex phenomenon. In chapter 7, it is shown that for $T_w = 80$ mK, the wall does indeed act as an absorptive surface. By evaporative cooling (see Sect. 2.5), the gas is then cooled to $T \simeq 60$ mK after loading. This temperature is sufficiently low to neglect the effects due to the presence of boundary surfaces and integrate the distribution function over entire phase space to obtain Eq. 2.10 as the density distribution.

2.3.3 Effective volume and sample dimensions

For the calculation of trap averaged quantities, it is very useful to introduce the magnetic density of states $\rho_M(B)$, where $\rho_M(B')dB'$ is defined to be equal to the

infinitesimal volume in real space occupied by the positions $\vec{r}$ for which $B' < B(\vec{r}) \leq (B' + dB')$:

$$\rho_M(B') = \frac{d}{dB'} \int_{B(\vec{r})<B'} d^3r. \tag{2.11}$$

Using Eq. 2.7, the magnetic density of states for the Ioffe trap can be calculated

$$\rho_M(B) = \frac{4\pi}{\alpha^2\sqrt{\beta}}[(B - B_0)^{3/2} + B_0(B - B_0)^{1/2}]. \tag{2.12}$$

We will encounter Eq. 2.12 in the calculation of spectra (see Sect. 4.7) and in the calculation of evaporative cooling rates (see Sect. 2.5 and chapter 7). In this section, it will be used for the calculation of the effective volume.

The effective volume of order $\ell(= 1, 2, 3, \ldots)$ is defined by

$$V_{\ell e} = \int^{V_{geo}} [n(\vec{r})/n_0]^\ell d^3r, \tag{2.13}$$

where V_{geo} is the geometrical cell volume. The low temperatures in the optical cooling experiments allow approximating $V_{\ell e}$ by integrating over the entire space. In this case, $V_{\ell e}(T) = V_{1e}(T/\ell)$ and knowledge of $V_{1e}(= N/n_0)$ is sufficient to calculate every higher order effective volume. For the"long trap", the geometrical cell volume almost coincides with the surface of constant field $B = 1.33\,\mathrm{T}$. The first-order effective volume can be easily evaluated by rewriting the volume integral in Equation. 2.13 to a field integral using Eq. 2.12. This gives

$$V_{1e} = V_0 \left(\frac{T}{T_0}\right)^{3/2} \left[1 + \frac{3}{2}\left(\frac{T}{T_0}\right)\right], \tag{2.14}$$

where $V_0 = 2\pi^{3/2} B_0^{5/2} \alpha^{-2} \beta^{-1/2}$ and $T_0 = \mu_B B_0 / k_B$. For the experiments in the "long trap", $V_0 = 0.0473\,\mathrm{cm}^3$ and $T_0 = 67\,\mathrm{mK}$. For the LIE experiments, $V_0 = 0.147\,\mathrm{cm}^3$ and $T_0 = 59\,\mathrm{mK}$.

In an analogous manner, the characteristic dimensions of the sample can be calculated. The effective length L_s is defined by

$$L_s \equiv \int_{-\infty}^{\infty} [n(0, z)/n_0]\, dz. \tag{2.15}$$

For the trapping field, Eq. 2.7, this gives for a d state gas

$$L_s = \sqrt{\pi k_B T / \mu_B \beta}. \tag{2.16}$$

For the "long trap" with $\beta = 0.0232\,\mathrm{T/cm}^2$, $L_s/\sqrt{T} = 14\,\mathrm{cmK}^{-1/2}$. The effective cross-sectional area of the sample is defined by

$$A_s \equiv \int_0^{\infty} 2\pi\rho\, [n(\rho, z_0)/n_0]\, d\rho. \tag{2.17}$$

The effective radius is defined as

$$R_s \equiv \sqrt{A_s/\pi}. \tag{2.18}$$

Using Eq. 2.7, this gives for the trapping field

$$R_s = \sqrt{2}\frac{B_0}{\alpha}\left(\frac{T}{T_0}\right)^{1/2}\sqrt{1+\frac{T}{T_0}}. \tag{2.19}$$

For $T \ll T_0$, the trap potential is harmonic and for the "long trap" we obtain $R_s/\sqrt{T} = 0.25\,\mathrm{cmK}^{-1/2}$. The ratio of length to diameter of the sample is then independent of temperature and equal to $L_s/2R_s = 28$.

2.3.4 Internal energy

The internal energy of a classical, ideal gas in thermal equilibrium is

$$E = \int\int (U_p(\vec{r}) + p^2/2m) f(\vec{r},\vec{p})\, d^3r d^3p. \tag{2.20}$$

For a gas in an infinite space this can be rewritten to

$$E = N\left(\gamma_{1e} + \frac{3}{2}\right)k_B T, \tag{2.21}$$

where $\gamma_{1e} \equiv (T/V_{1e})(\partial V_{1e}/\partial T)$ is the average potential energy of a trapped atom. For d state atoms, we obtain

$$\gamma_{1e} = \tfrac{3}{2}\left(\frac{1+\frac{5}{2}T/T_0}{1+\frac{3}{2}T/T_0}\right). \tag{2.22}$$

The higher-order effective average potential energies, defined by

$$\gamma_{\ell e} k_B T \equiv V_{\ell e}^{-1}\int^{V_{geo}} U_p(\vec{r})[n(\vec{r})/n_0]^{\ell}\, d^3r, \tag{2.23}$$

can be simply obtained for the limit of infinite space from the first-order average potential energy, $\gamma_{\ell e}(T) = \gamma_{1e}(T/\ell)/\ell$. The second-order average potential energy γ_{2e} will be encountered in the discussion of the heating associated with particle loss due to inelastic binary collisions.

2.4 Elastic and inelastic collision rates

A gas of trapped H$\uparrow$ is subject to intrinsic decay processes that convert these states to H$\downarrow$ which has the lowest energy in a magnetic field. The densities in trapped H$\uparrow$ are sufficiently low that only binary collisions have to be considered. The interaction

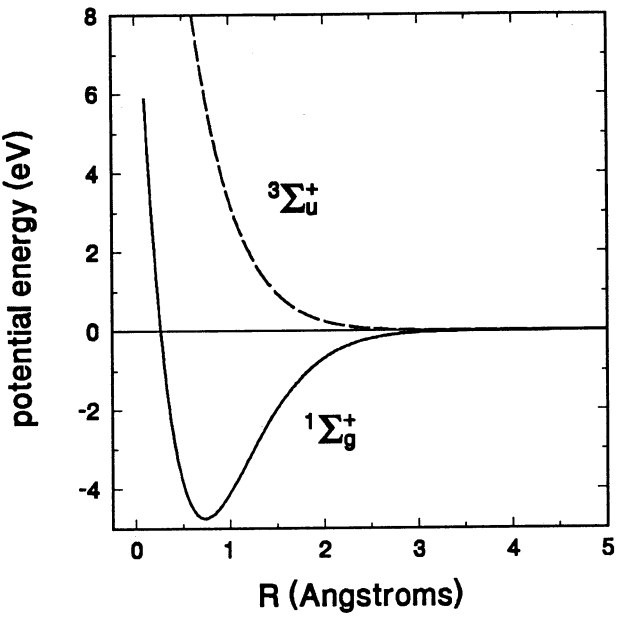

Figure 2.4: The singlet and triplet (dashed) interaction potential of atomic hydrogen.

between two H atoms is predominantly determined by the Coulomb interaction and can be calculated from first principles [9]. This makes the H-H pair potential the most accurately known potential to date. Although the different spin states of two interacting H atoms give rise to 16 interaction potentials (4×4 spin states) [10], it usually suffices to only consider the potentials for different electron spin. The Coulomb interaction then gives rise to the singlet potential for $S = 0$ and the triplet potential for $S = 1$, where $\vec{S} = \vec{s}_1 + \vec{s}_2$ is the sum of the electron spins. In Fig. 2.4, the singlet and triplet potentials are plotted as a function of interatomic distance. The triplet potential is essentially repulsive. It has the weakest attractive part of all interatomic potentials with a well depth of 6.46 K which is insufficient to support a bound state.

Two d atoms interact purely via the triplet potential. From this potential the s-wave scattering cross section for elastic collisions is calculated to be $\sigma_{el} = 8\pi a_T^2$ where $a_T = 0.72$ Å is the triplet scattering length [11]. Strictly speaking, this cross section only applies to the $T = 0$ limit, but due to the low temperature in the experiments contributions from higher order partial waves can be safely neglected. The elastic cross section for c-d collisions is $4\pi a_T^2$ due to the distinguishability of the atoms. The elastic cross section for c-c collisions is B-dependent and contains the singlet scattering length a_S. However, for $B \gg 0.05$ T, it can be approximated by $8\pi a_T^2$.

$10^{-13}\,\mathrm{cm}^{-3}\mathrm{s}^{-1}$. For the typical conditions $n_0 = 5 \times 10^{11}\,\mathrm{cm}^{-3}$ and $T = 50\,\mathrm{mK}$, we obtain $\tau_{se} \simeq 70\,\mathrm{s}$. These decay times show that after filling the trap, the c atoms will be rapidly lost due to spin exchange, leaving a gas of d atoms.

2.5 Evaporative cooling

Ordinary evaporative cooling of trapped atomic hydrogen has been experimentally studied and theoretically analyzed for the "long trap" by Luiten *et al.* [1, 2]. The optical cooling experiments were not aimed at studying evaporative cooling again and the subject may seem out of place in the present thesis were it not that evaporative cooling happened as a matter of course in *all* optical cooling experiments. In this section, we will briefly review the model for evaporative cooling as presented by Luiten [2] and give expressions for the evaporation rate. With these expressions the equilibrium temperature of a gas, after loading the trap, can be calculated.

The two essential assumptions for the evaporation model are:

(1) Every particle with total energy $\varepsilon = U_p(\vec{r}) + p^2/2m \geq \varepsilon_{tr}$ will reach the wall and be removed before colliding with another atom. This means that symmetries in the potential $U_p(\vec{r})$ are neglected which may give rise to conserved quantities of motion other than the total energy. An example of such a trajectory would be a wall-grazing orbit with conserved angular momentum. This trajectory has $\varepsilon > \varepsilon_{tr}$. Simulations have shown that these trajectories with other constants of motion than the total energy take up a neglegible part of phase space [15].

(2) During the evaporation the gas is in quasi-equilibrium. To understand the meaning of a quasi-equilibrium, we must first explain the idea of a pumped distribution i.e. a distribution truncated in phase space. For infinite space, the distribution function is given by Eq. 2.9. Now imagine that instantly a purely adsorptive wall is "switched on". On the basis of assumption (1), the distribution function, immediately after the wall is switched on, will be truncated in phase space by the condition $\varepsilon = U_p(\vec{r}) + p^2/2m \leq \varepsilon_{tr}$. The assumption of a thermal quasi-equilibrium means that during the evaporation the gas can be described by a pumped distribution with time-dependent n_0 and T. Of course, in reality the distribution will be distorted by the evaporation of atoms. Elastic collisions which do not produce atoms with $\varepsilon \geq \varepsilon_{tr}$ will tend to restore the pumped distribution. Since the thermalization rate τ_c^{-1} is much larger than the evaporation rate, the assumption of a quasi-equilibrium is well justified.

The evaporation rate is given by the rate at which atoms with a total energy $\varepsilon \geq \varepsilon_{tr}$ are produced by elastic s-wave collisions in the trapped gas. Just like in Eq. 2.25, the general equation for the elastic collision rate is written in terms of the

C.M. coordinates:

$$\Gamma_{ev} = \frac{n_0^2 \sigma_{el}}{2m}(2\pi m k_B T)^{-3} \int d^3r\, e^{-2U_p(\vec{r})/k_B T} \int d^3P\, e^{-P^2/mk_B T} \int d^3q\, q e^{-q^2/4mk_B T}, \tag{2.31}$$

where now the integration extends over a restricted region in phase space. This region is determined by the initial condition that both atoms must be from the truncated distribution

$$Pq|\cos\theta| \leq 2m(\varepsilon_{tr} - U_p(\vec{r})) - P^2 - \tfrac{1}{4}q^2, \tag{2.32}$$

where θ is the angle between P and q, and the final condition that one atom ends up with $\varepsilon \geq \varepsilon_{tr}$

$$Pq\cos\theta' \leq |2m(\varepsilon_{tr} - U_p(\vec{r})) - P^2 - \tfrac{1}{4}q^2|, \tag{2.33}$$

where θ' is the angle between P' and q' after the collision (notice that $q = q'$ for elastic collisions and $P = P'$ due to momentum conservation). The evaluation of this integral is a lengthy and tedious business and the interested reader is refered to Ref. [2] for the details of the calculation. In chapter 7 a similar (but even more lengthy) integral will be calculated to describe the collision rate between the trapped distribution and the distribution of atoms that have thermalized with the wall. The result of the integration in Eq. 2.31, evaluated under conditions 2.32 and 2.33, is

$$\dot{N}_{ev} = -\frac{4}{3\sqrt{\pi}} n_0^2 \sigma_{el} \bar{v}\, V_{3/2}, \tag{2.34}$$

where the volume V_ν is defined by

$$V_\nu \equiv \int_{U_p \leq \varepsilon_{tr}} d^3r \exp[-U_p(\vec{r})/k_B T] \int_0^{y_m} dy (y_m - y) y^\nu \exp(-y), \tag{2.35}$$

with $y_m(\vec{r}) = [\varepsilon_{tr} - U_p(\vec{r})]/k_B T$. Using the magnetic density of states $\rho_M(B)$, Eq. 2.12, the integral for V_ν can be calculated for $\nu = 3/2$ and $5/2$, values that are needed for $\dot{N}_{ev}$ and $\dot{E}_{ev}$ [2],

$$\begin{aligned} V_{3/2} = (9\sqrt{\pi}/8) V_0 (\xi\eta)^{-5/2} e^{-\eta} \{\eta - 5 + \tfrac{2}{3}\xi\eta(\eta - 4) + e^{-\eta} \times \\ [\tfrac{\eta^4}{24}(1 + \tfrac{8}{3}\xi) + \tfrac{\eta^3}{3}(1 + 2\xi) + \tfrac{3}{2}\eta^2(1 + \tfrac{4}{3}\xi) + 4\eta(1 + \tfrac{2}{3}\xi) + 5]\} \end{aligned} \tag{2.36}$$

and

$$\begin{aligned} V_{5/2} = (45\sqrt{\pi}/16) V_0 (\xi\eta)^{-5/2} e^{-\eta} \{\eta - 6 + \tfrac{2}{3}\xi\eta(\eta - 5) + e^{-\eta} \times \\ [\tfrac{\eta^5}{120}(1 + \tfrac{10}{3}\xi) + \tfrac{\eta^4}{12}(1 + \tfrac{8}{3}\xi) + \tfrac{\eta^3}{2}(1 + 2\xi) + 2\eta^2(1 + \tfrac{4}{3}\xi) + 5\eta(1 + \tfrac{2}{3}\xi) + 6]\}, \end{aligned} \tag{2.37}$$

where $\eta = \varepsilon_{tr}/k_B T$ and $\xi = B_0/(B_w - B_0)$. In the "long trap" $\eta T = 0.83$K and $\xi = 0.081$.

For $\eta > 8$, corresponding to temperatures in the experiment $T < 0.1\,\mathrm{K}$, we can neglect the $e^{-2\eta}$-terms. The evaporation rate can then be approximated by

$$\frac{\dot{N}_{ev}}{N} = -n_0 \sigma_{el} \bar{v}\, e^{-\eta} \frac{\eta - 5 + \frac{2}{3}\xi\eta(\eta-4)}{1 + \frac{2}{3}\xi\eta}. \tag{2.38}$$

The calculation of the evaporative cooling rate $\dot{E}_{ev}$ can be performed in a similar way as for the evaporation rate $\dot{N}_{ev}$. This gives

$$\dot{E}_{ev} = \dot{N}_{ev}\left(\varepsilon_{tr} + \frac{2V_{5/2}}{5V_{3/2}} k_B T\right). \tag{2.39}$$

For the range of temperatures of the optical cooling experiments $T < 0.1\,\mathrm{K}$, the following approximation can be used

$$\dot{E}_{ev} = \dot{N}_{ev}\left(\varepsilon_{tr} + k_B T \frac{\eta - 6 + \frac{2}{3}\xi\eta(\eta-5)}{\eta - 5 + \frac{2}{3}\xi\eta(\eta-4)}\right) = \dot{N}_{ev}(\eta + \kappa(\eta)) k_B T, \tag{2.40}$$

where ξ and η are defined as for $\dot{N}_{ev}$ (see Eq. 2.38) and $\kappa(\eta) k_B T$ is the average kinetic energy of the evaporating atoms. Notice that $\kappa(\eta)$ is not $\frac{3}{2}$ as for the bulk gas, but is smaller than one for the conditions of the experiment.

2.6 Heating mechanisms

The intrinsic processes that lead to the decay of a gas of trapped H$\uparrow$ also lead to heating of the gas. For a pure gas of d state atoms, magnetic dipolar relaxation, being a two-body decay mechanism, preferentially leads to a loss of atoms in regions of high density and, consequently, low potential energy. This results in an increase of the average internal energy of the remaining atoms and heating of the gas. The change in total internal energy of the gas due to dipolar decay is

$$\dot{E}_{dip}(T) = -\int d^3r\, G^d_{dd}(B,T)[U_p(\vec{r}) + \tfrac{3}{2} k_B T] n_d^2(\vec{r}). \tag{2.41}$$

Due to the weak temperature dependence of G^d_{dd} for $T \to 0$, this can be rewritten to

$$\dot{E}_{dip} \simeq -n_0^2 \langle G^d_{dd}\rangle V_{2e}\Big(\frac{T/2}{V_{2e}}\frac{\partial V_{2e}}{\partial T} + \frac{3}{2}\Big) k_B T = \dot{N}_{dip}(\gamma_{2e} + \tfrac{3}{2}) k_B T, \tag{2.42}$$

where $\gamma_{2e} k_B T$ is the second-order average potential energy (see Eq. 2.23).

In Eq. 2.42 we have considered the dipolar heating due to the loss of atoms. For the decay channels in which one atom decays to H$\downarrow$ state and the other atom to a H$\uparrow$ state there is an additional heating due to the energy difference between initial and final spin states, the so-called recoil heating

$$\begin{aligned} \dot{E}_{rec} &\simeq \int d^3r\, G_{rec}(B,T) \mu_B B(\vec{r}) n(\vec{r})^2 \\ &\simeq \langle G_{rec}\rangle n_0^2 V_{2e}\Big(\gamma_{2e} + \frac{\mu_B B_0}{k_B T}\Big) k_B T, \end{aligned} \tag{2.43}$$

where $G_{rec}(B,T) = G_{dd,ad}(B,T) + G_{dd,ac}(B,T)$. Using the values for $G_{dd,ad}$ and $G_{dd,ac}$ from Ref. [13], it turns out that for the "long trap" the recoil heating becomes comparable to the dipolar heating $\dot{E}_{dip}$ for temperatures $T \lesssim 5\,\mathrm{mK}$. In the LIE experiments, which were aimed at reaching temperatures $T \ll 5\,\mathrm{mK}$, the recoil heating was eliminated by adjusting the trap parameters such that $\varepsilon_{tr} < \mu_B B_0$ so that recoil products leave the trap. In the calculation of the evolution of T and n_0 during Doppler cooling in the "long trap", the recoil heating is included.

2.6.1 Evolution of temperature and density

In the experiments, a thermal gas of trapped H↑ is subject to intrinsic decay processes and evaporative and optical cooling. All these processes change the total number of trapped atoms N and the total internal energy E, where

$$E = N(\gamma_{1e} + \tfrac{3}{2})k_B T. \tag{2.44}$$

If the gas remains close to thermal equilibrium during during these processes, the change in temperature of the gas can be obtained from Eq. 2.44:

$$\dot{T} = \frac{\sum_i \dot{E}_i - \sum_i \dot{N}_i k_B T(\gamma_{1e} + \frac{3}{2})}{N k_B(\gamma_{1e} + T\partial\gamma_{1e}/\partial T + \frac{3}{2})}, \tag{2.45}$$

where the summation is over the different processes that change N and/or E of the gas. For $T \ll \varepsilon_{tr}/k_B$, $T\partial\gamma_{1e}/\partial T \ll \gamma_{1e}$ so that the heat capacity of the gas $Nk_B(\gamma_{1e} + T\partial\gamma_{1e}/\partial T + \frac{3}{2}) \simeq 3Nk_B$. Equation 2.45 is the central equation with which the evolution of T and n_0 of the trapped gas will be calculated under the influence of dipolar relaxation, evaporative cooling, Doppler cooling and LIE. The evolution for Doppler cooling and LIE will be calculated in chapters 5 and 6.

We will now calculate the equilibrium temperature T_{min} of a gas of trapped H subject to evaporative cooling and dipolar heating. This corresponds to the situation where the gas is not irradiated and the walls act like perfect absorbers. For the case that $T < 0.1\,\mathrm{K}$, Eq. 2.45 can be rewritten to

$$\frac{\dot{T}}{T} = \left(\frac{\eta^* - \gamma_{1e}}{\gamma_{1e} + \frac{3}{2}}\right)\frac{\dot{N}}{N}. \tag{2.46}$$

where η^* is given by

$$(\eta^* + \tfrac{3}{2}) = [\eta + \kappa(\eta)]\frac{\dot{N}_{ev}}{\dot{N}} + (\gamma_{2e} + \tfrac{3}{2})\frac{\dot{N}_{dip}}{\dot{N}}. \tag{2.47}$$

For $\dot{N}_{dip} \ll \dot{N}_{ev}$, $\eta = \eta^* + \frac{3}{2} - \kappa(\eta)$. The condition for the equilibrium temperature follows from $\dot{T} = 0$ or

$$\eta^* = \gamma_{1e}. \tag{2.48}$$

After substitution of $\dot{N}_{dip}$ (from 2.28) and Eq. 2.38 in condition 2.48, the equilibrium temperature can be numerically calculated. For the "long trap", we obtain a minimum temperature $T_{min} = 62\,\mathrm{mK}$ and for the LIE trap $T_{min} = 5\,\mathrm{mK}$. Notice that these temperatures only hold for the balance between evaporative cooling and dipolar heating. Just after loading the trap, there will be an enhanced decay due to spin exchange. This will slightly increase T_{min}. In Sect. 7.1.3 we will come back to this.

At T_{min}, the density of the trapped gas only decreases. In other words, the evolution of the gas is straight downwards in the T-n_0 plane. Cooling of a gas of H$\uparrow$ should ideally take place at increasing density to enter the regime of quantum degeneracy. Using Eq. 2.46, we can derive a condition that η^* must satisfy to cool at constant n_0. From $N = n_0 V_{1e}$ and $V_{1e} \sim (T)^{3/2}$ for $T \ll T_0$, we obtain

$$\frac{\dot{N}}{N} = \frac{\dot{n}_0}{n_0} + \frac{3}{2}\frac{\dot{T}}{T}. \tag{2.49}$$

To cool at constant n_0, one must have $\dot{T}/T = \frac{2}{3}\dot{N}/N$. Combined with Eq. 2.46, this puts the following condition on η^*

$$\eta^* = 3.5. \tag{2.50}$$

where we have assumed $T \ll T_0$ so that $\gamma_{1e} = \frac{3}{2}$. In the "long trap", $\kappa = 0.9$ for $T = 50\,\mathrm{mK}$ so η must be 4.1 to cool at constant n_0. In chapter 6 on LIE, we will see that the average kinetic energy of atoms that have been optically pumped to H$\downarrow$ states is $\frac{3}{2}k_B T$. For this case, cooling at constant n_0 is achieved by $\eta = 3.5$.

References

[1] O.J. Luiten, H.G.C. Werij, I.D. Setija, M.W. Reynolds, T.W. Hijmans, and J.T.M. Walraven, Phys. Rev. Lett. **70**, 544 (1993).

[2] O.J. Luiten, Ph. D. thesis, University of Amsterdam (1993).

[3] R. van Roijen, J.J. Berkhout, S. Jaakkola, and J.T.M. Walraven, Phys. Rev. Lett. **61**, 931 (1988).

[4] Y.V. Gott, M.S. Ioffe, and V.G. Tel'kovskii, Nucl. Fusion, 1962 Suppl., Pt. 3, 1045 (1962).

[5] D.E. Pritchard, Phys. Rev. Lett. **51**, 1336 (1983).

[6] W.N. Hardy, M.D. Hürlimann, and R.W. Cline, Jap. J. Appl. Phys. **26**, Suppl. 26-3, 2065 (1987).

[7] T.H. Bergeman, P. McNicholl, J. Kycia, H. Metcalf, and N.L. Balazs, J. Opt. Soc. Am. B **6**, 2249 (1989).

[8] T. Bergeman, G. Erez, and H.J. Metcalf, Phys. Rev. A **35**, 1535 (1987).

[9] W. Kolos and L. Wolniewicz, Chem. Phys. Lett. **24**, 457 (1974); W. Kolos and L. Wolniewicz, J. Mol. Spectrosc. **54**, 303 (1975).

[10] J.E. Harriman, M. Twerdochlib,M.B. Milleur, and J.O. Hirschfelder, Proceedings of the N.A.S. **57** (1967), 1558.

[11] D.G. Friend and R.D. Etters, J. Low Temp. Phys. **39**, 409 (1980).

[12] A. Lagendijk, I.F. Silvera, and B.J. Verhaar, Phys. Rev. B **33**, 626 (1986).

[13] H.T.C. Stoof, J.M.V.A. Koelman, and B.J. Verhaar, Phys. Rev. B **38**, 4688 (1988).

[14] R. van Roijen, Ph. D. thesis, University of Amsterdam (1989).

[15] E.L. Surkov, J.T.M. Walraven, and G.V. Shlyapnikov, Phys. Rev. A **49**, 4778 (1994).

Chapter 3

Experimental set-up

3.1 Introduction

Performing optical cooling and spectroscopy on magnetically trapped H↑ poses a number of experimental challenges, specific to this simplest member of the atomic species. To excite the Lyman-α transition ($1S \rightarrow 2P$, $\lambda = 121.56\,\mathrm{nm}$) vacuum ultraviolet (VUV) radiation is needed for which no lasers are commercially available. At present, this radiation can only be generated using pulsed lasers and non-linear optical techniques. In Sect. 3.2, the optical set-up is discussed that is used in the absorption spectroscopy and the optical cooling experiments. This set-up meets a number of requirements that are essential for performing optical cooling, like a bandwidth comparable to the natural linewidth of the L_α transition ($\Gamma/2\pi = 100\,\mathrm{MHz}$) and sufficient intensity.

The optical cooling experiments were performed in the same experimental cell as the first spectroscopic experiments on H↑ [1]. The design of this cell and the L_α detectors that were used to measure the transmission and the fluorescence of the sample are discussed in Sect. 3.3. These detectors meet the requirements of taking up as little space as possible and generating a signal under conditions (large magnetic field and sub-Kelvin temperatures) at which the standard photon counting devices, like photomultipliers and microchannel plates, cease to operate.

Allowing optical access to the experimental cell at a temperature of $\simeq 100\,\mathrm{mK}$, requires an extremely clean vacuum, not only because VUV light is absorbed in gases like air and water vapour, in organic solvents, oil, grease and in most solid materials (the only transparent materials that have a reasonable L_α transmission are MgF_2 and LiF), but also to prevent the formation of cryo-deposits on the MgF_2 entrance window to the cell over a period of three months (the average duration of an experiment). As an improvement to the optical access as used by Luiten *et al.*

[1] extra measures were taken to prevent room temperature radiation from entering the cell. In Sect. 3.4, we discuss the optical access that was designed to merge the optical and cryogenic techniques into a peaceful symbiosis.

3.2 Optical set-up

3.2.1 VUV generation

In the optical experiments with trapped H↑, a number of requirements have to be met in the generation of Lyman-α light. In the first place, the light must have a bandwidth comparable to the natural linewidth of the L_α transition to perform accurate spectroscopy and to enable optical cooling. Secondly, the intensity must be stable and sufficiently large to produce an optical cooling rate that can oppose the intrinsic heating mechanisms of the gas. Thirdly, the light must be tunable over the full spectral range of the trapped atoms. By way of absorption spectroscopy, temperature and density of the gas can then be determined. Finally, the method must be relatively easy to operate and reliable over periods of several months, the average duration of a cryogenic measuring run.

L_α light at sufficient intensity can, at present, only be generated using pulsed lasers and non-linear optical techniques. Guided by the requirement of reliability, a choice was made for non-resonant, third-harmonic generation in phase-matched Kr/Ar gas mixtures [2, 3, 4]. The 364.8 nm light that is used in the tripling, is generated by frequency doubling of 729.6 nm light in the optical set-up drawn in Fig. 3.1. Narrowband cw light of 729.6 nm (bandwidth $\simeq$ 1.5 MHz) is generated by a ring dye laser (Coherent 699-21), pumped by a Ar^+ ion laser (Coherent Innova 200). Cooling the dye (Pyridine 2) to 9 °C results in a single-mode output of $\simeq$ 750 mW at 6.5 W pump power. After passing an optical isolator, the 729.6 nm light is pulse amplified in three Rhodamine 700 pulsed dye amplifier stages (Lambda Physik 2003). A XeCl excimer laser (Lambda Physik LPX 210i, $\lambda = 308$ nm) is used as a pump source. The relatively long pulses of $\simeq$ 20 nsec ($\simeq$ 400 mJ per pulse) result in the smallest possible bandwidth of the amplified light. The maximum repetition rate is 100 Hz. The amplified pulses are frequency doubled in a KDP crystal and, subsequently, pulse-amplified once more in a DMQ dye cuvette. At a repetition rate of 50 Hz, the generated 364.8 nm light has an energy of $\simeq$ 18 mJ per pulse. The bandwidth of this light, as determined by using a confocal etalon with a Free Spectral Range (FSR) of 150 MHz, is $40 - 60$ MHz. From this we obtain an estimate for the upper bound of the L_α bandwidth of 150 MHz.

The 364.8 nm light is focused by a $f = 15$ cm lens into a the tripling cell, filled

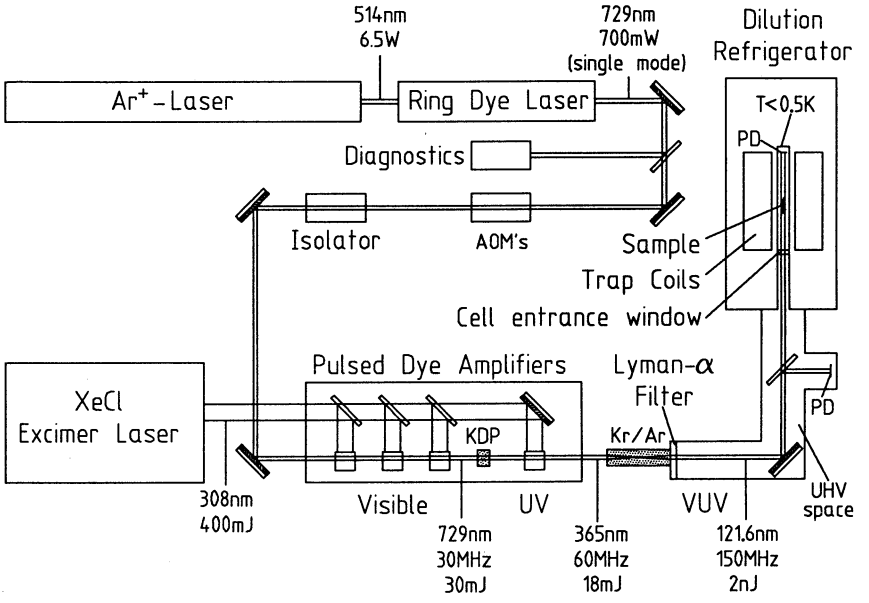

Figure 3.1: Optical set-up to generate the 365 nm used in the third-harmonic generation.

with a gas mixture of, typically, 160 mbar Kr and 480 mbar Ar. Here Kr is the non-linear medium for third-harmonic generation, whereas Ar is added for phase-matching purposes [5]. Under typical conditions, the generated L_α power is 2×10^9 photons per 10 nsec pulse. After the tripling cell, the VUV is separated from the UV by using the difference in refraction and dispersion for the two wavelengths as the light passes through two MgF_2 lenses. The L_α light is subsequently directed into the cryostat by way of a 45° mirror.

The present Kr/Ar mixture was determined after an optimization of the L_α yield for the present tripling set-up [6]. It was found that the generated L_α power is limited by electric breakdown in the gas mixture at too large pump intensities. This results in large fluctuations of the L_α intensity. To adjust the incoming UV intensity, a diaphragm is placed in front of the tripling cell. Also it was observed that the UV light showed an increasing higher-order mode structure with aging amplifier dyes which has a negative effect on the conversion efficiency and the threshold for electric breakdown. Increasing the conversion efficiency by an increase in Kr density is also limited by electric breakdown, since the threshold for breakdown is inversely proportional to the Kr pressure [7, 8]. Currently, the tripling set-up is being improved by enlarging the focal regime where the third harmonic generation

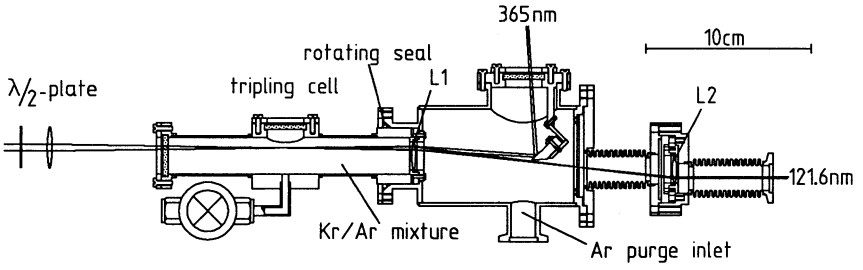

Figure 3.2: Tripling cell and monochromator in which the separation of the UV beam from the copropagating VUV beam takes place.

takes place. To prevent damage to the entrance and exit windows, the size of the tripling cell has been increased accordingly. An alternative, particularly efficient scheme for the generation of L_α radiation has been described by Marangos *et al.* [9]. This scheme, based on resonant third-order sum-difference frequency conversion in krypton, requires two dye lasers and is relatively more complex to operate than the present tripling set-up.

3.2.2 UV - VUV separation

In the tripling cell, the VUV radiation is generated with a conversion efficiency of $\sim 10^{-7}$. The UV beam exits the triple cell along the same path as the VUV beam and must be separated before entering the experimental cell to prevent a strong heating. To do this, use is made of the difference in refraction of two MgF_2 lenses for both wavelengths. In Fig. 3.2, we show the experimental set-up in which the UV-VUV separation takes place. The UV and the VUV beam exit the tripling cell off-axis through a MgF_2 lens $L1$ which focuses the VUV beam onto a pinhole while deflecting the UV beam onto a mirror and subsequently to a beam dump. This set-up has the advantage that a clean part of lens $L1$ can be obtained by a simple rotation of the tripling cell in the monochromator housing when the transmission of $L1$ has degraded due to the intense UV irradiation. Behind the pinhole, the L_α light passes a second MgF_2 lens ($L2$) off-axis which collimates the L_α beam and results in additional spectral filtering. The UV-intensity has now been reduced by at least 9 orders of magnitude. In front of the tripling cell, a half-wave plate is used to vary the orientation of the linear polarization of the incoming UV light. The generated L_α light is linearly polarized, but its polarization in the experimental cell was observed to be strongly influenced by the alignement. This is believed to be

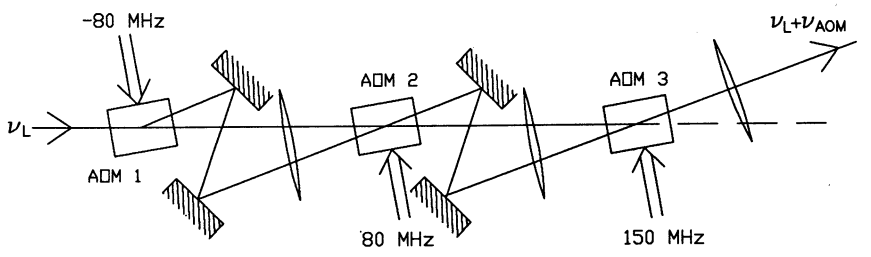

Figure 3.3: Set-up of three AOM's to change the frequency by −80 MHz, 80 MHz and 150 MHz.

due to the dielectric coating of the 45° mirror. By adjusting the half-wave plate the polarization of the L_α light can be changed from left-circular, through linear to right-circular.

The lens $L2$ is placed in a (x, y, z)-translational stage, attached to the monochromator and the clean vacuum of the optical access by way of bellows. This way the L_α beam can be collimated and aligned. Lens $L2$ is attached to its holder by way of an indium seal and separates the monochromator volume from the clean vacuum of the light guide leading to the experimental cell. The monochromator volume is constantly flushed with pure Ar at a pressure of $\simeq$ 20 Torr to prevent impurities sputtered by the UV beam to coat the lenses. In the clean vacuum, approximately 75 cm below the H sample, a 45°, high-quality VUV mirror (reflectivity $\simeq$ 85 %) is placed to deflect the L_α light towards the cell. In Sect. 3.4, the different parts in the light guide between the 45° mirror and the H sample will be discussed.

3.2.3 Frequency tuning and stability

To make a scan across the spectrum of the trapped gas, the output frequency from the ring dye laser (RDL) is tuned over a six times smaller frequency interval. The time it takes to scan the RDL depends on the magnitude of the frequency interval and the desired number of measurements taken at each frequency for averaging purposes. Typically, scans over the full H spectrum were performed in $30 - 40$ s. To measure processes taking place on shorter timescales or to be able to quickly switch to a different frequency while irradiating on another frequency, we use a configuration of three acousto-optic modulators (AOM) as sketched in Fig. 3.3. The three AOM's change the incident frequency by −80 MHz, 80 MHz and 150 MHz and are arranged such that the direction of the outgoing beam is the same when any one of the

three AOM's is switched on. This set-up enables pulse to pulse switching between three VUV frequencies with a frequency difference between them of 0.96 GHz and 0.42 GHz respectively. In the Doppler cooling experiments, this technique was used to rapidly record the transmission at two other frequencies while Doppler cooling the sample at one frequency. Using three-point spectroscopy (see Sect. 4.5), the evolution of density and temperature of the gas during Doppler cooling could then be obtained. Because of the long distance to the pulsed dye amplifier chain and the H↑ sample (7 m and 15 m, respectively), the beam alignment is rather stringent. To prevent changes in the beam alignement due to heating of the AOM's, the AOM's were only driven during 0.3 msec pulses, synchronized with the excimer laser pulses.

For a determination of the frequency, part of the 729 nm light is split off to a commercial wavemeter (Burleigh WA-20). The 0.3 GHz-resolution of this wavemeter is, however, insufficient for an accurate determination of the frequency. Since we would like to know the L_α frequency with an accuracy of approximately the natural linewidth of the L_α transition (100 MHz), the frequency of the light from the RDL should be determined with $\simeq$ 20 MHz accuracy. For this purpose, we made two confocal Fabry-Perot etalons, one piezo-driven etalon scanning $\sim$ 6 GHz at a repetition rate of 10 Hz and the other etalon without piezo, serving as a calibration standard correcting possible drifts in the piezo material. Both etalons have a Free Spectral Range (FSR) of 3.0 GHz and a measured finesse of 175, resulting in a resolution better than the required 20 MHz. Since the resolution of the wavemeter is smaller than the FSR of the etalons, there is no ambiguity as to which order of the etalon is observed. The frequency of the cw light can now be obtained from the applied piezo voltage. To minimize thermal drift and deviations from linearity, the etalons are made from invar which has a low thermal expansion coefficient. Similar motivations and the need for a low power dissipation led us to the choice for the piezo material (Quartz & Silice, P7-62). The piezo-driven etalon was measured to scan $\sim$ 18 MHz/V with a deviation from linearity of less than 5 MHz over a frequency range of 6 GHz. Both etalons are mounted in an extremely stable thermostat, developed in our laboratory by Michels and Van Lieshout for critical point experiments. The short-term stability of this thermostat is better than 20 μK/hour. To determine the long-term stability, the drift of the etalon transmission peaks was monitored with respect to a two-photon transition frequency in potassium ($4^2S_{1/2} \rightarrow 6^2S_{1/2}$, [10]). Over a period of 10 days, the tunable etalon had a drift of 365 kHz/hour, while the fixed etalon remained stable within 5 MHz.

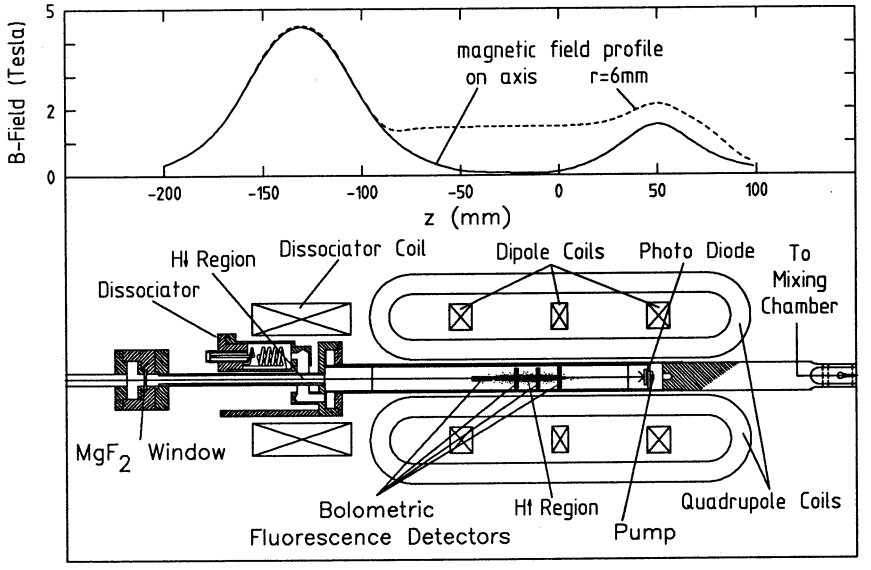

Figure 3.4: Drawing of the experimental cell. In reality the right side is the top side connected to the mixing chamber. The field profile of the "long trap" is also shown.

3.3 The experimental cell

To achieve the temperatures needed to stabilize H and to load a trap through the interaction with liquid He covered surfaces, the cell is connected to the mixing chamber of a ^{3}He/^{4}He-dilution refrigerator (Oxford Instruments). The maximum cooling power of the dilution unit is 250 μW at a mixing chamber temperature of 100 mK and a circulation rate of 500 μmole/s. The experimental cell is placed in the 16 mm bore of the magnetic trap that was designed and built by Van Roijen *et al.* [11]. The size of the bore put severe dimensional constraints on the design of the cell. The cell, that was designed and built by Luiten *et al.*, was used in the first spectroscopic experiments [1] and in the optical cooling experiments [12]. In Fig. 3.4, the experimental cell is drawn. The right side of the picture is actually the top side of the apparatus, connected to the mixing chamber of the dilution refrigerator. Also drawn are the four racetrack shaped quadrupole coils with the two confining dipole coils running through them. The dipole coil in the middle is the Majorana coil, meant to adjust the field in the center of the trap. Below the confinement coils is the dissociator coil, creating a high magnetic field to separate the high-field-seeking from the low-field-seeking atoms. All the coils can be separately driven. The entire

coil configuration, placed in a stainless steel can, is connected to the bottom of the main He bath at a temperature of 4.2 K.

In the region of confinement, the bore of the magnet has a diameter of 16 mm and 40 mm in the bore of the dissociator coil. To optimize the trapping depth, the diameter of the trapping region should be as large as possible with no objects protruding into this region. The upper part consists of a solid rod with an outer diameter of 15 mm, made of high purity copper [13], and connected to the mixing chamber by an 8 mm screwed joint. Soft-soldered to the solid rod is a copper tube with an outer diameter of 15 mm and an inner diameter of 13 mm. This copper tube has been given a special annealing treatment to optimize the thermal conductivity [6]. In the present experiments, this high thermal conductivity resulted in a temperature gradient of $\sim$ 10 mK over the full length of the cell (46 cm) extending from the mixing chamber to the holder for the MgF_2 window. The average temperature of the cell was 80 mK.

The lower part of the cell contains the MgF_2 window holder, the dissociator and a trigger bolometer. The entrance window (10 mm o.d., 1 mm thickness, 60 % L_α transmission at room temperature) separates the cell volume from the clean VUV vacuum and is clamped with indium in a brass window flange. The flange is connected by way of a copper tube (6 mm o.d., 4 mm i.d.) to the rest of the cell. The dissociator is a copper, resonant helical cavity with an inner diameter of 13 mm and height of 21 mm based on the design by Van Roijen *et al.* [14]. At low temperatures the cavity has a resonant frequency of 795 MHz and a quality factor $Q \simeq 400$. In Sect. 2.3.1 a more elaborate discussion of the dissociating mechanism is given. Energetic H and He atoms flow out of the dissociator to the cell through a thin-walled CuNi tube (6 mm o.d., 0.2 mm wall thickness). The purpose of this tube is to thermally isolate the dissociator, which is at $T \simeq 0.6$ K, from the rest of the cell, which is at $T = 80$ mK. The transport tube is constructed in such a way that there is no direct path to the trapping region. During their transport the H atoms collide with the He-coated walls and are cooled to the cell temperature, while the He atoms are absorbed into the He film. Under typical conditions this set-up produces 10^{12} H$\uparrow$ atoms/s. At the center of the dissociator coil, approximately 12 mm off-axis, a trigger bolometer is mounted to remove the remaining H$\downarrow$ atoms. A trigger bolometer is a small resistor suspended by two thin conductive wires. By dissipating so much power in the resistor that more He is evaporated than can be replenished by superfluid film flow along the wires, the resistor is made bare, thereby creating a site for enhanced recombination. A similar bolometer is also placed in the trapping region behind the photodiode. In the experiments of Luiten *et al.* this cell bolometer was used to trigger the evaporative cooling. In the optical cooling

experiments this bolometer is not used.

3.3.1 VUV detection at low temperatures

Detection of VUV radiation, produced in a cryogenic environment, can be performed locally or at a distance. The first method requires cryogenic VUV detectors, the second a method to guide the signal out of this environment. High-resolution detection (photon counting) of VUV is commonly performed by photomultipliers or microchannel plates. The behaviour of photomultipliers at low temperatures is not well understood. Certain photomultipliers function properly down to liquid nitrogen temperature, while others cease functioning completely at much higher temperatures [15]. Microchannelplates have been succesfully employed down to 30 K [16]. A severe drawback of both detectors is the strong sensitivity to magnetic fields. For photomultipliers in particular, fields of several gauss are sufficient to decrease the sensitivity by orders of magnitude. In the present experimental set-up, these photon counting devices would have to be placed at a distance from the trap, sufficiently large that the magnetic field has a neglegible influence on the detection. This would require guiding the light out through a clean vacuum or converting the VUV to a visible frequency and transporting this light through glass fibers. The dimensional constraints made us choose a method that would take up as little space as possible. Two different detectors were used: semiconductor photodiodes and bolometers. After testing several photodiodes at room temperature and at 4.2 K, a choice was made for a GaAsP Schottky photodiode (Hamamatsu G1126). With the protective window removed, this photodiode has a quantum efficiency (QE) for L_α of 14 % from room temperature to below liquid nitrogen temperature. Furthermore this diode has a good long-term reproducibility under VUV irradiation [17]. At liquid helium temperatures and below, the QE is about 10 % at the maximum bias voltage of 5 V. At these low temperatures the detector is not expected to function anymore as a photodiode as the density of free charge carriers becomes neglegibly small. Rather, it is believed that the QE is due to photo-emission of electrons from the GaAsP substrate or the gold layer on top. This belief is confirmed by the fact that the QE drops approximately by a factor of two when He is admitted to the cell and the photo-electrons are partially blocked by the He film. Furthermore, it was observed that a signal with the opposite sign was obtained after slightly misaligning the beam which is probably due to photo-emission from the diode housing, connected to the diode ground. A great advantage of this photodiode is the room-temperature sensitivity range up to 680 nm. During the assembly of the cell and the trap, UV as well as HeNe light can be used for alignment purposes.

the light guide. All connections are made using all-metal seals to prevent outgassing and to reach a high vacuum. Just below the bottom of the cryostat, the light guide can be closed off from the rest of the VUV vacuum by a valve. When not taking data this valve is closed to avoid exposure of the cell window to the room temperature vacuum. With these precautions the system did not show a deterioration of L_α transmission during a period of several months.

In designing the light guide, the diameter was determined by the maximum amount of room temperature radiation allowed to fall directly on to the cell window. In the first optical experiments [1], the incident power was measured to be much larger ($\simeq 300\,\mu$W) due to the internal reflection in the light guide which was initially neglected. In the present experiments, this heat load has been reduced by careful baffling of the light path. An 8 cm long, 5.4 mm o.d. brass tube, oxidized in air at 500°C for 24 hours, was slid into the stainless steel tube connecting the 4 K shield to the room temperature jacket. This tube was machined on the inside to give a row of baffles with a free aperture of 4.0 mm diameter and soft-soldered to the 4 K flange. The choice for the brass was made because, as most common metal oxides, the oxide has a high absorption coefficient for thermal radiation and is readily available. Metal oxides can also be made relatively clean so the VUV vacuum will not be contaminated by outgassing. In the connecting part of the light guide leading to the cell, an oxidized stainless steel helix is tightly fitted for the same purposes. Using these precautions, we were able to cool the cell down to 80 mK in the present experiments.

In the VUV vacuum, just below the valve, a MgF_2 beam splitter is placed to deflect part of the incident L_α radiation (5 % - 10 %) onto a solar blind vacuum photodiode (Hamamatsu R1187). With this signal a ratio measurement with the cell photodiode signal could be performed to reduce the 10 % pulse-to-pulse fluctuations.

References

[1] O.J. Luiten, H.G.C. Werij, I.D. Setija, M.W. Reynolds, T.W. Hijmans, and J.T.M. Walraven, Phys. Rev. Lett. **70**, 544 (1993).

[2] R. Mahon, T.J. McIlrath, and D.W. Koopman, Appl. Phys. Lett. **33**, 305 (1978).

[3] H. Langer, H. Puell, and H. Röhr, Opt. Commun. **34**, 137 (1980).

[4] R. Hilbig and R. Wallenstein, IEEE J. Quantum Electron. QE-**15**, 1566 (1981).

[5] G.C. Bjorklund, IEEE J. Quantum Electron. QE-**11**, 287 (1975).

[6] O.J. Luiten, Ph. D. thesis, University of Amsterdam (1993).

[7] G.M. Weyl, D.I. Rosen, J. Wilson, and W. Seka, Phys. Rev. A **26**, 1164 (1982).

[8] Y.R. Shen, *The Principles of Nonlinear Optics* (John Wiley & Sons, 1984), chapter 27.

[9] J.P. Marangos, N. Shen, H. Ma, M.H.R. Hutchinson, and J.P. Connerade, J. Opt. Soc. Am. B **7**, 1254 (1990).

[10] D.C. Thompson, M.S. O'Sullivan, B.P. Stoicheff, and G.X. Xu, Can. J. Phys. **61**, 949 (1983).

[11] R. van Roijen, J.J. Berkhout, S. Jaakkola, and J.T.M. Walraven, Phys. Rev. Lett. **61**, 931 (1988).

[12] I.D. Setija, H.G.C. Werij, O.J. Luiten, M.W. Reynolds, T.W. Hijmans, and J.T.M. Walraven, Phys. Rev. Lett. **70**, 2257 (1993).

[13] Certified grade according to ASTM f68/77, manufactured by Outokumpu Oy (Finland).

[14] R. van Roijen, Ph. D. thesis, University of Amsterdam (1989).

[15] A.T. Young, Appl. Opt. **2**, 51 (1963).

[16] J.M. Doyle and J.C. Sandberg, private communications.

[17] M. Krumrey, E. Tegeler, J. Barth, M. Krisch, F. Schäfers, and R. Wolf, Appl. Opt. **27**, 4336 (1988).

Chapter 4

Light propagation in magnetically trapped H

4.1 Introduction

In the experiments described in this thesis, we use Lyman-α (L_α) spectroscopy to determine the central density n_0 and temperature T of atomic hydrogen in magnetostatic traps. The propagation of a beam of resonant radiation through a dilute gas of spin-polarized atomic hydrogen provides us with a powerful probe to observe gas properties, like n_0 and T, but also with a tool to change these properties. In this chapter I will discuss the methods used to characterize the sample. In the next chapter I will turn to the discussion of the manipulation tools.

Luiten *et al.* [1] performed the first transmission spectroscopy experiments of magnetically trapped H using Lyman-α radiation. Previous detection schemes relied on indirect methods, like measuring the flux of atoms escaping from the trap either by decay to high-field seeking spin states [2] or by escape over the trap barrier [3]. Optical methods allow an *in situ*, non-destructive detection of magnetically, trapped atomic hydrogen. One can think of a number of methods to measure n_0 and T of a trapped gas. A very direct method would be to image the gas sample. A "picture" of the sample would be a direct reflection of the Boltzmann distribution from which the n_0 and T may be extracted. Experimental conditions (cryogenic environment and high magnetic fields) made this method very difficult to realize. Luiten *et al.* [4] used a detailed lineshape analysis of the total transmission spectrum to extract n_0 and T. In the present work we also use transmission spectroscopy for this purpose.

Reducing a transmission spectrum to a value for the n_0 and T is a straightforward but not an easy task. Many effects combine in a very complex manner in the formation of a transmission spectrum. In Lyman-α absorption, ground state ($1S$) H

atoms are excited in an electric dipole transition to the first excited state ($2P$), with an energy difference of 10.2 eV. The radiation corresponding to this energy lies in the vacuum ultraviolet (VUV) and has a wavelength of 121.56 nm. In a magnetic field the Zeeman effect lifts the degeneracy of the eigenstates. In a magnetic trap this makes the transition frequencies position dependent. For a cloud of atoms it results in inhomogeneous broadening of the spectral lines. Further, Doppler broadening arises due to the velocity distribution of the atoms. These broadening mechanisms make the linewidth an indication of the temperature of the gas. The transition probability also depends on $|\vec{B}(\vec{r})|$ and at the same time on the angle between $\vec{B}(\vec{r})$ and the polarization vector of the electromagnetic field. These properties influence the propagation of the light, not just by attenuating the beam but also by changing its polarization. In the experiments we use circularly or linearly polarized radiation. The transition probability for an atom depends on the polarization of the light and on the particular transition involved.

The resonant cross section for L_α absorption can be as large as $3\lambda_\alpha^2/2\pi$. For a central density $n_0 = 10^{12}\,\mathrm{cm}^{-3}$ this corresponds to a resonant extinction length $\ell_{re} \simeq 0.14\,\mathrm{mm}$. In the trapping experiments with hydrogen also larger densities are studied. No light will pass through such optically thick gases and the sample will cast a shadow on the transmission detector as the L_α beam radius R_b is larger than the effective radius R_s of the sample. Therefore, for a known beam intensity the transmission signal is a measure for the effective cross-sectional area of the sample. In the "long trap" (see Sect. 2.2), in which many of the experiments were performed, the sample has a needle-like shape. For

$$\ell_{re}/R_s \ll 1, \tag{4.1}$$

the absorbed photons will be multiply scattered in the gas. Although the mean free path of the photons is very small, the sample remains dilute from an atomic collisional point of view. Even for the highest densities achieved in trapped H ($\sim 10^{14}\,\mathrm{cm}^{-3}$)

$$\ell_c/R_s \gg 1, \tag{4.2}$$

where $\ell_c \simeq (n_0\sigma_{el})^{-1}$ is the collisional mean free path. In these dilute samples, $(n_0\lambda\!\!\!^{-3} \ll 1)$ collision broadening and collective excitations due to resonant dipole interaction [5] can be ignored and the propagation of the light is determined by single atom properties.

By optical pumping one can influence the population of the hyperfine ground states, thus changing the nuclear polarization of the gas. In a confining magnetic field this redistribution can also lead to population of non-trapped, electron-spin-down states which are ejected from the trapping region.

The propagation of light through a polarized gas is a very rich and complex phenomenon. In the thesis of Luiten this has been carefully and extensively analyzed. In this chapter I shall emphasize the main steps undertaken to arrive at the propagation equation for the electromagnetic field. After that I shall concentrate on the attenuation of the light through the sample, which is very important for understanding optical cooling. The attenuation will be analyzed with a simplified equation in which effects of dispersion are neglected. The optical cooling experiments were performed under conditions where this approximation is very good. This simple picture will then give results which will be used in the next chapter.

4.2 The inhomogeneous wave equation

The radiation field, propagating through an inhomogeneous medium, is described using a plane, electromagnetic wave with wavevector $\vec{k}$ and frequency ω. In the semiclassical approach the electric field vector $\vec{E}(\vec{r})$ is described by way of Maxwell's equations, while the interaction between the light and the atoms is described quantum mechanically by way of the optical Bloch equations. The inhomogeneous wave equation for $\vec{E}(\vec{r})$ is

$$\nabla^2\vec{E} - \frac{1}{c^2}\frac{\partial^2\vec{E}}{\partial t^2} = \frac{1}{\epsilon_0 c^2}\frac{\partial^2\vec{P}}{\partial t^2}, \tag{4.3}$$

where the polarization $\vec{P}$ is the induced dipole moment per unit volume in the medium. Since we are interested in the attenuation and dispersion of an electromagnetic plane wave, we write

$$\begin{aligned} \vec{E}(\vec{r},t) &= \vec{E}_0(\vec{r},t)e^{i(kz-\omega t)} \\ \vec{P}(\vec{r},t) &= \vec{P}_0(\vec{r},t)e^{i(kz-\omega t)} \end{aligned} \tag{4.4}$$

where $k = |\vec{k}| = \omega/c$ is the wavenumber in vacuum of a plane wave with a frequency ω. When we substitute Eq. 4.4 into Eq. 4.3 and make use of the approximation that $\vec{E}_0(\vec{r},t)$ and $\vec{P}_0(\vec{r},t)$ change on a much longer length scale than the wavelength of the light (slowly-varying-envelope approximation) we get [6]

$$\frac{\partial\vec{E}_0}{\partial z} = \frac{ik}{2\epsilon_0}\vec{P}_0. \tag{4.5}$$

This equation describes the attenuation and dispersion of an electromagnetic wave as a result of the induced polarization. To describe the polarization we have to analyze the interaction of the radiation field with the atoms. For this purpose we shall derive in the next section an expression for the complex electric susceptibility tensor $\overleftrightarrow{\chi}$ defined by

$$\vec{P}_0 = \epsilon_0 \overleftrightarrow{\chi}\, \vec{E}_0. \tag{4.6}$$

4.3 Two-level atom in a weak radiation field

As a result of resonant interaction with the electromagnetic field, the atom is excited and an electric dipole moment is induced. The evolution of the electric dipole moment and the rate of excitation are accurately described by way of the optical Bloch equations [7]

$$\dot{\rho}_{22} = -2\gamma\rho_{22} - \tfrac{1}{2}i(\Omega\rho_{12} - \Omega^*\rho_{21}) \tag{4.7}$$

$$\dot{\rho}_{12} = -(\gamma - i\Delta)\rho_{12} - \tfrac{1}{2}i\Omega^*(\rho_{22} - \rho_{11}) \tag{4.8}$$

where ρ_{ij} are the elements of the density matrix of a two-level atom, subject to the conditions $\rho_{11} + \rho_{22} = 1$ and $\rho_{12} = \rho_{21}^*$, $\gamma \equiv \Gamma/2$ is the half width at half maximum (HWHM) and $\Delta \equiv (\omega_{21} - \omega)$. With the densities in the experiment ($n_0 \lesssim 10^{14}\,\mathrm{cm}^{-3}$), effects due to collisional broadening are neglegible. The atomic transition rate, stimulated by the applied electromagnetic field is expressed by the Rabi frequency

$$\Omega = \frac{-\vec{d}_{21} \cdot \vec{E}_0}{\hbar} = -(\vec{d}_{21} \cdot \hat{\varepsilon})\frac{E_0}{\hbar} \tag{4.9}$$

where $\vec{d}_{21} = -e\vec{r}_{21} = -e\langle 2|\vec{r}|1\rangle$ is the electric dipole transition matrix element (e is the positive elementary charge) and $\hat{\varepsilon}$ is the polarization unit vector of the electromagnetic field. The ρ_{11} and ρ_{22} describe the time dependence of the ground and excited state population; ρ_{12} and ρ_{21} describe the evolution of the electric dipole moment [8]

$$\vec{P}' = n\langle\vec{d}\rangle = 2n\rho_{21}\vec{d}_{12}e^{i(kz-\omega t)}, \tag{4.10}$$

where the prime means the atoms have been assumed to be at rest.

For pulsed radiation $\vec{E}_0$ is a function of time, which makes the optical Bloch equations difficult to solve. For high intensities, when there is a substantial population of the excited state, the solutions of the optical Bloch equations will become sensitive to the detailed shape of the pulse which is a difficulty since the pulse shape and light intensity are parameters with a large experimental uncertainty. For low light intensities, however, the sensitivity to these parameters is much weaker. For light intensities so low that the Rabi frequency $|\Omega| \ll \gamma$, the excited state population is neglegible with respect to the ground state population and it suffices to take the solution to lowest order in Ω. Put into terms of intensity, this condition for hydrogen is $I \ll I_{sat} = 3.6\,\mathrm{W\,cm}^{-2}$. In the experiments we typically had $\simeq 5 \times 10^7$ photons per 10 nsec pulse in a beam with a radius of $\simeq 1$ mm which is equivalent to $I \simeq 0.25\,\mathrm{W\,cm}^{-2}$. In this intensity regime it is a good approximation to use a first-order solution to the optical Bloch equations. Since the pulse duration is much

longer than the excited state lifetime, the solution for ρ_{21} is

$$\rho_{21} = \frac{-\frac{1}{2}\Omega}{(\omega_{21} - \omega) - i\gamma}. \tag{4.11}$$

Substituted into Eq. 4.10 this gives the electric susceptibility for a two-level atom

$$\overleftrightarrow{\chi}_0 = \frac{6\pi n}{k^3} \frac{\vec{d}_{12}\vec{d}^*_{12}}{|\vec{d}_{12}|^2} \left(\frac{\gamma}{\omega_{12} - \omega - i\gamma}\right) \tag{4.12}$$

where we have used $\gamma = (\omega_{21}/c)^3 |\vec{d}_{12}|^2/6\pi\epsilon_0\hbar \simeq k^3|\vec{d}_{12}|^2/6\pi\epsilon_0\hbar$ [7]. For a multilevel system this can be easily extended to

$$\overleftrightarrow{\chi}_0 = \frac{6\pi}{k^3} \sum_{h,j} n_h \frac{\vec{d}_{hj}\vec{d}^*_{hj}}{\sum_f |\vec{d}_{fj}|^2} \left(\frac{\gamma}{\omega_{hj} - \omega - i\gamma}\right), \tag{4.13}$$

where $\vec{d}_{hj}$ is the electric dipole matrix element between a ground state h and an excited state j, ω_{hj} the corresponding transition frequency and n_h the density of atoms in the h-state. A necessary condition for Eq. 4.13 is that $\omega_{hj} \simeq \omega$ because then $\omega_{hj}/c \simeq k$, which is clearly true in the case of the $1S - 2P$ transitions in hydrogen. In this approximation $\gamma_j = k^3 \sum_f |\vec{d}_{fj}|^2/6\pi\epsilon_0\hbar = \gamma$.

Substituting ρ_{21} and ρ_{12} from Eq. 4.11 into Eq. 4.7, we obtain

$$\dot{\rho}_{22} = -2\gamma\rho_{22} + \frac{|\Omega|^2\gamma/2}{(\omega_{21} - \omega)^2 + \gamma^2}. \tag{4.14}$$

The second term on the right-hand side is the absorption rate $(I/\hbar\omega)\sigma$, where the intensity $I = \frac{1}{2}c\epsilon_0 E_0^2$ and σ is the absorption cross section. Using Eq. 4.9, σ can be written in the following form

$$\sigma = \frac{|\vec{d}_{21} \cdot \vec{\varepsilon}|^2}{|\vec{d}_{21}|^2} \sigma_L, \tag{4.15}$$

where

$$\sigma_L(\Delta) = \sigma_0 \frac{\gamma^2}{\Delta^2 + \gamma^2} \tag{4.16}$$

is the well-known Lorentzian lineshape. The factor in front of σ_L in Eq. 4.15, describes the dependence of the absorption cross section on the angle between the atomic dipole moment and the direction of the laser beam. The cross section for a polarized gas is maximally $\sigma_0 = 3(\lambda^2/2\pi)$. As is well-known for the non-polarized gas, the resonant cross section equals $\lambda^2/2\pi$.

Due to the Doppler effect and the photon recoil, the light from every atom will be absorbed at a slightly different frequency ω_{abs}, determined by the velocity of the atom,

$$\Delta_{abs} \equiv \omega_{abs} - \omega = \omega_{hj} - \omega + \vec{k} \cdot \vec{v} + E_r/\hbar, \tag{4.17}$$

where $\vec{k}$ is the wavevector of the incident photon, $\vec{v}$ is the velocity of the atom before absorption and the recoil energy $E_r = \hbar^2 k^2/2m$. For hydrogen, the recoil shift $E_r/\hbar = 8.4 \times 10^7\,\mathrm{s}^{-1}, (E_r/k_B = 0.64\,\mathrm{mK})$. To include this inhomogeneous broadening in our expression for the electric susceptibility, we have to replace ω_{hj} in Eq. 4.13 by ω_{abs} and average over a Maxwell velocity distribution. For incoming photons, travelling along the z-axis, this gives

$$\begin{aligned} \overleftrightarrow{\chi} &= \langle \overleftrightarrow{\chi}_0 (\Delta_{abs}) \rangle \\ &= i\frac{6\pi^{3/2}}{k^3} \sum_{h,j} n_h \frac{\vec{d}_{hj}\,\vec{d}^{\,*}_{hj}}{\sum_f |\vec{d}_{fj}|^2} \frac{\gamma}{b} w(\zeta_{hj}), \end{aligned} \tag{4.18}$$

where the angular brackets denote an average over the Maxwell velocity distribution. In the last expression $b = k\sqrt{2k_BT/m}$ ($b/\sqrt{2}$ is the R.M.S. spread of the Gaussian distribution), $w(\zeta) = e^{-\zeta^2}\mathrm{erfc}(-i\zeta)$ is the complex error function, and $\zeta_{hj} = (\omega - \omega'_{hj} + i\gamma)/b$ where $\omega'_{hj} = \omega_{hj} + E_r/\hbar$.

The Doppler broadening also effects the absorption cross section in Eq. 4.16

$$\sigma_V(\omega, T) = \langle \sigma_L(\Delta_{abs}) \rangle = \sigma_0 \sqrt{\pi} \frac{\gamma}{b} \mathrm{Re}\, w(\zeta_{21}). \tag{4.19}$$

The real part of the complex error function w is the Voigt profile, a Doppler broadened Lorentzian.

4.4 Transition frequencies and probabilities

So far we have only derived the general expressions for the electric susceptibility and the cross section. In order to evaluate these for the case of hydrogen, we have to calculate the transition frequencies and probabilities.

The atomic structure and optical properties of atomic hydrogen are very well established. Therefore we will not dwell too long on the calculation of the eigen states and energies, since these can be found in most books on atomic structure [9]. The ground state hyperfine structure was described in Sect. 2.1. Here we will look at the fine structure of the $2P$ multiplet. The hyperfine structure of the $2P$ multiplet does not play a role in our experiments. For magnetic fields $B \gtrsim 0.05\,\mathrm{T}$ [4] the hyperfine interaction for the $2P$ multiplet and the Zeeman energy of the proton introduce a splitting of the fine structure levels which is smaller than the natural linewidth of the $2P$ states. Moreover, hyperfine admixtures turn out not to influence the transition probability appreciably.

The $2P$ fine structure is described by the Hamiltonian

$$H_{FS} = E_1 + \tfrac{2}{3}\Delta\vec{\ell} \cdot \vec{s} + \mu_B(\vec{l} + g_e\vec{s}) \cdot \vec{B}. \tag{4.20}$$

Here the reference energy $E_1 = \frac{3}{4}hcR_\infty(1+m_e/m_n)^{-1} + E_{LS}$ with R_∞ the Rydberg constant, m_e and m_n the mass of the electron and the nucleus, respectively, and E_{LS} contains relativistic and Lamb shift corrections; Δ is the $B = 0$ fine structure splitting, $\vec{\ell}$ the electron orbital angular momentum, $\vec{s}$ the electron spin and g_e the electron g-factor. The total electron angular momentum $\vec{j} = \vec{\ell} + \vec{s}$. The zero of energy is defined as the $B = 0$ energy of the $1^2S_{1/2}$ ground state, neglecting the hyperfine interaction (see Sect. 2.1). For the $1S-2P$ transition the reference energy E_1 for hydrogen is $E_1/h = 2\,466\,068$ GHz [10] and the fine structure splitting is $\Delta/h = 10.969$ GHz.

In zero field the $2P$ multiplet consists of two discrete states with $j = \ell + s = \frac{3}{2}$ and $j = \ell - s = \frac{1}{2}$ and energies

$$\begin{aligned} E(2^2P_{3/2}) &= E_1 + \tfrac{1}{3}\Delta \\ E(2^2P_{1/2}) &= E_1 - \tfrac{2}{3}\Delta. \end{aligned} \tag{4.21}$$

For $B \neq 0$ the degeneracy in $m_j = m_\ell + m_s$ is lifted. The eigenstates and -energies, obtained after diagonalizing H_{FS}, are listed in Table 4.1. The eigenenergies of the $2P$ multiplet are expressed in the dimensionless parameter

$$x \equiv \frac{(g_e - 1)\mu_B B}{\Delta} = \frac{B}{0.7819T}. \tag{4.22}$$

The eigenstates are expressed in the $|m_\ell, m_s\rangle$ basis, which is an abbreviation of the $|n, \ell, m_\ell, s, m_s\rangle$ basis. The fine structure mixing angles are defined by

$$\sin\theta_\pm \equiv \sqrt{\frac{1+\delta_\pm}{2}}, \tag{4.23}$$

where

$$\delta_\pm = \frac{x \pm 1/3}{\sqrt{1 \pm 2x/3 + x^2}}. \tag{4.24}$$

Although experimentally only the $2P$ fine structure can be resolved, each $2P$ state in Table 4.1 is doubly degenerate with respect to the orientation of the proton spin $\vec{i}$. Each fine structure state consists of two hyperfine states, one with $m_i = +\frac{1}{2}(\uparrow)$ and one with $m_i = -\frac{1}{2}(\downarrow)$, differing by $|\Delta m_F| = 1$, where $\vec{F} = \vec{\ell} + \vec{s} + \vec{i}$ and $m_F = m_\ell + m_s + m_i$.

In Fig. 4.1 we plot the energy levels of the $1S$ and $2P$ multiplet of atomic hydrogen as a function of magnetic field. Also the energy levels are plotted for the $2S$ state which is used in two-photon spectroscopy. In Fig. 4.1 the transitions from the d state to the $2P$ multiplet, as they are given by the electric dipole selection rules, are indicated by arrows. In an electric dipole transition the electron and nuclear spin projections are conserved, $\Delta m_s = \Delta m_i = 0$, while $\Delta m_\ell = 0, \pm 1$. The

Table 4.1: Energy levels and eigenstates of the ground state hyperfine structure and the first excited state fine structure of hydrogen in a magnetic field.

	m_j	energy	state
$2^2P_{3/2}$	$\frac{3}{2}$	$E_1 + \Delta/3 + (1+g_e/2)\mu_B B$	$\|1\uparrow\rangle$
	$\frac{1}{2}$	$E_1 - \Delta/6 + \mu_B B/2 + (\Delta/2)\sqrt{1+2x/3+x^2}$	$\sin\theta_+\|0\uparrow\rangle + \cos\theta_+\|1\downarrow\rangle$
	$-\frac{1}{2}$	$E_1 - \Delta/6 - \mu_B B/2 + (\Delta/2)\sqrt{1-2x/3+x^2}$	$\sin\theta_-\|-1\uparrow\rangle + \cos\theta_-\|0\downarrow\rangle$
	$-\frac{3}{2}$	$E_1 + \Delta/3 - (1+g_e/2)\mu_B B$	$\|-1\downarrow\rangle$
$2^2P_{1/2}$	$\frac{1}{2}$	$E_1 - \Delta/6 + \mu_B B/2 - (\Delta/2)\sqrt{1+2x/3+x^2}$	$-\cos\theta_+\|0\uparrow\rangle + \sin\theta_+\|1\downarrow\rangle$
	$-\frac{1}{2}$	$E_1 - \Delta/6 - \mu_B B/2 - (\Delta/2)\sqrt{1-2x/3+x^2}$	$-\cos\theta_-\|-1\uparrow\rangle + \sin\theta_-\|0\downarrow\rangle$
	h		
$1^2S_{1/2}$	d	$a_h/4 + \mu^- B/2$	$\|0\uparrow\uparrow\rangle$
	c	$-a_h/4 + (a_h/2)[1+(\mu^+B/a_h)^2]^{1/2}$	$\cos\theta\|0\uparrow\downarrow\rangle + \sin\theta\|0\downarrow\uparrow\rangle$
	b	$a_h/4 - \mu^- B/2$	$\|0\downarrow\downarrow\rangle$
	a	$-a_h/4 - (a_h/2)[1+(\mu^+B/a_h)^2]^{1/2}$	$\sin\theta\|0\uparrow\downarrow\rangle - \cos\theta\|0\downarrow\uparrow\rangle$

transitions, given by these rules, have been labelled by the letter σ (*senkrecht*) to describe the transitions with $\Delta m_\ell = \pm 1$ which can only be induced by circularly polarized radiation with the polarization vector perpendicular to the magnetic field $\vec{B}$ and by the letter π (*parallel*) to describe the transitions with $\Delta m_\ell = 0$ which can only be excited by linearly polarized radiation with the polarization vector parallel to $\vec{B}$. For $\Delta m_\ell = +1$ (σ^+ transition) one needs radiation with the polarization vector rotating anti-clockwise for an observer towards whom the light is moving (left circularly polarized, LCP). For $\Delta m_\ell = -1$ (σ^- transition) one needs radiation with the polarization vector rotating clockwise (right circularly polarized, RCP).

From the d state one σ^+ transition, two σ^- transitions and two π transitions are allowed. These transitions have been labelled in Fig. 4.2. They connect the $1S_{1/2,m_J=1/2}$ state to the following excited states: σ_1 to the $2P_{3/2,m_J=3/2}$ state, π_1

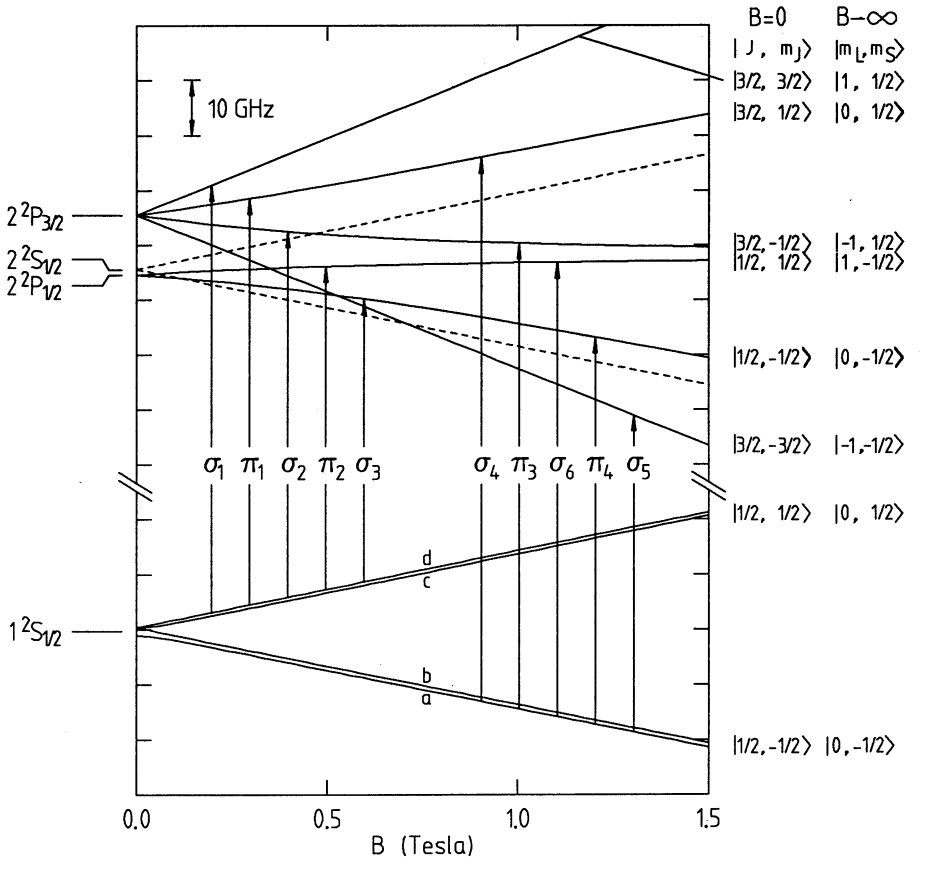

Figure 4.1: Energy levels of the ground state and first excited state of H. The arrows denote the allowed optical transitions from the d state and from the high-field seeking spin state.

to the $2P_{3/2,m_J=1/2}$ state, σ_2 to the $2P_{3/2,m_J=-1/2}$ state, π_2 to the $2P_{1/2,m_J=1/2}$ state and σ_3 to the $2P_{1/2,m_J=-1/2}$ state. Taking proton spin into account, the transition probability is actually determined by the $|\uparrow\uparrow\rangle$ component of the $2P$ states just mentioned. Applying the spin selection rules for transitions from the d state it suffices to only consider the $2P$ fine structure. The corresponding transition frequencies are plotted in Fig. 4.2. Of these transitions only the σ_1 transition forms a closed cycle: from the excited state the atom can only decay back to the same ground state. This makes this transition very suitable for Doppler cooling (see chapter 5) since no particles are lost due to optical pumping to non-trapped states. Another advantage of the σ_1 transition, in this respect, is that it is spectrally well separated from the

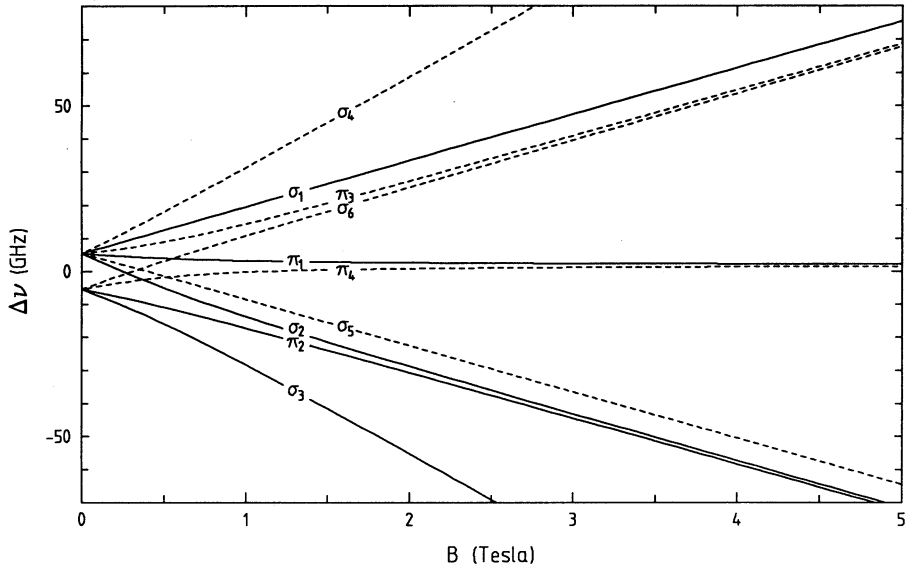

Figure 4.2: Transition frequencies for the five allowed transitions from the d state as a function of magnetic field. The frequencies for the transitions starting from the high-field seeking spin state are indicated in dashed lines.

other transitions. On any of the other transitions the atom has a finite probability of decaying to the high-field seeking ground state after which it will be ejected from the trap. In Light-Induced Evaporation (LIE, see chapter 6), this method is used as an energy-selective "bouncer"to remove the atoms from the trap. The probability to decay either to the high-field seeking ground state or to the low-field seeking ground state, can easily be read from Table 4.1. The probability for decay, for example, from the $2P_{3/2,m_J=-1/2}$ to the d state (the σ_2 transition, used in LIE) is $\Gamma_{\sigma 2} = \Gamma \sin^2 \theta_-$. The probability for decay to the high-field seeking ground state is the complement $\Gamma \cos^2 \theta_-$. In Fig. 4.3 the decay probabilities to the d state for the other transitions are plotted as a function of magnetic field: $\Gamma_{\pi 1} = \Gamma \sin^2 \theta_+$, $\Gamma_{\pi 2} = \Gamma \cos^2 \theta_+$ and $\Gamma_{\sigma 3} = \Gamma \cos^2 \theta_-$.

Applying the dipole selection rules to the c state atoms gives five allowed transitions from the $|0\uparrow\downarrow\rangle$ part of the c state, analogous to the five allowed transitions from the d state, only shifted by the c-d frequency difference ($\simeq 0.6\,\mathrm{GHz}$ for $B \geq 0.1\,\mathrm{T}$). The transition probability can be simply obtained by multiplying the corresponding d state transition probabilities (see Fig.4.3) by $\cos^2 \theta$ where θ is the hyperfine mixing angle (see Sect.2.1). For fields $B \geq 0.1\,\mathrm{T}, \cos^2 \theta \geq 0.95$. The $|0\downarrow\uparrow\rangle$ part of the c state also gives rise to five allowed transitions (two σ^+, one σ^- and two π transitions) of

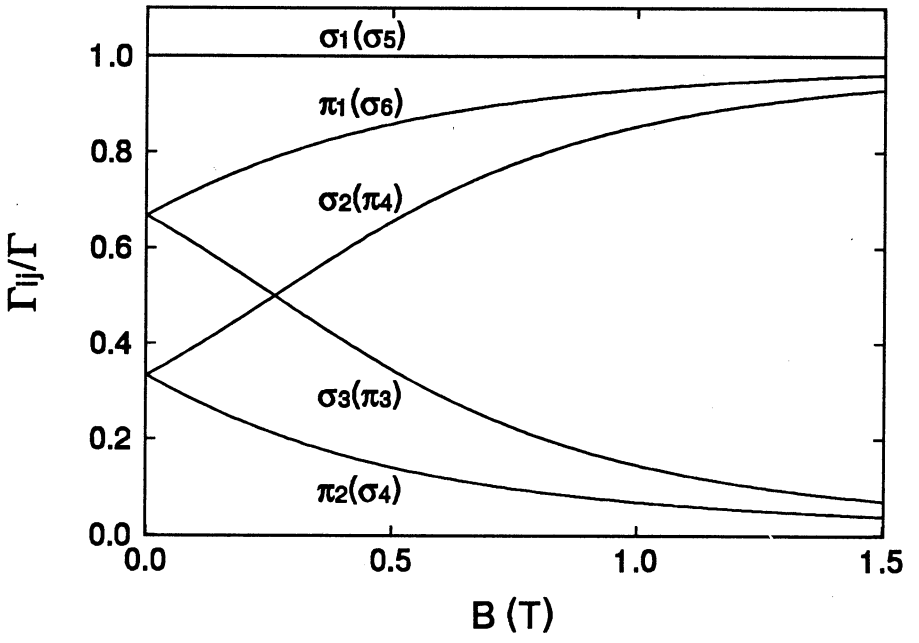

Figure 4.3: Transition probabilities for the five allowed transitions from the d state and the b state as a function of magnetic field.

which the σ^- transition excites the $2P_{3/2,m_J=-3/2}$ state. This transition is forbidden for the d state. Transitions from this part of the c state have small transition probabilities due to the hyperfine mixing angles ($\sin^2\theta \leq 0.05$ for $B \geq 0.1$ T). Because the c-d energy difference and the transition probabilities from the $|0\downarrow\uparrow\rangle$ part are so small, effects due to the presence of c atoms are blurred by the Zeeman and Doppler broadening at higher temperatures. At the lowest temperatures ($T \lesssim 5$ mK) reached in the LIE experiments, a clear signature of the presence of c atoms is observed (see Sect. 6.6).

4.5 Spectroscopy of magnetically trapped H

For the spectroscopic determination of density and temperature of the trapped gas, we compare the measured spectra with calculated spectra. Details on the parameters that are varied in the calculation of a spectrum will be discussed later in this section.

With the transition frequencies and energy eigenstates, derived in Sect. 4.4, we will now evaluate the electric susceptibility. To do this we have to calculate the electric dipole matrix elements from Eq. 4.13 for the different transitions. This can be simplified by choosing a convenient basis $(\hat{\varepsilon}'_+, \hat{\varepsilon}'_3)$ where $\hat{\varepsilon}'_3$ is parallel to the

direction of the magnetic field (spin polarization) and $\hat{\varepsilon}'_{\pm} = (\hat{\varepsilon}'_1 \pm i\hat{\varepsilon}'_2)/\sqrt{2}$, where $\hat{\varepsilon}'_1$ and $\hat{\varepsilon}'_2$ are orthogonal vectors in the plane normal to $\hat{\varepsilon}'_3$. For the transitions from the d state the electric susceptibility $\overleftrightarrow{\chi}$ can then be written as

$$\left[\overleftrightarrow{\chi}\right]' = \begin{pmatrix} \chi_+ & 0 & 0 \\ 0 & \chi_- & 0 \\ 0 & 0 & \chi_z \end{pmatrix}. \tag{4.25}$$

where

$$\begin{aligned} \chi_+ &= i(6\pi^{3/2}/k^3)\, n_d\, (\gamma/b)\, w(\zeta_{\sigma 1}), \\ \chi_- &= i(6\pi^{3/2}/k^3)\, n_d\, (\gamma/b)\, [\sin^2\theta_-\, w(\zeta_{\sigma 2}) + \cos^2\theta_-\, w(\zeta_{\sigma 3})], \\ \chi_z &= i(6\pi^{3/2}/k^3)\, n_d\, (\gamma/b)\, [\sin^2\theta_+\, w(\zeta_{\pi 1}) + \cos^2\theta_+\, w(\zeta_{\pi 2})]. \end{aligned} \tag{4.26}$$

The d atom density, the fine structure mixing angles $\theta_{\pm}$ and the frequency detuning parameters ζ_{hj} are magnetic field dependent.

In the experiment the electric field is described in the $(\hat{\varepsilon}_{\pm}, \hat{\varepsilon}_3)$ basis

$$\vec{E}_0 = E_{0+}\hat{\varepsilon}_+ + E_{0-}\hat{\varepsilon}_-, \tag{4.27}$$

where $\hat{\varepsilon}_3$ is parallel to the direction of the laser beam. To obtain the electric susceptibility, $\overleftrightarrow{\chi}'$ has to be transformed to the $(\hat{\varepsilon}_{\pm}, \hat{\varepsilon}_3)$ basis [4]. Substituted into Eq. 4.5 this gives the propagation equations for the electric field in the circular basis

$$\begin{aligned} \partial E_{0+}/\partial z &= (ik/8)\{[\chi_+(1+\cos\theta_B)^2 + \chi_-(1-\cos\theta_B)^2 + 2\chi_z \sin^2\theta_B]\, E_{0+} \\ &\quad +(2\chi_z - \chi_+ - \chi_-)\sin^2\theta_B\, E_{0-}\} \\ \partial E_{0-}/\partial z &= (ik/8)\{(2\chi_z - \chi_+ - \chi_-)\sin^2\theta_B\, E_{0+} \\ &\quad +[\chi_+(1-\cos\theta_B)^2 + \chi_-(1+\cos\theta_B)^2 + 2\chi_z \sin^2\theta_B]\, E_{0-}\}. \end{aligned} \tag{4.28}$$

In these equations θ_B is the angle between the $\vec{B}$ and $\vec{k}$, $\cos\theta_B = B_z/B$.

The propagation equations, a set of coupled differential equations, form the heart of Lyman-α spectroscopy and describe the attenuation of the LCP component (E_{0+}) and the RCP component (E_{0-}) of the electric field. For $\theta_B = 0$ the equations are decoupled and the terms with χ_z disappear from the equations: along the z-axis the electric field is perpendicular to the magnetic field, so π transitions cannot be excited.

For the numerical integration of Eq. 4.28 a number of parameters are needed: the density of the gas in the center of the trap n_0, the gas temperature T, the fraction of atoms in the c state (which is important for fitting spectra at $T \lesssim 10\,\mathrm{mK}$), the helicity of the light and the radial beam profile. For a particular value of n_0, T and the fraction of c atoms, Eq. 4.28 is numerically integrated. The intensity in

the diode plane is weighted with the radial beam profile and integrated to give the transmission. This is performed once for initially LCP light and a second time for initially RCP light. Both spectra are essential for fitting the helicity of the incident light. Comparison of calculated spectra with data gives an accuracy in the determination of n_0 and T of $\sim 25\%$, mainly limited by imprecise knowledge of the beam shape.

A spectrum is measured by scanning the laser frequency along the $2P$ multiplet. Full spectra require a scan time of 30 s. For longer scan periods, the decay due to intrinsic decay mechanisms, at typical gas densities of $\sim 10^{12}\,\mathrm{cm}^{-3}$, or optical pumping cannot be neglected. For a determination of n_0 and T it suffices to perform a spectral scan of only the π_1 and the σ_1 line. This requires a scan time of 15 s. If we want to measure n_0 and T during processes that occur on shorter time scales, we make use of three-point spectroscopy. In this technique, we measure the transmission at three different frequencies which can be generated for each pulse by activating a particular acousto-optic modulator in the configuration as described in Sect. 3.2.3. These three values for the transmission are then used in fitting density and temperature keeping the other parameters constant at a value which is obtained by first measuring a full spectrum.

4.6 Attenuation on the σ_1 transition

In this section, we will more closely look at the propagation of LCP light tuned to the σ_1 transition, a situation encountered in the Doppler cooling measurements. We will introduce a simplified equation for the propagation of light, neglecting effects due to polarization and dispersion. This equation, the equation of radiative transfer, will be used to illustrate the essential features of light absorption on the σ_1 transition.

Due to the spectral separation of the σ_1 line, the contribution from the other transitions to the electric susceptibility can be neglected. The equations 4.28 in this case simplify to

$$\begin{aligned} \partial E_{0+}/\partial z &= (ik/8)\{\chi_+(1+\cos\theta_B)^2\,E_{0+} - \chi_+ \sin^2\theta_B\,E_{0-}\} \\ \partial E_{0-}/\partial z &= (ik/8)\{-\chi_+ \sin^2\theta_B\,E_{0+} + \chi_+(1-\cos\theta_B)^2\,E_{0-}\}. \end{aligned} \tag{4.29}$$

Let us consider Eqs. 4.29 for the simplified case of resonant radiation propagating in a homogeneous gas and at a constant angle θ_B. This provides some feeling for the behaviour of the two polarization components. If we irradiate this gas with LCP light ($E_{0-} = 0$ at $z = -\infty$), the E_{0-} component will increase as the gas propagates through the gas. The reason is that in the atomic reference frame, the atom, polarized along the magnetic field, will see elliptically polarized light which can

be decomposed in an E_{0+} and an E_{0-} component. Since the E_{0+} component will be more strongly absorbed on the σ_1 transition, a relative increase of the E_{0-} component will be the result. After the light has propagated over a certain distance, the E_{0+} component will have decreased so much that it will cancel the change induced by the E_{0-} component. From that moment onwards the magnitude of both components will not change anymore. For this limit the Eqs. 4.29 give the ratio E_{0+}/E_{0-} which is only a function of θ_B. For the case of a constant χ_+ and θ_B, Eqs. 4.29 can be easily solved, giving a solution for the $E_{0+}(z)$ and the $E_{0-}(z)$ component which approaches a limiting value. This final magnitude of both components is also only a function of the angle θ_B. For the E_{0-} component we get

$$E_{0-}(z \to \infty) = \frac{\sin^2 \theta_B}{2 + 2\cos^2 \theta_B}. \tag{4.30}$$

In the experiments, θ_B is position dependent which makes the solution of Eqs. 4.29 more complicated, but similar effects will occur when irradiating the σ_1 transition with LCP light. Along the z-axis, $\theta_B = 0$ and there will be only absorption of LCP light. At a distance ρ from the z-axis, $\theta_B \neq 0$ and irradiating the gas with LCP light will result in the appearance of an E_{0-} component of the radiation. For the magnetic trapping field, however, the angle θ_B is small as the light propagates through the sample. The contribution of the E_{0-} component in the Doppler cooling experiments will therefore be small. For the analysis of the Doppler cooling experiments it is important to know the light absorption as a function of position for LCP as well as RCP light since both can be absorbed and cause cooling. This is obtained from the numerical calculations of the spectrum by keeping track of the change in intensity $|E_{0+}\vec{\varepsilon}_+ + E_{0-}\vec{\varepsilon}_-|^2$ as the light propagates through the sample.

We just mentioned that in the experimental trapping geometries the E_{0-} component will be small due to the small angles θ_B. It is therefore a good approximation to neglect changes in polarization and only consider the attenuation of the E_{0+} component. By setting $\theta_B = 0$ in Eq. 4.29 and substituting $\overleftrightarrow{\chi}_+$ from Eq. 4.26, the attenuation of the incident light is described by the following equation

$$\frac{\partial I(\vec{r},\omega)}{\partial z} = -n(\vec{r})\,\sigma_V(\vec{r},\omega)\,I(\vec{r},\omega) \tag{4.31}$$

where $I(\vec{r},\omega) = \frac{1}{2}\epsilon_0 c|\vec{E}_0(\vec{r},\omega)|^2$ is the intensity distribution of a monochromatic light beam of frequency ω traversing the sample with a density distribution $n(\vec{r})$ and with a local Doppler broadened absorption cross section $\sigma_V(\vec{r},\omega)$ given by Eq. 4.19. It should be emphasized that, although Eq. 4.31 is very well suited to describe the phenomenology of light absorption on the σ_1 line, the spectra are calculated using Eq. 4.28 without the simplifying assumptions just mentioned.

Equation 4.31 has been justified here for the σ_1 transition, but does not apply to that transition alone. It applies generally to the extinction of light if effects due to polarization and dispersion are neglegible. For the propagation of LCP light on the σ_1 transition, this equation gives a good description of the attenuation and it will, therefore, be used in the rest of this chapter to derive conditions for the optically thin and optically thick limit and to derive approximate expressions for $I(\vec{r},\omega)$ which will be useful for understanding the optical cooling experiments. The formal solution to Eq. 4.31 is

$$I(\rho,z,\omega) = I_0(\rho)\exp\Big[-\int_{-\infty}^{z} n(\rho,z')\sigma_V(\rho,z',\omega)\,dz'\Big], \tag{4.32}$$

where $I_0(\rho)$ is the radial intensity profile of the incoming beam. The total number of absorbed photons of frequency ω per unit time is

$$\Lambda(\omega,n_0,T) = \int_V \frac{I(\vec{r},\omega)}{\hbar\omega} n(\vec{r})\sigma_V(\vec{r},\omega)\,d^3r. \tag{4.33}$$

Since the optical cooling rate is proportional to the intensity (see Sect. 5.2), $I(\vec{r},\omega)$ is an important quantity to know. For our experiments, calculating $I(\vec{r},\omega)$ can only be done numerically due to the detailed shape of the trap and the $\vec{B}$ dependence of the transition frequencies and probabilities. In a number of cases the solution to Eq. 4.31 can be simplified:

1. For the σ_1 transition the transition probability is independent of $|\vec{B}|$ ($\Gamma_{\sigma 1} = \Gamma$, see Sect. 4.4) and the transition frequency is linearly proportional to $|\vec{B}|$.

2. For temperatures $T \ll T_0 = 67\,\mathrm{mK}$ (see Sect. 2.2), the trap profile is to a very good approximation parabolic.

3. *Gaussian approximation* ($b \gg \gamma, |\Delta\omega| < |\Delta\omega_G|$) : for high temperatures ($T \gg 2.2\,\mathrm{mK}$ for hydrogen) or a small atomic mass, the Voigt lineshape, Eq. 4.19, can be asymptotically approximated by the following expression [11],

$$\mathrm{Re}\,w[(\omega-\omega_0'+i\gamma)/b] \simeq \exp\Big[-(\frac{\omega-\omega_0'}{b})^2\Big] + \frac{\gamma/b}{\sqrt{\pi}((\omega-\omega_0')/b)^2}, \tag{4.34}$$

provided $(\omega-\omega_0') \gg \gamma$. This approximation has Lorentzian behaviour in the wings and Gaussian behaviour near the center of the line. The Gaussian and Lorentzian profiles make equal contributions when

$$((\omega-\omega_0')/b)^2\exp((\omega-\omega_0')/b)^2 = \frac{\gamma}{b\sqrt{\pi}}. \tag{4.35}$$

Condition 4.35 determines a detuning $|\Delta\omega_G|$ at which the Lorentzian behaviour in the wings of the Voigt lineshape crosses over to Gaussian behaviour near

the center of the line. For $|\Delta\omega| < |\Delta\omega_G|$, the Voigt line can be approximated by a Gaussian lineshape

$$\sigma_G = \sigma_0\sqrt{\pi}\frac{\gamma}{b}\exp\Big[-(\frac{\omega-\omega_0'}{b})^2\Big]. \tag{4.36}$$

4. *Lorentzian approximation* ($b \ll \gamma$) : for low temperatures or a large atomic mass, the Voigt profile can be approximated by a Lorentzian, see Eq. 4.16.

$$\lim_{b\ll\gamma} \mathrm{Re}\, w[(\omega-\omega_0'+i\gamma)/b] = \frac{b}{\gamma\sqrt{\pi}}\frac{1}{(\omega-\omega_0')/\gamma)^2+1}. \tag{4.37}$$

At a given temperature the condition $b \ll \gamma$, is always satisfied for particles with a large enough mass. In the case of hydrogen one should have $T \ll 2.2\,\mathrm{mK}$.

These points will be used in the coming sections. In the next chapter, we will show that the Gaussian and Lorentzian approximations are very useful for the calculation of the Doppler cooling rate and cooling limit for very light, "exotic"atoms and very heavy atoms, respectively. For hydrogen, which is an intermediate case, the Voigt profile must be used.

4.6.1 Resonant shells

As an example of how the presence of gas influences the propagation of the Lyman-α beam through the trapping region, we plot in Fig. 4.4 the absorption coefficient $n(z)\sigma_V(z)$ for a temperature of 30 mK, a positive detuning of 450 MHz from the resonance frequency at the trap center and a density of $n_0 = 1.4 \times 10^{10}\,\mathrm{cm}^{-3}$ (a density chosen for purposes of illustration only). Also plotted in Fig. 4.4 is the intensity along the z-axis of LCP light irradiated on the σ_1 transition, for the same temperature and detuning but different densities. Clearly we see the appearance of resonant shells where the laser light is resonant with the atoms located in regions around equipotential surfaces. For atoms outside the resonant surface the laser light is detuned to the red, for atoms in the inner region of the resonant surface this light is detuned to the blue. For light tuned below the resonance frequency at the trap center, no atoms are resonant. In the latter case absorption takes place in a central cloud and diminishes rapidly with increasing detuning, see Fig. 4.5. The thickness of the shells is determined by the width of the Voigt line $\Delta\omega_V$. If the detuning from the resonant frequency at the trap center is smaller than $\Delta\omega_V$, the shells will overlap to form a central cloud of resonant atoms (see Fig. 4.5) and the description in terms of shells breaks down.

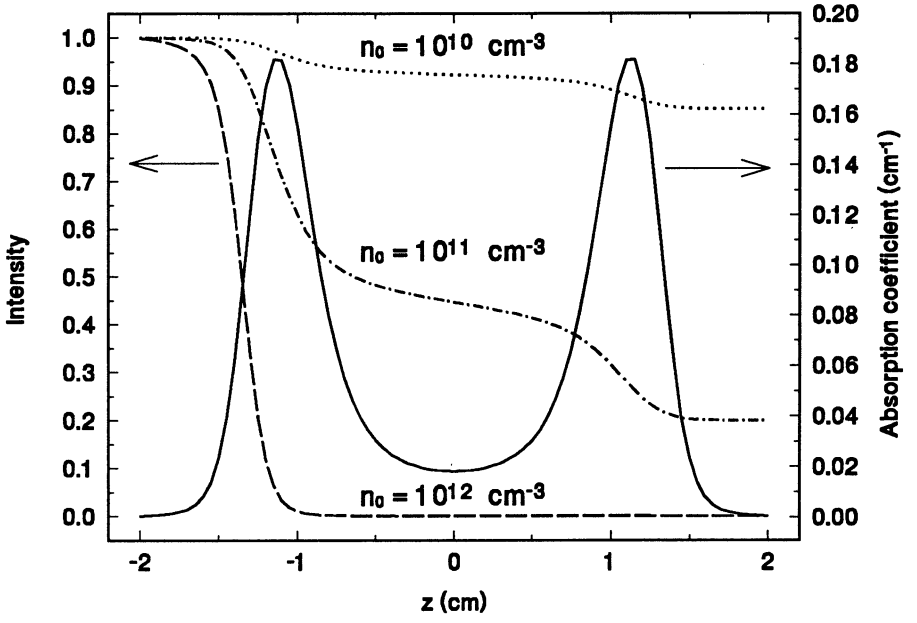

Figure 4.4: Absorption coefficient and intensity along the z-axis for a temperature of 30 mK, a positive detuning of 450 MHz and three values for the density: $1.0 \times 10^{10}\,\mathrm{cm}^{-3}$, $1.0 \times 10^{11}\,\mathrm{cm}^{-3}$ and $1.0 \times 10^{12}\,\mathrm{cm}^{-3}$. For the absorption coefficient a density $n_0 = 1.4 \times 10^{10}\,\mathrm{cm}^{-3}$ has been chosen to illustrate the shape.

It is interesting to estimate the thickness of the resonant shell, the Voigt thickness, as introduced by Luiten [4]. For $T \gg 2.2\,\mathrm{mK}$, $\Delta\omega_V$ can be well approximated by the "Doppler" width of a Gaussian line shape $\Delta\omega_D = 2b\sqrt{\ln 2} \equiv 2\pi\Delta\nu_D$. For atomic hydrogen $\Delta\nu_D/\sqrt{T} = 1.76\,\mathrm{GHz\,K}^{-1/2}$. For the σ_1 transition, the change in the magnetic field over one Voigt width is $\Delta B_V = \hbar\Delta\omega_V/\mu_B \simeq \hbar\Delta\omega_D/\mu_B = 0.13\sqrt{T}$ T with T in Kelvin. For $T \ll 2.2\,\mathrm{mK}$, the spread in Zeeman shifts of the σ_1 resonance frequency has become smaller than the natural linewidth. In this temperature limit the description in terms of resonant shells breaks down.

The thickness of the resonant shell is determined by the Voigt width and depends on the position on the shell. Along the axial direction $\partial B/\partial z = 2\beta(z - z_0)$ and the Voigt thickness

$$\ell_V^{ax} = \Delta B_V/[2\beta(z - z_0)]. \tag{4.38}$$

For a given temperature, a typical Voigt thickness is obtained for $z - z_0 = L_s/2$ where L_s is the effective length of the sample (see Sect. 2.3.3). If we use the expression for the Doppler width, we obtain a typical value for the axial Voigt thickness $\ell_V^{ax} = 5.5\,\mathrm{mm}$, independent of the temperature. At the trap center Eq. 4.38 diverges. In

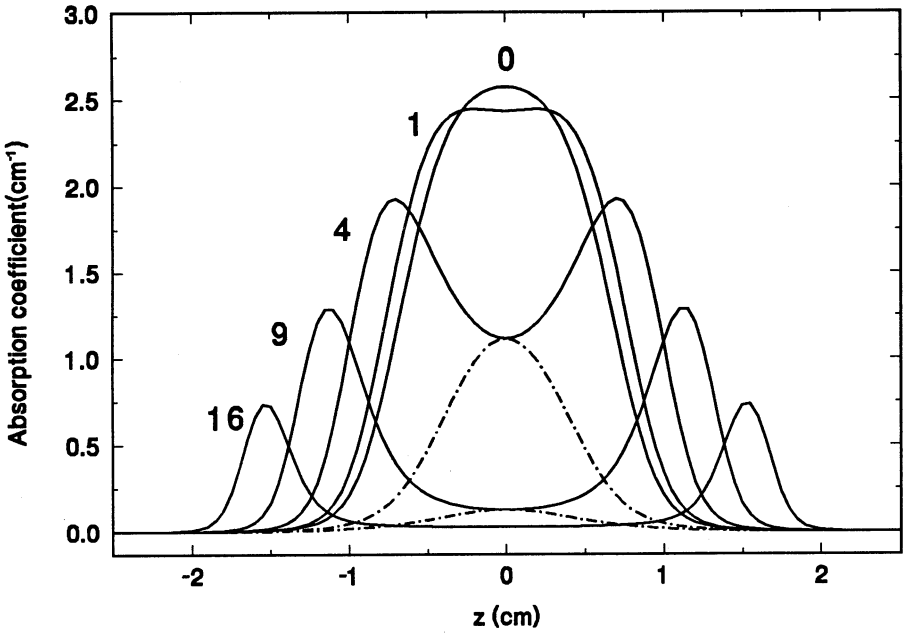

Figure 4.5: Absorption coefficient for normalized detunings $(\omega - \omega_{\sigma 1}(B_0))/\gamma$ = 16,9,4,1,0, -4,-9. The negative detunings are dash-dotted. The plot is for $n_0 = 1.0 \times 10^{11}\,\mathrm{cm}^{-3}$ and $T = 30\,\mathrm{mK}$.

this case ℓ_V^{ax} is determined by the second-order derivative of $B(z)$, giving $\ell_V^{ax}(z = z_0) = \sqrt{2\Delta B_V/\beta}$. For $T = 50\,\mathrm{mK}$, $\ell_V^{ax}(z = z_0) = 1.6\,\mathrm{cm}$. Along the radial direction in the $z = z_0$ plane $\partial B/\partial\rho = \alpha^2\rho(B_0^2 + \alpha^2\rho^2)^{-1/2}$ and the Voigt thickness is

$$\ell_V^{rad} = \frac{\Delta B_V}{\alpha\rho}\sqrt{B_0^2 + \alpha^2\rho^2}. \tag{4.39}$$

As a typical value we can take $\rho = R_s$, where R_s is the effective radius of the sample (see Sect. 2.3.3). For high temperatures ($T \gg T_0$) we then obtain an expression for ℓ_V^{rad} which is temperature dependent. For low temperatures ($T \ll T_0$), when the trap becomes parabolic in the radial direction, the radial Voigt thickness becomes independent of temperature. In this case $\ell_V^{rad} \simeq 0.1\,\mathrm{mm}$. The resonant shells are much thinner in the radial direction than in the axial direction. In the calculation of the Voigt thickness we have neglected the change in density over the resonant shell. This is allowed because for $k_B T \gg \hbar\Delta\omega_D$ ($T \gg 7\,\mathrm{mK}$), the relative change in density over this magnetic field interval ($|n^{-1}(\partial n/\partial B)\Delta B_V| = 0.084(T/\mathrm{K})^{-1/2}$) is always smaller than the relative change in the cross section for the experimental range of temperatures.

Another important length scale determining the attenuation of light is the reso-

nant extinction length, the extinction length at the center of the resonant absorption shell

$$\ell_{re}(\omega) \equiv [n(B_{res}(\omega))\sigma(\omega, B_{res}(\omega))]^{-1}, \tag{4.40}$$

where B_{res} is the magnetic field where the atoms are resonant with the laser frequency ω. For irradiation of the σ_1 line with LCP light, tuned to the resonant frequency at the trap center $\ell_{re} = (n_0\sigma_0)^{-1}$. When $\ell_{re} \gg \ell_V$ the gas is optically thin. When the laser frequency and the gas density are such that $\ell_{re} \ll \ell_V$, the sample is optically thick and the light will be absorbed before it reaches the resonant shell. Along the axial direction the sample becomes optically thick at $z = L_s/2$ for a local density $n \gg 2.5 \times 10^{10}\,\mathrm{cm}^{-3}$. Along the radial direction this happens for a local density which is approximately $50\times$ larger. The experiments were mostly done under conditions for which the sample was optically thin in the radial direction while being optically thick in the axial direction ($n_0 \simeq 5 \times 10^{10} - 2 \times 10^{12}\,\mathrm{cm}^{-3}$). At the highest densities ($n_0 \sim 10^{13}\,\mathrm{cm}^{-3}$), the sample was also optically thick in the radial direction.

4.7 Optically thin limit

The low density case, sketched in Fig. 4.4, is an example of an optically thin sample. The condition for an optically thin sample is

$$\int_{-\infty}^{\infty} n(z)\sigma_V(z,\omega)\,dz \ll 1, \tag{4.41}$$

or in terms of length scales $\ell_{re} \gg \ell_V$ as discussed in the previous section. Condition 4.41 enables a considerable simplification in the calculation of the transmission spectrum. For small optical thickness the exponent in the integral in Eq. 4.32 can be approximated by the first term in the Taylor expansion, which gives for $\Lambda(\omega, n_0, T)$, defined in Eq. 4.33,

$$\begin{aligned}\Lambda(\omega, n_0, T) &\simeq \frac{I_0}{\hbar\omega}\int_V n(\vec{r})\sigma_V(\vec{r},\omega)\,d^3r \\ &\simeq \frac{I_0}{\hbar\omega}\int_{B_0}^{\infty} \rho_M(B)n(B)\sigma_V(B,\omega)\,dB\end{aligned} \tag{4.42}$$

where $\rho_M(B)$ is the magnetic density of states (see Sect. 2.3.3). In this equation we have assumed the incoming intensity I_0 to be constant over the sample diameter, which is true in the low temperature limit. For the "long trap" this condition is fulfilled for temperatures $T \ll 40\,\mathrm{mK}$.

For $T \gg 2.2\,\mathrm{mK}$, the Voigt line can be approximated by a Gaussian profile and the total absorption on the σ_1 transition in the Ioffe quadrupole trapping field

becomes

$$\Lambda(\omega, n_0, T) = \frac{I_0}{\hbar\omega} n_0 \sigma_0 \frac{4\pi}{\alpha^2\sqrt{\beta}} \int_{B_0}^{\infty} dB\,[(B-B_0)^{3/2} + B_0(B-B_0)^{1/2}] \times \exp(-\mu_B(B-B_0)/k_BT)\sqrt{\pi}\frac{\gamma}{b}\exp\left[-(\frac{\omega-\omega_{\sigma 1}(B)}{b})^2\right]. \quad (4.43)$$

In this limit a closed expression for the line shape function can be obtained. For $T \ll 2.2\,\mathrm{mK}$, the Voigt profile can be approximated by a Lorentzian and the line shape function is given by

$$\Lambda(\omega, n_0, T) = \frac{I_0}{\hbar\omega} n_0 \sigma_0 \frac{4\pi}{\alpha^2\sqrt{\beta}} \int_{B_0}^{\infty} dB\,[(B-B_0)^{3/2} + B_0(B-B_0)^{1/2}] \times \exp(-\mu_B(B-B_0)/k_BT)\frac{1}{[(\omega-\omega_{\sigma 1}(B))/\gamma]^2+1}. \quad (4.44)$$

Also in this case a closed expression for the line shape function can be obtained (see Ref. [12]). In chapter 5 on Doppler cooling, we will come back to this point and show that, for the case of hydrogen, the cross over from the Lorentzian approximation to the Gaussian approximation almost coincides with the Doppler limit, $T_D = 2.99\,\mathrm{mK}$. For these low temperatures the Zeeman shift over the sample is smaller than the natural linewidth ($k_BT \lesssim \hbar\Gamma$) which means there are no resonant shells anymore. In Sect. 4.8 we will derive for this low temperature limit an analytical expression for the transmission spectrum for *all* densities. There is an interesting difference between hydrogen and the heavier elements, like Na and Cs. The cross over from the Lorentzian to the Gaussian approximation for these elements ($T = 12\,\mathrm{mK}$ for Na) takes place at temperatures much higher than the Doppler limit ($T_D = 240\,\mu\mathrm{K}$ for Na). Using the Lorentzian approximation one can then derive a closed expression for the Doppler cooling rate of an inhomogeneous gas in the optically thin limit. For very light atoms, like positronium, the cross over takes place at temperatures lower than the Doppler limit which means the Gaussian approximation may be used to calculate the Doppler cooling rate in the optically thin limit.

The resonant shell model is valid for temperatures $k_BT \gtrsim \hbar\gamma$ (for hydrogen $T \gtrsim 2.4\,\mathrm{mK}$). The optically thin limit then enables one to determine a simple relation between the location of the peak in the absorption spectrum and the temperature [4]. As the light is hardly attenuated in passing through the sample, absorption will be strongest at the resonant shell, the location of which is determined by the laser frequency. In the measurement of a transmission spectrum, the absorption will be maximal when the resonant shell coincides with the shell containing most atoms. The magnetic field B_p where this shell is located can be calculated from the function $\rho_M(B)\exp(-\mu_B(B-B_0)/k_BT)$ describing the number of atoms in a magnetic field

interval $(B, B+dB)$, where $\rho_M(B)$ is the magnetic density of states, Eq. 2.12. The magnetic field B_p is related to the temperature T by

$$T = \frac{\mu_B B_p}{k_B} \frac{B_p - B_0}{3B_p/2 - B_0}. \tag{4.45}$$

For $T \ll T_0$, $\mu_B(B_p - B_0)/k_B T \simeq \frac{1}{2}$. This equation shows a fundamental property of the transmission spectrum in the optically thin limit: as the gas cools, the difference $(B_p - B_0)$ becomes smaller which means the line in the transmission spectrum gets narrower.

4.8 Optically thick limit

The condition for an optically thick sample is given by the complement of Eq. 4.41

$$\int_{-\infty}^{\infty} n(z)\sigma_V(z,\omega)\, dz \gg 1, \tag{4.46}$$

or in terms of length scales, $\ell_{re} \ll \ell_V$. In the high-density case, illustrated in Fig. 4.4, the sample is optically thick and the light is totally absorbed before the resonant shell. In this limit, the picture we had in the optically thin limit, where absorption is strongest in the resonant shell, breaks down. From the discussion of the Voigt thickness in Sect. 4.6.1 we can now show for what densities the sample is optically thick. There it was shown that, in the axial direction, typically $\ell_V \simeq 5.5\,\mathrm{mm}$. This means that for densities $n_0 \gg 10^{11}\,\mathrm{cm}^{-3}$ the sample is optically thick. In Fig. 4.4 this limit is illustrated for $n_0 = 10^{12}\,\mathrm{cm}^{-3}$. For $n_0 = 10^{11}\,\mathrm{cm}^{-3}$, $\ell_{re} \simeq \ell_V$ and the light is absorbed in passing both shells. To locate the region of maximum absorption, $I(\rho, z, \omega)$ will have to be found from Eq. 4.32. We will now consider the attenuation of the light in the Gaussian and in the Lorentzian approximation.

Gaussian approximation ($T \gg 2.2\,\mathrm{mK}$ for hydrogen). We can make a few simplifying assumptions. For densities at which the absorption will take place close to resonance, the absorption coefficient will be mainly determined by the peak of the Voigt profile which, to a very good approximation, has a Gaussian behaviour up to its halfwidth (see Sect. 4.6),

$$\sigma_V(\omega, T, z) \simeq \sigma_G(\omega, T, z) = \sigma_0 \sqrt{\pi} \frac{\gamma}{b} \exp\left[-\left(\frac{\Delta\omega_{B0}}{b} - \frac{\mu_B \beta z^2}{\hbar b}\right)^2\right], \tag{4.47}$$

where $\Delta\omega_{B0} = \omega - \omega_{\sigma 1}(B_0)$ is the detuning from the resonance frequency at the trap center. Increasing the density, keeping the laser frequency constant, will move the regime of absorption further out in the wings of the Voigt line where the behaviour is mainly Lorentzian. The location of the regime of maximum absorption will be

strongly dependent on the density, while the width of the absorption regime is independent of density and depends only weakly on temperature and detuning. A closed expression for the intensity $I(\rho, z, \omega)$ cannot be given. If the region of strongest absorption lies close to the resonant shell, however, we can derive an approximate expression for the integral in Eq. 4.32. The integral can be evaluated if we multiply the argument of the integral with a factor $f = -z(\hbar\Delta\omega_{B0}/\mu_B\beta)^{-1/2}$ which is equal to unity at the peak of the gaussian line shape. This is allowed only because the integral is strongly peaked and contributes only over a narrow interval Δz over which the factor f is close to unity. This modified integral forms a good approximation to the actual absorption integral close to resonance and for normalized detunings $\Delta\omega_{B0}/\gamma > 1$. In this limit the attenuation along the z-axis can be derived from

$$\int_{-\infty}^{z} n(z')\sigma_V(\omega, z')\, dz' \simeq$$
$$n_0\sigma_0\sqrt{\frac{\hbar\gamma}{\mu_B\beta}}\frac{\pi}{4\sqrt{\Delta\omega_{B0}/\gamma}}\exp(-\frac{\hbar\Delta\omega_{B0}}{k_BT})\,\mathrm{erfc}[\frac{\mu_B\beta z^2}{\hbar b} - \frac{\Delta\omega_{B0}}{b}]. \qquad (4.48)$$

In Fig. 4.6 we compare the integral in Eq. 4.32 for a Voigt line shape, a Lorentzian and a Gaussian with the approximation from Eq. 4.48. The plot shows that the Gaussian approximation works well close to resonance. The modified integral from Eq. 4.48 at resonance gives an absorption coefficient which differs by $\simeq 15\,\%$ from the value obtained by numerical integration. In the next chapter on Doppler cooling we will see that this condition of total absorption close to the resonant shell plays an important role in optimizing the cooling rate in the optically thick regime. We will then use Eq. 4.48 to derive an approximate condition for optimal cooling in the limit of an optically thick shell.

Lorentzian approximation ($T \ll 2.2\,\mathrm{mK}$ for hydrogen). This approximation coincides with the condition $k_BT \ll \hbar\gamma$, which effectively means that the atoms may be considered to be all located in the center of the trap in the field B_0. In this case the trapping potential is parabolic (see Sect. 2.2) and Eq. 4.32 can be solved analytically for *all* densities.

$$I(\rho, z, \omega)/I_0(\rho) =$$
$$\exp\left(\frac{-n_0\sigma_0}{(\Delta\omega_{B0}/\gamma)^2+1}\exp(-\frac{\mu_B(\alpha^2/2B_0)\rho^2}{k_BT})\int_{-\infty}^{z} dz'\,\exp(-\frac{\mu_B\beta z'^2}{k_BT})\right). \qquad (4.49)$$

Let us now consider the optically thick limit in which the sample casts a shadow on the detector. The radius of this shadow, which I refer to as the optical radius R_{opt}

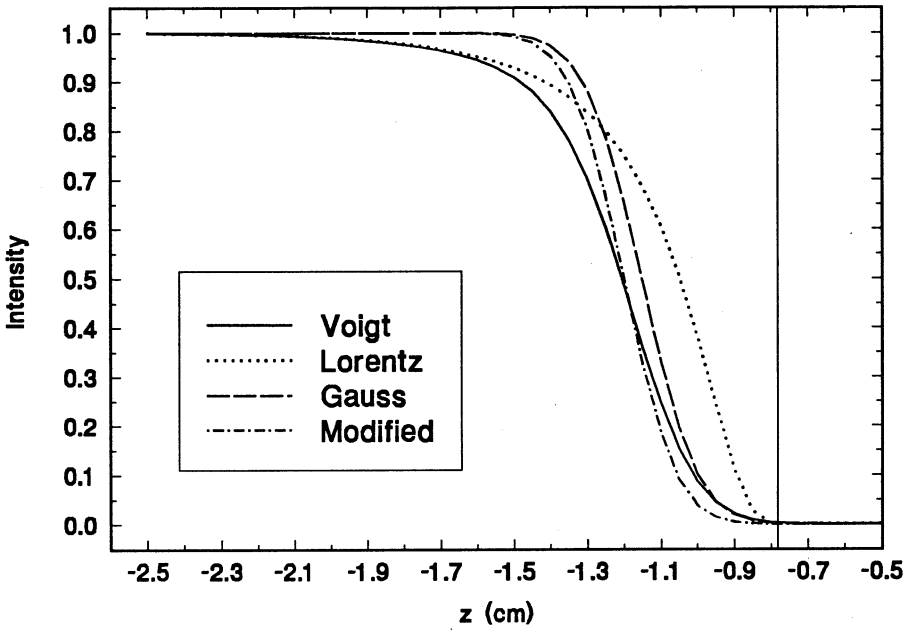

Figure 4.6: Comparison of the numerically integrated absorption coefficient using a Voigt profile, a Lorentzian and a Gaussian with the result from the modified integral near resonance. The plot is for $n_0\sigma_0 = 1, \Delta\omega_{B0}/\gamma = 4$ and $T = 50\,\mathrm{mK}$.

of the sample, is defined by the radius at which the transmission has increased to a value e^{-1}:

$$R_{opt}^2 = \frac{k_B T}{\mu_B(\alpha^2/2B_0)} \ln\left[\frac{n_0\sigma_0 L_s}{(\Delta\omega_{B0}/\gamma)^2+1}\right], \tag{4.50}$$

where L_s is the effective length of the sample (see Sect. 2.3.3). The optical radius can be larger than the effective radius R_s.

In Eq. 4.49 one of the interesting properties of optically thick, cold samples can be seen: if one cools a fixed number of atoms from temperature T_1 to T_2, n_0 increases inversely proportional to the effective volume so by a factor $(T_1/T_2)^{3/2}$ and faster than L_s decreases. At $\rho = 0$, for example, one has to detune further to make the sample optically thin again which means that the line in the transmission spectrum has become wider. As opposed to the resonant shells model (see Eq. 4.45), the lines in the transmission spectrum become broader as the sample cools.

The total number of absorbed photons of frequency ω, Eq. 4.33, is

$$\Lambda(\omega, n_0, T) = \Phi_0\left\{1 - \epsilon(T)\left(\frac{n_0\sigma_0 L_s}{(\Delta\omega_{B0}/\gamma)^2+1}\right)^{-\epsilon(T)} \gamma\left[\epsilon(T), \frac{n_0\sigma_0 L_s}{(\Delta\omega_{B0}/\gamma)^2+1}\right]\right\} \tag{4.51}$$

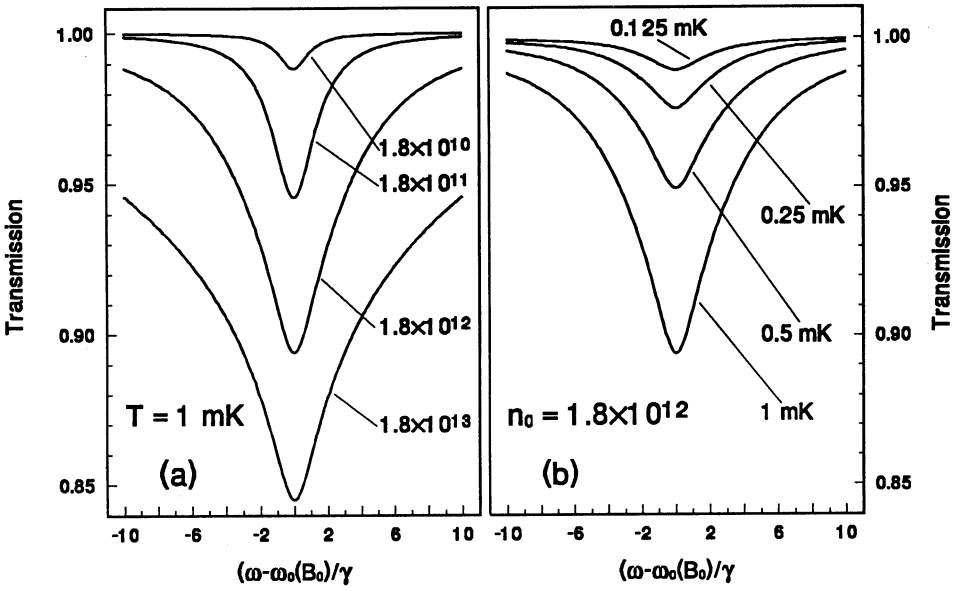

Figure 4.7: Transmission spectra for cold samples ($T \lesssim 2.2\,\mathrm{mK}$) when the Zeeman broadening is neglegible: (a) for a constant temperature of 1 mK and for densities of $1.8 \times 10^{10}, 1.8 \times 10^{11}, 1.8 \times 10^{12}$ and $1.8 \times 10^{13}\,\mathrm{cm}^{-3}$ (b) for a constant density of $1.8 \times 10^{12}\,\mathrm{cm}^{-3}$ and for temperatures of 0.5, 1.0, 1.5 and 2.0 mK.

where Φ_0 is the total incoming photon flux and $\epsilon(T) = k_B T/(\mu_B(\alpha^2/2B_0)R_b^2)$ gives the ratio of the sample cross section to the beam cross section, R_b is the radius of a Gaussian laser beam at its e^{-1} point (in the experiment $\simeq 0.5\,\mathrm{mm}$) and $\gamma[a,x]$ is the incomplete gamma function. For the experimental conditions, $\epsilon(T) \ll 1$ ($\simeq 0.04$ at 1 mK) and $n_0\sigma_0 L_s \gg 1$ in the limit of an optically thick shell. In Fig. 4.7 transmission spectra are plotted for different densities and temperatures. From the plots it is clear that for higher densities at constant temperature the absorption peak height and width increase. For constant density and increasing temperature the absorption peak increases while the width changes very little. This weak temperature dependence is due to the effective length, L_s, which we can see from Eq. 4.49. Taking the case for $\rho = 0$, the total absorption after traversing the sample has only increased due to the larger sample dimensions at higher temperature.

References

[1] O.J. Luiten, H.G.C. Werij, I.D. Setija, M.W. Reynolds, T.W. Hijmans, and J.T.M. Walraven, Phys. Rev. Lett. **70**, 544 (1993).

[2] R. van Roijen, J.J. Berkhout, S. Jaakkola, and J.T.M. Walraven, Phys. Rev. Lett. **61**, 931 (1988).

[3] J.M. Doyle, J.C. Sandberg, I.A. Yu, C.L. Cesar, D. Kleppner, and T.J. Greytak, Phys. Rev. Lett. **67**, 603 (1991)

[4] O.J. Luiten, Ph. D. thesis, University of Amsterdam (1993).

[5] Yu. Kagan, B.V. Svistunov, and G.V. Shlyapnikov, JETP Lett. **48**, 56 (1988).

[6] See, for instance : L. Allen and J.H. Eberly, Optical Resonance and Two-Level Atoms (John Wiley & Sons, 1975).

[7] R. Loudon, The Quantum Theory of Light (Oxford University Press, 1983).

[8] P.W. Milonni and J.H. Eberly, Lasers (John Wiley & Sons, 1988).

[9] H.A. Bethe and E.E. Salpeter, Quantum Mechanics of One- and Two-electron Atoms (Plenum Publishing Corporation, New York, 1977).

[10] R.G. Beausoleil, Ph. D. Thesis, Stanford University (1986).

[11] D.G. Hummer, Mem. R. astr. Soc. **70**, 1 (1965).

[12] The line shape function can be obtained by first rewriting the Lorentzian to the real part of $(1 + i[(\omega - \omega_{\sigma 1}(B))/\gamma])^{-1}$. The integral can then be evaluated using the following expression

$$\int_0^\infty \frac{y^\nu}{y+a} e^{-py}\, dy = a^\nu e^{ap} \Gamma(\nu+1)\Gamma(-\nu, ap), \tag{4.52}$$

where $\Gamma(\nu, z)$ is the incomplete gamma function, from: F. Oberhettinger and L. Badii, Tables of Laplace Transforms (Springer-Verlag, 1973).

Chapter 5

Doppler cooling of atomic hydrogen in magnetostatic traps

5.1 Introduction

Lyman-α radiation offers a powerful tool to manipulate hydrogen atoms. One may select for this purpose a closed optical transition, in which the atoms decay back to their initial hyperfine state and only the kinetic motion of the atoms is affected, or choose an optical pumping transition in which the population is transferred to another hyperfine state. If this is a "high-field-seeking" hyperfine state, the atoms are ejected from the trap (see chapter 6). In this thesis both methods are used to optically cool atomic hydrogen. In this chapter, I present Doppler cooling on the (closed) σ_1 transition ($1S_{1/2,m_J=1/2} \rightarrow 2P_{3/2,m_J=3/2}$). Chapter 6 will be devoted to light-induced evaporation based on the optical pumping transition σ_2 ($1S_{1/2,m_J=1/2} \rightarrow 2P_{3/2,m_J=-1/2}$).

First proposed by Hänsch and Schawlow [1], and by Wineland and Dehmelt [2] for the case of ions bound in an electromagnetic trap, Doppler cooling has become a standard technique for slowing down atomic beams [3, 4] and cooling of neutral atoms (see, for example, the special issue of JOSA B [5]). The method is based on the preferential deceleration of atoms with a velocity opposing the direction of a laser beam, by irradiation with light tuned slightly below the resonance frequency of an atom at rest. For two atoms with equal speed but opposite velocity vector, due to the Doppler effect the atom moving towards the light source scatters the light more strongly than the atom moving in opposite direction. In a single scattering event, the momentum $\vec{p}$ of the atom changes by $\Delta\vec{p} = \hbar(\vec{k} - \vec{k}')$, where $\vec{k}$ and $\vec{k}'$ are the wavevectors of the incident and scattered photons respectively. If the intensity of the incident light is low to the extent that stimulated emission may be neglected, after

many scattering events, the momentum transfer per event averages out to $\Delta\vec{p} = \hbar\vec{k}$, as the photons are scattered in random directions. The corresponding average recoil velocity per event is $v_r = \hbar k/m$. The random character of the scattering makes the atom undergo a random walk in phase space which results in a residual heating. The minimum temperature that can be reached with Doppler cooling, the Doppler limit T_D, is determined by a balance between the cooling and the residual heating due to the photon recoil.

A first glance at the magnitude of the basic quantities shows that Doppler cooling is a very efficient cooling mechanism for hydrogen. The large momentum of a Lyman-α photon ($\lambda = 121.6\,\mathrm{nm}$) and the small mass of the hydrogen atom make the recoil velocity very large ($v_r \simeq 3.3\,\mathrm{m/s}$) as compared to the case of e.g. sodium, where $v_r \simeq 3\,\mathrm{cm/s}$ for excitation of the $3S_{1/2} \rightarrow 3P_{3/2}$ transition at $\lambda = 589\,\mathrm{nm}$. A room temperature beam of atomic hydrogen with a typical velocity of $2.7 \times 10^3\,\mathrm{m/s}$, could be slowed and stopped with approximately 830 L_α photons if the laser beam could be kept tuned for optimal deceleration. However, due to the absence of a cw light source of sufficiently narrow band these ideas have, up to this moment, not been experimentally realized. Before discussing hydrogen, some differences with optical cooling of other systems will be mentioned.

Doppler cooling of a gas of neutral atoms has first been performed on sodium [6]. By irradiating the gas with six cw laser beams an optical molasses is formed at the intersection of the six beams, cooling all three degrees of freedom. The atoms in an optical molasses are not actually trapped, but experience a strong damping force opposing their motion. To load an optical molasses with atoms, an atomic beam is first slowed down and cooled by a single, opposing laser beam to produce atoms at velocities which can be captured in the molasses. The slowing laser is kept tuned for optimal deceleration by compensating the Doppler shift, which decreases as the atoms slow down, by a changing Zeeman shift [3] or by tuning the frequency of the slowing laser [4]. Recently, optical traps have been loaded to densities of $\sim 10^{11}\,\mathrm{cm}^{-3}$ [7]. At these densities the elastic collision time is longer than the lifetime of the gas. In typical optical cooling experiments with alkali atoms, the lifetime in this molasses ($\sim 1\,\mathrm{sec}$) is determined by collisions with background gas.

For atomic hydrogen the situation is different. H is trapped cryogenically and subsequently Doppler cooled with a *single, pulsed* beam of Lyman-α radiation. Since H is confined in a trap, one beam suffices to cool the degree of freedom along the direction of the beam. The orthogonal motion is subsequently cooled as the degrees of freedom are coupled by elastic collisions. The cryogenic filling method (see Sect. 2.3.1), produces higher densities, up to $\sim 10^{14}\,\mathrm{cm}^{-3}$, than are achieved in the optical cooling experiments with alkali atoms. At these higher densities,

the thermalization time, which is of the order of the elastic collision time τ_c, is smaller than the Doppler cooling time τ_D, which means that, during cooling, we have a quasithermal gas. Another attractive aspect of the cryogenic environment is the extremely high vacuum that can be created, in fact the best vacuum that can be achieved in any experimental situation. This enables long trapping times. In practice the lifetime of the gas is limited by intrinsic decay mechanisms. This allows the use of low intensity light, $\sim 10^6$ times weaker than in typical experiments with Na, or pulsed light with a duty factor $\sim 10^6$ times smaller as compared to Na experiments, to perform Doppler cooling.

Doppler cooling of neutral atoms in a magnetostatic field, much like the experiments described in this thesis, were performed previously by Helmerson *et al.* [8] with Na in the collisionless regime. In these experiments, the samples were optically thin. Our experiments were performed with a gas in thermal equilibrium at densities covering both the optically thin and the optically thick regime. The results will be interpreted using the shell model, introduced in the previous chapter (see Sect. 4.6.1). The atoms that are resonant with the incident light will be located in the resonant shell. Photons absorbed by atoms outside the σ_1 resonant shell, are red-shifted with respect to the local resonant frequency and preferentially give rise to cooling. Photons absorbed by atoms in the inner region of the shell, preferentially give rise to heating. I will show that in the optically thin regime, the Doppler limit is slightly higher than in the homogeneous case and will derive a simple condition for the laser detuning to achieve optimal cooling. In the optically thick regime, the Zeeman shift and the optical thickness combine in a unique fashion to shield the atoms in the inner region of the resonant shell from the light. This will increase the cooling rate and slightly lower the Doppler limit, although not below the value of the Doppler limit for the homogeneous case. The optical thickness is accompanied by effects of multiple scattering. A numerical simulation has shown [9] that the additional heating caused by multiple scattering has a neglegible effect up to the highest densities reached in our Doppler cooling experiments, $n_0 \sim 5 \times 10^{12}\,\mathrm{cm}^{-3}$.

During cooling we spectroscopically monitor the evolution of n_0 and T. Doppler cooling has the advantage that it cools the gas without removing atoms. As the gas cools, n_0 increases which is attractive for compressing the trapped gas to densities at which other cooling techniques, such as evaporative cooling, can be used.

In the following sections, I will first consider Doppler cooling of a homogeneous thermal gas, emphasizing the effects a small atomic mass will have on the cooling process. Then I will turn to the case of Doppler cooling in an inhomogeneous magnetic field. The optically thin and optically thick limit will be discussed to explain the influence optical thickness has on the cooling process. This will be used

in the subsequent section to understand the results of a numerical calculation of the cooling rate for the conditions of the experiments. These results will be implemented in the equation describing the evolution of a thermal gas subjected to several energy- and particle loss terms: dipolar heating, evaporative cooling and Doppler cooling. The Doppler cooling experiments will be described and to conclude, the results from these experiments will be compared with the results from the model.

5.2 The Doppler cooling integral

Laser cooling may be described in terms of radiative forces in which the effects of absorption and emission are considered separately. The absorption of photons results in radiation pressure. The spontaneous emission, due to its random character, produces a randomly fluctuating force. To obtain the motion of the atoms under the influence of these two forces, one can make use of a Fokker-Planck equation [10, 11] or a Langevin equation [12]. For a gas of trapped hydrogen we do not follow this approach. At densities investigated, interatomic collisions will act to maintain a Boltzmann distribution and the effect of Doppler cooling will be to decrease the temperature of the distribution. In a trapped collisional gas, it is justified to assume a thermal distribution if

$$\tau_D^{-1} \ll \tau_c^{-1}, \tag{5.1}$$

where τ_D^{-1} is the Doppler cooling rate and τ_c^{-1} is the elastic collision rate. We use the approach of Wineland and Itano [13], who described Doppler cooling of a thermal gas of neutral atoms with a single beam of cw radiation with an intensity far below the saturation limit. Many aspects of their approach apply to our experimental situation. However, the approach has to be extended to the case of atoms in an inhomogeneous field and to the case of pulsed radiation. Moreover, we put emphasis on the optically thick limit.

The pulsed character of the light ($\tau_{puls} \simeq 20$ nsec) results in a finite bandwidth of the light source. For the Lyman-α transition, $\tau_{puls} \gg \gamma^{-1}$ where γ is the natural halfwidth ($\gamma \equiv \frac{1}{2}\Gamma$), so that the excited-state population practically reaches its steady-state value [14]. The time between pulses ($\tau_{rep} \simeq 20$ msec) is sufficiently long: $\tau_{rep} \gg \gamma^{-1}$, to let all the atoms decay back to their ground state and to let them perform several oscillations in the trap so that irradiation will not result in local cooling of the sample. In the subsequent sections, we will, for the time being, neglect the bandwidth of the light source and assume monochromatic radiation, taking into account the pulsed character of the light by introducing a duty factor, which for our apparatus is $\sim 10^{-6}$.

To find the Doppler cooling rate τ_D^{-1}, one has to determine the change in internal energy of the gas per scattered photon. If the density of the gas is sufficiently low, $n_0 \lambda\!\!\!^{-3} \ll 1$, collective excitations of the gas (polaritons) and collision broadening may be neglected and the change in internal energy may be obtained from the non-relativistic expressions for conservation of energy and momentum in the scattering of a photon from a single atom.

$$\begin{aligned} m\vec{v} + \hbar\vec{k} &= m\vec{v}' + \hbar\vec{k}' \\ \tfrac{1}{2}mv^2 + \hbar\omega &= \tfrac{1}{2}mv'^2 + \hbar\omega', \end{aligned} \tag{5.2}$$

where $\vec{v}, \vec{k}$ and $\omega = c|\vec{k}|$ are respectively the velocity of the atom, the photon wavevector and the resonant frequency in the laboratory reference frame before scattering and $\vec{v}', \vec{k}'$ and ω' after scattering. If we take the incident wavevector $\vec{k}$ to lie along the z-axis of a polar coordinate system and use that $|\vec{k}| \simeq |\vec{k}'|$, we obtain

$$\hbar\omega - \hbar\omega' = 2E_r(1 - \cos\theta') + \hbar\vec{k} \cdot \vec{v}(1 - \cos\theta'), \tag{5.3}$$

where the polar angle θ' refers to the direction into which the photon is scattered and $E_r = \hbar^2k^2/2m$ is the recoil energy (for hydrogen, $E_r/k_B = 0.64\,\mathrm{mK}$). The first term on the r.h.s. of Eq. 5.3 is the recoil shift, the second term is the first-order Doppler shift. Because the probability for scattering into a solid angle $d\Omega'$ in the direction (θ', ϕ') is equal to the probability that the photon is scattered in the direction $(\theta' + \pi, \phi')$, the $\cos\theta'$ terms average to zero. The energy change of the atom, averaged over all scattering angles is then

$$\Delta E_{kin} = \hbar(\omega - \omega') = 2E_r + \hbar\vec{k} \cdot \vec{v}. \tag{5.4}$$

The recoil energy enters twice because the atom suffers a recoil during the absorption and the emission of a photon.

In Doppler cooling we consider a near-resonant process. The cross section for absorption, well below saturation, has a Lorentzian lineshape,

$$\sigma_L(\vec{r}, \omega) = \frac{\sigma_0}{((\omega - \omega_{abs})/\gamma)^2 + 1} \tag{5.5}$$

where σ_0 is the resonant cross section for exciting a polarized hydrogen atom on the σ_1 transition with $\vec{B}$ parallel to the z-axis (see Eq. 4.16) and $\omega_{abs} = \omega_0(\vec{r}) + \vec{k}\cdot\vec{v} + E_r/\hbar$ is the resonant frequency in the laboratory frame, which in the trap is position dependent due to the Zeeman shift. In the experiments, the intensity $I \ll I_{sat} = 3.6\,\mathrm{W\,cm^{-2}}$. For intensities $I \gtrsim I_{sat}$, the propagation of the electromagnetic field through the gas and, consequently, the Doppler cooling rate will become sensitive to the detailed shape of the light pulse which is not well-known (see Sect. 4.3). For

a discussion of the effect stimulated emission and power broadening will have on Doppler cooling in the limit $I \gtrsim I_{sat}$ using cw light, the reader is referred to Refs. [15, 16].

For a collection of atoms in an infinitesimal volume element d^3r, the rate of change of internal energy E is

$$d\dot{E} = \frac{I(\vec{r},\omega)}{\hbar\omega} \left\langle \alpha_L(\vec{r},\omega - kv_z)(2E_r + \hbar k v_z) \right\rangle d^3r \tag{5.6}$$

where $\alpha_L(\vec{r},\omega - kv_z)$ is the absorption coefficient at position $\vec{r}$ due to particles with velocity $\vec{v}$ and the brackets denote an average over the Maxwell velocity distribution.

To describe the physical picture as transparent as possible, we will, for the time being, neglect the effects of the polarization of the light and describe the relative attenuation in terms of an absorption cross section $\sigma_L(\vec{r},\omega - kv_z)$. For this case, we can write $\alpha_L(\vec{r},\omega - kv_z) = n(\vec{r})\sigma_L(\vec{r},\omega - kv_z)$. Integrating Eq. 5.6 over the total volume of the gas then gives the total rate of change of internal energy of the gas due to Doppler cooling,

$$\dot{E} = \dot{Q}_r(\omega) + \dot{Q}_D(\omega) = 2E_r \int_V \frac{I(\vec{r},\omega)}{\hbar\omega} n(\vec{r}) \left(\sigma_V(\vec{r},\omega) - \frac{k_B T}{\hbar} \frac{\partial \sigma_V}{\partial \omega} \right) d^3r, \tag{5.7}$$

where the recoil heating $\dot{Q}_r(\omega)$ (i.e., the total absorption rate times $2E_r$) corresponds to the first term between brackets, the Doppler cooling $\dot{Q}_D(\omega)$ corresponds to the second term between brackets, $\sigma_V(\vec{r},\omega)$ is the Doppler broadened absorption cross section (see Eq. 4.19) and the function $I(\vec{r},\omega)$ describes the spatial intensity distribution of a light beam of frequency ω traversing the sample (see Sect. 4.6). Notice that Eq. 5.7 is not only valid for small velocities of the atoms, but also for velocities for which the Doppler shift $b \gg \gamma$. It holds for light intensities well below saturation, $\theta_B = 0$ and if polarization and dispersion effects may be neglected. For the σ_1 transition, it was shown in Sect. 4.6 the attenuation of the light could be very well approximated by the solution of Eq. 4.31 which was derived under the same assumptions as Eq. 5.7. Although Eq. 5.7 is very useful to illustrate the phenomenology of Doppler cooling, comparison with experiments was always based on Eq. 5.6. In Sect. 5.4.2 we will show how Eq. 5.7 can be rewritten to a form in which it can obtained from the solution of Eqs. 4.29. The small effects due to polarization and $\theta_B \neq 0$ are then automatically included. We emphasize that this equation is also valid in the optically thick regime as long as the collision broadening and heating due to multiple scattering can be neglected.

Often Doppler cooling will be discussed in terms of the change in internal energy of the gas per *scattered* photon, $\dot{E} = 2E_r \xi_D \Lambda(\omega, n_0, T)$ where $\Lambda(\omega, n_0, T)$ is the

absorption rate given by Eq. 4.33 and

$$\xi_D = 1 - \frac{k_B T}{\hbar \Lambda} \int \frac{I(\vec{r},\omega)}{\hbar\omega} n(\vec{r}) \frac{\partial \sigma_V}{\partial \omega} d^3r. \tag{5.8}$$

This quantity will be called the Doppler cooling parameter.

Neglecting any loss of particles, for a given frequency ω the gas will cool until a minimum temperature is reached for which $\dot{E} = 0$ or equivalently $\xi_D(\omega, N, T) = 0$ and the recoil heating is balanced by the Doppler cooling. The lowest temperature for which $\dot{E} = 0$ is satisfied is the Doppler limit T_D. For the optically thick limit (see Sect. 5.4.2), T_D is weakly density-dependent. The expression for the Doppler cooling rate can be quantitatively understood for the Lorentzian approximation ($b \ll \gamma$) and for the Gaussian approximation ($b \gg \gamma$, see Sect. 4.6).

For the Lorentzian approximation, we rewrite the second term in Eq. 5.6 in the following form

$$d\dot{Q}_D = \frac{I(\vec{r},\omega)}{\hbar\omega} \tfrac{1}{2} \langle \hbar k v_z \, \sigma_L(\omega + k v_z) - \hbar k v_z \, \sigma_L(\omega - k v_z) \rangle_+ \, n(\vec{r}) d^3r$$

where the contribution from equal but opposite velocity v_z has been explicitly written down. The angular brackets $\langle \ \rangle_+$ now denote an average over the Maxwell velocity distribution for positive v_z. To conserve normalization, the expression between brackets has to be multiplied by $\frac{1}{2}$. Clearly we see now how the cooling is caused by a difference in absorption cross section of atoms with equal but opposite velocities. For small velocities, this can be written as

$$d\dot{Q}_D \simeq \frac{I(\vec{r},\omega)}{\hbar\omega} \hbar k^2 \langle v_z^2 \rangle_+ \frac{\partial \sigma_L}{\partial \omega} n(\vec{r}) d^3r.$$

Averaging over positive v_z, one obtains $\langle v_z^2 \rangle_+ = k_B T/m$, which results in the expression for $\dot{Q}_D$ given in Eq. 5.7, but with a Lorentzian absorption cross section. The frequency derivative of σ_L is a result of the fact that for a given Doppler shift the cooling rate is proportional to the difference in cross section of atoms moving with velocity $+v_z$ and $-v_z$. Very far in the wings of a line, $(\partial\sigma_L/\partial\omega) \ll 1$, which means that nearly as much atoms with velocity v_z as with velocity $-v_z$ are excited and the cooling rate is small.

For the Gaussian approximation, averaging over the Maxwell velocity distribution in Eq. 5.6 results in the frequency derivative of the Gaussian absorption cross section. This is a result of the fact that the fraction of atoms at large velocities is exponentially suppressed and the Doppler shift is linearly proportional to the velocity. For both the Lorentzian and the Gaussian approximation (although for different physical reasons) we see that optimum cooling is achieved at the position of maximum slope in the lineshape. For the general case, optimum cooling is achieved at the position of maximum slope in the Voigt lineshape.

5.3 Doppler cooling of a homogeneous gas

For the homogeneous case of a gas of free atoms confined in a volume V, the resonant cross section is position-independent and Eq. 5.8 can be written as

$$\xi_D(\omega, T) = 1 - \frac{k_B T}{\hbar \sigma_V(\omega)} \frac{\partial \sigma_V}{\partial \omega}. \tag{5.9}$$

Atomic hydrogen is the lightest atom that has been Doppler cooled so far. We will calculate the minimum temperature that can be achieved with Doppler cooling in a homogeneous gas of atomic hydrogen and more closely consider the influence of a small mass, and consequently a large recoil energy, on the cooling process. H is in the cross over regime from the heavy atoms, with $E_r \ll \hbar\gamma$, to the light, "exotic" atoms, like positronium and muonium, with $E_r \gg \hbar\gamma$. Doppler cooling of "exotic" atoms is less of an academic problem than it may seem at first sight. The lifetimes of ortho-positronium and muonium (140 nsec [17] and 2.2 μsec [18] respectively) are sufficiently long that laser spectroscopic experiments have been performed [19].

In Fig. 5.1(a) and (b), the Doppler cooling parameter

$$\xi_D = 1 - (\frac{k_B T}{\hbar b}) \frac{\mathrm{Re}\, w'[(\Delta + i)\gamma/b]}{\mathrm{Re}\, w[(\Delta + i)\gamma/b]}, \tag{5.10}$$

is plotted for different temperatures and different values of $E_r/\hbar\gamma$ (for hydrogen $\hbar\gamma/k_B = 2.39$ mK). To obtain Eq. 5.10, we have used Eq. 4.19 for the Voigt lineshape where $w'(\zeta) \equiv (\partial w/\partial \zeta)$ and $\Delta \equiv (\omega - \omega_0')/\gamma$ is the reduced detuning. For a particular range of negative detunings, $-\Delta_1 < \Delta < -\Delta_0$, $\xi_D < 0$, i.e., there is cooling as can be seen in Fig. 5.1 (a). The temperature for which $\Delta_1 = \Delta_0$, is the Doppler limit T_D for this particular value of $E_r/\hbar\gamma$. When ξ_D does not intersect the frequency axis, the gas is at a temperature below the Doppler limit and there is no cooling.

The cooling parameter ξ_D has a complex temperature dependence, decreasing from a linear T-dependence in the Lorentzian approximation to no T-dependence in the Gaussian approximation. The effect of a decrease in mass of the atom, keeping the optical properties (γ and k) and the temperature constant, can be seen in Fig. 5.1 (b). The only effect of a smaller mass is a broader Voigt lineshape which results in a decrease of ξ_D proportional to the atomic mass in the Gaussian approximation. In the Lorentzian approximation, ξ_D is not mass dependent.

Case $b \gg \gamma$. When the temperature is so high or the atomic mass is so low that the Doppler width is much larger than the natural halfwidth, we can use the asymptotic approximation for the Voigt lineshape, Eq. 4.34 to obtain an approximate expression for the Doppler limit. After substitution into Eq. 5.10, the detuning for

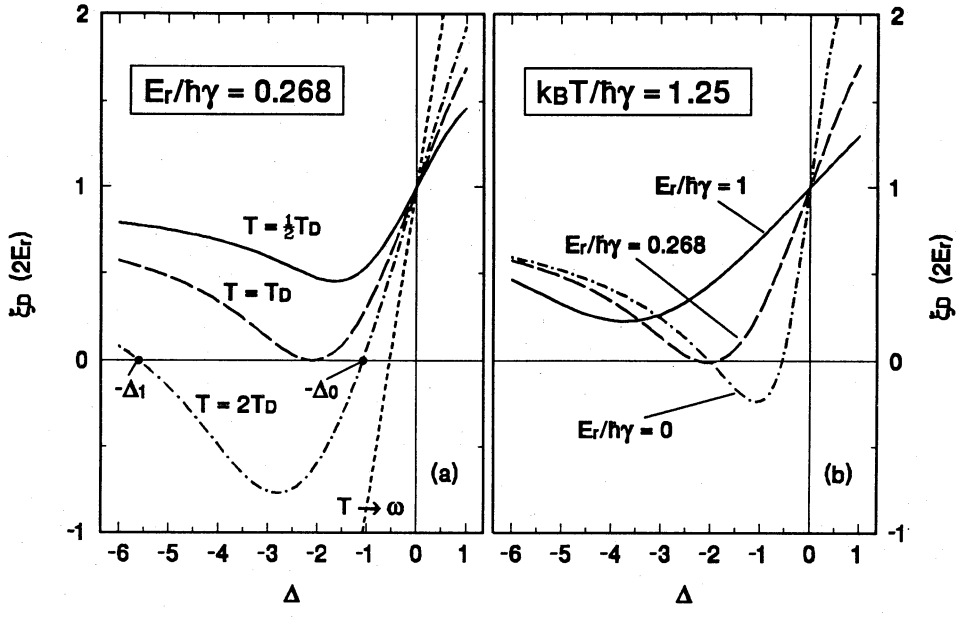

Figure 5.1: The Doppler parameter ξ_D. In Fig.(a), we plot ξ_D for constant $E_r/\hbar\gamma = 0.268$, which corresponds to the case of hydrogen, and temperatures $T/T_D = 0.5$, 1 and 2. In Fig.(b), we plot ξ_D for constant temperature $k_BT/\hbar\gamma = 1.25$ and $E_r/\hbar\gamma = 0$, 0.268 and 1.

optimal cooling can be calculated

$$\Delta \simeq -\frac{b}{\gamma}\sqrt{\ln(\tfrac{1}{2}\sqrt{\pi}\frac{b}{\gamma})} \qquad (\gamma/b \to 0). \tag{5.11}$$

After substituting Eq. 5.11 back into ξ_D, the Doppler limit can be found by applying condition 5.9. For large $(E_r/\hbar\gamma)$, this gives

$$\frac{k_BT_D}{\hbar\gamma} \simeq \frac{E_r}{\hbar\gamma}\left(\tfrac{1}{2}\ln(\frac{k_BT_D}{\hbar\gamma}) + \tfrac{1}{2}\ln(\frac{E_r}{\hbar\gamma}) - 1\right)^{-1}. \tag{5.12}$$

From Eq. 5.12, we see that for large $(E_r/\hbar\gamma)$ the Doppler limit is a more slowly increasing function of the inverse atomic mass than the recoil temperature.

Using Eq. 4.34, we can also roughly determine the detuning Δ_G at which the Lorentzian behaviour in the wings of the lineshape crosses over to Gaussian behaviour in the center of the line. For $|\Delta| \ll \Delta_G$, the Voigt profile can be well approximated by a Gaussian (see the Gaussian approximation, Eq. 4.36 in Sect. 4.6). For the limit $\gamma/b \to 0$, we can use the Gaussian approximation to calculate Δ_0. Substituting a Gaussian profile into condition 5.9, we find that cooling can only be

obtained for a detuning Δ more positive than $-2\Delta_r$, where

$$\Delta_r = \frac{E_r}{\hbar\gamma} \tag{5.13}$$

corresponds to the Doppler shift for atoms moving with the recoil velocity v_r.

Case $b \ll \gamma$. For a temperature so low or an atomic mass so high, that the Doppler width is much smaller than the natural halfwidth, the Voigt lineshape approaches a Lorentzian lineshape, Eq. 4.37. Substituting Eq. 4.37 into condition 5.9, we obtain the minimum temperature that can be reached with Doppler cooling for a particular detuning

$$\frac{k_B T}{\hbar\gamma} \simeq -\frac{\Delta^2 + 1}{2\Delta} \qquad (\gamma/b \ll 1). \tag{5.14}$$

For this case the Doppler limit is

$$k_B T_D \simeq \hbar\gamma \tag{5.15}$$

at a detuning $\Delta = -1$. A temperature lower than $\hbar\gamma/k_B$ can never be reached with Doppler cooling. The Voigt lineshape cannot become narrower than the Lorentzian lineshape which puts an upper bound on the slope of the lineshape and, therefore, results in a finite Doppler limit.

In Fig. 5.2, we plot the minimum temperature that can be achieved with Doppler cooling as a function of $(\Delta - 2\Delta_r)$ for the case of Na, H and a hypothetical element for which $E_r = k_B T_D$. The curve for Na is very well described by the case $b \ll \gamma$. At the Doppler limit ($T_D = 240\,\mu$K for a detuning of $(\Delta - 2\Delta_r) = -1$), $\gamma/b \simeq 7.1$. The recoil temperature $E_r/k_B = 1.2\,\mu$K. Positronium is well characterised by the case $b \gg \gamma$. The Doppler limit for positronium ($T_D \simeq 32.3\,\hbar\gamma/k_B = 38.8\,$mK at a detuning of $(\Delta - 2\Delta_r) \simeq -38$) is smaller than the recoil temperature $E_r/k_B \simeq 123\,\hbar\gamma/k_B = 148\,$mK. For positronium the ratio $\gamma/b \simeq 0.008$ at the Doppler limit. Hydrogen is an intermediate case for which the Doppler limit $T_D = 1.25\,\hbar\gamma/k_B = 2.99\,$mK at a detuning $(\Delta - 2\Delta_r) = -1.55$. The recoil temperature $E_r/k_B = 0.64\,$mK. At the Doppler limit $\gamma/b \simeq 0.86$.

Notice that a): for large $(E_r/\hbar\gamma)$ the Doppler limit is a more slowly increasing function of the inverse mass than the recoil temperature and b): for an infinite mass the Doppler limit $(k_B T_D/\hbar\gamma = 1)$ is larger than the the recoil temperature $(E_r/\hbar\gamma = 0)$. This implies that for a particular value of $(E_r/\hbar\gamma)$ the Doppler limit and the recoil temperature will coincide. Solving Eq. 5.9 with the condition $E_r = k_B T_D$, shows that this occurs at $(E_r/\hbar\gamma) = 2.6267$. In Fig. 5.2, a curve for this condition is plotted. For atoms with $(E_r/\hbar\gamma) > 2.6267$ Doppler cooling of a thermal gas will result in a final temperature smaller than the recoil temperature.

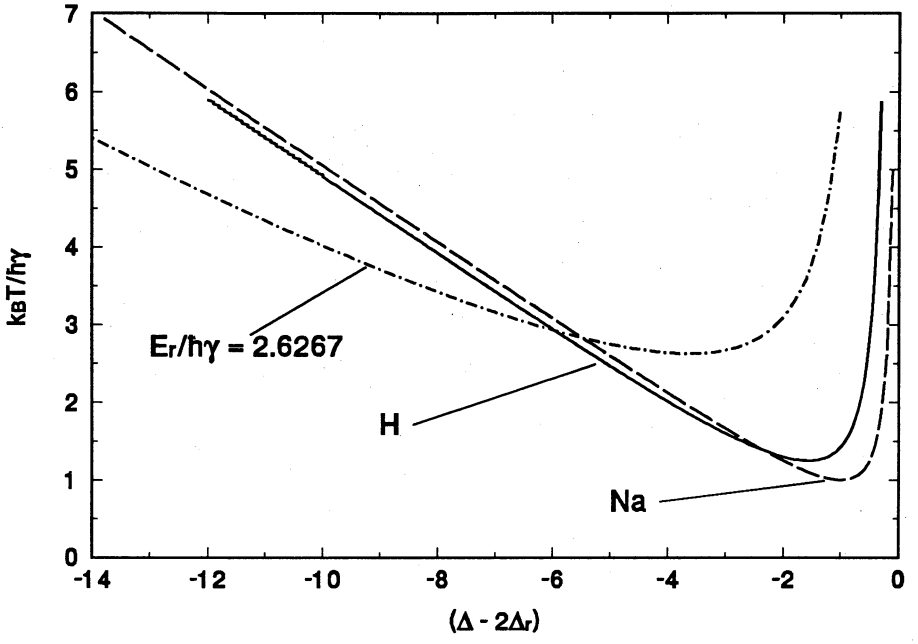

Figure 5.2: Minimum temperature that can be achieved with Doppler cooling for $E_r/\hbar\gamma = 5 \times 10^{-3}$, 0.268 and 2.6267, corresponding to Na, H and a hypothetical element for which $k_B T_D = E_r$ respectively. All curves are frequency shifted with respect to $2\Delta_r$.

5.4 Doppler cooling in an inhomogeneous field

For atoms confined in an inhomogeneous magnetic field, the situation becomes very different. In Sect. 4.6.1, we showed that due to the position dependence of the resonance frequency, the atoms that are resonant with the incident radiation are located in shells around equipotential surfaces. For atoms at rest outside the resonant shell, the incident radiation is red-detuned and scattering will predominantly lead to cooling. In the inner region of the resonant shell, atoms at rest will see light which is detuned to the blue and scattering will, therefore, predominantly lead to heating. In the following two sections, we will use the results that were derived for the optically thin limit (see Sect. 4.7) and for the optically thick limit (see Sect. 4.8) to illustrate how the attenuation of the light influences the Doppler cooling.

5.4.1 The optically thin limit

In the optically thin limit and for a temperature $T > \hbar\gamma/k_B$ (see Sect. 4.7), most light of a given frequency will be absorbed in the resonant shell. To find for what

frequency Doppler cooling is optimal, we will rewrite Eq. 5.7, making use of the fact that in the optically thin limit the intensity distribution of the light beam in the sample is essentially independent of the frequency of the light, $I(\vec{r}) \simeq I_0(\vec{r})$, and the differentiation with respect to ω can be taken outside the integral. The Doppler cooling parameter ξ_D for the inhomogeneous case then becomes

$$\xi_D = \left(1 - \frac{k_B T}{\hbar \Lambda(\omega, n_0, T)} \frac{\partial \Lambda}{\partial \omega}\right). \tag{5.16}$$

From Eq. 5.16, we see that, although the absorption spectrum may be strongly inhomogeneously broadened as compared to the homogeneous case, the cooling rate $\dot{Q}_D$ remains optimal at the frequency where the absorption spectrum has the maximum positive slope. It turns out that this frequency is equal to the resonant frequency at the trap center. It is not surprising that tuning to $\omega \leq \omega_{\sigma 1}(B_0)$ will result in cooling because the laser light is then red-detuned for all atoms. What will happen for tuning to $\omega \geq \omega_{\sigma 1}(B_0)$ can be understood from the shell model. For this purpose, we rewrite the cooling term $\dot{Q}_D$ from Eq. 5.7 to

$$\dot{Q}_D \simeq -2E_r \frac{I_0}{\hbar \omega} \int_{B_0}^{\infty} dB\, \rho_M(B) n(B) \frac{k_B T}{\hbar} \frac{\partial \sigma_V(\omega - \mu_B B/\hbar)}{\partial \omega}, \tag{5.17}$$

where $\rho_M(B)$ is the magnetic density of states (see Sect. 2.3.3) and where we have assumed the incoming intensity to be constant over the sample radius. The local Doppler cooling rate consists of the factor $N(B) = \rho_M(B) n(B)$ which gives the number of atoms per unit of magnetic field at field B and the term $(k_B T/\hbar\sigma_0)(\partial\sigma_V/\partial\omega)$ which gives the average Doppler shift of an atom per incident photon in units of $2E_r$. Both are plotted in Fig. 5.3. The case sketched in Fig. 5.3 corresponds to the case of tuning to $\omega_{\sigma 1}(B_0)$, the resonant frequency of an atom at rest in the trap center. For this case cooling is optimal because $N(B)$ has the optimum slope at $B = B_0$. The convolution with $(\partial\sigma_V/\partial\omega)$ will then give the optimum slope at $\omega = \omega_{\sigma 1}(B_0)$. If the incident light is tuned to frequencies larger than $\omega_{\sigma 1}(B_0)$, a resonant shell appears and moves towards larger magnetic fields. This will initially increase the overlap of $N(B)$ with the cooling wing, but will increase the overlap of $N(B)$ with the heating wing much more strongly. This means the cooling rate will decrease. Tuning the laser to smaller frequencies than $\omega_{\sigma 1}(B_0)$ will decrease the overlap of the cooling wing with $N(B)$ and decrease the cooling rate.

Due to the inhomogeneous magnetic field, the absorption spectrum in Eq. 5.16 will be inhomogeneously broadened which will decrease the slope of the lineshape and, consequently, the Doppler cooling rate. Therefore, we expect the Doppler limit for the inhomogeneous case to be slightly higher than for the homogeneous case. To calculate this Doppler limit for the optically thin case, we must numerically evaluate

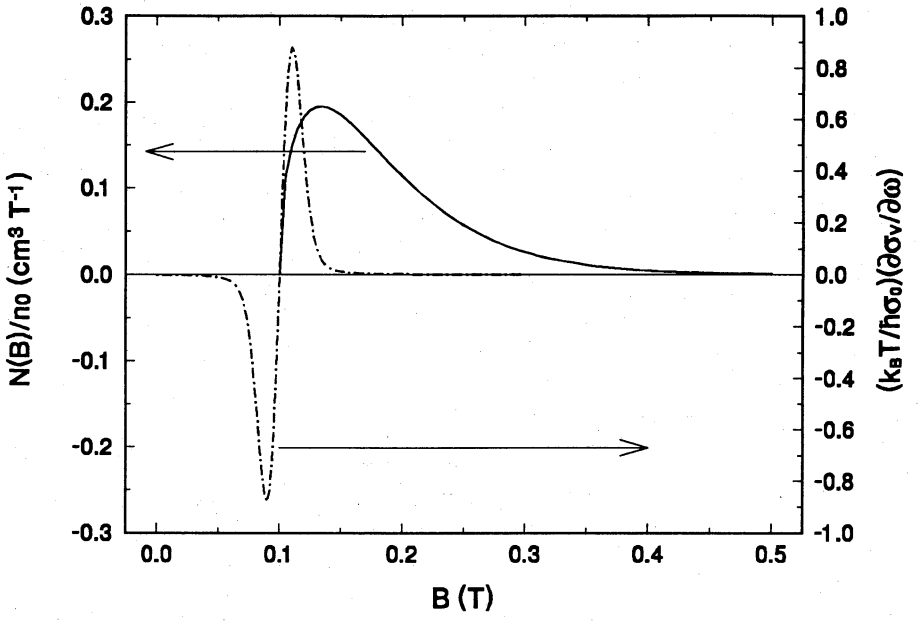

Figure 5.3: The function $N(B)/n_0$ plotted as a solid line, where $N(B)$ is the total number of atoms per unit of magnetic field at field B, and the average Doppler shift of an atom per incident photon in units of $2E_r$, $(k_BT/\hbar\sigma_0)(\partial\sigma_V/\partial\omega)$ at $\omega = \omega_{\sigma 1}(B_0)$, plotted as a dash-dotted line. The convolution is proportional to the Doppler cooling rate $\dot{Q}_D$ for the σ_1 line. The plot is made for a temperature of 30 mK.

Eq. 5.16. This will be performed in Section 5.4.2, where the Doppler limit will be numerically calculated for a number of densities ranging from the optically thin to the optically thick limit. For the optically thin limit we then find: $T_D = 3.32\,\mathrm{mK}$ for a detuning of $-70\,\mathrm{MHz}$ with respect to $\omega_{\sigma 1}(B_0)$.

Doppler cooling in the optically thin limit can best be illustrated for the case of a heavy neutral atom, like Na or Cs, in a Ioffe trap. In Sect. 5.3, we saw that in this limit the Lorentzian approximation can be used to derive a closed expression for the absorption spectrum (see Eq. 4.44). With this expression we can calculate the Doppler cooling rate and the Doppler limit. Both results are plotted in Fig. 5.4. The position of maximal cooling hardly changes as the gas becomes colder and practically coincides with $\omega_{\sigma 1}(B_0)$. The sharp peak of the frequency regime for which cooling occurs, is a consequence of the Lorentzian lineshape and the steep slope of the σ_1 left flank. For a Voigt lineshape, this peak will be broadened. The Doppler limit $T_D = 1.12\,\hbar\gamma/k_B$ at a detuning of $\Delta \simeq -0.5$ with respect to the resonance frequency at the trap center, is not very different from the homogeneous case $T_D = \hbar\gamma/k_B$.

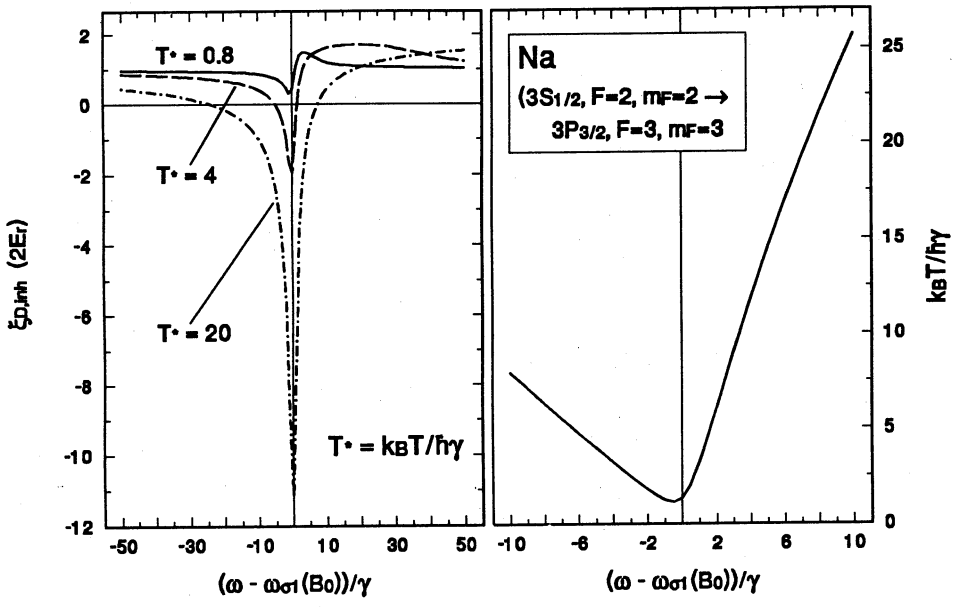

Figure 5.4: Fig.(a): Doppler cooling parameter ξ_D of a gas of Na atoms, as a function of reduced detuning from the resonance frequency at the trap center for three reduced temperatures: $T^* \equiv k_B T/\hbar\gamma = 0.8$, $T^* = 4$ and $T^* = 20$. Fig.(b): Doppler limit as a function of reduced detuning. Both plots are made for the "long trap".

5.4.2 The optically thick limit

In the optically thick limit (see Sect. 4.8), the attenuation of a light beam, as it propagates through the sample, must be calculated numerically. In section 5.4.2, we will show how the attenuation of the intensity and the Doppler cooling rate are obtained from the numerical solution of Eqs. 4.28. The effects of multiple scattering, which inevitably play a role in the optically thick regime, will be discussed in section 5.5.

Intuitive picture

How the attenuation of the light changes with increasing density and how this influences the Doppler cooling can be seen in Fig. 5.5. In Fig. 5.5(a), the attenuation per incident photon, $I(z)/I_0$, and in Fig. 5.5(b), the local Doppler cooling per incident photon in units of $2E_r$, $(d\dot{Q}_D/dz)(\hbar\omega/I_0\, 2E_r)$ are plotted along the z axis ($\rho = 0$). Both quantities, as obtained from a numerical solution of Eq. 4.32, are plotted for a number of densities. For the lowest density (curve 0), the light is hardly attenuated

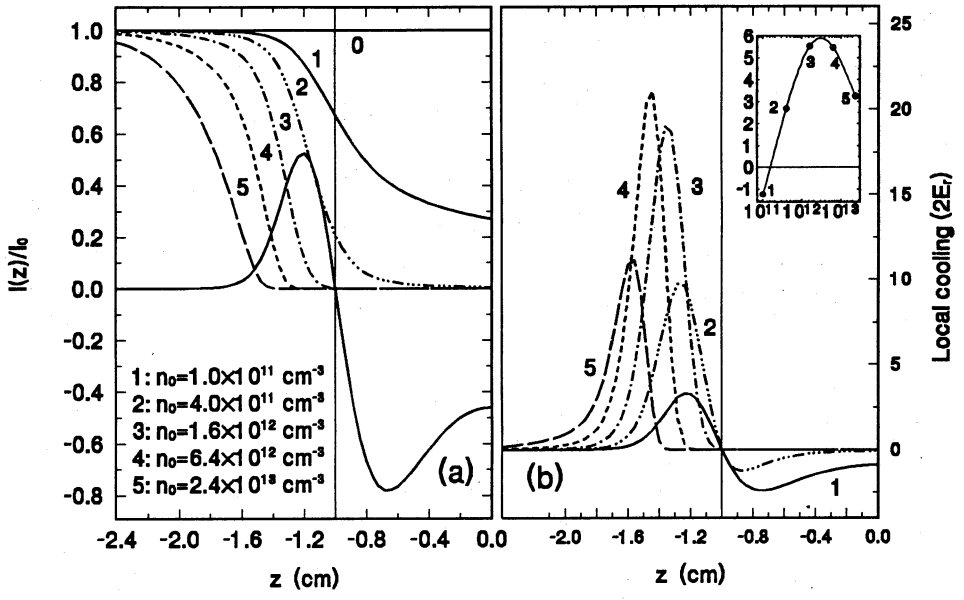

Figure 5.5: Fig.(a): Attenuation per incident photon, $I(z)/I_0$, along the z-axis for five densities, ranging from the optically thin to the optically thick regime, a detuning from the resonant frequency at the trap center $\Delta\omega/\gamma = 6.52$ and $T = 40\,\mathrm{mK}$. Also plotted is the shape of the frequency derivative of the normalized absorption coefficient, $(n(z)/n_0)(k_BT/\hbar\sigma_0)(\partial\sigma_V/\partial\omega)$. Fig.(b): Local Doppler cooling per incident photon along the z-axis in units of $2E_r$, $(d\dot{Q}_D/dz)(\hbar\omega/I_0\,2E_r)$ for the corresponding densities. The inset shows the total Doppler cooling rates along the z axis for the respective densities.

as it passes through the resonant shell. The atoms in the inner region of the resonant shell are preferentially heated. As the density increases (curve 1 and 2), the light is more strongly attenuated until a density is reached (curve 3, $n_0 = 1.6 \times 10^{12}\,\mathrm{cm}^{-3}$) where $\ell_V \simeq \ell_{re}$ and the light is completely absorbed before it reaches the inner region of the resonant shell. Absorption then takes place at a detuning from resonance where the frequency derivative of the absorption coefficient and, consequently, the cooling rate is high. As the density increases, absorption takes place at a larger detuning from resonance (curve 4) which decreases the total cooling rate (the inset in Fig. 5.5(b) shows the total Doppler cooling rate $\dot{Q}_D(\hbar\omega/I_0\,2E_r)$ for the respective densities). For the highest density (curve 5), absorption takes place at a large detuning from the resonant shell where $(\partial\sigma_V/\partial\omega)$ is much lower than for curve 4 and the cooling rate decreases strongly. We see that the effect of optical thickness on Doppler cooling in an inhomogeneous field, is to enhance the cooling rate by shielding those

atoms from the light that would be heated in the optically thin regime.

For temperatures $T \gg 2.2\,\mathrm{mK}$ in the case of hydrogen, we can make the Gaussian approximation and give a closed expression describing the attenuation of the light close to the resonant shell (see Sect. 4.8). Since Doppler cooling in the optically thick limit occurs close to the resonant shell, we can use Eq. 4.48 to derive a relation, describing roughly the optimal detuning for Doppler cooling in the optically thick regime as a function of T and n_0. For complete absorption close to resonance $\ln(I(z_{res})/I_0) \lesssim -1$, where z_{res} is the z-coordinate of the center of the resonant shell. Using Eq. 4.48, we then obtain

$$\frac{\Delta\omega_{B0}}{\gamma} \lesssim \frac{k_B T}{\hbar\gamma}\left[\ln\left(n_0\sigma_0\sqrt{\frac{\hbar\gamma}{\mu_B\beta}}\right) - \ln\left(\frac{4}{\pi}\sqrt{\frac{\Delta\omega_{B0}}{\gamma}}\right)\right]. \tag{5.18}$$

For ρ smaller than the radius of the resonant shell, we have $\ell_{re} \ll \ell_V$ and light will not penetrate through the shell. Although the exact shape of the attenuation profile changes, the result for the case $\rho \neq 0$ will qualitatively be the same as for the case $\rho = 0$. For ρ much larger than the radius of the resonant shell, the sample will be optically thin and the Doppler cooling rate will be small.

Numerical results

To calculate the Doppler cooling rate for the conditions of the experiment, Eq. 5.7 cannot be used as we cannot use a description in terms of an absorption cross section. The attenuation of polarized light in an electron-spin-polarized gas is described with the propagation equations 4.28 for the electromagnetic field (see Sect. 4.5). In Sect. 4.6, we considered the attenuation of LCP light on the σ_1 transition, the situation of the Doppler cooling experiments. There, we showed that as the E_{0+} component of the light propagates, due to the finite angle between the photon $\vec{k}$ vector and the magnetic field $\vec{B}$, the E_{0-} component grows. This RCP light can also be absorbed on the σ_1 transition (as was experimentally observed in the spectroscopic experiments of Luiten *et al.* [20]) and cause cooling. To take these polarization effects into account, we must use Eq. 5.6 for the local Doppler cooling rate in terms of the absorption coefficient $\alpha_L(\vec{r}, \omega - kv_z)$ due to atoms from a particular velocity class. The total Doppler cooling rate then becomes

$$\dot{E} = \dot{Q}_r + \dot{Q}_D = 2E_r \int_V \frac{I(\vec{r},\omega)}{\hbar\omega}\left(\alpha_V(\vec{r},\omega) - \frac{k_B T}{\hbar}\frac{\partial\alpha_V}{\partial\omega}\right) d^3r, \tag{5.19}$$

where $\alpha_V(\vec{r},\omega) = \langle\alpha_L(\vec{r},\omega - kv_z)\rangle = -(1/I(\vec{r},\omega))(\partial I/\partial z)$ describes the relative attenuation of the light beam. Before Eq. 5.19 can be numerically calculated, $I = \frac{1}{2}\varepsilon_0 c|E_{0+} + E_{0-}|^2$, $\alpha_V(\omega)$ and $\partial\alpha_V/\partial\omega$ are calculated using the same numerical

procedure that is used to integrate Eqs. 4.28. This way of calculating $\dot{Q}_D$ is not completely correct as the derivative with respect to frequency of α_V in Eq. 5.19 assumes a constant polarization. However, as Eqs. 4.28 are numerically integrated for light of subsequent frequencies ω and $(\omega + \Delta\omega)$ to determine $\partial\alpha_V/\partial\omega$, there will be a very small difference in polarization. This effect is neglegibly small. In this approach, the presence of the nearby π_1 transition is properly taken into account for the propagation of the light. However, as the absorption on the π_1 transition is small, both optical pumping and Doppler cooling on this transition are neglected.

Since in the experimental situation we irradiate the gas with a known initial photon flux, we will discuss the Doppler cooling rate in terms of

$$\Xi_D \equiv \xi_D(\omega, n_0, T)\frac{\Lambda(\omega, n_0, T)}{I_0/(\hbar\omega)} = -\int \frac{1}{I_0}\frac{\partial I}{\partial z}\left(1 - \frac{k_B T}{\hbar\alpha_V}\frac{\partial\alpha_V}{\partial\omega}\right) d^3r, \qquad (5.20)$$

where Ξ_D gives the change in internal energy of the gas per *incident* photon in units of $2E_r$.

During cooling it is important to know where to tune the laser to get an optimal cooling rate. In Fig. 5.6, we plot Ξ_D as obtained from a numerical integration of Eq. 5.20 as a function of ω for several values of n_0 and T such that the total number of atoms is constant. For comparison, the resonant frequency of an atom at rest in the trap center is also shown. The f_{ref} in the plot is defined as $hf_{ref} = E_1 - \frac{3}{4}hcR_\infty(1 + m_e/m_n)^{-1} - \Delta/6$, where E_1 and Δ are given in Sect. 4.4. Although the gas at 100 mK is optically thick ($\ell_{re} = 0.4\,\text{cm} < \ell_V = 1.9\,\text{cm}$), the frequency for optimal cooling in this case is still seen to lie close (within one natural linewidth) to the resonant frequency at the trap center, the optimal cooling frequency in the optically thin regime (see Sect. 5.4.1). For a constant total number of atoms, cooling of the gas will result in an increase of the density to a value where the optical thickness can enhance the cooling rate by shielding light of the appropriate frequency from the region enclosed by the resonant shell. Cooling is now optimal for the frequency at which the light is completely absorbed just before it reaches the inner region of the resonant shell ($\ell_{re} \simeq \ell_V$). This resonant shell is the shell with the largest radius that is still optically thick. As the temperature decreases to 30 mK, the change in energy per scattered photon is seen to decrease less than the increase in size of the resonant shell at which cooling is optimal, caused by the increase in density. The net effect is an increase in cooling rate. The increase in size of the optimal cooling shell with increasing density is limited by the decrease in sample size as the gas cools. For 10 mK, the optimal cooling shell is at approximately the same detuning as for 30 mK. For 3 mK, the size of this shell and the change in energy per scattered photon have decreased so much that cooling has stopped. The Doppler limit T_D ends up slightly above 3 mK.

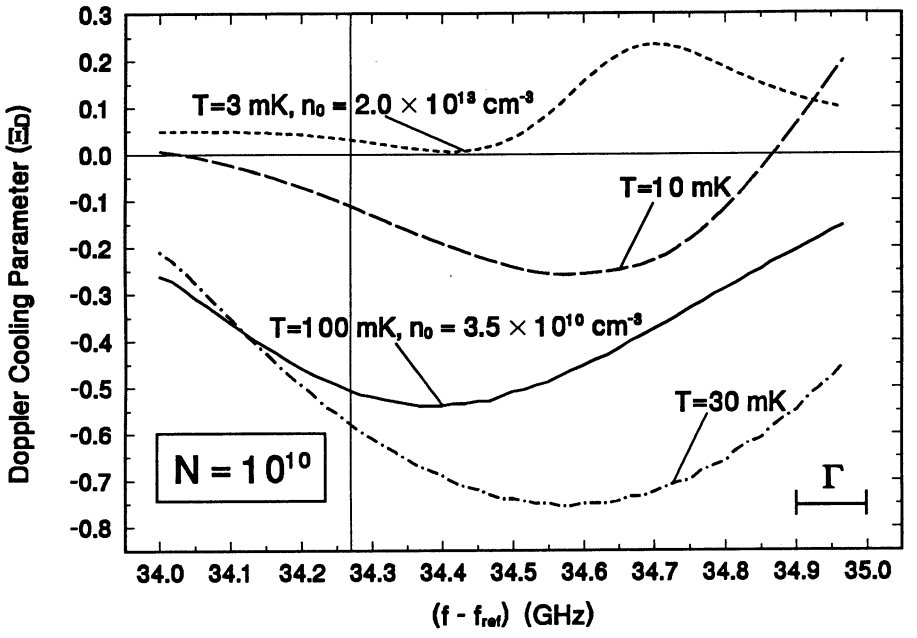

Figure 5.6: Doppler cooling parameter Ξ_D as a function of frequency for different densities and temperatures such that the total number of atoms is constant. The resonant frequency at the trap center $\omega_{\sigma 1}(B_0) = 34.27\,\mathrm{GHz}$ for the scale of the plot. The f_{ref} is defined in the text.

In Fig. 5.7, we plot Ξ_D in a contour plot as a function of T and n_0 for a constant laser frequency of 34.48 GHz, the frequency used in the experiments. The effect of the optical thickness on Ξ_D is clearly visible for increasing n_0 and constant T. Increasing T for constant n_0 is accompanied by an increase in cooling rate due to the increased thermal velocity of the atoms (see Eq. 5.7). The Doppler limit T_D as a function of density for this detuning is determined by the position where Ξ_D is zero.

In Fig. 5.8, we plot the minimum temperature that can be achieved with Doppler cooling as a function of laser frequency for different densities. From the plot we see that the minimum temperature that can be achieved with Doppler cooling decreases slightly with increasing density and becomes more weakly dependent on the detuning. This plot describes the density regime where the sample changes from optically thin to the optically thick regime. The resonant frequency at the trap center is 34.27 GHz in the units of this plot. The frequency that we used in the experiment was 34.48 GHz.

The Doppler cooling rate for irradiation with light of a finite bandwidth is ob-

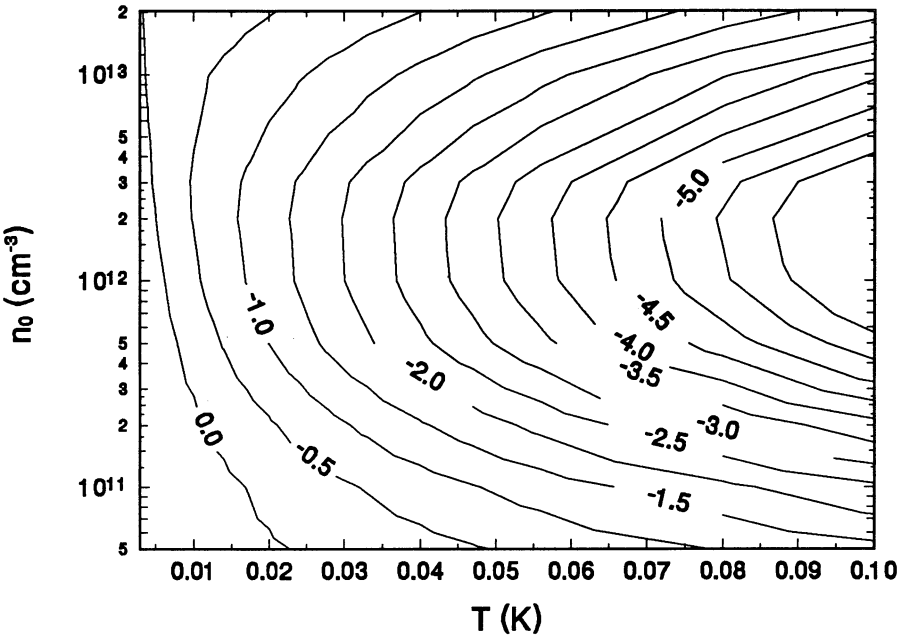

Figure 5.7: Contour plot of the Doppler cooling parameter Ξ_D as a function of n_0 and T for a fixed detuning $f - f_{ref} = 34.48\,\mathrm{GHz}$.

tained by forming the convolution of Ξ_D and the laser lineshape. For the minimum temperature achieved with Doppler cooling, Fig. 5.8, this will result in a slight increase.

5.5 Influence of multiple scattering

The optically thick limit, defined by $\ell_{re} \ll \ell_V$ (see Sect. 4.6.1), is accompanied by effects of multiple scattering. In Sect. 4.6.1, we found that the Voigt width ℓ_V^{ax} in the axial direction is different from the Voigt width in the radial direction ℓ_V^{rad}. In the axial direction $\ell_{re} \ll \ell_V$ for densities $n_0 \gg 5 \times 10^{10}\,\mathrm{cm}^{-3}$. In the radial direction this happens for $n_0 \gg 2 \times 10^{12}\,\mathrm{cm}^{-3}$. For densities $n_0 \ll 2 \times 10^{12}\,\mathrm{cm}^{-3}$, the long pencil-like shape of the sample will result in a large probability of escape from the sample after the first scattering event. For $n_0 \gg 2 \times 10^{12}\,\mathrm{cm}^{-3}$, a photon that is scattered once will have a large probability to scatter again. A photon that has lead to cooling in the first scattering event will be blue-shifted. The resonant shell for this scattered photon will be outside the resonant shell for the incoming photon. A second scattering event within the resonant shell of the scattered photon will predominantly lead to heating. A second scattering event outside this shell will

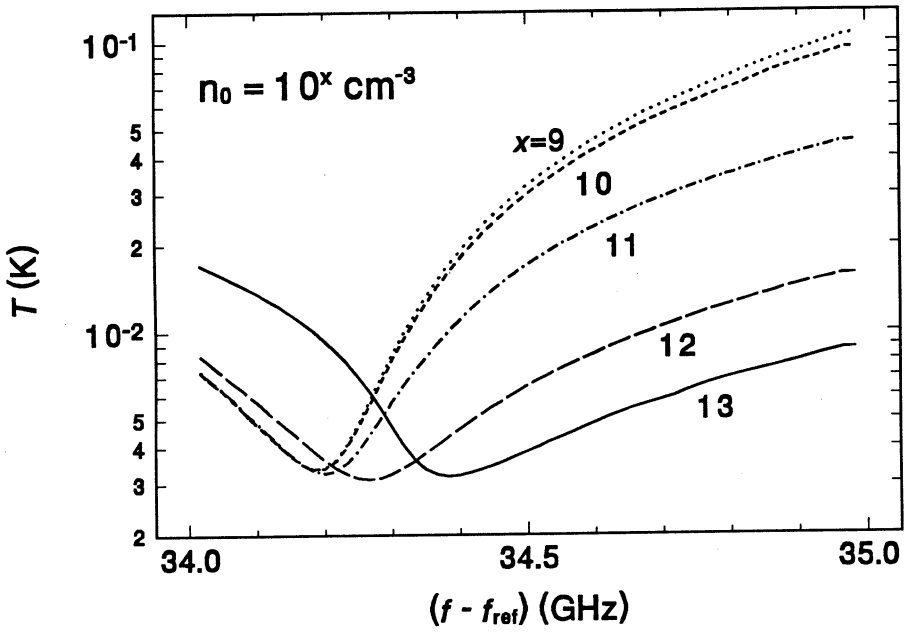

Figure 5.8: Minimum temperature that can be achieved with Doppler cooling as a function of detuning for different densities.

predominantly lead to cooling. Since the photon has a small probability to escape through this shell to the outside region, multiple scattering will lead to heating of the gas. In this simplified picture we have neglected the dependence of the scattering cross section on the angle between the photon wavevector and the magnetic field and we have neglected effects due to changes in polarization.

To take fully into account the detailed shape of the sample, the strongly direction-dependent scattering probability and a blue-shift of the photon that varies with the direction of scattering, a numerical simulation was performed by Van der Veeken [9] for our experimental conditions. In this Monte Carlo simulation the propagation of the photon through the gas is described as a diffusive motion through an inhomogeneous density distribution with a mean free path for the photon determined by a position dependent density and a Lorentzian cross section for which the resonant frequency is dependent on the position in the trap and is Doppler shifted according to a Maxwellian velocity distribution. The frequency of the photon is adjusted after every scattering event. In this approach, the dependence of the cross section on the angle between the wavevector $\vec{k}$ and the direction of the magnetic field is neglected.

During the propagation of the photon a number of quantities are recorded, like the location of the first scattering event, the number of scattering events per ab-

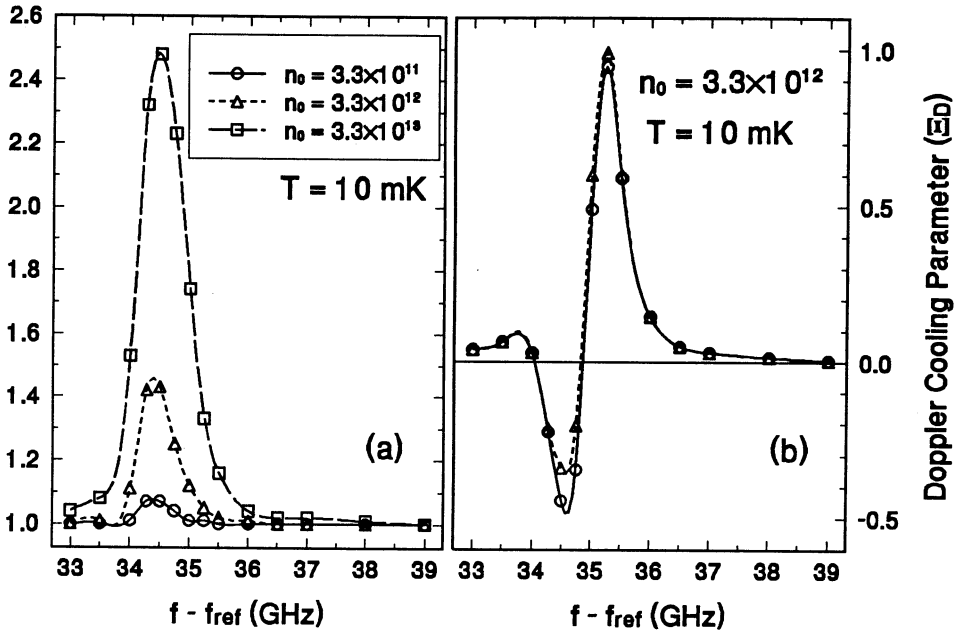

Figure 5.9: (a): number of interactions per scattering photon for different densities and (b): Doppler cooling parameter Ξ_D with (dashed) and without (solid) multiple scattering.

sorbed photon and the energy change per scattering event. When the photon has left the gas sample, these data are collected to deduce the total energy change of the gas. Some of the results from this simulation are given in Fig. 5.9. Multiple scattering generally results in extra heating of the gas. It is established that for large densities ($n_0 \gtrsim 3 \times 10^{12}\,\mathrm{cm}^{-3}$) this heating starts to have a substantial influence on the Doppler cooling rate. This gives additional confidence that the influence of multiple scattering in our Doppler cooling experiments, which were performed at lower densities, can be neglected. In the LIE experiments, where we rely on high densities ($n_0 \sim 10^{13}\,\mathrm{cm}^{-3}$), multiple scattering will play a role.

5.6 Evolution of temperature and density during Doppler cooling

In Sect. 2.6 we derived the equation describing the evolution of temperature and density of a thermal gas as a result of processes that change the total number of particles, N, and/or the total energy, E. In the Doppler cooling experiments dipolar decay and evaporation result in particle loss and heating, respectively cooling of the

gas. Including Doppler cooling, the total heating of the gas is now given by

$$\dot{Q}_{tot} = \dot{Q}_{dip} + \dot{Q}_{ev} + \Xi_D \, 2E_r I_0/\hbar\omega. \tag{5.21}$$

This expression substituted into Eq. 2.45, together with the equation for the change in particle number

$$\dot{N}_{tot} = \dot{N}_{dip} + \dot{N}_{ev} \tag{5.22}$$

will now determine the evolution of the gas. In Sect. 2.6, expressions for $\dot{Q}_{dip}$ (Eq. 2.42) and $\dot{Q}_{ev}$ (Eq. 2.40) are given. The parameter Ξ_D is calculated numerically for one frequency (in the Doppler cooling experiments we irradiated the σ_1 line at one frequency) and a range of temperatures and densities. During the numerical integration of Eq. 2.45, Ξ_D is constantly adjusted to the value corresponding to the instantaneous temperature and density. In solving Eqs. 5.21 and 5.22, we have included a non-heating, first-order decay process with a time constant of $\simeq 3500$ s. The reason for this will be addressed in the next section on the experimental results.

In Fig. 5.10 we plot the evolution of the trapped gas in the T-n_0 plane for different initial densities, an initial temperature of 80 mK and a total incident flux of $1.7 \times 10^9\,\mathrm{s}^{-1}$. The relative laser frequency is kept constant at 34.48 GHz, approximately the position of maximum slope in the red wing of the σ_1 line in the optically thin regime. For a low initial density (curve a), we see how the gas cools, almost along a line of constant particle number, to the point where the Doppler cooling rate has decreased so much it is just able to oppose the dipolar heating. From that moment on the gas will only loose atoms, but will not cool any further. The density will only decrease, initially following the cooling limit as a function of density. Again we see how the cooling limit for a given frequency, rises towards lower densities. Notice that for low temperatures, the line of the cooling limit is steeper than the line of constant N. While dipolar decay will try to move the gas away from the line of constant N in the T-n_0 plane (see curve d), Doppler cooling will try to move the gas along the line of constant N back to the curve of the cooling limit. For temperatures and densities above the cooling limit, the evolution as a result of Doppler cooling will also be towards the cooling limit. When the slope of the line of constant N is larger than the slope of the cooling limit the evolution as a result of Doppler cooling will be away from the cooling limit. In Fig. 5.10, we see how, as a result of this effect, the evolution takes T and n_0 below the cooling limit as the slope of the line of constant N approaches the slope of the cooling limit curve. For a ten times higher initial density (curve b), the gas starts to cool at an increasing density. Then the density decreases and increases again as the Doppler cooling takes over. The initial change in density is due to evaporative cooling. This effect is much more pronounced in curve c where the initial period, due to a ten times higher initial

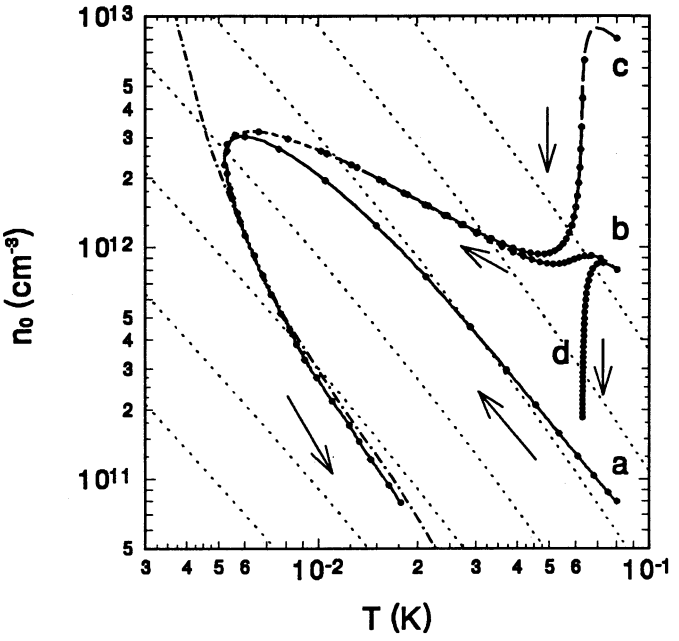

Figure 5.10: Evolution of the hydrogen gas for fixed frequency $(f - f_{ref}) = 34.48\,\mathrm{GHz}$ and for initial densities a: $n_0 = 8 \times 10^{10}\,\mathrm{cm}^{-3}$, b: $n_0 = 8 \times 10^{11}\,\mathrm{cm}^{-3}$ and c: $n_0 = 8 \times 10^{12}\,\mathrm{cm}^{-3}$. The gas starts at a temperature of 80 mK. The total photon flux $\Phi = 1.7 \times 10^9\,\mathrm{s}^{-1}$. The curve d is the evolution without light. The dash-dotted curve is the Doppler limit as a function of density and the series of dotted curves are the lines of constant particle number.

density, is completely dominated by evaporative cooling. Atoms will be rapidly lost until again the point is reached where the Doppler cooling is able to take over the evolution of the gas ($T = 60\,\mathrm{mK}$ and $n_0 = 4 \times 10^{12}\,\mathrm{cm}^{-3}$). From that point on the gas cools as the density decreases. The smaller slope of $n_0(T)$ shows that the dipolar heating is stronger and that cooling is accompanied by a considerable loss of particles. Curve d is added with the same initial conditions as for curve b, but with the Doppler cooling turned off. It shows how the gas, after an initial evaporative cooling period will only loose atoms and will approach the equilibrium temperature of 58 mK determined by a balance between evaporative cooling and dipolar heating (see Sect. 2.6). The points on all the curves indicate time intervals of 100 s to give an impression of the cooling rate. All curves reach approximately the same maximum value of density ($n_0 \simeq 3 \times 10^{12}\,\mathrm{cm}^{-3}$ at the same minimum value of temperature ($T \simeq 5\,\mathrm{mK}$).

The way to achieve a higher final density is to increase the time-averaged intensity I_0. In Fig. 5.11, the evolution of the gas is plotted for the same fixed frequency

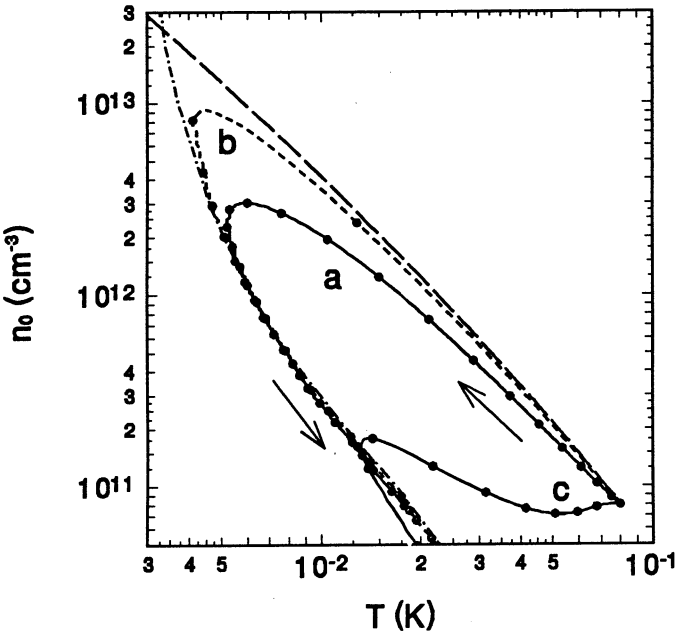

Figure 5.11: Evolution of the gas for fixed frequency $(f - f_{ref}) = 34.48\,\mathrm{GHz}$, an initial density of $8 \times 10^{10}\,\mathrm{cm}^{-3}$, an initial temperature of 80 mK and photon fluxes of a: $\Phi = 1.7 \times 10^{9}\,\mathrm{s}^{-1}$, b: $\Phi = 1.7 \times 10^{10}\,\mathrm{s}^{-1}$ and c: $\Phi = 1.7 \times 10^{8}\,\mathrm{s}^{-1}$. The long-dashed line is the curve of constant initial particle number. The dash-dotted line is the cooling limit as a function of n_0.

as Fig. 5.10, an initial density of $8 \times 10^{10}\,\mathrm{cm}^{-3}$, an initial temperature of 80 mK and different laser intensities well below the saturation limit. In the experiments, we actually had a photon flux of $1.7 \times 10^{9}\,\mathrm{s}^{-1}$ (curve a). From the plots we see how increasing I_0 by a factor of ten (curve b), would have resulted in a three times higher maximum density within a much shorter time (within $\simeq 200$ s). The theoretical limit to the density that can be reached by Doppler cooling is determined by the intersection of the minimum temperature curve and the line of constant initial particle number. In calculating the evolution during Doppler cooling for photon fluxes higher than for curve b, one should keep the intensity $I_0 \ll I_{sat}$. Of course, at these high densities the heating due to multiple scattering has to be included. This heating will increase the Doppler limit above a density of $\simeq 3 \times 10^{12}\,\mathrm{cm}^{-3}$. This will slightly decrease the maximum attainable density. For a ten times lower photon flux (curve c), Doppler cooling is only able to cool the gas to $\simeq 13$ mK at a slightly increasing density. The points on curves a and b also indicate 100 s time intervals. On curve c they indicate 1000 s time intervals.

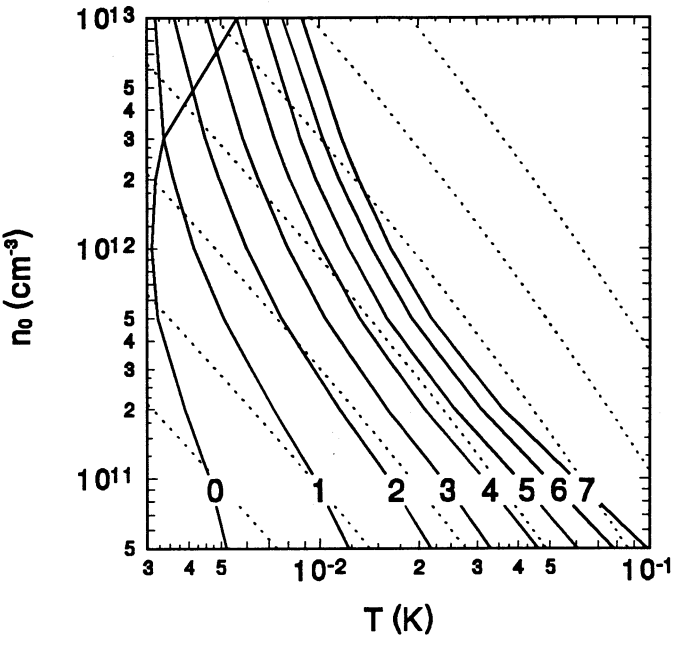

Figure 5.12: Cooling limit curves for different detunings. The label i corresponds to a detuning of i x 100 MHz. The dashed lines indicate constant total atom number N.

Fig. 5.12 does not show an evolution, but shows the cooling limit curves for different detunings and the lines of constant total atom number. For a sufficiently large initial photon flux I_0 and starting at low n_0, the gas will follow a line of constant N. Depending on initial n_0 and T, the cross section of the line of constant N and the cooling limit for a particular detuning, gives an upper bound on the maximum n_0 and minimum T that can be obtained by Doppler cooling at this detuning. For example, for a density of $10^{13}\,\mathrm{cm}^{-3}$ the Doppler limit $T_D \simeq 3.1$ mK is reached for a detuning of 100 MHz.

5.7 Experimental results

Doppler cooling is performed by excitation of the σ_1 transition. The laser is programmed to execute the following sequence of actions after the trap has been filled with H: first a spectrum is taken of the π_1 and the σ_1 line for an accurate determination of T and n_0 and to locate the frequency where the σ_1 line has a maximum slope in the low frequency flank, then the sample is irradiated close to this frequency ν_1 (see Fig. 5.13) for 15 minutes. During these 15 minutes AOM2 and AOM3 are switched on every 15 seconds (see Sect. 3.2.3), each during a period of 0.5 second.

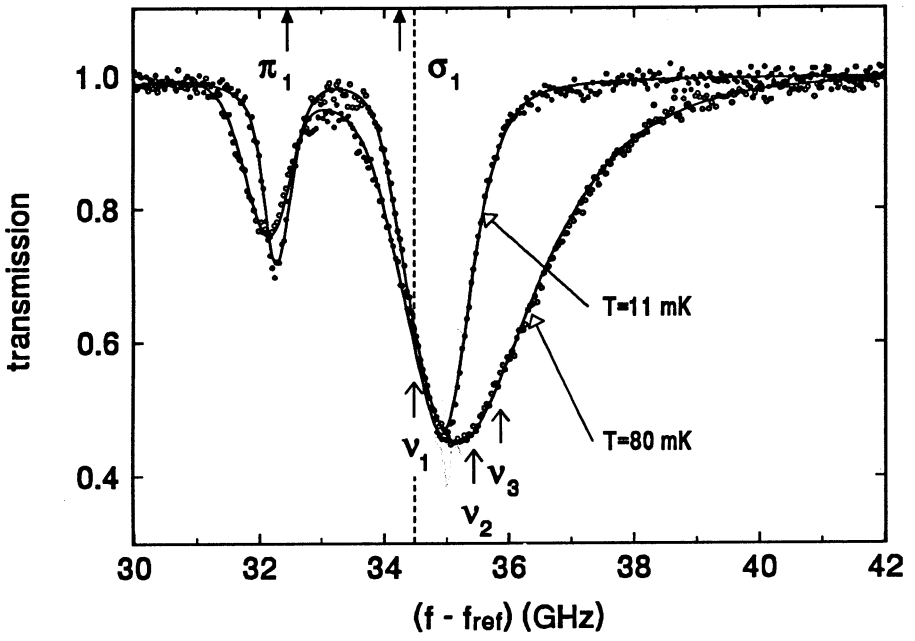

Figure 5.13: Transmission spectra before and after Doppler cooling. The solid lines are calculated spectra for $n_0 = 8(2) \times 10^{10}\,\mathrm{cm}^{-3}, T = 80(10)\,\mathrm{mK}$ and $1.3(4) \times 10^{12}\,\mathrm{cm}^{-3}, T = 11(2)\,\mathrm{mK}$, respectively. Resonant frequencies for the π_1 and σ_1 at the trap minimum are indicated.

This enables us to monitor the transmission at frequencies ν_2 and ν_3 (see Fig. 5.13). The time it takes to measure a spectrum ($10-30$ s) is too long to do a time-resolved measurement of the evolution of the gas, so we turn to 3-point spectroscopy for a determination of T and n_0 (see Sect. 4.5). After these 15 minutes, again a spectrum of the π_1 and the σ_1 line is taken for an accurate determination of the final temperature and density. In Fig. 5.13 the initial and final spectra of a typical Doppler cooling experiment are plotted. The solid lines running through the data points are calculated spectra, indicating that the density has increased by a factor of $\simeq 16$ and the temperature has decreased by a factor of $\simeq 8$. The narrowing of the σ_1 line is a clear signature of a lower temperature. The fact that a higher density does not result in a higher absorption peak, is a consequence of the decreasing sample diameter as the temperature decreases.

The transmission at frequencies ν_1, ν_2 and ν_3 is plotted in Fig. 5.14. By monitoring these three signals during the experiment, we can see whether the σ_1 line is narrowing and the gas is cooling.

After the cooling sequence plotted in Fig. 5.13, we left the gas to evolve in the

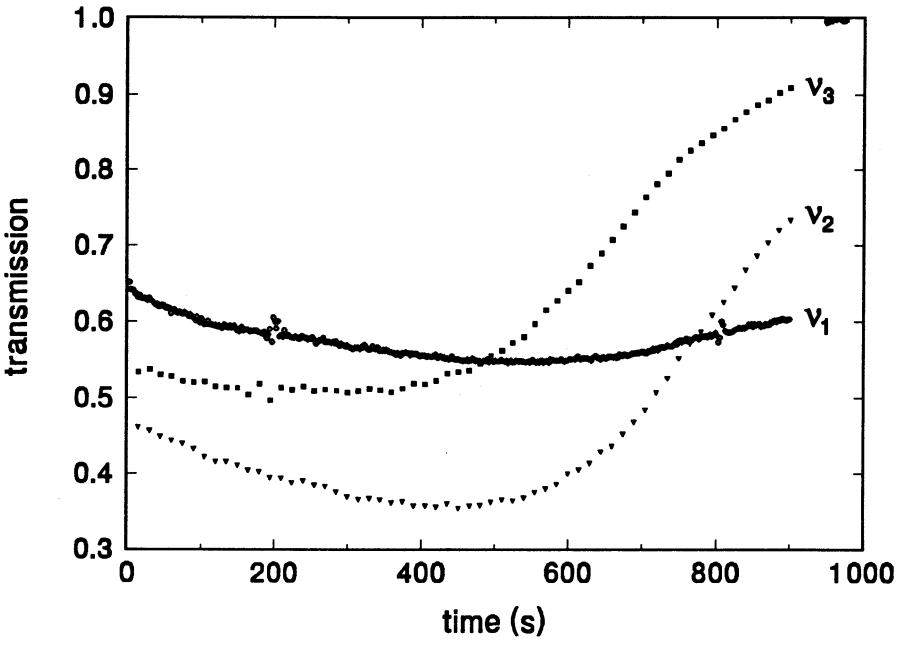

Figure 5.14: Transmission at the three AOM frequencies as a function of time.

dark for 37 minutes to observe only the effects of dipolar heating. We then applied the same cooling sequence once more, resulting in a final density of $n_0 \simeq 3\times10^{11}\,\mathrm{cm}^{-3}$ and a final temperature of $T \simeq 8\,\mathrm{mK}$. In Fig. 5.15, we plot the results of both Doppler cooling sequences in a T-n_0 plot. In Fig. 5.16, we plot two examples of full Doppler cooling loops. In these experiments, we started the second and third cooling sequence immediately after the first one.

5.8 Discussion

Figures 5.13, 5.15 and 5.16 demonstrate clearly that we have for the first time performed Doppler cooling of atomic hydrogen. During these first experiments, the model for Doppler cooling in magnetic traps was not as well developed as in the preceding sections, so that these experiments, rather than aiming at a detailed study, were aimed at a demonstration of Doppler cooling in magnetic traps. There were also a number of experimental imperfections that made a detailed study of Doppler cooling difficult to perform. The initial conditions of the sample, shortly after loading, are mostly $n_0 \sim 10^{11}\,\mathrm{cm}^{-3}$ and $T \sim 50\,\mathrm{mK}$, but are difficult to control. The laser frequency was not very well stabilized, so that during a period of 15 minutes the frequency can drift over a frequency interval of maximally 60 MHz. The Lyman-

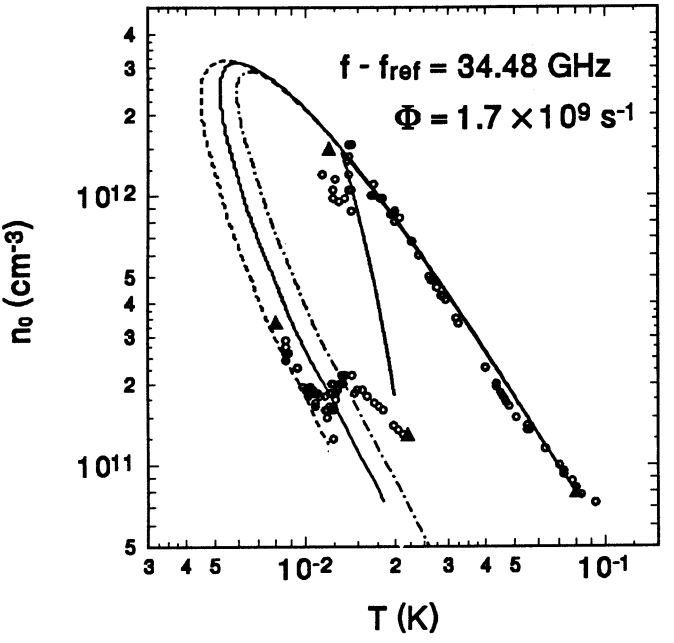

Figure 5.15: Evolution of the gas during both Doppler cooling sequences and a "black" period of 37 minutes. The data from the full spectra are indicated in triangles, the 3-point spectra are indicated in black circles. The lines are fits from the model, using the initial densities and temperatures and a photon flux of $1.7 \times 10^9\,s^{-1}$. The solid line is for a frequency of 34.48 GHz, the dash-dotted line is for a frequency 50 MHz higher and the dashed line for a frequency 50 MHz lower.

α detector in the cell is not calibrated, so that during a Doppler cooling cycle we do not know the absolute photon flux at the location of the sample. The typical value of $2 \times 10^9\,s^{-1}$ was actually inferred from optical pumping rates in another experiment. In a number of measurements, we noticed from the reference signal (outside the cell) that during a cooling cycle the intensity could change by as much as 30 %.

Taking these imperfections in mind and the fact that the laser actually has a bandwidth of $\simeq$ 150 MHz, we have plotted in Fig. 5.15 the calculated evolution for the typical photon flux of $1.7 \times 10^9\,s^{-1}$ and a laser frequency of 34.48 ± 0.05 GHz. The fit shows that we, unaware of the exact cooling rates, stopped the period of irradiation too early. The dipolar decay takes the sample to an approximately ten times lower density and a slightly higher temperature. From there the second period of irradiation cools the gas, approximately along a line of constant density, towards the cooling limit. The reason for the strange wiggle in the 3-point spectra is not clear. Problems with the stability of the laser may have caused a frequency shift

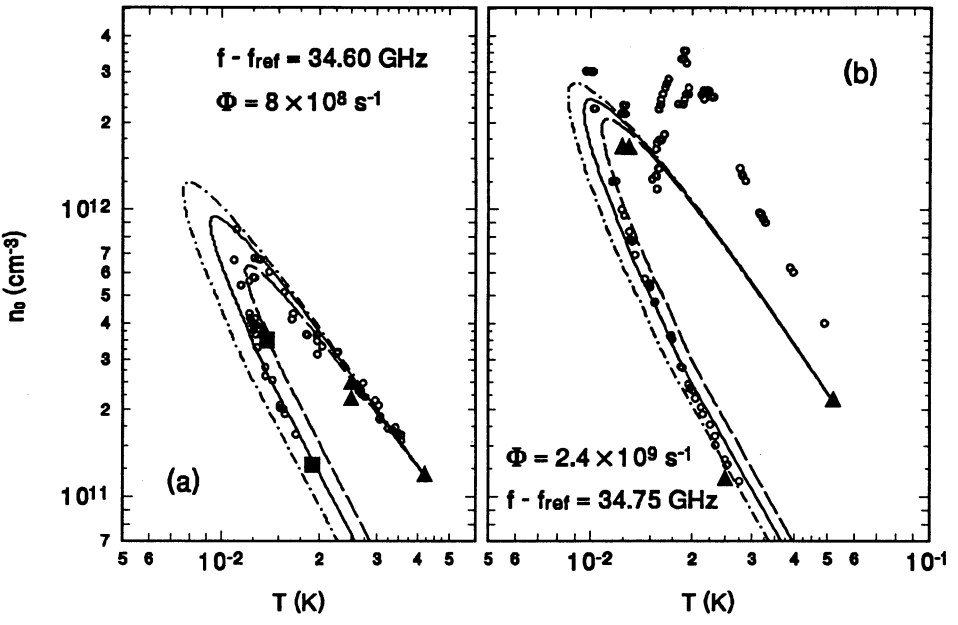

Figure 5.16: Two full Doppler cooling loops. Fig.(a) shows three consecutive cooling sequences. The solid line is the calculated evolution. Fig.(b) shows two consecutive cooling sequences. The solid triangles and blocks are T and n_0 as obtained from a full spectrum. The circles are obtained from 3-point spectra. The dashed and dash-dotted lines are for frequencies 50 MHz higher and lower respectively.

towards a lower value. When this happens, the results from the 3-point fits become unreliable. The theoretical fit includes a non-heating, first-order decay mechanism with a decay time of $\simeq$ 3500 s. This extra particle loss mechanism is introduced to fit the dipolar decay during the dark period. Without this loss mechanism, the final density at the end of the dark period would be $\simeq 4\times$ higher than the observed density. The effect on the evolution during Doppler cooling is very small. A similar extra decay process was also observed in experiments to study the decay kinetics of trapped H over periods of hours (see Sect. 7.1.2). In those experiments the first-order character of this extra decay process was clearly observed. The cause for this first-order decay mechanism is not understood. In Sect. 7.1.2 a more elaborate discussion is given.

Figures 5.16(a) and (b) show two full Doppler cooling loops. Although the temperatures reached are not as low as in Fig. 5.15, these figures nicely demonstrate how the evolution "turns around" towards lower densities and higher temperatures. The calculated evolution for Fig. 5.16(b) does not coincide as well with the data as

the evolution for Fig. 5.16(a). The strong deviation of the results from the 3-point spectra is not understood but probably result from a frequency shift during the irradiation.

There is a good qualitative agreement between the data and the model, although more experiments are definitely needed to confirm the model. Shortly after the completion of the experiments, the laser frequency has been stabilized which will enable us to perform experiments aimed at investigating the influence of frequency detuning on the evolution of the gas. With an improved optical set-up, also the influence of photon flux can be investigated. By rapidly cooling the gas to high densities ($n_0 \gtrsim 3 \times 10^{12}\,\mathrm{cm}^{-3}$) the heating due to multiple scattering can be measured. The results from these experiments could make Doppler cooling a truly manageable precooling method to temperatures at which other cooling methods could be used to cool below the Doppler limit.

References

[1] T.W. Hänsch and A.L. Schawlow, Optics Communications **13**, 68 (1975).

[2] D.J. Wineland and H.G. Dehmelt, Bull. Am. Phys. Soc. **20**, 637 (1975).

[3] J. Prodan, A. Migdall, W.D. Phillips, I. So, H. Metcalf, and J. Dalibard, Phys. Rev. Lett. **54**, 992 (1985).

[4] W. Ertmer, R. Blatt, J.L. Hall, M. Zhu, Phys. Rev. Lett. **54**, 996 (1985).

[5] Special issue "Laser Cooling and Trapping of Atoms", J. Opt. Soc. Am. B **6**, 2020 (1989).

[6] S. Chu, L. Hollberg, J.E. Bjorkholm, A. Cable, and A. Ashkin, Phys. Rev. Lett. **55**, 48 (1985).

[7] M. Stephens and C. Wieman, Phys. Rev. Lett. **72**, 3787 (1994).

[8] K. Helmerson, A. Martin, and D.E. Pritchard, J. Opt. Soc. Am. B **9**, 1988 (1992).

[9] "Monte Carlo Simulation of Doppler Cooling of Magnetically Confined Atomic Hydrogen", Donald van der Veeken, masters thesis, University of Amsterdam, 1993 (supervisor Dr. J.P.J. Michels).

[10] J. Javanainen and S. Stenholm, Appl. Phys. **21**, 283 (1980).

[11] S. Stenholm, Rev. Mod. Phys., **58**, 699 (1986).

[12] W.M. Itano and D.J. Wineland, Phys. Rev. A **25**, 35 (1982).

[13] D.J. Wineland and W. Itano, Phys. Rev. A **20**, 1521 (1979).

[14] The case for short pulses, where $\tau_{puls} \lesssim \Gamma^{-1}$, has also been analyzed, see for instance P.D. Lett, P.L. Gould, and W.D. Phillips, Hyperfine Interactions **44**, 335 (1988) and K. Mølmer, Phys. Rev. Lett. **66**, 2301 (1991).

[15] P.D. Lett, W.D. Phillips, S.L. Rolston, C.E. Tanner, R.N. Watts, and C.I. Westbrook, J. Opt. Soc. Am. B **6**, 2084 (1989).

[16] "Laser Light Pressure on Atoms" by V.G. Minogin and V.S. Letokhov, Chapter 2 (Gordon and Breach, 1987).

[17] C.I. Westbrook, D.W. Gidley, R.S. Conti, and A. Rich, Phys. Rev. Lett. **58**, 1328 (1987).

[18] G. Feinberg and L.M. Lederman, Ann. Rev. Nucl. Sci. **13**, 431 (1963).

[19] S. Chu in *The Hydrogen Atom*, edited by G.F. Bassani, M. Inguscio, and T.W. Hänsch (Springer-Verlag, 1989), p. 144.

[20] O.J. Luiten, Ph. D. thesis, University of Amsterdam (1993).

Chapter 6

Light-induced evaporative cooling

6.1 Introduction

Evaporative cooling is based on the preferential removal of those atoms from a thermal gas that have a higher total energy than the average internal energy per particle [1, 2]. By elastic collisions the remaining gas will approach a new thermal equilibrium with a lower internal energy per particle, i.e., a lower temperature. Cooling continues until a minimum temperature T_{min} is reached, determined by a balance between internal heating mechanisms and evaporative cooling.

Evaporative cooling was first demonstrated by Hess *et al.* [3] who reached $T_{min} \simeq 40\,\mathrm{mK}$ where the intrinsic heating is caused by preferential magnetic dipolar relaxation in the center of the trap. The evaporation was realized by letting atoms escape over a static trap barrier with height ε_{tr}. In the experiments of Luiten *et al.* [4] a bolometer was placed in high field. By burning the He film of the bolometer, a site for efficient recombination was created in a region which could only be reached by the energetic atoms from the distribution. Another wall-induced evaporation mechanism will be discussed in chapter 7. With decreasing temperature, the fraction of atoms with energy exceeding ε_{tr} is suppressed exponentially. To continue cooling, the evaporation has to be forced by lowering the barrier height, which, in turn, results in a lower T_{min}. This process is called forced evaporative cooling [5, 6].

The lowest temperatures reached in magnetically trapped gases of atomic hydrogen have been obtained by forced evaporative cooling [6]. In these experiments a temperature $T = 100\,\mu\mathrm{K}$ was reached at a central density $n_0 = 8 \times 10^{13}\,\mathrm{cm}^{-3}$. The determination of n_0 and T took place by way of a destructive method. By ramping down the trap barrier much faster than the thermalization rate of the remaining par-

ticles and measuring the total number of escaped atoms as a function of ε_{tr}, Doyle *et al.* [7] were able to obtain information about the energy distribution function of the trapped gas. This enabled them to obtain a value for the temperature. Luiten *et al.* [4], performing three-point spectroscopy (see Sect. 4.5) on the sample, were able to perform an *in situ* observation of the evolution of n_0 and T of a quasithermal gas during evaporative cooling. This was then compared to an analytical model for the evaporation process [8].

In the experiments described in the present thesis, a new cooling method was developed, light-induced evaporative cooling (LIE) which is an optical analogue of forced evaporative cooling. By optically pumping hydrogen atoms from H$\uparrow$ to H$\downarrow$ in regions of high magnetic field, the most energetic atoms are ejected from the trap (see Sect. 4.4) and the gas will be evaporatively cooled. The preferential absorption of light by the atoms in high field can be achieved by tuning to the Zeeman shifted resonance frequency of the atoms in high field or by using the optical thickness of the sample. The LIE experiments presented in this thesis were based on the latter method. In the optically thick limit, the light will be absorbed in the outer edges of the sample before it reaches the shell where the atoms are resonant with the light. In Sect. 4.8, this situation was described by the condition $\ell_{re} \ll \ell_V$, where ℓ_{re} is the resonant extinction length and ℓ_V is the (Voigt) thickness of the resonant shell (see Sect. 4.6.1). For a suitable choice of the laser frequency only the atoms with an energy much higher than the average energy will be optically pumped and the gas will be evaporatively cooled. In the LIE experiments, we irradiated the σ_2 transition ($1S_{1/2,m_J=1/2} \rightarrow 2P_{3/2,m_J=-1/2}$) since it has the largest probability for decay to the electron-spin-down hyperfine state ($\cos^2\theta_- = \frac{2}{3}$ in $B_0 = 0\,\mathrm{T}$, see Sect. 4.4). A minimum temperature was reached of 3 mK at a density $n_0 = 3.9 \times 10^{12}\,\mathrm{cm}^{-3}$ [9].

In Sect. 6.2 I will discuss conditions for the gas to stay close to thermal equilibrium during cooling and derive an expression for the LIE cooling rate, using the same approach as was followed for the Doppler cooling rate in Sect. 5.2. Then I will discuss LIE for the optically thin limit. I will show that in this limit LIE can be used to cool a gas at an increasing density. The process that ultimately limits LIE cooling is also discussed. In the optically thick limit, the cooling limits of LIE are lower. A numerical calculation of the cooling rates will be presented in Sect. 6.4 and will be discussed in the light of the shell model. For very low temperatures, we can use the approximation of a neglegible Zeeman broadening ($T \ll 2.4\,\mathrm{mK}$, see Sect. 4.8). In this limit all the atoms have the same resonance frequency $\omega_{\sigma 2}(B_0)$. From this case, one can obtain an understanding of the mechanisms that ultimately limit cooling by LIE. In the subsequent section, we will use the numerically calculated values of the LIE cooling rate as a function of n_0, T and ω to calculate cooling trajectories in

the T-n_0 plane, analogous to the Doppler cooling trajectories (see Sect. 5.6). Then, the experimental results will be discussed. Finally, a suggestion will be made for lowering the LIE cooling limit. It will be shown that this method will not enable cooling to the regime of quantum degeneracy.

6.2 Influence of optical pumping on a thermal distribution

In forced evaporative cooling across a trap barrier [1, 2], it is essential that this barrier is lowered at a rate slower than the thermalization rate of the trapped gas. This is a necessary condition for the gas to cool while maintaining a quasi-equilibrium. This condition also applies to LIE. It means that the rate of optical pumping has to be smaller than the rate at which the energy distribution is restored by elastic collisions. The rate at which the thermal equilibrium is restored is of the order of the elastic collision rate τ_c^{-1}. A gas of trapped atomic hydrogen is intrinsically heated by magnetic dipolar relaxation. To have efficient cooling, the optical pumping rate τ_{LIE}^{-1} must be much larger than the dipolar loss rate τ_{dip}^{-1}. Both timescales impose a limit to the operating range of LIE,

$$\tau_{dip}^{-1} \ll \tau_{LIE}^{-1} \ll \tau_c^{-1}. \tag{6.1}$$

When this condition is met, the gas is cooled and a Boltzmann distribution may be assumed in the calculation of optical pumping rates and cooling rates.

6.2.1 Optical pumping rate

The local optical pumping rate is proportional to the local intensity of the light beam, which can be obtained from Eq. 4.28. For the optically thin limit, the strongest absorption will take place in the region where the atoms are resonant with the incident light, i.e., in the resonant shell (see Sect. 4.6.1). In the optically thick limit, the light is absorbed in the outer regions of the sample before reaching the resonant shell. A typical situation for LIE at a temperature $T = 3\,\mathrm{mK}$ and a density $n_0 = 3 \times 10^{12}\,\mathrm{cm}^{-3}$, is illustrated in Fig. 6.1 where we show the intensity profile, the absorption coefficient and the density distribution along the trap axis. In ordinary evaporative cooling, every atom with an energy $\varepsilon > \varepsilon_{tr}$ is removed. The rate at which this high-energy tail is removed is given by the rate at which atoms with an energy $\varepsilon > \varepsilon_{tr}$ are produced by elastic collisions between trapped atoms from a truncated Boltzmann distribution with $\varepsilon \leq \varepsilon_{tr}$. In the model for evaporative cooling of Luiten *et al.* [8], a closed expression is derived for this evaporation rate (see also

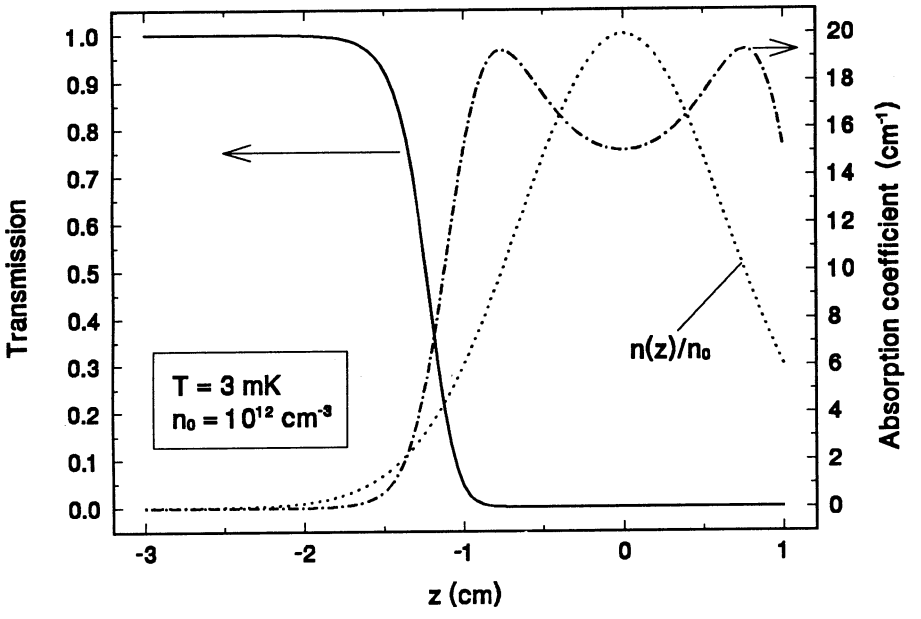

Figure 6.1: Typical situation for optical cooling using LIE. The absorption coefficient and the intensity along the z-axis $I(z)$ are plotted for $T = 3\,\mathrm{mK}$, $n_0 = 3 \times 10^{12}\,\mathrm{cm}^{-3}$ and a reduced detuning from the trap center $(\omega - \omega_{\sigma 2}(B_0))/\gamma = -2.265$. The density distribution is plotted as a dotted line.

Sect. 2.5). As opposed to ordinary evaporative cooling, in LIE the truncation of the Boltzmann distribution function cannot be as sharply defined. Atoms will be optically pumped at a rate determined by the intensity $I(\vec{r})$. For a sufficiently high density optical pumping can occur in a relatively localized region in space. The distortion of the Boltzmann distribution function will occur for a range of energies for which the atom is resonant with the light. The rate at which atoms with an energy in the interval $(\varepsilon, \varepsilon + d\varepsilon)$ are optically pumped is

$$\begin{aligned} \dot{N}_p(\varepsilon) &= \int d^3r \frac{I(\vec{r},\omega)}{\hbar\omega} n(\vec{r}) \cos^2\theta_- \langle \sigma_L(\omega_0' + kv_z)\delta[\varepsilon - (\tfrac{1}{2}mv^2 + U_p(\vec{r})]\rangle \\ &= \frac{1}{k_B T} e^{-\varepsilon/k_B T} \int_{U_p \le \varepsilon} d^3r \frac{I(\vec{r},\omega)}{\hbar\omega} n_0 \sigma_0 \cos^2\theta_- \, F(\varepsilon, \vec{r}, \omega, T) \end{aligned} \tag{6.2}$$

where $I(\vec{r},\omega)$ is the local intensity of the incident light at frequency ω, $n(\vec{r})$ is the density distribution, Eq. 2.10, $\cos^2\theta_-$ is the branching ratio for pumping an atom from the d state to the a state on the σ_2 transition (see Sect. 4.4), $\sigma_L(\omega)$ is a Lorentzian absorption cross section (Eq. 4.16) including the Doppler shift and the angular brackets denote an average over the Maxwell distribution. In the second

line of Eq. 6.2 the lineshape function F equals

$$F(\varepsilon,\vec{r},\omega,T)=\frac{1}{\sqrt{\pi}}\frac{\gamma}{b}\Big(\arctan[(\omega-\omega_0'+bx)/\gamma]-\arctan[(\omega-\omega_0'-bx)/\gamma]\Big), \quad (6.3)$$

where $\omega_0'=\omega_0+E_r/\hbar$ and $x=\sqrt{(\varepsilon-U_p)/k_BT}$. In general Eq. 6.2 can only be numerically calculated. The light-induced evaporation rate is given by

$$\tau_{LIE}^{-1}=\frac{\dot{N}_{LIE}}{N}=\frac{1}{N}\int d^3r\frac{I(\vec{r},\omega)}{\hbar\omega}\sigma_V(\vec{r},\omega)\cos^2\theta_-n(\vec{r})\,d^3r, \quad (6.4)$$

where $\sigma_V(\vec{r},\omega)$ is the Doppler broadened absorption cross section (see Sect. 4.6). To get a feeling for the magnitude of the light-induced evaporation rate, it is calculated for the typical conditions of Fig. 6.1. The branching ratio is taken constant to its value at the trap minimum $\cos^2\theta_-=\frac{2}{3}$. As a typical photon flux we had 3×10^7 photons/pulse at a repetition rate of 50 Hz and for the conditions of Fig. 6.1, $N=1.4\times10^9$. Assuming a typical relative absorption of $\simeq 0.2$, we obtain $\tau_{LIE}^{-1}\simeq 0.14\,\mathrm{s}^{-1}$.

6.2.2 The LIE cooling rate

The calculation of the LIE cooling rate goes along the same lines as the calculation of the Doppler cooling rate in Sect. 5.2 and is, in fact, an extension to the case of non-closed optical pumping cycles. The energy change, caused by optically pumping one atom to an H$\downarrow$ state, is $p^2/2m+U_p(\vec{r})$. The fraction of excited atoms that decays to the H$\downarrow$ state is given by the branching ratio $\cos^2\theta_-$. The complement of this probability, $\sin^2\theta_-$, gives the probability that the atom decays back to the same H$\uparrow$ state and undergoes a Doppler cooling cycle. The cooling rate in an infinitesimal volume element d^3r is

$$\begin{aligned}d\dot{Q}_{LIE}(\vec{r}) &= \frac{I(\vec{r},\omega)}{\hbar\omega}\sin^2\theta_-\,\langle\sigma_L(\omega_0'+kv_z)(\hbar kv_z+2E_r)\rangle\,n(\vec{r})d^3r\;-\\ &\quad\frac{I(\vec{r},\omega)}{\hbar\omega}\cos^2\theta_-\,\langle\sigma_L(\omega_0'+kv_z)(\tfrac{1}{2}mv^2+U_p(\vec{r}))\rangle\,n(\vec{r})d^3r. \quad (6.5)\end{aligned}$$

When condition 6.1 is met, the atoms have a Maxwell velocity distribution and the average can be calculated. For the Doppler cooling term this was performed in Sect. 5.2. The second average in Eq. 6.5 can be straightforwardly evaluated. Analogous to the Doppler cooling integral, the average of $\sigma_L\frac{1}{2}mv_z^2$ gives a second-order frequency derivative of the Voigt lineshape. The total LIE cooling rate is now given by

$$\begin{aligned}\dot{Q}_{LIE}=2E_r\int_V\frac{I(\vec{r},\omega)}{\hbar\omega}n(\vec{r})\left(\sigma_V(\vec{r},\omega)-\frac{k_BT}{\hbar}\frac{\partial\sigma_V}{\partial\omega}\right)\sin^2\theta_-\,d^3r\;-\\ \int_V\frac{I(\vec{r},\omega)}{\hbar\omega}n(\vec{r})\left[\Big(U_p(\vec{r})+\tfrac{3}{2}k_BT\Big)\sigma_V(\vec{r},\omega)+E_r\Big(\frac{k_BT}{\hbar}\Big)^2\frac{\partial^2\sigma_V}{\partial\omega^2}\right]\cos^2\theta_-\,d^3r.\end{aligned} \quad (6.6)$$

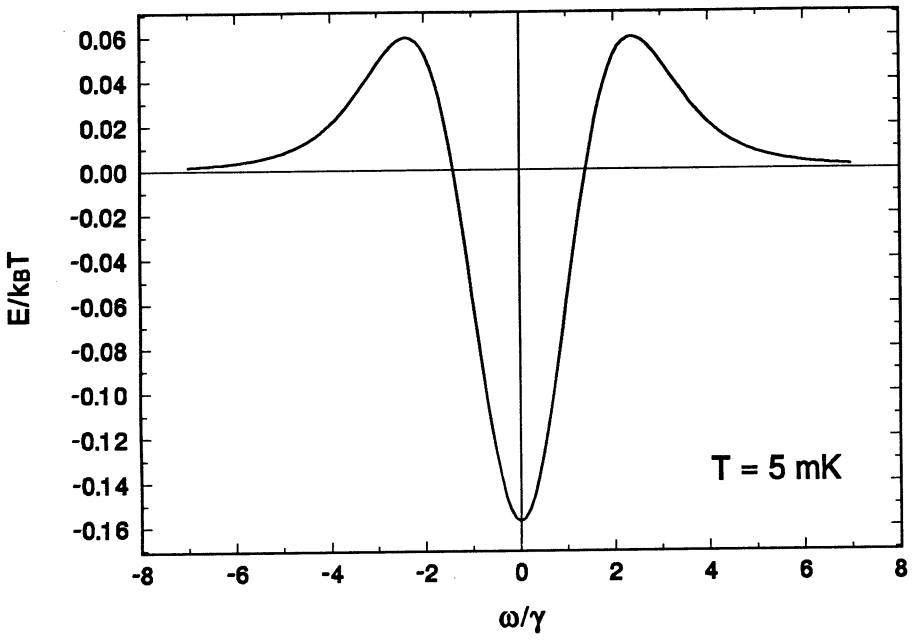

Figure 6.2: Correction to the average kinetic energy of the pumped atoms due to velocity-selective excitation. The correction is plotted for a homogeneous gas in units of k_BT as a function of normalized frequency $\Delta\omega/\gamma$ and for a temperature of 5 mK.

The second-order derivative appearing in the average energy of the pumped atoms, is due to the velocity-selective excitation parallel to the laser beam. For the case of a homogeneous gas, we plot the energy correction term in units of k_BT for a temperature of 5 mK as a function of frequency. When tuned to resonance, mainly atoms with $v_z = 0$ are excited which makes the average kinetic energy of the optically pumped atoms smaller than $\frac{1}{2}k_BT$. As the laser is detuned more from resonance, atoms with higher velocity are excited which increases the average energy of the pumped atoms. In the wings of the Voigt line this effect is reduced by the exponentially decreasing number of atoms with high velocities. For the Voigt lineshape this energy correction is small. For light tuned to resonance in a homogeneous gas it is maximally $\simeq -0.16\,k_BT$ at $T = 7\,\mathrm{mK}$, decreasing to $\simeq -0.1\,k_BT$ at 1 mK. In the following sections, it will, therefore, be neglected in the calculation of LIE cooling rates and the average kinetic energy of an optically pumped atom will be taken equal to $\frac{3}{2}k_BT$.

In the discussion of evaporative cooling, an important quantity is the change in potential energy of the gas due to LIE in units of k_BT, analogous to $\eta = \varepsilon_{tr}/k_BT$

for ordinary evaporative cooling (see Sect. 2.5).

$$\eta_{LIE} \equiv \frac{1}{k_B T}\frac{\dot{Q}_{LIE}}{\dot{N}_{LIE}} - \frac{3}{2} \simeq \frac{\langle U_p \rangle}{k_B T} - \tan^2\theta_-(B_0)\frac{2E_r}{k_B T}\xi_D(\omega, n_0, T). \tag{6.7}$$

This equation consists of the potential energy of an optically pumped atom and a correction due to Doppler cooling. The average potential energy of an optically pumped atom is

$$\langle U_p \rangle = \frac{\int_V U_p(\vec{r}) I(\vec{r},\omega) n(\vec{r}) \sigma_V(\vec{r},\omega)\, d^3r}{\int_V I(\vec{r},\omega) n(\vec{r}) \sigma_V(\vec{r},\omega)\, d^3r}, \tag{6.8}$$

where the integral in the numerator is the rate of potential energy removal and the integral in the denominator is the absorption rate. The Doppler cooling term is written in terms of $\xi_D(\omega, n_0, T)$, the change in internal energy of the gas per *scattered* photon in units of $2E_r$ (see Eq. 5.20). In this equation we have approximated the branching ratio by its value at the trap center. Since the branching ratio is very weakly dependent on the magnetic field (see Fig. 4.3), this approximation is very good for the temperatures at which the LIE experiments were performed ($T = 3 - 10\,\mathrm{mK}$). The Doppler cooling term in η_{LIE} is small for the temperature range of the LIE experiments. At $T \leq 10\,\mathrm{mK}$, $\xi_D \simeq 1$ for the large detunings that are used in LIE, so that the correction due to the Doppler cooling mechanism on η_{LIE} is of the order of $E_r/k_B T$ which only becomes dominant at temperatures below the recoil temperature. For $k_B T \gg E_r$, we can assume $\eta_{LIE} \simeq \langle U_p \rangle / k_B T$.

Analogous to the case of ordinary evaporative cooling (see Sect. 2.6.1), we can derive a condition for cooling at constant or increasing density. This condition is

$$\eta^*_{LIE} = \eta_{LIE}\frac{\dot{N}_{LIE}}{\dot{N}} + \gamma_{2e}\frac{\dot{N}_{dip}}{\dot{N}} \geq 3.5, \tag{6.9}$$

where we have assumed $\kappa(\eta_{LIE}) = \frac{3}{2}$ (see Eq. 2.50). For temperatures $T \gg E_r/k_B$, this boils down to a calculation of $\langle U_p \rangle / k_B T$ and see whether condition 6.9 is met for the experimental range of n_0 and T. In general, $\langle U_p \rangle$ must be numerically calculated which will be the subject of Sect. 6.4. In the optically thin limit a few simplifying assumptions can be made.

6.3 LIE in the optically thin limit

The optically thin limit for the σ_2 transition in the axial direction applies to densities $n_0 \ll 2 \times 10^{11}\,\mathrm{cm}^{-3}$, i.e., slightly higher than in the case of the σ_1 transition. For these densities, we have $I(\vec{r},\omega) \simeq I_0(\vec{r})$ and $\langle U_p \rangle$ becomes independent of n_0. If we further assume that the intensity of the incoming beam is constant over the sample,

which is a very good approximation at $T \ll 40\,\mathrm{mK}$ (see Sect. 4.7), we can take $I_0(\vec{r}) \simeq I_0$ and Eq. 6.8 reduces to

$$\langle U_p \rangle \simeq \frac{\int_V U_p(\vec{r}) n(\vec{r}) \sigma_V(\vec{r},\omega)\, d^3r}{\int_V n(\vec{r}) \sigma_V(\vec{r},\omega)\, d^3r}. \tag{6.10}$$

To establish whether we can cool a gas at constant density by LIE in the optically thin limit, we must verify the condition 6.9. To do this, we will first rewrite the integral in the numerator of Eq. 6.10 to magnetic field variables in a similar manner as for Doppler cooling in the optically thin regime.

$$\int_{B_0}^{\infty} dB\, \rho_M(B) n(B) \mu_B(B - B_0)\, \sigma_V(B,\omega). \tag{6.11}$$

The denominator can be rewritten in a similar fashion. If we oversimplify the situation and assume infinitely thin shells, η_{LIE} can be simply obtained by taking $\sigma_V \sim \delta[\omega - \omega_{\sigma 2}(B_{res})]$

$$\eta_{LIE} \simeq \frac{\langle U_p \rangle}{k_B T} \simeq \frac{\mu_B(B_{res}(\omega) - B_0)}{k_B T}. \tag{6.12}$$

This is indicated by the long-dashed line in Fig. 6.3. This is clearly an oversimplification, since the density at the location of the shell decreases exponentially for increasing shell size. For very large shells, the dominant absorption takes place in the center of the trap due to the Lorentzian tails. Therefore, as the σ_2 transition has a negative Zeeman shift, $\eta_{LIE} \simeq \frac{3}{2}$ for very large negative detunings. Also for large positive detunings, when no atoms are resonant, $\eta_{LIE} \simeq \frac{3}{2}$. For increasing detuning from the trap center, η_{LIE} will initially increase proportionally to $(\omega - \omega_{\sigma 2}(B_0))$ until the detuning is reached for which the contribution to Eq. 6.11 from the resonant shell equals the contribution from the non-resonant atoms enclosed by the resonant shell. This detuning can be roughly obtained from the equality

$$\Delta B_V \rho_M(B) n(B) \sigma_0 \sqrt{\pi} \frac{\gamma}{b} \mu_B(B - B_0) = \int_{B_0}^{B^*} dB\, \rho_M(B) n(B) \frac{\sigma_0 \mu_B(B - B_0)}{((\omega - \omega_{\sigma 2}(B))/\gamma)^2}, \tag{6.13}$$

where $B^* = B_{res}(\omega - b)$ and we have approximated the Voigt line by a Gaussian for $|\Delta\omega| < b$ and by a Lorentzian for $|\Delta\omega| > b$. Numerical evaluation of the r.h.s of Eq. 6.13 shows that the equation is satisfied for $U_p/k_B T \simeq 10$ at 5 mK increasing to 15 at 50 mK. This rough estimate shows that, when the shell thickness is much smaller than the sample size, condition 6.9 can be fulfilled and LIE can be applied as a method to optically cool a gas at a constant or even increasing density.

To see whether LIE is still as efficient a cooling method for temperatures so low that the shell model does not apply, Eq. 6.10 must be numerically calculated. In Fig. 6.3, we plot $\langle U_p \rangle / k_B T$ and τ_{LIE}^{-1} for a number of relevant temperatures.

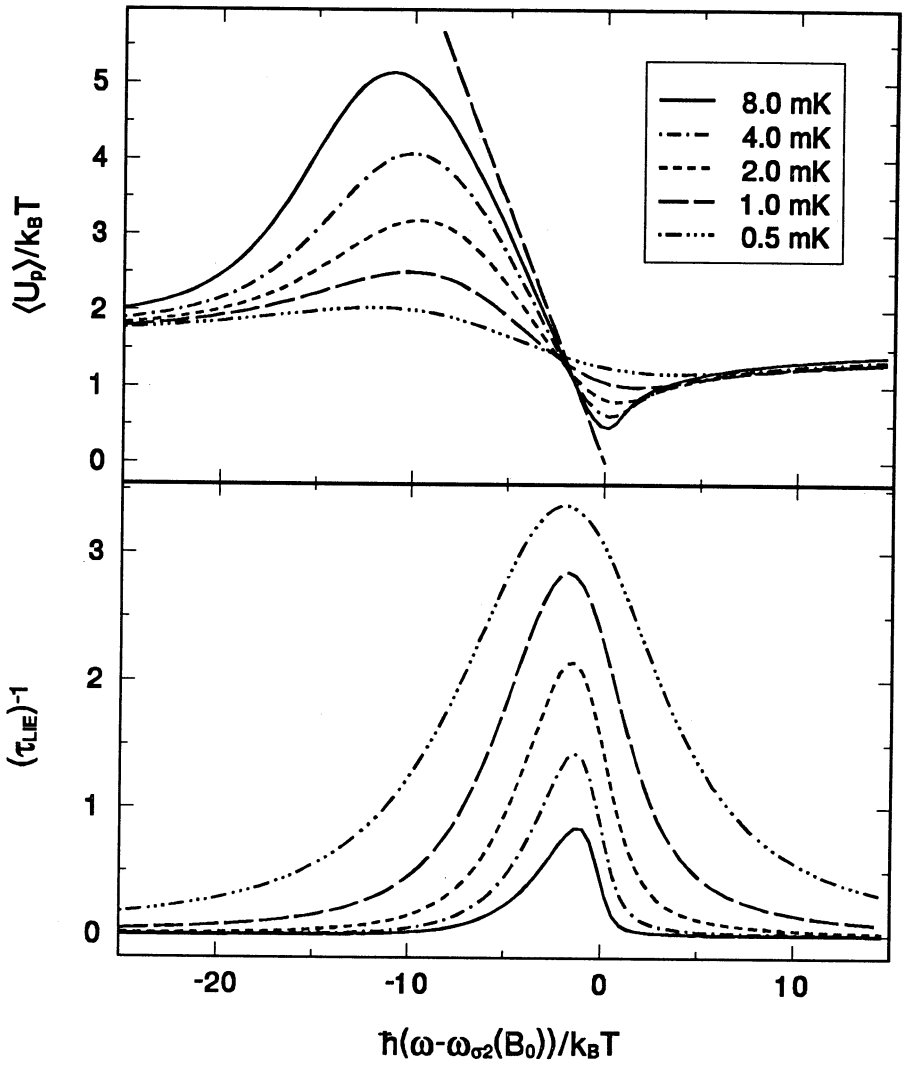

Figure 6.3: Average potential energy $\langle U_p \rangle / k_B T$ of an optically pumped atom and LIE optical pumping rate τ_{LIE}^{-1}, in the optically thin limit for temperatures $T = 0.5$, 1.0, 2.0, 4.0 and 8.0 mK. Both curves are specific to the σ_2 transition. For the calculation of τ_{LIE}^{-1} a typical photon flux of $2 \times 10^9\,\mathrm{s}^{-1}$ has been assumed in a 1 mm diameter beam.

Notice that all curves are plotted with respect to the detuning from the trap center $\hbar(\omega - \omega_{\sigma 2}(B_0))/k_B T$. For low fields ($B \ll 0.78\,\mathrm{T}$, see Sect. 4.4), $(\omega - \omega_{\sigma 2}(B_0)) = -\frac{3}{2} U_p/\hbar$. From the plot it can be seen that the maximum value for $\langle U_p \rangle / k_B T$ occurs at $U_p/k_B T \simeq 7$, roughly in accordance with the estimate from Eq. 6.13.

For $T \gg 2.4\,\mathrm{mK}$, LIE is well described by the shell model. For $T \lesssim 2.4\,\mathrm{mK}$, the Voigt thickness becomes comparable to the sample size. In this case irradiation cannot result in Zeeman selective excitation and $\langle U_p \rangle / k_B T \simeq \frac{3}{2}$. From Fig. 6.3 can be concluded that condition 6.9 is satisfied for temperatures $T > 3\,\mathrm{mK}$. For a typical temperature of 10 mK and a density of $5 \times 10^{10}\,\mathrm{cm}^{-3}$ at which the sample is optically thin, $\tau_c^{-1} \simeq 3 \times 10^{-2}\,\mathrm{s}^{-1}$ and $\tau_{dip}^{-1} \simeq 2 \times 10^{-5}\,\mathrm{s}^{-1}$. For these conditions, $\tau_{LIE}^{-1} \simeq 10^{-2}\,\mathrm{s}^{-1}$, so that condition 6.1 is satisfied.

The curve for $T = 0.5\,\mathrm{mK}$ in Fig. 6.3 satisfies the condition for the Lorentzian approximation, $T \ll 2.2\,\mathrm{mK}$. Since $I(\vec{r}, \omega) \simeq I_0(\vec{r})$ and σ_L is temperature independent, Eq. 6.8 can be rewritten to

$$\frac{\langle U_p \rangle}{k_B T} \simeq -\frac{T}{\Lambda(\omega, T)} \frac{\partial \Lambda}{\partial T}. \tag{6.14}$$

In the Lorentzian approximation a closed expression for $\Lambda(\omega, T)$ can be derived (see Eq. 4.44). The LIE experiments with H were performed at $T \geq 3\,\mathrm{mK}$, just above the Doppler limit, where the Voigt lineshape cannot be expected to be very well approximated by a Lorentzian lineshape. For heavier elements, like Na and Cs, the Lorentzian approximation is valid at temperatures much higher than the Doppler limit. For these temperatures closed expressions for the cooling rate can be derived for LIE as well as for Doppler cooling (see Sect. 5.4.1).

For the optically thin limit, we have shown that LIE can cool a gas down to $T \simeq 3\,\mathrm{mK}$ determined by the temperature at which the resonant shell thickness becomes comparable to the sample size. LIE is, therefore, not suited for cooling an optically thin gas to the regime of quantum degeneracy. An alternative method, which is not limited by the width of the transition, is the use of microwaves to pump the atoms to H$\downarrow$ states. Very recent experiments with trapped alkali atoms [10, 11] have demonstrated the feasibility of this cooling method.

6.4 LIE in the optically thick limit

In the optically thick limit, where the shell model is not valid, the limitations, discussed in the previous section, do not exist and the gas can be cooled to much lower temperatures. The average potential energy of the optically pumped atoms, Eq. 6.8, is calculated in parallel with the calculation of the spectrum. During the numerical integration of Eqs. 4.28, the product of $U_p(\vec{r})$ with the local attenuation of the light, $(\partial I / \partial z)$, is integrated over the sample. Together with the total number of scattered photons, $\langle U_p \rangle / k_B T$ and η_{LIE} are calculated. Because temperatures lower than the recoil temperature can be reached, the Doppler cooling term in Eq. 6.7

cannot be neglected as it is for the optically thin limit. We will see later that it is this term that ultimately limits cooling by LIE in the optically thick case.

Multiple scattering: in the analysis of the experiments, we will neglect the effects of multiple scattering. In the case of LIE, the photon that is scattered first can leave an atom in the d state or optically pump an atom to the a state. In the latter case, the emitted photon gains an extra energy due to the Zeeman splitting between the a and d levels. In the LIE trap (see Sect. 2.2), this photon is then 100 MHz detuned from the σ_1 transition at the trap center. The effects of multiple scattering on the σ_1 transition were discussed in Sect. 5.5. At the maximum densities reached in the LIE experiments ($n_0 \simeq 10^{13}\,\mathrm{cm}^{-3}$) numerical simulations showed that a resonant photon scatters on the average 1.5 times, each time increasing the energy of the atom with approximately the recoil energy. If the atom decays back to the d state, the emitted photon remains resonant with the σ_2 transition and will most probably pump the atom to the a state the next time it scatters. Due to the high densities for which multiple scattering plays a role, the optical pumping will take place not very far from the location of the first scattering and η_{LIE} will be roughly equal to the η_{LIE} caused by the atom that was pumped in the first scattering event. From this very qualitative argument, the correction on η_{LIE} due to multiple scattering can be estimated to be of the order of $(1+\sin^2\theta_-(B_0))N_{ms}2E_r/k_BT$ where N_{ms} is the average number of scatterings a resonant photon makes after optically pumping an atom to the a state and all terms of order $\sin^4\theta_-(B_0)$ or smaller have been neglected.

In this section, we will first discuss the results of the numerical calculation of η_{LIE} for the range of temperatures and densities in the experiments. We will then discuss LIE in the limit of low temperatures ($T \ll 2.2\,\mathrm{mK}$) where we can use the Lorentzian approximation and neglect the Zeeman shift of the resonant frequency.

6.4.1 Numerical results

The η_{LIE} is a function of ω, n_0 and T. In this section, the discussion of η_{LIE} will be for two particular cases : $\eta_{opt} \equiv \eta_{LIE}(\omega_{opt})$, where ω_{opt} is the frequency for which η_{LIE} has its maximum for given n_0 and T, and $\eta_p \equiv \eta_{LIE}(\omega_p)$, where ω_p is the frequency of maximum absorption for given n_0 and T. In Fig. 6.4, we plot the contours of η_{opt} and η_p for the range of T and n_0 of the experiment. At the lowest density in the plot, η_{opt} is a strongly varying function of temperature and a very weakly varying function of density. The values of η_{opt} and η_p at the lowest density in the plot correspond to the values we obtain from Fig. 6.3. The value of η_p is a weakly varying function of density but an even more weakly varying function of temperature. The frequency detuning corresponding to η_{opt} and η_p can

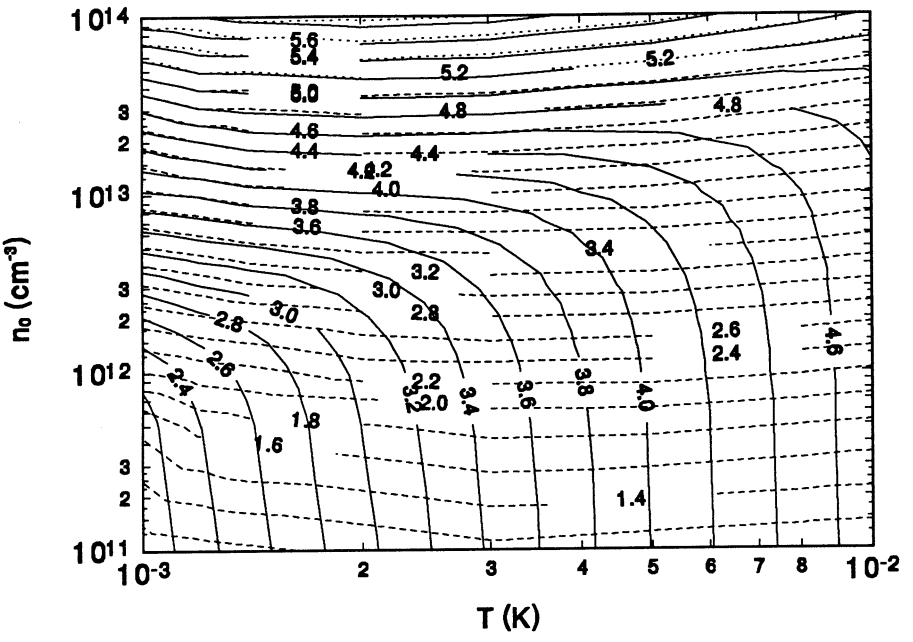

Figure 6.4: Contour plot of η_{opt} (solid line) and η_p (dashed line) for the range of temperatures and densities in the experiment.

be found in Fig. 6.5 to which we will turn our attention later. When we move in the direction of increasing density in Fig. 6.4 for a constant temperature, initially η_{opt} hardly changes. Since $|\omega_{opt} - \omega_{B0}| > |\omega_p - \omega_{B0}|$, the optical thickness when tuned to maximum absorption will be larger than the optical thickness when tuned to ω_{opt}. At constant detuning $(\omega_p - \omega_{B0})$ and increasing density, the light will be absorbed at an increasingly negative detuning from the resonant shell until for a certain density the light is absorbed at the detuning $(\omega_{opt} - \omega_{B0})$. For this density, $\omega_{opt} = \omega_p$ and η_p coincides with η_{opt} (the solid and the dashed lines begin to overlap in Fig. 6.4). For even larger densities, η_{opt} and η_p will both increase as the light is absorbed at larger detunings and correspondingly larger potential energies. Since in the optically thin regime $\hbar|\omega_{opt} - \omega_p| \simeq 9k_BT$, the density at which η_{opt} and η_p begin to overlap will be larger for higher temperatures. Notice that for the plotted temperature range in Fig. 6.4, $\eta_{opt} > \frac{3}{2}$ and tuning to ω_{opt} will always result in cooling, possibly accompanied by a loss of density. In Fig. 6.5, ω_{opt} and ω_p are plotted. A remarkable feature is that ω_{opt} hardly depends on n_0 for the range of densities considered. Detuning to $\omega < \omega_{opt}$ will move the resonant shell outwards and decrease the absorption in the shell so that atoms at lower magnetic fields will be excited. Detuning to $\omega > \omega_{opt}$ will move the resonant shell inwards so that maximum

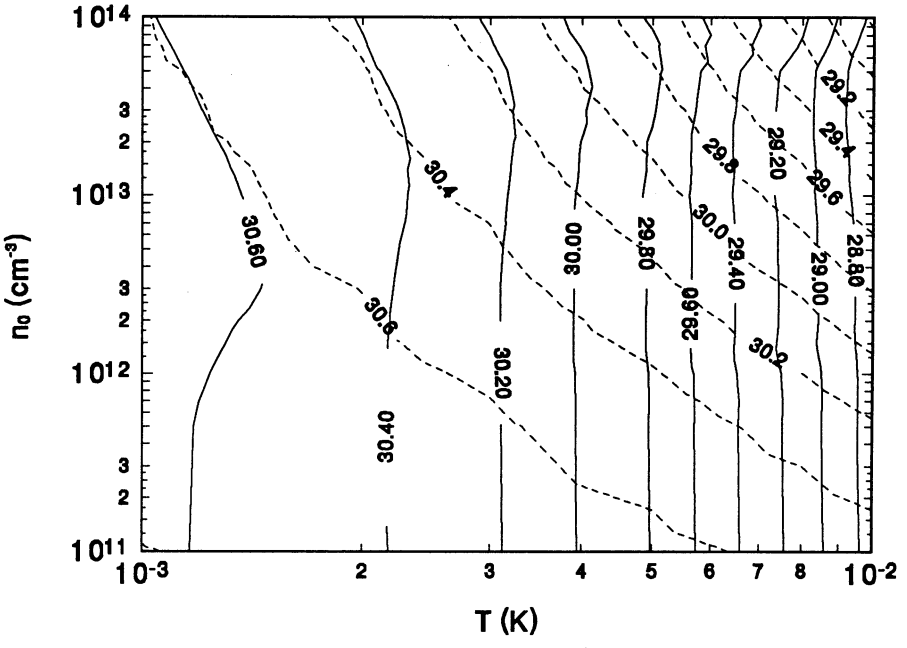

Figure 6.5: Contour plot of ω_{opt} (solid line) and ω_p (dashed line) with respect to a particular reference frequency, for the range of temperatures and densities in the experiment. The resonant frequency at the trap center in these units is 30.86 GHz.

absorption will also take place at smaller detunings and η_{LIE} will decrease. The ω_p is weakly dependent on T and n_0. For an increasing density, at constant temperature, maximum absorption will take place at an increasingly negative detuning from the resonant shell. Also in this plot we see how η_p coincides with η_{opt}, at a density that increases with temperature.

6.4.2 The limit of no Zeeman broadening

In Sect. 6.4.1, η_{LIE} was calculated for the range of n_0 and T of the experiment. We will now discuss the cooling rate for lower temperatures and the cooling limit for LIE. For $T \ll 2.2\,\mathrm{mK}$, we can use the Lorentzian approximation and neglect the Zeeman shift. In this regime, all atoms have the resonance frequency at the trap center and there are no resonant shells. In Sect. 4.8, we showed that for this limit we could give a closed expression for the attenuation of the light for *all* densities, Eq. 4.49. We will use these expressions to discuss LIE for temperatures $T \ll 2.2\,\mathrm{mK}$. The heating due to multiple scattering will be neglected which means that for densities $n_0 \gtrsim 3 \times 10^{12}\,\mathrm{cm}^{-3}$ the cooling limit can only be expected to form a lower bound.

At these temperatures, Doppler cooling by velocity-selective excitation will be very small and the dominant contribution to the Doppler cooling integral will be the photon recoil heating. In this case, the cooling parameter $\xi_D \simeq 1$ and Eq. 6.7 reduces to

$$\eta_{LIE} \simeq \frac{\langle U_p \rangle}{k_B T} - \tan^2 \theta_-(B_0) \frac{2E_r}{k_B T} \tag{6.15}$$

Equation 6.15 shows the limiting mechanisms of cooling by LIE. A constant fraction of the atoms decays to the same initial state, in which their energy is increased by the photon recoil. Since the photon recoil energy is constant ($E_r = 0.64\,\mathrm{mK}$), this heating will ultimately balance the cooling due to optical evaporation.

For the temperatures at which the Lorentzian approximation is valid, the magnetic field profile is nearly parabolic. For the σ_2 transition the resonant cross section $\sigma_L(0) = \sigma_0 \sin^2 \theta_-(B_0)$, which for the trapping field that was used ($B_0 = 0.0876\,\mathrm{T}$) can be well approximated by $\sigma_L(0) \simeq \lambda^2/2\pi$. Combined with the closed expression, Eq. 4.49, for the attenuation of a light beam, $\langle U_p \rangle$ can be numerically calculated using Eq. 6.8. In Fig. 6.6, the contours of η_{LIE} are plotted for $\omega = \omega_{\sigma 2}(B_0)$ as a function of n_0 and T. For cooling at constant density, the lowest attainable temperature at the highest attainable density in a magnetic trap ($\sim 10^{14}\,\mathrm{cm}^{-3}$), is $\simeq 230\,\mu\mathrm{K}$. Starting at any position in the T-n_0 plane where $\eta_{LIE} = 3.5$, will take the gas to the regime where $\eta_{LIE} < 3.5$. Therefore, to cool without a loss of density one requires $\eta_{LIE} > 3.5$. As it turns out, one can cool at 1 mK and constant η_{LIE} by following the evolution given by $\dot{n}_0/n_0 \simeq -\frac{1}{2}(\dot{T}/T)$ which corresponds to $\eta^*_{LIE} \simeq 4.5$.

6.5 Evolution of temperature and density during LIE

To prepare for LIE, we load the LIE trap (see Sect. 2.2) and rely on the same wall-induced recombination mechanism as in the Doppler cooling experiments (see chapter 7) to evaporatively cool the gas. The LIE experiments are performed shortly after loading, when the gas has almost reached a steady-state temperature (see Sect. 2.6) and the gas is completely isolated from the walls. Under these conditions, the particle loss rate and cooling due to ordinary evaporation may be neglected in the calculations of the evolution. The first-order, non-heating loss mechanism, observed in the Doppler cooling measurements, takes place on a time scale much longer than the LIE experiments and will also be neglected.

The heating rate of the gas is given by

$$\dot{Q}_{tot} = \dot{Q}_{dip} + (\eta_{LIE} + \tfrac{3}{2}) k_B T \dot{N}_{LIE}. \tag{6.16}$$

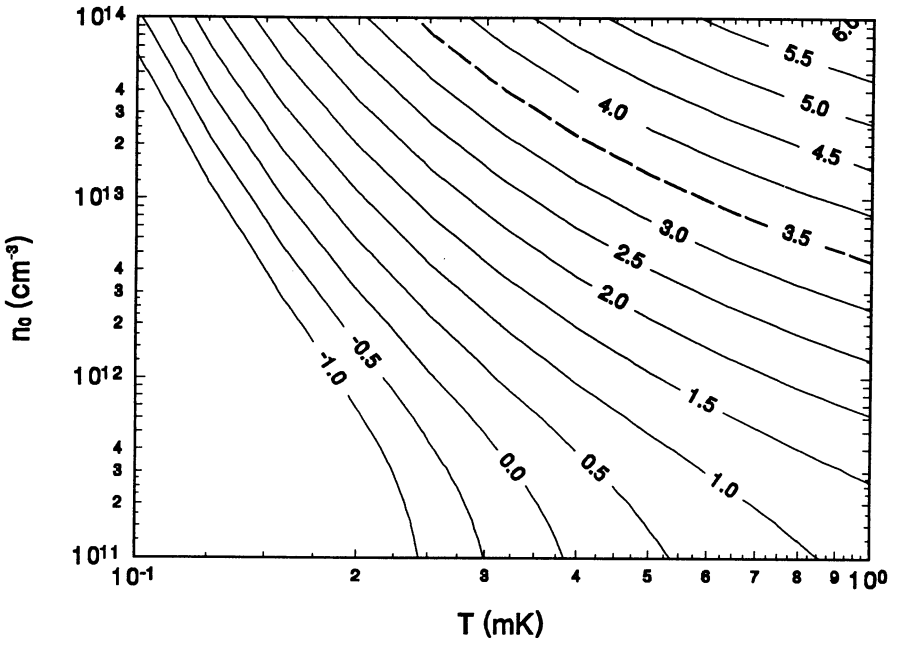

Figure 6.6: Contour plot of η_{LIE} using the Lorentzian approximation as a function of n_0 and T. The plot is made for tuning to the trap center ($\omega = \omega_{\sigma 2}(B_0)$) only taking into account the Doppler recoil heating. The long-dashed line indicates the curve for $\eta_{LIE} = 3.5$, corresponding to cooling at constant density.

The total particle loss is given by

$$\dot{N}_{tot} = \dot{N}_{dip} + \dot{N}_{LIE}. \tag{6.17}$$

Equations 6.16 and 6.17 are substituted into Eq. 2.45 which is numerically solved form two cases: for tuning to ω_{opt} and for tuning to ω_p. The values of η_{LIE} and the optical pumping rate $\dot{N}_{LIE} = \cos^2\theta_- \Lambda(\omega, n_0, T)$ are constantly adjusted to the instantaneous value of n_0 and T during the numerical integration. In Fig. 6.7, we plot the evolution of n_0 and T in the T-n_0 plane for these two cases. The numerical calculations of η_{LIE} in Fig. 6.4 already showed that for the optically thin limit tuning to ω_p results in a cooling rate that is smaller than for the case of tuning to ω_{opt}. This can also be seen from Fig. 6.7, where for the lowest density tuning to ω_{opt} results in a lower temperature than tuning to ω_p. As the density increases, the difference between η_p and the value of η_{opt} decreases until for a particular density, depending on the temperature, they coincide. The initial decrease in n_0 at the large starting densities is a result of the dipolar decay. LIE will start to cool the gas if the density, and consequently the dipolar heating, have decreased enough for the LIE cooling

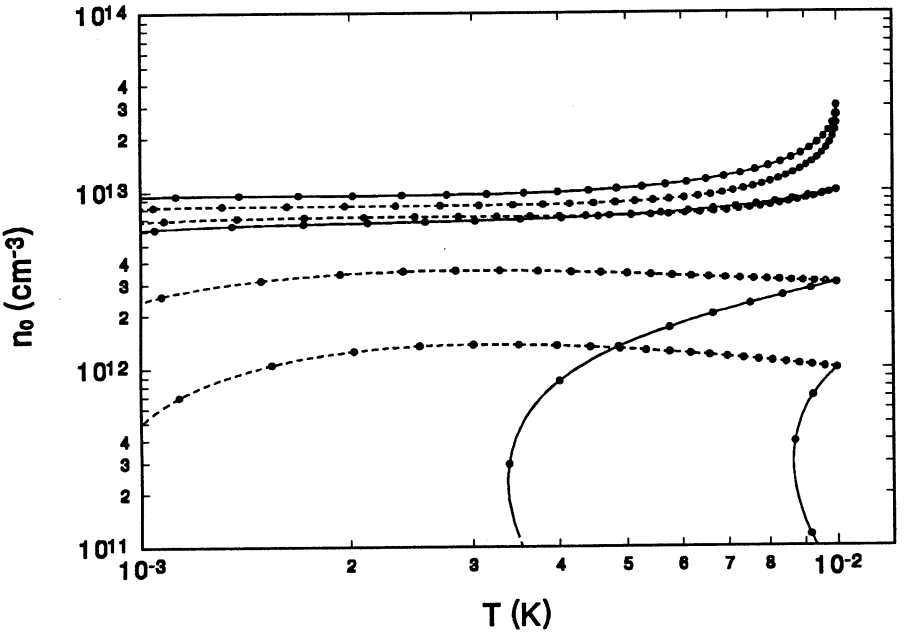

Figure 6.7: Evolution of temperature and density during LIE on the σ_2 transition in the T-n_0 plane. The evolution is calculated for an initial photon flux $\Phi_0 = 2 \times 10^9\,\mathrm{s}^{-1}$ and for the two cases of tuning to ω_{opt} (dashed line) and ω_p (solid line), starting at four initial densities $n_0 = 10^{12}\,\mathrm{cm}^{-3}$, $3 \times 10^{12}\,\mathrm{cm}^{-3}$, $10^{13}\,\mathrm{cm}^{-3}$ and $3 \times 10^{13}\,\mathrm{cm}^{-3}$. The dots indicate 10 s periods.

rate to take over. For the photon flux in Fig. 6.7, the cooling for the highest densities roughly takes place at constant n_0. By increasing the photon flux, the LIE cooling rate can become large enough for n_0 to increase during cooling. In Fig. 6.8, we plot the evolution of n_0 and T for tuning to ω_{opt} for the same initial densities as in Fig. 6.7 and for two different photon fluxes. At the lowest densities in the plot, the dipolar heating is neglegibly small. As the photon flux is increased, $\dot{Q}_{LIE}$ and $\dot{N}_{LIE}$ will increase proportionally and the effect will be that the same evolution in the T-n_0 plane will be followed as for the low photon flux, but in a shorter time interval. As the density is increased, the dipolar heating becomes stronger. An increase in photon flux will then give a proportional increase in LIE cooling rate. For a high enough photon flux the LIE cooling rate is larger than the dipolar heating rate and n_0 increases during cooling.

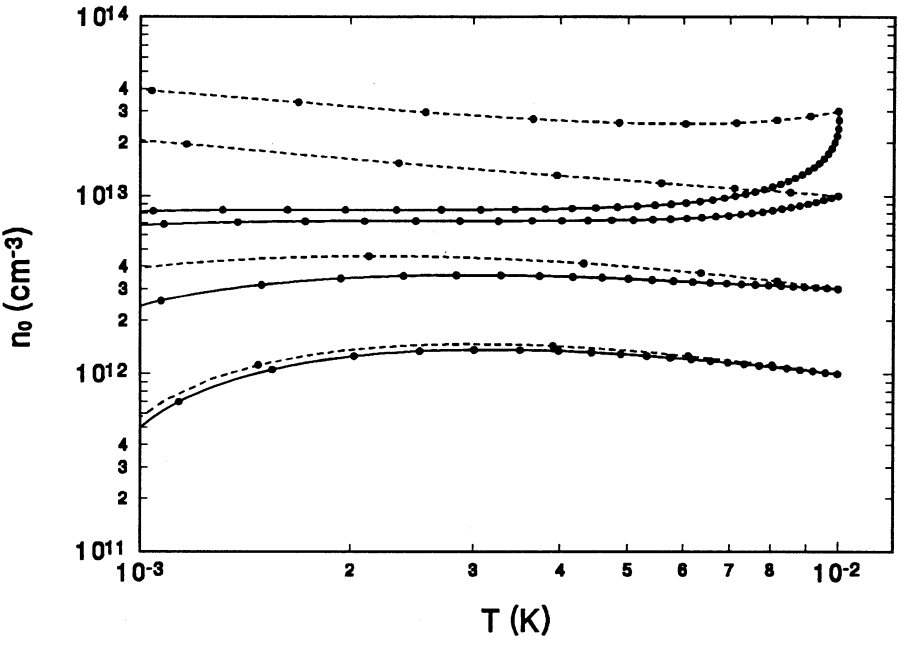

Figure 6.8: Evolution of n_0 and T for two different photon fluxes $\Phi_0 = 2 \times 10^9\,\mathrm{s}^{-1}$ (solid line) and $10^{10}\,\mathrm{s}^{-1}$ (dashed line). The evolution is calculated for tuning to ω_{opt}, starting at four initial densities $n_0 = 10^{12}\,\mathrm{cm}^{-3}$, $3 \times 10^{12}\,\mathrm{cm}^{-3}$, $10^{13}\,\mathrm{cm}^{-3}$ and $3 \times 10^{13}\,\mathrm{cm}^{-3}$. The dots indicate 10 s periods.

6.6 Experimental results

Light-induced evaporation was performed on the σ_2 transition (see Sect. 4.4). This transition has the highest branching ratio ($\cos^2\theta_-(B) \simeq \frac{2}{3}$) to the electron-spin-down hyperfine state for the magnetic field strength $B_0 \simeq 0.1$ T of the trapping geometry and is spectrally well separated from the other transitions. All efforts were aimed at performing LIE under optimal conditions ($\omega = \omega_p \simeq \omega_{opt}$) with n_0 as high as possible. Experiments with $\omega = \omega_{opt}$ in the optically thin limit were not performed. To achieve a large starting density and low initial temperature, we used regular forced evaporative cooling. By filling a deep trap ($\varepsilon_{tr} = 320\,\mathrm{mK}$) and subsequently lowering the trap barrier to 57 mK, we achieved an initial density between 10^{12} and $10^{13}\,\mathrm{cm}^{-3}$ and an initial temperature between 9 and 13 mK. The final trap depth was chosen to let the recoiling atoms, produced after dipolar relaxation (e.g. $dd \rightarrow ad$) with an energy $\varepsilon_{kin} \simeq \mu_B B_0$, escape over the trap barrier. The magnetic field parameters of the LIE trap are given in Sect. 2.2.

To determine density and temperature of the cold gas before LIE, a spectrum

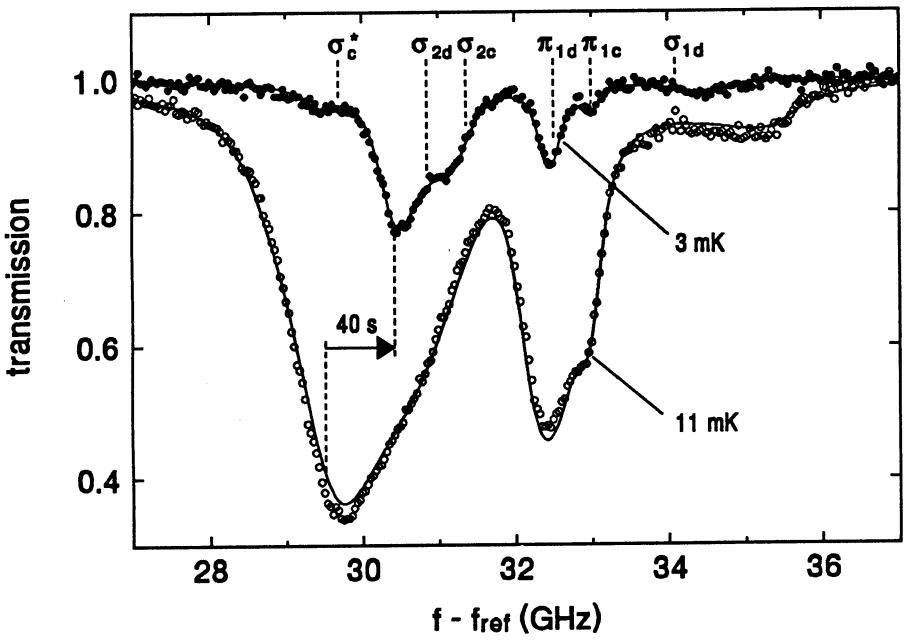

Figure 6.9: Transmission spectra before (open circles) and after (closed circles) LIE cooling. The solid lines are calculated spectra for $T = 11(2)\,\mathrm{mK}$, $n_0 = 4.8(2.1)\times 10^{12}\,\mathrm{cm}^{-3}$ and $T = 3(1)\,\mathrm{mK}$, $n_0 = 3.9(1.7)\times 10^{12}\,\mathrm{cm}^{-3}$, respectively. The subscripts c and d refer to transitions from the corresponding ground states. The c-state fraction $n_{c0}/n_0 \sim 0.1$. For the various lines the transition frequencies at $B = B_0$ are indicated.

was taken of the σ_2 and the π_1 line using RCP (right-circularly polarized) light (see Sect. 4.4). Then the laser was tuned to a frequency $\omega \simeq \omega_p$ and the sample was irradiated for $30 - 80\,\mathrm{s}$. The laser frequency was adjusted to follow the shift in ω_p during cooling. This was done by a preprogrammed linear chirp of the RDL frequency in time. On-line determination of ω_p during the measurements was not possible. Moreover, during the measurement no information on n_0 was available. In all cases it was assumed that optimal cooling would be obtained by tuning to ω_p. After the irradiation period at ω_p, a spectral scan was again taken to determine the final density and temperature. In Fig. 6.9 a typical transmission spectrum before and after an LIE cooling cycle is shown. By comparing the measured spectra with calculated spectra, it is shown that LIE has cooled the gas from 11 mK to 3 mK. To check that this was indeed due to LIE, a second sample was prepared in an identical manner and left to evolve in the dark. Only minor changes in T and n_0 were observed in this case. To ensure high starting densities for LIE, the evaporative precooling was initiated shortly after the filling. The c state was, therefore, not yet depopulated

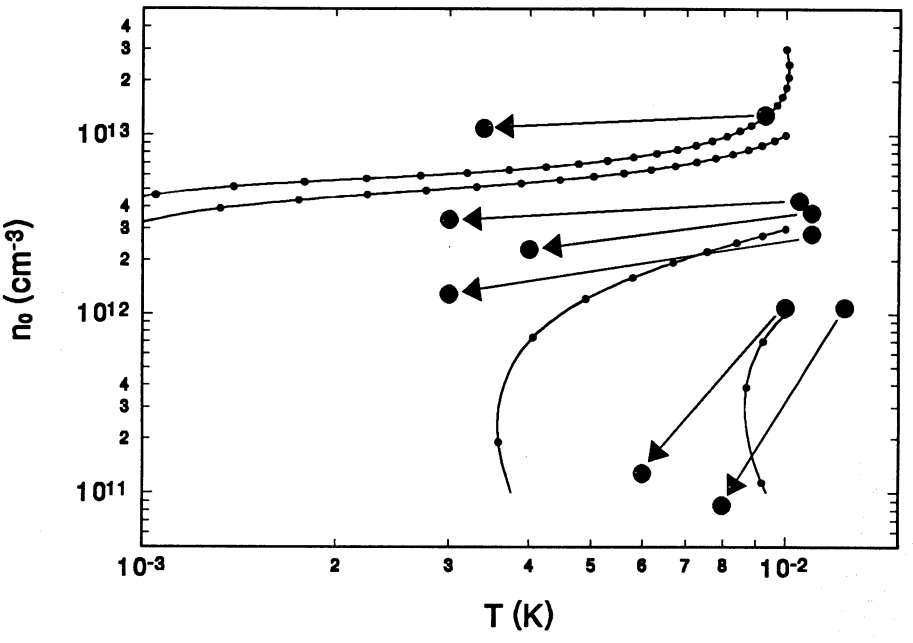

Figure 6.10: Experimental results for a number of LIE cooling cycles, plotted in the T-n_0 plane. The solid lines are the curves of evolution for the particular LIE trapping field, an initial photon flux of $\Phi_0 = 2 \times 10^9\,\mathrm{s}^{-1}$ and for the case of tuning to ω_p.

which can be seen in the cold spectrum where the lines due to excitations from the c state are resolved. The line labelled σ_c^* corresponds to excitation to the $^2P_{3/2,m_J=-3/2}$ state which is forbidden for d-state atoms, but weakly allowed for c-state atoms.

In Fig. 6.10, the initial and final temperatures and densities of a number of LIE experiments are plotted, together with the curves of evolution for the particular LIE trapping field, an initial photon flux of $\Phi_0 = 2 \times 10^9\,\mathrm{s}^{-1}$ and for the case of tuning to ω_p. Due to the presence of c atoms, the total decay rate is slightly increased due to spin exchange. This increased decay is included in the calculation of the evolution. There is a qualitative agreement between the direction of cooling in the LIE experiments and the calculated evolution curves. The observed deviations are probably due to the fact that the laser frequency was not locked to ω_p which particularly in the case of low densities, where $\eta_p < \eta_{opt}$, can give rise to large deviations.

6.7 Discussion

The LIE experiments were in the first place aimed at demonstrating the principle of LIE as a cooling method. Although cooling to temperatures below 1 mK should be possible, according to the calculations, in practice signal-to-noise requirements limited the experiments to $T \simeq 3\,\mathrm{mK}$. With the beam diameter of $\sim 1\,\mathrm{mm}$, at temperatures $T \lesssim 3\,\mathrm{mK}$ and $n_0 \sim 10^{13}\,\mathrm{cm}^{-3}$ the overall absorption is so small that a reliable comparison with calculated spectra cannot be made. Under these conditions, one should use a narrower beam or rely on fluorescence spectroscopy to determine T and n_0. In future experiments, LIE must be performed with an improved control over the beam shape or an increased sensitivity of the fluorescence bolometers.

One of the remarkable results from the calculations of η_{LIE} is that cooling to temperatures below 1 mK can also be obtained starting from a low initial density ($n_0 \sim 10^{12}\,\mathrm{cm}^{-3}$). One should then tune to ω_{opt}. Since there are no simple features in the transmission spectrum from which ω_{opt} can be obtained, one should derive this frequency from a determination of n_0 and T. Therefore, it is desirable in a new experiment to have this information available during the measurements.

Inevitably the question arises whether LIE can be used to cool a trapped gas to temperatures where effects of quantum degeneracy start to play a role. In Sect. 6.4.2, it was shown that at temperatures $T \lesssim E_r/k_B$ the heating due to photon recoil will limit cooling at constant density to $T \simeq 230\,\mu\mathrm{K}$ at $10^{14}\,\mathrm{cm}^{-3}$. The heating due to multiple scattering will raise this cooling limit. The critical temperature at which one enters the quantum degenerate regime at $n = 10^{14}\,\mathrm{cm}^{-3}$ is $T_c = 35\,\mu\mathrm{K}$. The analysis presented in this chapter shows that for the trapping field that was used in the LIE experiments this temperature cannot be reached. Speculating on other methods to approach T_c by LIE, one may point out that the influence of the photon recoil can be reduced by increasing the branching ratio for decay to the low-field-seeking spin state. The σ_2 transition is not suitable for this purpose since the branching ratio to the a state cannot be made large. However, there are two transitions for which the branching ratio for decay to the a state increases with increasing B: the σ_3 and the π_2 transition, of which the σ_3 transition is best suited. Because at low temperatures the sample will be located in a small region around the trap center, where $\vec{B}$ is mainly directed along the z-axis, the σ_3 transition will have a larger transition probability than the π_2 transition (see Sect. 4.4). In Fig. 6.11, we plot the contours of η_{LIE} as a function of T and $\Gamma_{\sigma 3}/\Gamma$ in the limit of no Zeeman broadening. Starting at $T = 200\,\mu\mathrm{K}$, the minimum temperature does indeed decrease with decreasing $\Gamma_{\sigma 3}/\Gamma$. At a certain branching ratio, however, the resonant cross section has decreased so much that the sample starts to become optically thin

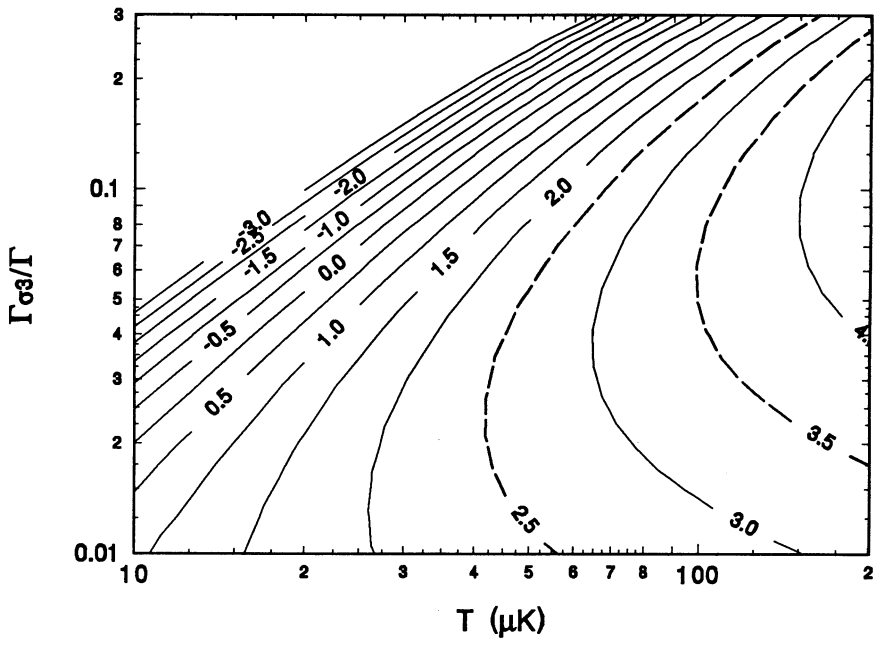

Figure 6.11: Contours of η_{LIE} in the limit of no Zeeman broadening as a function of T and the branching ratio $\Gamma_{\sigma 3}/\Gamma$. The long-dashed lines indicates $\eta_{LIE} = 3.5$ and 2.5. At the latter value the evolution proceeds parallel to the line $T_c(n)$.

again. When this happens, η_{LIE} decreases. For cooling at constant density, the plot shows a minimum temperature of 100 μK at a branching ratio $\Gamma_{\sigma 3}/\Gamma = 0.06$. For the σ_3 transition this corresponds to a field $B = 1.6$ T. The heating due to multiple scattering for this transition is neglegible, since the radiation emitted by atoms decaying to the a state is not resonant with any other transition. The closest resonance is the π_1 transition which, in a field of 1.6 T, is 1.53 GHz = 31γ detuned.

In conclusion, it can be said that decreasing the branching ratio for decay back to the d state can reduce the photon recoil heating, but will simultaneously reduce the resonant cross section. This last mechanism will prevent obtaining temperatures much lower than 100 μK.

References

[1] Harald F. Hess, Phys. Rev. B **34**, 3476 (1986).

[2] T.J. Tommila, Europhys. Lett. **2**, 789 (1986).

[3] H.F. Hess, G.P. Kochanski, J.M. Doyle, N. Masuhara, D. Kleppner, and T.J. Greytak, Phys. Rev. Lett. **59**, 672 (1987).

[4] O.J. Luiten, H.G.C. Werij, I.D. Setija, M.W. Reynolds, T.W. Hijmans, and J.T.M. Walraven, Phys. Rev. Lett. **70**, 544 (1993).

[5] N. Masuhara, J.M. Doyle, J.C. Sandberg, D. Kleppner, T.J. Greytak, H.F. Hess, and G.P. Kochanski, Phys. Rev. Lett. **61**, 935 (1988).

[6] J.M. Doyle, J.C. Sandberg, I.A. Yu, C.L. Cesar, D. Kleppner, and T.J. Greytak, Phys. Rev. Lett. **67**, 603 (1991).

[7] J.M. Doyle, J.C. Sandberg, N. Masuhara, I.A. Yu, D. Kleppner, and T.J. Greytak, J. Opt. Soc. Am. B **6**, 2244 (1989).

[8] O.J. Luiten, Ph. D. thesis, University of Amsterdam (1993).

[9] I.D. Setija, H.G.C. Werij, O.J. Luiten, M.W. Reynolds, T.W. Hijmans, and J.T.M. Walraven, Phys. Rev. Lett. **70**, 2257 (1993).

[10] K.B. Davis, M-O. Mewes, M.A. Joffe, and W. Ketterle, *Evaporative cooling of sodium atoms*, presented on the *Fourteenth International Conference on Atomic Physics*, (1994).

[11] W. Petrich, M.H. Anderson, J.R. Ensher, and E.A. Cornell, *Evaporative cooling of Rubidium atoms in a magnetic trap*, presented on the *Fourteenth International Conference on Atomic Physics*, (1994).

Chapter 7

Decay kinetics of trapped atomic hydrogen

7.1 Introduction

The long lifetimes of the gas enabled a study of the decay kinetics of trapped H↑ for up to 4 hours. By comparing the measured decay rate with calculated values we could find out whether the stability of the gas was indeed limited by spin relaxation as predicted by theory [1, 2] or was influenced by external decay mechanisms. In the experiments of Luiten *et al.* [3, 4] such a study was not possible due to a limited lifetime of the gas, most probably caused by He background gas from the MgF_2 entrance window which was at $T \simeq 0.5\,\mathrm{K}$. Due to a strong reduction of the thermal radiation impinging on the window, the cell temperature reached in the experiments described in this thesis was much lower ($T_w \simeq 80\,\mathrm{mK}$).

Decay processes in trapped H↑ were first studied by Van Roijen *et al.* [5]. In these experiments the decay of the gas was studied by measuring the flux of H↓ produced by decay processes in the trapped gas. The gas was kept at the temperature of the cell surfaces surrounding the trapping region. In the present experiments, Lyman-α spectroscopy was used to perform an *in situ* determination of density and temperature of the gas. This enabled a study of the decay of H↑ at temperatures much lower than the wall temperature $T_w = 80\,\mathrm{mK}$. By forced evaporation we cooled the gas to temperatures at which the Zeeman shift and the Doppler broadening are so small that the lines due to transitions from the c state are resolved. By separately monitoring the density of c and d atoms as a function of time, we were able to compare their decay with the rate constants for spin exchange.

In this section, I will first give the rate equations for a gas of H↑ as a result of spin relaxational decay. The decay of the gas was experimentally studied under

two conditions: over very long periods, of several hours, when we expect the gas to consist of mainly d atoms and the decay to be mainly caused by magnetic dipolar relaxation, and shortly after filling, when the c state decay is caused by spin exchange. Both experiments turn out to indicate that external decay processes play a role. The spin exchange measurements also clearly show that the trapped gas is still in thermal contact with the cell surfaces surrounding the trapping region. Therefore, section 7.2 will be devoted to a discussion of surface-related decay processes. It will be shown that the dominant decay process is the recombination of evaporated d state atoms with adsorbed H$\uparrow$ atoms, produced by dipolar relaxation in the gas. In the experiments of Van Roijen *et al.* [5] and Luiten *et al.* [3] the influence of these high-field-seeking atoms on the trapped gas was neglected. In the present experiments, conditions are achieved for which a surface density of adsorbed H$\uparrow$ atoms is built up sufficiently large to remove a sizable fraction of the evaporated atoms by recombination. Evaporated atoms that have thermalized with the walls (we will call these atoms "tail atoms", a name that will be explained in Sect. 7.3) and desorb before they recombine to the molecular state, can collide with a trapped gas atom which in general will lead to heating. In Section 7.3, I calculate collision rates between tail atoms and trapped atoms using the formalism presented by Luiten [4] to describe evaporative cooling. In the last section I will show that for the conditions of these experiments, the recombination between adsorbed H$\uparrow$ atoms and evaporated d atoms is larger than the collision rate between trapped atoms and tail atoms so that the gas is evaporatively cooled.

7.1.1 Rate equations

The following rate equations describe the decay of a gas of H$\uparrow$ due to spin relaxation [6]. Since in the experiments the temperature of the gas varied neglegibly during decay, we can write the rate equations for the central c and d density as

$$\begin{aligned} \dot{n}_{0c}\frac{V_{1e}}{V_{2e}} &= -\langle G^c_{dd}\rangle n^2_{0d} - \langle G^c_{cd}\rangle n_{0c}n_{0d} - \langle G^c_{cc}\rangle n^2_{0c} \\ \dot{n}_{0d}\frac{V_{1e}}{V_{2e}} &= -\langle G^d_{dd}\rangle n^2_{0d} - \langle G^d_{cd}\rangle n_{0c}n_{0d} - \langle G^d_{cc}\rangle n^2_{0c}, \end{aligned} \tag{7.1}$$

where the angular brackets denote an average over the trap (see Sect. 2.4) and the loss rate constants $G^{h_3}_{h_1h_2}$ are defined by

$$\begin{aligned} G^c_{cc} &\equiv 2G_{cc,aa} + G_{cc,ac} + 2G_{cc,bd} \\ G^d_{cc} &\equiv -G_{cc,bd} \\ G^c_{cd} &\equiv +G_{cd,aa} + G_{cd,ab} + G_{cd,ad} + G_{cd,bd} - G_{cd,cc} + G_{cd,dd} \end{aligned}$$

$$
\begin{aligned}
G^d_{cd} &\equiv +G_{cd,aa} + G_{cd,ab} + G_{cd,ac} + G_{cd,bc} + G_{cd,cc} - G_{cd,dd} \\
G^c_{dd} &\equiv -2G_{dd,cc} - G_{dd,ac} - G_{dd,cd} \\
G^d_{dd} &\equiv +2(G_{dd,aa} + G_{dd,ac} + G_{dd,cc}) + G_{dd,ad} + G_{dd,cd}.
\end{aligned} \tag{7.2}
$$

The event rate constants $G_{h_1h_2,h_3h_4}$ for a thermal gas have been calculated as a function of T and B by Stoof *et al.* [2]. Notice that the above rate constants assume that after a decay in which one H$\downarrow$ and one H$\uparrow$ are produced, the H$\uparrow$ remains trapped. This atom gets an extra energy of $\simeq \mu_B B_0$ from the H$\uparrow$-H$\downarrow$ energy difference. The spin exchange measurements were performed in a trap with $\varepsilon_{tr} < \mu_B B_0$ which means that in every decay channel producing one H$\uparrow$ and one H$\downarrow$, the H$\uparrow$ is also lost from the trap.

7.1.2 Magnetic dipolar decay

A gas of only d state atoms decays due to magnetic dipolar relaxation while a gas of only c state atoms is subject to the much faster spin exchange decay (see Sect. 2.4). To obtain a gas of purely d state atoms, we waited sufficiently long after filling the trap, for the c state atoms to decay away by spin exchange. The change in c fraction, $\hat{c} = n_{0c}/n_{0d}$, can be obtained using Eqs. 7.1

$$
\begin{aligned}
\frac{d\hat{c}}{dt} &= \frac{\dot{n}_{0c}}{n_{0d}} - \hat{c}\frac{\dot{n}_{0d}}{n_{0d}} \\
&= -\frac{V_{2e}}{V_{1e}} n_{0d} \left[\langle G^c_{dd} \rangle + \left(\langle G^c_{cd} \rangle - \langle G^d_{dd} \rangle \right) \hat{c} + \left(\langle G^c_{cc} \rangle - \langle G^d_{cd} \rangle \right) \hat{c}^2 - \langle G^d_{cc} \rangle \hat{c}^3 \right].
\end{aligned} \tag{7.3}
$$

There will always be a residual, steady-state c fraction $\hat{c}_0$ due to the production of c states by magnetic dipolar decay. It can be calculated by taking $d\hat{c}/dt = 0$. For a gas in the "long trap" at a typical temperature $T = 50\,\mathrm{mK}$, this gives $\hat{c}_0 \simeq 3\,\%$. The c state decay time can be calculated by solving Eq. 7.3 with only the term containing $\langle G^c_{cc} \rangle$, the other terms being much smaller. If we neglect the variation in n_{0d} during the c state decay, we obtain $\hat{c}(t) \simeq [1 + (V_{2e}/V_{1e}) n_{0d} \langle G^c_{cc} \rangle t]^{-1}$, where we have taken $\hat{c}(t = 0) = 1$ immediately after filling. Using $\langle G^c_{cc} \rangle = 1.08 \times 10^{13}\,\mathrm{cm^{-3}s^{-1}}$ at $T = 50\,\mathrm{mK}$ (see Sect. 2.4) and $n_{0d} \simeq 5 \times 10^{12}\,\mathrm{cm^{-3}}$ after filling, we obtain that $\hat{c} = 0.1$ after 72 s.

The magnetic dipolar decay measurements were performed in the "long trap" (see Sect. 2.2). After filling the trap to $n_0 \sim 5 \times 10^{12}\,\mathrm{cm^{-3}}$, we waited for 11 minutes to let the c atoms decay away by spin exchange. We then scanned the π_1 and σ_1 lines every 15 minutes for almost 3 hours. The recorded spectra were then compared with calculated spectra to give the density and temperature as a function of time. Since at the observed temperature $T = 50(12)\,\mathrm{mK}$ we were not able to discern between

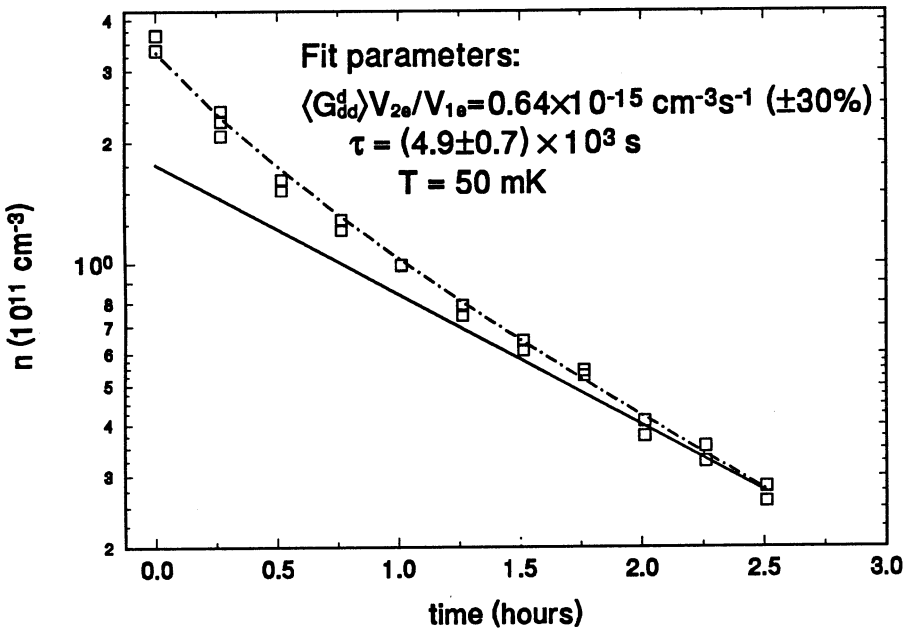

Figure 7.1: Monitoring the density during a long dipolar decay run. Spectra were fitted at a constant temperature of 50 mK. The solid line indicates the exponential tail with a decay time $\tau = (4.9 \pm 0.7) \times 10^3$ s. The dash-dotted line includes a second-order process to fit the initial decay. The second-order rate constant agrees within 30 % with the theoretical value for magnetic dipolar relaxation.

the c and d state atoms, we measured the total density $n_0(t) = n_{0c}(t) + n_{0d}(t)$. The decay of the total density is given by

$$\dot{n}_0 = -\alpha_c \Big(\langle G^c_{dd} \rangle + \langle G^d_{dd} \rangle \Big) \frac{V_{2e}}{V_{1e}} n_0^2, \tag{7.4}$$

where α_c is a correction factor due to the c state density

$$\alpha_c = \frac{1}{(1+\hat{c})^2} \left[1 + \frac{\langle G^c_{cd} \rangle + \langle G^d_{cd} \rangle}{\langle G^c_{dd} \rangle + \langle G^d_{dd} \rangle} \hat{c} + \frac{\langle G^c_{cc} \rangle + \langle G^d_{cc} \rangle}{\langle G^c_{dd} \rangle + \langle G^d_{dd} \rangle} \hat{c}^2 \right]. \tag{7.5}$$

For $\hat{c}_0 = 0.03$, $\alpha_c = 0.99$. For the "long trap" and $T = 50$ mK the averaged decay rate $\alpha_c(\langle G^c_{dd} \rangle + \langle G^d_{dd} \rangle) V_{2e}/V_{1e} = 0.64 \times 10^{-15}\,\mathrm{cm^3 s^{-1}}$, using the theory of Stoof *et al.*, which will be compared to the value from the experiment. In Fig. 7.1 we plot the central density as a function of time during one of the long dipolar decay measurements.

This experiment shows a number of interesting phenomena. In the first place, the gas is, indeed, stable over long periods of time. Secondly, after filling the trap, the gas

cools to a temperature $T_g \simeq 50\,\mathrm{mK}$, significantly lower than the wall temperature $T_w = 80\,\mathrm{mK}$, and stays at that temperature for the rest of the experiment and thirdly, the data clearly show that the decay is dominated by a first-order decay mechanism. In the analysis of the data, the exponential tail is fitted with a decay time of $\tau = 1.4 \pm 0.2\,\mathrm{hours}$. The second-order decay can only be observed in the beginning of the measurement. The measured second-order decay rate agrees within 30 % with the theoretical value for magnetic dipolar relaxation.

The second point is surprising if we realize that during filling the gas thermalizes with the walls and that no intentional attempt was undertaken to evaporatively cool the gas (optical cooling has not taken place since the gas was not irradiated). By some mechanism energetic atoms are removed. In the following sections, I will show that the gas is evaporatively cooled by recombination of the energetic atoms from the trapped gas with high-field-seeking atoms adsorbed on the He film covering the surfaces surrounding the trapping region. The evaporation causes an extra loss of atoms. Since the temperature is constant, we can use Eq. 2.46 to obtain the evaporative flux $\dot{N}_{ev} = 0.079\dot{N}_{dip}$. This extra second-order loss mechanism is too small to be resolved in the experiments.

The third point is still unresolved. Indications for a first-order decay with a decay time of approximately an hour were also found in the Doppler cooling experiments (see Sect. 5.8). The most obvious reason for a first-order decay would be a background gas of He atoms. In this scenario energetic He atoms collide with the trapped H atoms, giving them enough energy to reach the cell walls where they recombine with the adsorbed H$\downarrow$ atoms. At the moment, it is not clear what could be the cause of a He background gas. In the experiment, there are two sources of a flux of He atoms. The first is the bolometer which is placed in the high-field region near the dissociator. By burning the He film of this bolometer, a site for efficient recombination is created which will destroy the high-field-seeking atoms. The high-field bolometer does not directly look out onto the trapped gas. Since a He atom has to collide minimally 3-4 times with the walls before it has reached the cell and the sticking probability for a He atom on a He film is almost unity, the fraction of He atoms that reaches the cell will be neglegibly small. The cell bolometer, used in the evaporative cooling experiments of Luiten *et al.*, was not used in these experiments. A second possible source for fluxing He atoms is the MgF_2 window at the bottom of the cell. The heat load due to room temperature radiation falling directly on the MgF_2 window is $\simeq 6\,\mu\mathrm{W}$. Assuming that this power is completely absorbed in the MgF_2 window and that the local temperature rise is determined by the thermal impedance of the window to the edge that is clamped in the window holder, this will result in a small spot on the MgF_2 window with a locally increased temperature

$T \simeq 240\,\mathrm{mK}$. This will result in a flux of He atoms [7]

$$\Phi = \frac{A}{4\pi^2}\frac{m_{He}}{\hbar^3}k_B^2 T^2 \exp(-L_{He}/k_B T) \simeq 2 \times 10^9\,\mathrm{s}^{-1}, \tag{7.6}$$

where the latent heat per He atom, $L_{He}/k_B = 7.16\,\mathrm{K}$ is assumed temperature independent. This flux too small to explain the observed decay rate. Taking a typical value for the ^{4}He-H scattering cross section $\sigma_4 = 5\,\mathrm{\AA}^2$ [4], a flux of $\Phi \simeq 10^{14}\,\mathrm{s}^{-1}$ would be needed to explain the observed decay time.

The measurement of the magnetic dipolar relaxation could be improved by monitoring the decay at higher densities where the second-order decay is dominant. Since at the high densities, shortly after filling the trap, the decay of gas is still dominated by spin exchange and evaporative cooling, it is difficult to perform a clean measurement of the dipolar decay rate. A possible solution would be to wait after filling for the c atoms to decay away and for the gas to cool to a sufficiently low temperature that thermal contact with the wall is neglegibly small. By Doppler cooling, the temperature of the gas is then lowered and the density is increased to values where the second-order decay is dominant. In the experiments described in this thesis no attempts were undertaken to measure the magnetic dipolar decay in this way.

7.1.3 Spin exchange relaxation

Using L_α spectroscopy, we have been able to measure the c and d state density separately and study the decay due to spin exchange in magnetic traps. For fields $B \geq 0.1\,\mathrm{T}$, the transition frequencies from the c state and the five corresponding allowed transitions from the d state differ by $\simeq 0.6\,\mathrm{GHz}$. At high temperatures this difference is blurred by the Zeeman and Doppler broadening. By cooling the gas to $T \lesssim 10\,\mathrm{mK}$, we could resolve the c lines and monitor the evolution of the c state density n_{0c} in time.

Spin exchange is a decay process that rapidly depletes the c state after filling the trap. In Sect. 2.4, it was shown that for a gas in the "long trap" at 50 mK this depletion takes place approximately 40 times faster than the decay of the d state due to dipolar relaxation. For the experimental range of magnetic fields and temperatures, the rate equations, Eq. 7.1, can be well approximated by

$$\begin{aligned} \dot{n}_{0c}\frac{V_{1e}}{V_{2e}} &\simeq -\langle G^c_{cc}\rangle n^2_{0c} - \langle G^c_{cd}\rangle n_{0c} n_{0d} \\ \dot{n}_{0d}\frac{V_{1e}}{V_{2e}} &\simeq -\langle G^d_{dd}\rangle n^2_{0d} - \langle G^d_{cd}\rangle n_{0c} n_{0d}. \end{aligned} \tag{7.7}$$

For the "long trap" and the trap used in the spin exchange measurement discussed in this section, Eqs. 7.7 can be further simplified. Since $n_{0c} < n_{0d}$ and $\langle G^c_{cd}\rangle, \langle G^d_{cd}\rangle <$

$\langle G^d_{dd}\rangle \ll \langle G^c_{cc}\rangle$, the cross terms have a very small effect on the c and d decay. In the analysis of the data, these terms will therefore be neglected. In this approximation, the c fraction will approach a limiting value $\hat{c}_{se} = \langle G^d_{dd}\rangle / \langle G^c_{cc}\rangle$. This limiting value, of course, only holds as long as n_{0c} has not decreased so much that cd dipolar decay becomes comparable to the cc spin exchange decay.

To obtain a cold gas immediately after loading the trap, we used forced evaporative cooling and relied on the same wall-induced evaporative cooling mechanism as in the dipolar decay measurements to precool the gas to $T \simeq 10\,\mathrm{mK}$. Neither Doppler cooling nor LIE could cool the gas rapidly enough to have sufficient c state density left after precooling. The traps that were used in the spin exchange measurements had a trap depth $\varepsilon_{tr} < \mu_B B_0$ to let the energetic H$\uparrow$ atoms, resulting from relaxation recoil, escape from the trap. This extra loss mechanism changes the loss rate constants to

$$\begin{aligned} G^c_{cc} &\equiv 2G_{cc,aa} + 2G_{cc,ac} + 2G_{cc,bd} \\ G^d_{dd} &\equiv 2(G_{dd,aa} + G_{dd,ac} + G_{dd,cc}) + 2G_{dd,ad} + G_{dd,cd}. \end{aligned} \tag{7.8}$$

The equilibrium temperature T_{min} is determined by a balance between the evaporative cooling rate $\dot{E}_{ev}$ and the relaxational heating rate $(\gamma_{2e} + \frac{3}{2})\dot{N}_{rel}$, where $\dot{N}_{rel} = (\dot{n}_{0c} + \dot{n}_{0d})V_{1e}$. By substituting $\dot{N}_{rel}$ for $\dot{N}_{dip}$ in Eq. 2.47, T_{min} can be calculated. Since spin exchange is a more rapid process than magnetic dipolar decay, the intrinsic heating of the gas will decrease after loading the trap with decreasing c fraction.

Experimental procedure. The spin exchange experiments were performed for a number of traps differing in the value for B_0 to determine the magnetic field dependence of the spin exchange rate constants. All traps had a trap depth $\varepsilon_{tr} < \mu_B B_0$. Loading of the trap was done in two different ways: immediately loading of the trap with ε_{tr} (procedure I) or loading of a deeper trap and shortly afterwards lowering the trap barrier to ε_{tr} (procedure II). After precooling we scanned the π_1 and the σ_1 line every 15 s during 5 minutes. As an example, we plot in Fig. 7.2 the evolution of n_{0c} and n_{0d} as a function of time for the trap with $B_0 = 0.28\,\mathrm{T}$ after loading with procedure II. For the particular trap configuration used in this experiment, we can calculate the theoretical rate constants $\langle G^c_{cc}\rangle V_{2e}/V_{1e} = 1.72 \times 10^{-14}\,\mathrm{cm^3 s^{-1}}$ and $\langle G^d_{dd}\rangle V_{2e}/V_{1e} = 1.44 \times 10^{-15}\,\mathrm{cm^3 s^{-1}}$. With these values we can calculate the equilibrium temperature T_{min} to be expected in this trap. For $\hat{c} = 1$, we then obtain $T_{min} = 6.4\,\mathrm{mK}$, decreasing to $T_{min} = 5.5\,\mathrm{mK}$ for a c fraction $\hat{c} = 0.1$. This is significantly lower than the temperature from the data $T = 12 \pm 3\,\mathrm{mK}$. The rate constants found from the fit to the data are approximately a factor 2 and 3.5 larger than the theoretical values for $\langle G^c_{cc}\rangle$ and $\langle G^d_{dd}\rangle$ respectively. Towards the end

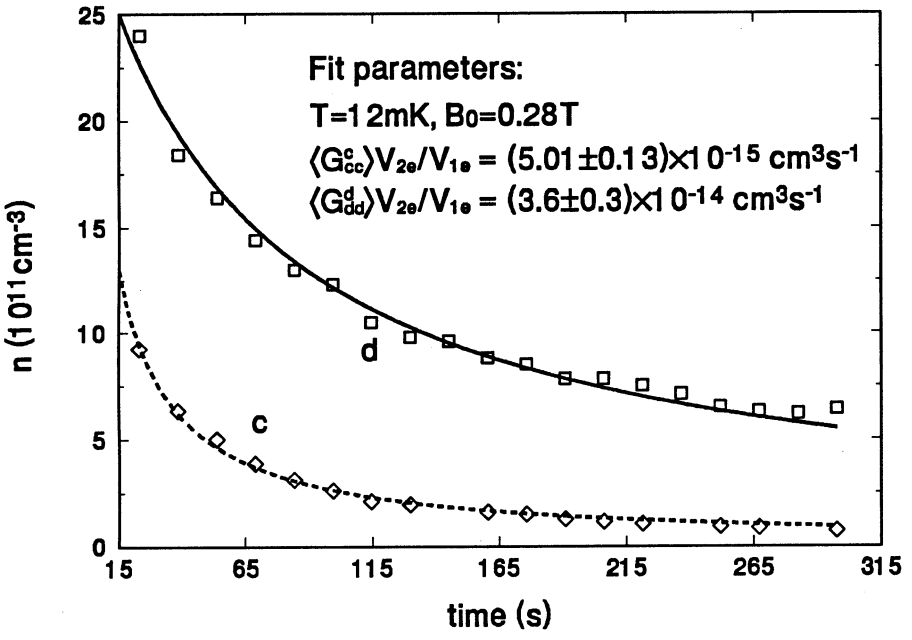

Figure 7.2: Decay of a gas of c and d atoms as a result of spin exchange and dipolar decay. The trap used in this experiment had $B_0 = 0.28\,\mathrm{T}$ and the trap depth at 57 mK. The temperature of the gas was $12 \pm 3\,\mathrm{mK}$.

of the experiment $\hat{c} \simeq 0.11$, close the value determined by the experimental rate constants: $\hat{c}_{se} \simeq 0.14$.

At the observed temperature, $\eta_{ev} = \varepsilon_{tr}/k_B \simeq 5.2$ which means the evaporation rate is large. Using Eq. 2.34, we can calculate that $\dot{N}_{ev}/\dot{N}_{rel} \simeq 10$ for $\hat{c} = 0.2$ as in the experiment. This loss rate is much larger than the observed loss rate. For reasons that are not yet understood, the gas is at a temperature substantially higher than T_{min} and the loss rate is substantially lower than the evaporation rate at that temperature. Speculating on a possible explanation, it may be that the wall-induced evaporative cooling mechanism is not working properly. Not every energetic c or d state atom that reaches the wall will recombine and will, therefore, return to the trapped gas with a much higher energy. This process results in a gain of atoms and internal energy. The experiments in the same trap using loading procedure I gave qualitatively very different spectra. The π_1 and σ_1 line were broader and the c state decay took place more slowly. These results are not yet understood.

Spin exchange measurements have been performed in a number of different trap configurations. The measured decays cannot be explained in terms of a spin relaxational decay. Since in all measurements the gas is still in weak thermal contact

with the walls, surface-related decay processes must play a role. Under these conditions, it is difficult to perform a clean measurement of spin exchange decay. Waiting for the evaporative cooling to have decreased to a value smaller than the intrinsic decay rates, unfortunately also reduces the c density to values which are very hard to resolve experimentally.

A study of the decay kinetics of trapped H$\uparrow$ has shown that external decay processes influence the stability of the gas and the decay shortly after filling. The most obvious origin for an enhanced decay would be recombination or relaxation on the walls surrounding the gas sample. Surface recombination would explain the initial cooling when the gas is still in contact with the walls. When recombination on the walls is not sufficient to let all the evaporating atoms recombine, these atoms will thermalize with the wall, desorb and heat the trapped gas causing a higher gas temperature then expected on the grounds of evaporative cooling alone. Nuclear spin flip relaxation by magnetic impurities in the substrate changes d to c states. If this happens faster than the desorption rate, it can influence the observed spin exchange decay rates. In the next sections we will concentrate on these wall-induced decay channels and investigate the interaction between wall atoms and gas atoms.

7.2 Wall-induced recombination and relaxation

The surface density, σ, of adsorbed atoms in thermal equilibrium with the trapped gas, is given by the adsorption isotherm:

$$\sigma = n_g(B_w)\lambda_{th}\exp(\varepsilon_a/k_BT), \tag{7.9}$$

where $\lambda_{th} = \sqrt{2\pi\hbar^2/mk_BT}$ is the thermal de Broglie wavelength, $n_g(B_w)$ is the volume density of gas atoms just above the surface and $\varepsilon_a/k_B = 1.011(10)\,\mathrm{K}$ [8] is the binding energy of a hydrogen atom on the surface of liquid helium. In case the surface coincides with an equipotential surface of the magnetic field (which is the case for the "long trap") $n_g(B_w) = n_0\exp(-\varepsilon_{tr}/k_BT)$, where $\varepsilon_{tr} = \mu_B(B_w - B_0)$. The average time an adsorbed atom spends on the surface, the surface residency time τ_{res}, in thermal equilibrium is determined by the balance between the adsorption rate $\frac{1}{4}n_g(B_w)\bar{v}A\,s$, where s is the sticking probability on a He film, and the desorption rate $\sigma A\tau_{res}^{-1}$, giving

$$\tau_{res} = \frac{2\pi\hbar}{s(T)k_BT}\exp(\varepsilon_a/k_BT). \tag{7.10}$$

The residency time is strongly dependent on the temperature of the He film, e.g. for $T = 200\,\mathrm{mK}$, $\tau_{res} = 5.4\times10^{-7}\,\mathrm{s}$, while for $T = 80\,\mathrm{mK}$, $\tau_{res} = 6\,\mathrm{ms}$. A longer residency time makes the adsorbed atoms much more susceptible to decay mechanisms on the

wall. In the limit that $\tau_{res} \gg \tau_{rec}$, the decay time due to surface recombination, the walls will act as a sorption pump.

The sticking probability of H on He has been measured between 100 μK and 1 mK and qualitatively studied between 1 mK and 20 mK by Doyle *et al.* [9]. To evaluate the residency times for our experimental conditions, we used the relation: $s(T) = 0.33\,T$, for the sticking probability of H on pure ^{4}He films as measured by Berkhout *et al.* [10]. This relation has been experimentally established for $145 < T < 526$ mK and down to 73 mK for ^{3}He/^{4}He films. Within experimental error, however, no difference was observed after the addition of ^{3}He and we will use this relation also for the pure ^{4}He case.

7.2.1 Recombination between H↑ states

Two d atoms can not recombine due to their parallel spin states. For recombination to take place, at least one of the atoms has to have its spin state changed. We will discuss a mechanism for nuclear spin flip relaxation, induced by magnetic impurities in the substrate, in a later section, but will for the time being just denote the corresponding relaxation rate constant by G^s_{icd} so that the rate equations on the surface become

$$\dot{\sigma}_c = -2K^s_{cc}\sigma_c^2 - K^s_{cd}\sigma_c\sigma_d - G^s_{icd}(\sigma_c - \sigma_d) + \tfrac{1}{4}n_c\bar{v}s - \sigma_c/\tau_{res} \qquad (7.11)$$

$$\dot{\sigma}_d = -K^s_{cd}\sigma_c\sigma_d + G^s_{icd}(\sigma_c - \sigma_d) + \tfrac{1}{4}n_d\bar{v}s - \sigma_d/\tau_{res}. \qquad (7.12)$$

The K^s_{cd} and K^s_{cc} are two-body surface recombination rate constants. In the limit that the recombination and the relaxation rates are much smaller than the desorption rate σ/τ_{res}, the desorption rate and the adsorption rate $\frac{1}{4}n\bar{v}s$ will be equal and cancel. When the $c \leftrightarrow d$ impurity relaxation rate is much higher than the recombination rate, the c and d states will be in thermal equilibrium with each other. For $k_BT \gg (E_d - E_c)$ ($T \gg 29$ mK for $B \geq 0.1$ T) the rate equations then sum up to

$$\dot{\sigma} = -K^s\sigma^2, \qquad (7.13)$$

where $K^s = \frac{1}{2}(K^s_{cc} + K^s_{cd})$ and $\sigma_d = \sigma_c = \frac{1}{2}\sigma$.

There have never been direct measurements of K^s_{cc} and K^s_{cd}, but due to the symmetry in the spin states, the numerical values will not differ from the values for the aa and ab recombination rate constants [11]. We therefore take

$$K^s_{cc}B^2T^{-1/2} = 7.5 \times 10^{-8}\,\mathrm{cm^2s^{-1}T^2K^{-1/2}} \qquad (7.14)$$

$$K^s_{cd}B^2T^{-1/2} = 2.5 \times 10^{-8}\,\mathrm{cm^2s^{-1}T^2K^{-1/2}}. \qquad (7.15)$$

This gives $K^s = 0.8 \times 10^{-8}\,\mathrm{cm^2s^{-1}}$ for the recombination rate constant on the wall where $B = 1.33$ T and $T = 80$ mK.

7.2.2 Relaxational processes on the wall

Intrinsic relaxation processes in the adsorbed state are very weak. Spin exchange rates for hydrogen atoms in the adsorbed state have been calculated by Morrow and Berlinsky [12] for the case of zero magnetic field. The magnetic field dependence is discussed in Ref. [13]. The rate constants are much smaller than the corresponding recombination rate constants. Just like in the case of a bulk gas, spin exchange mainly influences the population of c states. Since the adsorbing atoms are in the d state, this relaxation mechanism cannot explain the presence of c atoms.

Magnetic dipolar relaxation on the surface can change the hyperfine state of two d atoms. This proces has been observed experimentally [14] and studied theoretically [15, 16] for a and b states. Most experimental observations were dominated by three-body surface recombination except for very low surface densities. The rate constant for the proces $aa \rightarrow ab$ is very small and strongly dependent on the angle between the magnetic field and the surface normal. Due to the symmetry in spin states, these results can also be applied to an adsorbed gas of c and d atoms. To get an order of magnitude for this rate constant, we will use a theoretical value for the surface dipolar relaxation constant, averaged over the surface roughness [16]. For a wall temperature of 80 mK and a field of 1.3 T as in this experiment: $G^s_{cd}(\mathrm{dip}) \simeq 10^{-12}\,\mathrm{cm^2 s^{-1}}$. Rate constants for electronic dipolar relaxation are an order of magnitude smaller. For the surface densities of d atoms in this experiment, this relaxation channel and three-body surface recombination can be neglected.

Nuclear spin flip relaxation, attributed to magnetic impurities in the substrate, was the bottleneck for obtaining a gas of H$\downarrow\downarrow$ in the first experiments with atomic hydrogen. In these experiments, it can constitute an important relaxation channel for an adsorbed gas of doubly-polarized atoms, depending on the impurity concentration of the substrate. Although the copper parts of the experimental cell have been carefully etched to remove iron parts left behind by machining, the cell contains a number of objects of which the magnetic content is unknown (fluorescence detection bolometers) or known to be substantial (UV diode). The housing of the UV diode is therefore covered with a layer of epoxy to keep the magnetic impurities at a distance.

Impurity relaxation has been theoretically [17] and experimentally [18] studied for spin-down-polarized gases. In the model by Berlinsky *et al.* an adsorbed atom moves as a free particle over the He surface with a velocity $\vec{v}$. Due to this motion it experiences a fluctuating magnetic field originating from the magnetic impurities in the substrate. Writing this field as a sum of Fourier components with wave vector $\vec{q}$ in the plane of the surface, the frequency of the fluctuating field experienced by the atom is $\omega = \vec{q} \cdot \vec{v}$. When this frequency is close to a hyperfine transition the field

can induce a change in spin state.

This model can also be used to calculate the impurity relaxation rate constant for an adsorbed gas of d atoms. It gives a first-order surface relaxation rate constant of

$$G^s_{icd} = 40nX\,\mathrm{s}^{-1}. \tag{7.16}$$

This equation contains all the experimental parameters of the experiment. A cylinder with $A/V = 3.1\,\mathrm{cm}^{-1}$ was used to characterize the size and shape of the substrate, the magnetic inhomogeneity of the copper substrate is given by the fraction X of iron atoms in the substrate in the form of 75 Å clusters containing n iron atoms (in the experiments of Statt *et al.* OFHC copper was used with $X = 0.1\,\%$ and $nX = 18.8$), the magnetic field dependence is contained in the transition dipole moment and in the frequency of the c-d transition, the temperature $T_w = 80\,\mathrm{mK}$ and the adsorbed atom is located a distance $d = 90$ Å above the substrate (the thickness of the He film at the height of the sample above the bulk He).

As mentioned, the impurity concentration is not known in these experiments. The impurity concentration of the copper is $\sim 10\,\mathrm{ppm}$ but the bolometers and the UV diode probably have an impurity concentration higher than 0.1 %. Electronic spin flip rates ($d \rightarrow a$) can also be calculated with this model, but give neglegible relaxation rate constants due to the large energy difference between the a and d hyperfine states. For the following discussion of surface recombination, it turns out that the presence of adsorbed c state atoms is irrelevant. We will, therefore, assume that the nuclear spin flip relaxation is neglegible and that the adsorbed H↑ atoms are d state atoms.

7.2.3 High-field-seeking atoms on the wall

Although impurity relaxation will not spin flip H↑ to H↓ on the wall, H↓ atoms are present as they are constantly produced by decay processes in the trapped gas. The strongest dipolar decay channels for a gas of d atoms produce a flux of a atoms which, by the strong radial field gradient, will immediately be pulled towards the wall. In Fig. 7.3, we plot the potential as experienced by the a atoms. Once created by decay at the top of the potential hill, the a atoms are pulled towards the walls. From Fig. 7.3, we see that for the "long trap" the magnitude of the magnetic field on the wall at the axial position of the trapped gas is almost constant, which means that the adsorbed atoms will move freely until they reach the ends of the cell where, at the top end, they will collect near the UV diode or, at the bottom end, will be pulled towards the high-field region where they will recombine on the trigger bolometer. The surface density of a atoms will be determined by the diffusion coefficient in the

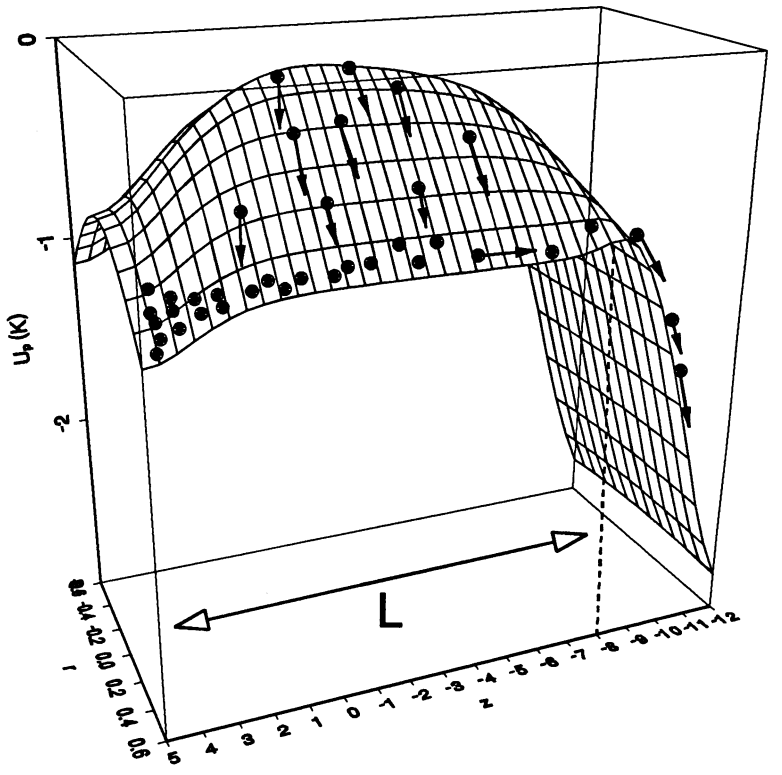

Figure 7.3: Potential energy as experienced by the a state atoms in the "long trap". By the radial field gradient they are pulled towards the walls where they collect and drift towards the high-field region.

adsorbed state and the recombination rate with adsorbed d state atoms. Because of the large electron-spin-down component of the a state, the a-d recombination rate constant for the conditions of the experiment is $\sim 10^3$ times larger than the rate constant between H$\uparrow$ atoms. The rate constants for recombination between adsorbed atoms in different hyperfine states with opposite electron spin are approximately the same. Therefore, we will not distinguish between the separate hyperfine states and we will use the rate constant

$$K_{ad}^{s} T^{-1/2} = 3.9 \times 10^{-5}\,\mathrm{cm^2 s^{-1} K^{-1/2}}, \tag{7.17}$$

which is equal to the value of K_{bc}^{s} as measured by Mertig *et al.* [19].

Diffusion by hopping of a state atoms. The a atoms will also desorb from the He film, but will then immediately experience the large radial field gradient, pulling them back with an acceleration $g = \mu_B(\partial B/\partial r)/m = 1.2 \times 10^6\,\mathrm{m\,s^{-2}}$. For atoms leaving the wall with a cosine distribution, the mean free path due to hopping is

$\lambda_{hop} = \pi k_B T/mg$, taking an average time of $\tau_{hop} = 1/g\sqrt{2\pi k_B T/m}$, which for a wall temperature of 80 mK is 1.7 mm in 5.2×10^{-5} s. This gives an average velocity parallel to the surface of $\bar{v}_s = \sqrt{\pi k_B T/2m}$, equal to the average velocity of an adsorbed atom moving freely over the surface. A desorbed atom makes on the average $1/s$ bounces, where s is the sticking probability of H on a He film. The He film has a thickness of $\simeq$ 90 Å which is not thick enough to smoothen out the surface irregularities. Due to the surface roughness, the atom will not only leave the surface in a random direction after desorption but also after an elastic collision. In this model, the motion of the atom, as it is bouncing over the surface, will therefore be described by a random walk with a diffusion constant $D_{hop} = \frac{1}{2}\bar{v}_s\lambda_{hop}$. For $T_w = 80\,\mathrm{mK}$, $D_{hop} = 2.7\times10^2\,\mathrm{cm^2s^{-1}}$.

Diffusion of adsorbed a state atoms. When the atom is adsorbed on the He film, it moves essentially free-particle-like. It interacts with the elementary excitations of the He film, the ripplons or quantized capillary waves, through a number of processes: emission and absorption of ripplons, scattering by thermal ripplons and second-order processes involving virtual transitions to an unbound state. Zimmerman and Berlinsky [20] calculated the relaxation time for these different processes and found the first one to be the dominant process for momentum relaxation of adsorbed H. For a temperature $T_w = 80\,\mathrm{mK}$, the relaxation time $\langle\tau\rangle = 6.1\times10^{-8}\,\mathrm{s}$, giving a mean free path of $\lambda_a = \bar{v}_s\langle\tau\rangle = 2\times10^{-6}\,\mathrm{m}$. Since this is much longer than the thermal de Broglie wavelength at this temperature ($\lambda_{th} = 62$ Å) the motion of the adsorbed atom is free-particle-like. The reason for these long mean free paths is that at low temperatures the long-wavelength ripplons are ineffective at scattering the adsorbed atoms. They will merely cause a slow shift of the level of the He surface which results in an adiabatic change of the wave function. The diffusion coefficient for the adsorbed atoms is $D_{ads} = \frac{1}{2}\bar{v}_s\lambda_a$. For a temperature $T_w = 80\,\mathrm{mK}$, $D_{ads} = 0.32\,\mathrm{cm^2s^{-1}}$.

Diffusion of the a atoms along the surface thus takes place in these two modes: by hopping diffusion and by diffusion in the adsorbed state. In Fig. 7.4, these two diffusion modes are illustrated. The density of hopping atoms is related to the density of adsorbed atoms by the adsorption isotherm under the conditions that the adsorption rate per atom is larger than the loss rate due to diffusion out of the constant field region or due to recombination. At 80 mK, the diffusion time $\tau_{diff} \simeq ((\pi/2L)^2 D_{hop})^{-1} \simeq 250\,\mathrm{ms}$ (L is the length of the constant-field region, see Fig. 7.3) and is much longer than the thermalization time $\tau_{hop}/s \simeq 2\,\mathrm{ms}$. The recombination time is determined by the surface density of d atoms and will be discussed later. The ratio κ of the density of hopping atoms to the density of

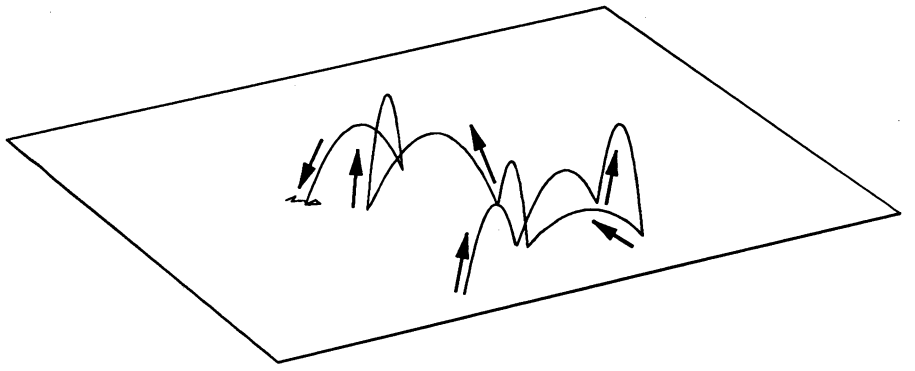

Figure 7.4: Hopping diffusion of an a atom followed by diffusion in the adsorbed state.

adsorbed atoms is then given by the ratio of the residency times in both states

$$\kappa = \frac{\sigma_{hop}}{\sigma_a} = \frac{\tau_{hop}/s}{\tau_{res}} = \frac{k_B T}{mg\lambda_{th}} \exp(-\varepsilon_a/k_B T). \tag{7.18}$$

Notice that κ has an exponential temperature dependence. For $T = 87\,\mathrm{mK}$, $\kappa = 1$. For lower temperatures, diffusion will predominantly take place in the adsorbed mode. For higher temperatures, the dominant diffusion mode will be the hopping mode. For our experimental conditions, $T = 80\,\mathrm{mK}$ and $\kappa = 0.33$.

The density of a atoms is determined by the following set of equations

$$\begin{aligned} \frac{\partial \sigma_a}{\partial t} &= D_{ads}\frac{\partial^2 \sigma_a}{\partial z^2} - \frac{\sigma_a}{\tau_{res}} + \frac{\sigma_{hop}}{\tau_{hop}} s + I_a - K^s_{ad}\sigma_a\sigma_d - K^s_{aa}\sigma_a^2 \\ \frac{\partial \sigma_{hop}}{\partial t} &= D_{hop}\frac{\partial^2 \sigma_{hop}}{\partial z^2} + \frac{\sigma_a}{\tau_{res}} - \frac{\sigma_{hop}}{\tau_{hop}} s. \end{aligned} \tag{7.19}$$

Due to the cylindrical symmetry of the surface the density is only z dependent. In Eq. 7.19, I_a is the flux of a atoms per unit surface area reaching the walls due to decay of the trapped gas. Because of the strong radial acceleration of the a atoms, the atoms will reach the wall at almost the same axial position where they were produced. Therefore I_a will be an image of the axial relaxation rate distribution. For computational purposes we will assume the following approximate expression for I_a

$$I_a = \frac{\dot{N}_a}{2\pi R L_a} \exp(-\pi z^2/L_a^2), \tag{7.20}$$

where $\dot{N}_a$ is the total flux of a atoms due to relaxation in the trap ($\dot{N}_{dip}$ in Sect. 2.4), $R = 0.65\,\mathrm{cm}$ is the radial distance from the trap center to the surface, $L_a = \sqrt{\pi k_B T/2\mu_B \beta}$ is the characteristic length of the relaxation rate distribution and z is measured with respect to the axial position of the trap center. In steady-state,

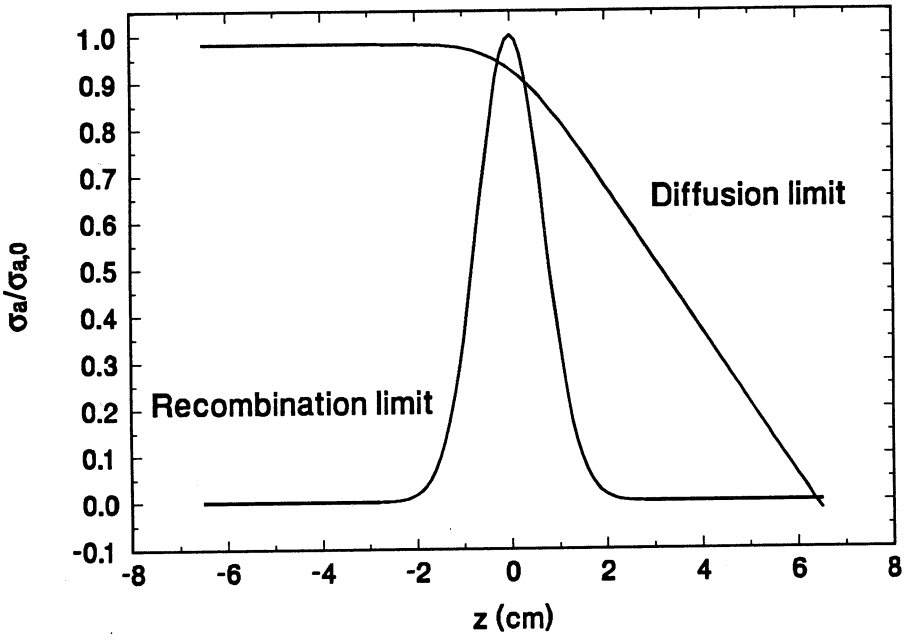

Figure 7.5: Normalized surface density $\sigma_a/\sigma_{a,0}$ for the diffusion limit and the recombination limit; $\sigma_{a,0}$ for both limits is defined in the text. For this plot we have taken for the diffusion limit $T_g = 50\,\mathrm{mK}$ and $T_g = 90\,\mathrm{mK}$ for the recombination limit.

Eqs. 7.19 can be summed up to

$$D_{hop}\kappa\frac{\partial^2\sigma_a}{\partial z^2} + I_a - K^s_{ad}\sigma_a\sigma_d = 0, \tag{7.21}$$

where we have neglected the diffusion due to adsorbed atoms and the aa recombination rate with respect to the ad recombination rate. In Fig. 7.5, σ_a is plotted for two limits: the diffusion limit when σ_a is mainly determined by the diffusive motion of the atoms, so

$$K^s_{ad}\sigma_a\sigma_d \ll I_a = -D_{hop}\kappa\frac{\partial^2\sigma_a}{\partial z^2}, \tag{7.22}$$

and the recombination limit, when σ_a is mainly determined by the recombination with d atoms,

$$D_{hop}\kappa\frac{\partial^2\sigma_a}{\partial z^2} \ll I_a = K^s_{ad}\sigma_a\sigma_d. \tag{7.23}$$

In the recombination limit, either σ_d is very large or the diffusion of hopping a atoms is very small. The latter condition is achieved by a small gradient in σ_a or a wall temperature $T_w \ll 87\,\mathrm{mK}$ when most atoms are in the adsorbed state. For the calculated surface density profiles in Fig. 7.5, the magnetic field profile along the surface has been approximated by a region of constant potential over a length of

$L = 13\,\text{cm}$ with the trapped gas placed at $z = 0$ at a distance $R = 0.65\,\text{cm}$ from the walls. At the lower end of the cell (positive z in Fig. 7.5) the field increases linearly over a distance of 5 cm with a gradient of 1.0 T/cm. For the diffusion limit we used the boundary conditions $(\partial\sigma_{hop}/\partial z)(z = -\frac{1}{2}L) = 0$ at the top end of the cell and $D_{hop}\kappa(\partial\sigma_a/\partial z)(z = \frac{1}{2}L) = -v_{drift}\sigma_a(z = \frac{1}{2}L)$ at the bottom end, where the r.h.s. of the equation is the flow of particles drifting with a velocity $v_{drift} = (D_{hop}/k_BT)\vec{F}$ under the influence of a force $\vec{F} = \mu_B(\partial B_w/\partial z)$. Due to the strong magnetic field gradient, the drift velocity for the experimental conditions is $v_{drift} = 2.3\times10^3\,\text{cms}^{-1}$.

From Eq. 7.21, the density of a atoms at $z = 0$ for the diffusion limit is

$$\sigma_{a,0} \simeq \frac{\dot{N}_a L}{4\pi R D_{bou}\kappa} \tag{7.24}$$

and for the recombination limit is

$$\sigma_{a,0} = \frac{\dot{N}_a}{2\pi R L_a K^s_{ad}\sigma_d}. \tag{7.25}$$

Let us estimate for typical conditions in the diffusion limit, the surface density of a atoms using Eq. 7.24: for a trapped gas at 50 mK and a density $n_0 = 10^{12}\,\text{cm}^{-3}$, the flux of a atoms $\dot{N}_a = 4.2\times10^7\,\text{s}^{-1}$ and $\sigma_{a,0} = 7.5\times10^5\,\text{cm}^{-2}$. For adsorbed d atoms this corresponds to a recombination lifetime of $(K^s_{ad}\sigma_a)^{-1} = 0.13\,\text{s}$. Notice that this time is only 20 times larger than the surface residency time. To calculate σ_a in the recombination limit, we have to calculate the density of adsorbed d atoms. This will be the subject of the next section.

7.3 Interaction between trapped and tail atoms

7.3.1 Two distributions

By elastic collisions in the trapped gas, atoms are constantly produced with an energy greater than the trap depth. These atoms can collide elastically with or adsorb on the He film. In the first case the atom will reflect specularly with respect to the local surface normal. In the latter case the atom will thermalize with the wall. The probability to collide in the gas depends on the position and direction of desorption. It also depends on the density and temperature of the trapped gas. We will come back to the calculation of this probability later, but will, for the time being, use a simple upper bound, given by the probability to collide with an atom in the trapped gas if the atom leaves the wall at $z = 0$

$$P_{c,up} = P_{dia}P_\Omega = \sigma_{el}n_0\sqrt{\frac{\pi k_B T 2B_0}{\mu_B\alpha^2}}\left(\frac{2R_s}{\pi R}\right), \tag{7.26}$$

where P_{dia} is the probability to hit an atom in the gas in a diametrical traversal using the parabolic field approximation (see Sect. 2.2) and $P_\Omega \simeq 2R_s/\pi R$ is the probability for atoms leaving the wall with a cosine distribution to be emitted within the solid angle subtended by the sample with diameter $2R_s$ and length $L_s \gg R = 0.65\,\mathrm{cm}$ (see Sect. 2.3.3). For typical conditions in the experiment ($n_0 = 10^{12}\,\mathrm{cm}^{-3}$, $T_g = 50\,\mathrm{mK}$ and $T_w = 80\,\mathrm{mK}$) : $P_{c,up} \simeq 4 \times 10^{-6} \ll s = 0.33\,T_w = 2.6 \times 10^{-2}$, which means that the atom will definitely thermalize with the He film before it collides with an atom in the gas. This means we in fact have two different distributions: the distribution at temperature T_g truncated in phase space by the condition $\varepsilon = p^2/2m + U_p(\vec{r}) \leq \varepsilon_{tr}$, called the "trapped distribution" and the distribution at temperature T_w truncated in phase space by the condition $\varepsilon \geq \varepsilon_{tr}$, which will be referred to as the "tail distribution". The density of trapped atoms is (see also Ref. [4])

$$n_g(\vec{r}) = \int_{\varepsilon \leq \varepsilon_{tr}} d^3p\, n_{0g} (2\pi m k_B T_g)^{-3/2} \exp\left(-\frac{p^2/2m + U_p(\vec{r})}{k_B T_g}\right), \tag{7.27}$$

where the reference density n_{0g} is chosen in such a way that the trapped distribution is normalized with respect to the total number of trapped particles $N_g = \int d^3r\, n_g(\vec{r})$ (for $\varepsilon_{tr}/k_B T_g \to \infty$, n_{0g} is the density at the center of the trap). The density of tail atoms is

$$\begin{aligned} n_w(\vec{r}) &= \int_{\varepsilon \geq \varepsilon_{tr}} d^3p\, n_{0w} (2\pi m k_B T_w)^{-3/2} \exp\left(-\frac{p^2/2m + U_p(\vec{r})}{k_B T_w}\right) \\ &= n'_w(\vec{r}) \left[1 - \mathrm{erf}\left(\sqrt{\frac{\varepsilon_{tr} - U_p(\vec{r})}{k_B T_w}}\right) + \frac{2}{\sqrt{\pi}} \sqrt{\frac{\varepsilon_{tr} - U_p(\vec{r})}{k_B T_w}} \exp\left(-\frac{\varepsilon_{tr} - U_p(\vec{r})}{k_B T_w}\right)\right] \end{aligned} \tag{7.28}$$

where the reference density n_{0w} is chosen in such a way that the tail distribution is normalized with respect to the total number of tail particles $N_w = \int d^3r\, n_w(\vec{r})$ and $n'_w(\vec{r}) = n_{0w} \exp(-U_p(\vec{r})/k_B T_w)$. For the limit $\varepsilon_{tr}/k_B T_w \to 0$, $n_{0w} = n_w(B_0)$ the density at the trap center. In Fig. 7.6, the density of tail atoms in the radial direction at $z = 0$ is plotted. To assure a quasithermal distribution for the trapped and the tail atoms, the rate at which the trapped atoms evaporate or the tail atoms scatter into trapped states, must be much smaller than the thermalization rate for both distributions. Analogous to the case for a trapped gas, we can introduce an effective volume V_{1e}^w. However, it is convenient to define V_{1e}^w with respect to the bulk density of tail atoms just above the surface $n_w(B_w) = n_{0w} \exp(-\varepsilon_{tr}/k_B T_w)$,

$$V_{1e}^w \equiv \frac{N_w}{n_w(B_w)} = \int_{U_p \leq \varepsilon_{tr}} \frac{n_w(\vec{r})}{n_w(B_w)}\, d^3r. \tag{7.29}$$

The integral in Eq. 7.29 can be simply evaluated. For the conditions of the experiments ("long trap" and $T = 80\,\mathrm{mK}$), it gives $V_{1e}^w = 28\,\mathrm{cm}^{-3}$, of the same order of magnitude as the geometrical cell volume.

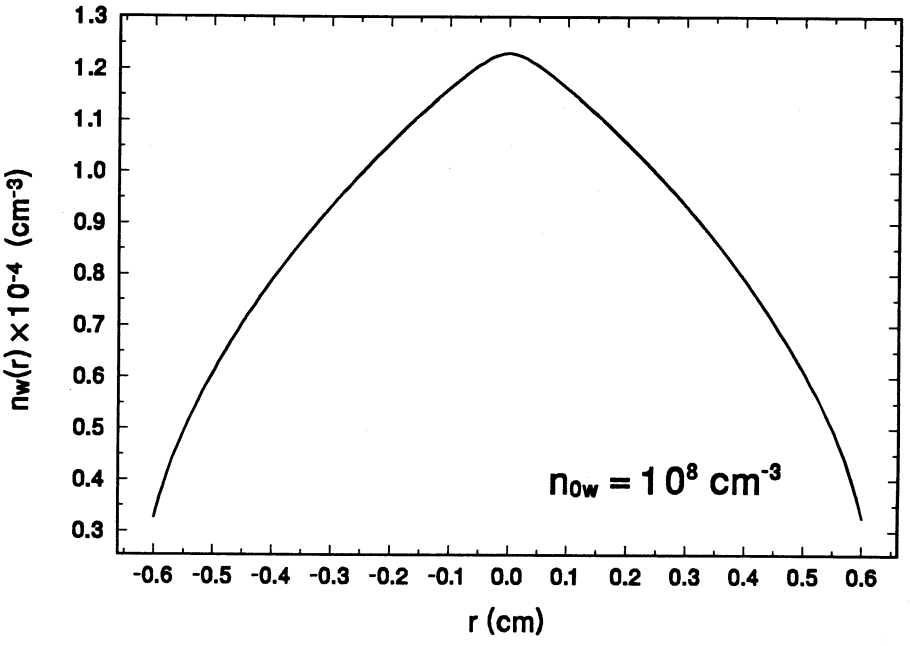

Figure 7.6: Bulk density of wall atoms along the radial direction at $z = 0$ for the "long trap". A typical value for n_{0w} in the diffusion limit is assumed.

7.3.2 Rate equations for the tail atoms

In this section, we will discuss the rate equations that govern the population and the depopulation of the tail distribution. Atoms are constantly lost from the distribution through recombination with a atoms in the adsorbed state and collisions with the trapped gas. Atoms are contributed to the distribution through evaporation of the trapped gas. The rate equations that describe the change in surface density σ_d and bulk density $n_w(B_w)$ are

$$\begin{aligned} \dot{\sigma}_d &= I_d - \frac{\sigma_d}{\tau_{res}} + \tfrac{1}{4} n_w(B_w)\bar{v}s - K^s_{ad}\sigma_a\sigma_d \\ \dot{n}_w(B_w) &= \frac{\sigma_d}{\tau_{res}}\Big(\frac{A}{V^w_{1e}}\Big) - \tfrac{1}{4} n_w(B_w)\bar{v}s\Big(\frac{A}{V^w_{1e}}\Big) - \frac{n_w(B_w)}{\tau_w}, \end{aligned} \tag{7.30}$$

where I_d is the flux of evaporated d atoms per unit surface area. Since most d atoms rattle around the cell a few times before they actually adsorb on the He film, we assume I_d is constant over the cell wall as opposed to I_a. Also we assume σ_d to be homogeneous. The rate τ_w^{-1} at which the wall atoms collide with the gas atoms will be considered later but, just as in the beginning of Sect. 7.3.1, we will use an upper

bound

$$\tau_w^{-1} \leq \frac{P_{c,up}}{\tau_{dia}} \tag{7.31}$$

where τ_{dia} is the time for a diametrical traversal of the cell. For an atom leaving the wall with an energy of 80 mK, $\tau_{dia} = 1.5 \times 10^{-4}$ s. Due to the strong acceleration of the desorbed d atoms, the initial velocity does not strongly influence τ_{dia}. In steady-state, Eqs. 7.30 sum up to

$$\frac{\dot{N}_{ev}}{V_{1e}^w} - \frac{n_w(B_w)}{\tau_w} - \frac{K_{ad}^s \sigma_d}{V_{1e}^w} \int \sigma_a \, dA = 0, \tag{7.32}$$

where $\dot{N}_{ev} = I_d A$ is the evaporation flux.

For σ_d and $n_w(B_w)$ to be related by the adsorption isotherm, the loss rate due to collisions with trapped atoms must be smaller than the adsorption rate and the characteristic time for surface recombination must be larger than the surface residency time

$$\tau_w^{-1} \ll \tfrac{1}{4}\bar{v}s(A/V_{1e}^w) \tag{7.33}$$

$$K_{ad}^s \sigma_a \ll \tau_{res}^{-1}. \tag{7.34}$$

The second condition puts an upper bound on σ_a. At $T_w = 80$ mK it gives $\sigma_a \ll 1.5 \times 10^7$ cm^{-2}. Equations 7.21 and 7.32 are the central equations that determine σ_a and σ_d.

The diffusion limit ($D_{hop}\kappa(\partial^2\sigma_a/\partial z^2) + I_a = 0$). With Eq. 7.32 and the solution for σ_a, a value for σ_d can be obtained and condition 7.22 can be verified. It turns out that this condition is never completely fulfilled over the entire cell surface. At the upper end of the cell, for $z \simeq -\frac{1}{2}L$, the flux I_a is so small that it is not satisfied. To obtain a proper solution for σ_a one has to solve Eq. 7.21 including the recombination term. A necessary condition for the diffusion limit is that $\dot{N}_a > \dot{N}_{ev}$. For the "long trap" this condition is satisfied for $T_g < 76$ mK, a temperature which, by coincidence, lies close to the wall temperature. Condition 7.22 is then satisfied in a region around $z = 0$ of which the width increases as the gas temperature decreases, since σ_d is proportional to $\dot{N}_{ev}$ which decreases exponentially with the temperature of the trapped gas. For $n_0 > 3 \times 10^{12}$ cm^{-3} and $T_g \lesssim 70$ mK, $\sigma_{a,0} \gtrsim 10^7$ cm^{-2} so that condition 7.34 is not satisfied and σ_d and $n_w(B_w)$ are not related by the adsorption isotherm. Under these conditions, we predominantly loose the a atoms by diffusion and the d atoms by recombination. When all the d atoms recombine before they desorb, the term $n_w(B_w)/\tau_w$ in Eq. 7.32 can be omitted and σ_d is determined by a balance between the evaporative flux from the gas and a-d recombination.

The recombination limit ($I_a - K_{ad}^s \sigma_a \sigma_d = 0$). Solving Eqs. 7.21 and 7.32 gives

$$\sigma_a(z) = \frac{V_{1e}^w}{K_{ad}^s(\dot{N}_{ev} - \dot{N}_a)} \frac{1}{\tau_w \lambda_{th}} \exp(-\frac{\varepsilon_a}{k_B T_w}) \, I_a(z). \tag{7.35}$$

In this limit the position dependence of σ_a is the same as that of I_a. Equation. 7.35 combined with condition 7.23 determines the validity of the recombination limit. For the "long trap", a necessary condition for the recombination limit is that $T_g > 76$ mK so that $\dot{N}_{ev} > \dot{N}_a$. For $T_w \approx T_g = 80$ mK condition 7.23 is only satisfied for high trapped gas densities. For $n_0 > 3\times10^{12}\,\mathrm{cm}^{-3}$, $\dot{N}_{ev}$ is so large that $\sigma_d \gtrsim 10^7\,\mathrm{cm}^{-2}$ and the first-order recombination time for a atoms $(K^s_{ad}\sigma_d)^{-1} < \tau_{res}$. In this limit σ_a and σ_{hop} are not related by the adsorption isotherm. When all a atoms recombine before they desorb, $\sigma_{hop} = 0$ and the a atoms will only diffuse in the adsorbed state. Since $D_{hop}/D_{ads} \simeq 10^3$ (see Sect.7.2.3), condition 7.23 will be more strongly satisfied. For $n_0 = 5 \times 10^{12}\,\mathrm{cm}^{-3}$, the recombination limit then gives $\sigma_a = 7.3 \times 10^5\,\mathrm{cm}^{-2}$ and $\sigma_d = 2.8 \times 10^7\,\mathrm{cm}^{-2}$. Since the recombination time for d atoms $(K^s_{ad}\sigma_a)^{-1} > \tau_{res}$, σ_d and $n_w(B_w)$ are well related by the adsorption isotherm.

7.3.3 Collision rate between trapped and tail atoms

In Sect. 7.3.1 we approximated the collision probability between trapped atoms and tail atoms by an upper bound $P_{c,up}$. The true collision probability depends strongly on the position and direction of desorption. To obtain an average collision rate one would have to perform an average over the surface of the wall and over all possible directions of desorption. For the conditions described in Sect. 7.3.1, an elegant method can be employed to calculate this average, analogous to the method used by Luiten [4] to calculate the evaporation rate for a gas of trapped atoms with a thermal distribution truncated in phase space.

In this problem we have two thermal distributions: the trapped gas atoms with a temperature T_g, truncated in phase space by the condition $\varepsilon = p^2/2m + U_p(\vec{r}) < \varepsilon_{tr}$ and the tail atoms with temperature T_w, truncated in phase space by the condition $\varepsilon \geq \varepsilon_{tr}$. A necessary condition for describing the gas in this fashion is that the rate at which atoms are lost from the trapped distribution by evaporation is much smaller than the internal elastic collision rate and that the rate at which atoms are lost from the tail distribution by collisions with the trapped gas atoms is much smaller than the tail thermalization rate. For the tail atoms this thermalization rate is not the internal elastic collision rate, but the adsorption rate on the walls.

Collisions between a trapped and a tail atom can have three different results, visualized in Fig. 7.7. In process 1, the tail atom gets trapped after the collision. The atom is lost from the tail distribution and deposits an energy of at least ε_{tr} to the trapped distribution. In process 2 either the trapped and the tail atom remain in their original distributions after the collision and only exchange energy or they exchange distributions. In process 3, the tail atom gives the trapped atom sufficient

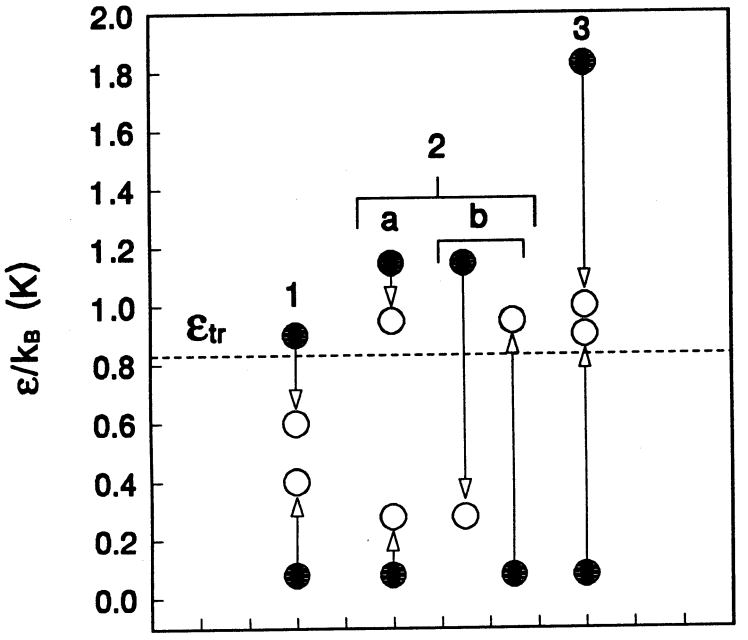

Figure 7.7: Three different processes that can take place in a collision between a trapped and a tail atom: 1) the tail atom gets trapped, 2) the tail atom does not get trapped, but only exchanges energy with the trapped atom and 3) the tail atom kicks out a trapped atom and retains an energy larger than ε_{tr}.

energy to become part of the tail distribution while remaining a tail atom itself. The event rates for these three processes can be calculated by evaluating the collision integral

$$\Gamma_c = \frac{\sigma_{el}}{2m} \int d^3r \int d^3p_w \int d^3p_g |\vec{p}_w - \vec{p}_g| f_w(\vec{r}, \vec{p}_w) f_g(\vec{r}, \vec{p}_g), \tag{7.36}$$

for conditions describing these processes. The initial condition is that before the collision one of the atoms is a tail atom and the other is a trapped atom

$$p_w^2 > 2m(\varepsilon_{tr} - U_p(\vec{r})) \tag{7.37}$$

$$p_g^2 < 2m(\varepsilon_{tr} - U_p(\vec{r})). \tag{7.38}$$

Changing to center-of-mass and relative momentum coordinates $\vec{P} = \frac{1}{2}(\vec{p}_w + \vec{p}_g)$ and $\vec{q} = \vec{p}_w - \vec{p}_g$. We then obtain

$$\cos\theta > \left| \frac{Q^2 - P^2 - \frac{1}{4}q^2}{Pq} \right|, \tag{7.39}$$

where θ is the angle between $\vec{P}$ and $\vec{q}$ and $Q^2 = 2m(\varepsilon_{tr} - U_p(\vec{r}))$. Conditions 7.37

and 7.38 have as a necessary conditions, respectively

$$\begin{aligned}(P+\frac{1}{2}q)^2 &\geq Q^2 \\ (P-\frac{1}{2}q)^2 &\leq Q^2.\end{aligned} \tag{7.40}$$

The final condition depends on which of the three processes we consider. In the experiment, the elastic collisions between trapped and tail atoms will be dominated by process 1. Since the thermal energy of the tail atoms is much lower than the trap depth, the part of phase space into which the atoms can scatter after a collision is much smaller for process 2 than for process 1. For process 3 to occur the desorbed tail atom should have an energy of at least the trap depth. The number of these atoms is exponentially small. Since process 1 is dominant, we will only consider the collisional integral for this case. After process 1 both atoms stay trapped. This gives as a condition

$$|\cos\theta'| < \frac{Q^2 - P^2 - \frac{1}{4}q^2}{Pq} \tag{7.41}$$

with as a necessary condition

$$P^2 + \frac{1}{4}q^2 \leq Q^2. \tag{7.42}$$

In conditions 7.41 and 7.42, we have used that $P = P'$ and $q = q'$ after an elastic collision.

Since we are dealing with s-wave collisions, all final angles (θ', ϕ') are equally probable. The fraction of colliding pairs, that scatter according to process 1, is given by

$$F = \frac{1}{4\pi}\int_0^{2\pi} d\phi' \int d\theta' \sin\theta' \tag{7.43}$$

where the θ' integration is restricted by condition 7.41. Evaluation of this integral gives

$$F_1(\vec{r}, P, q) = \frac{Q^2 - P^2 - \frac{1}{4}q^2}{Pq}. \tag{7.44}$$

The total collision rate for process 1 is

$$\begin{aligned}\Gamma_{c1} = \frac{n_{0w}n_{0g}}{2m}\sigma_{el}(2\pi m k_B T_w)^{-3/2}(2\pi m k_B T_g)^{-3/2}\int_{U_p \leq \varepsilon_{tr}} d^3r \exp(-\frac{U_p(\vec{r})}{k_B T_w} - \frac{U_p(\vec{r})}{k_B T_g}) \\ \int d^3P \int d^3q\, q F_1 \exp\left(-\frac{P^2+\frac{1}{4}q^2}{2mk_BT_w} - \frac{P^2+\frac{1}{4}q^2}{2mk_BT_g} - \frac{Pq\cos\theta}{2m}(\frac{1}{k_BT_w} - \frac{1}{k_BT_g})\right)\end{aligned} \tag{7.45}$$

where the integration over (θ, ϕ) is restricted by condition 7.39 and the integration over (P, q) is restricted to the region determined by the necessary conditions 7.40 and 7.42.

The argument of the integral shows that the local collision probability depends on the angle θ between P and q. Since we consider two atoms from different distributions, so with different average energies, not all angles are equally probable as opposed to two atoms from the same distribution. It is this extra angular dependence which makes the evaluation of the integral in Eq. 7.45 a very lengthy and tedious business.

After evaluation of the momentum integrals, the volume integral can rewritten to an integral over the magnetic field using the magnetic density of states from Sect. 2.3.3

$$\rho_M(B) = \frac{4\pi}{\alpha^2\sqrt{\beta}}[(B-B_0)^{3/2} + B_0(B-B_0)^{1/2}]. \tag{7.46}$$

For the "long trap", this is a very good approximation since the $B_w = 1.33\,\mathrm{T}$ equipotential surface nearly coincides with the cell walls. The total collision rate for process 1 can now be written in the following manner

$$\Gamma_{c1} = \frac{1}{\sqrt{2\pi}} n_{0g} n_{0w} \exp\Big(-\frac{\varepsilon_{tr}}{k_B T_w}\Big)\sigma_{el}\sqrt{\frac{8k_B T_w}{\pi m}} V_{wg,1}, \tag{7.47}$$

where we have introduced the effective volume for trapped-tail collisions giving two trapped atoms

$$\begin{aligned} V_{wg,1} = {} & \frac{4\pi}{\alpha^2\sqrt{\beta}}\left(\frac{k_B T_g}{\mu_B}\right)^{5/2} \exp(-\varepsilon_{tr}/k_B T_g) \\ & \int_0^{\eta_g} d\alpha_g \Big[(\eta_g-\alpha_g)^{3/2} + \frac{T_0}{T_g}(\eta_g-\alpha_g)^{1/2}\Big] \Big([(\tfrac{5}{2}-\tfrac{3}{2}\delta) - \delta^{-1}]\sqrt{\alpha_g} + \\ & [(1-\delta)\alpha_g - (\tfrac{5}{2}-\tfrac{3}{2}\delta)]e^{\alpha_g}\tfrac{1}{2}\sqrt{\pi}\,\mathrm{erf}\,(\sqrt{\alpha_g}) + \delta^{-3/2}e^{\delta\alpha_g}\tfrac{1}{2}\sqrt{\pi}\,\mathrm{erf}\,(\sqrt{\delta\alpha_g})\Big)\,. \end{aligned} \tag{7.48}$$

In this equation $\alpha_g = (\varepsilon_{tr} - U_p(\vec{r}))/k_B T_g$ is the integration variable, $\delta = 1 - T_g/T_w$ is the normalized temperature difference and $\eta_g = \varepsilon_{tr}/k_B T_g$.

The expression for Γ_{c1} shows that the collision rate is linearly dependent on the central trap density and the density of tail atoms just above the surface (see Sect. 7.3.1). The wall temperature dependence is contained in the thermal velocity of the tail atoms and in $V_{wg,1}$. In the experiment T_w is constant while T_g varies. In Fig. 7.8 we plot $V_{wg,1}$ as a function of T_g for the "long trap" and $T_w = 80\,\mathrm{mK}$. In Fig. 7.8 we also plot the effective volume as given by the upper bound for the collision rate, Eq. 7.31. It turns out that this effective volume is actually very close to the true effective volume. For $T_w = 80\,\mathrm{mK}$ and $T_g = 50\,\mathrm{mK}$ the averaged collision rate from Eq. 7.31 differs only 10 % from the actual value.

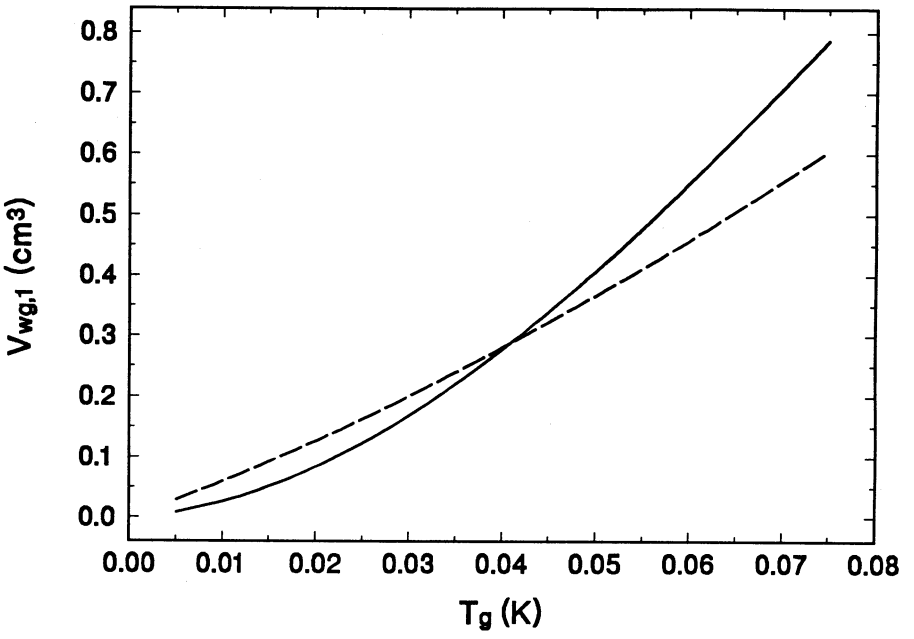

Figure 7.8: Effective volume $V_{wg,1}$, for collisions between trapped atoms and tail atoms producing two trapped atoms. In this plot $T_w = 80\,\mathrm{mK}$ and the parameters for the "long trap" have been used. For comparison the analogous effective volume using the upper bound $P_{c,up}$ is plotted as the dashed curve.

7.4 Relaxation-induced evaporative cooling

If decay processes on the wall would not exist Eq. 7.47 would give the rate at which the tail distribution and the trapped distribution thermalize. In the previous sections we have shown, however, that decay processes on the wall do play an important role. If evaporated atoms that adsorb on the wall recombine at a rate larger than the trapped-tail collision rate, Eq. 7.47, the trapped gas will be evaporatively cooled. For the conditions as described in Sect. 7.1.2, we can now show that this is the mechanism by which the trapped gas is evaporatively cooled. After filling, the gas temperature T_g approaches the wall temperature $T_w = 80\,\mathrm{mK}$ and the gas has a high density ($n_0 \geq 5 \times 10^{12}\,\mathrm{cm}^{-3}$). The gas is then in the recombination limit. In this limit, σ_a is determined by recombination with adsorbed d atoms. Since $(K^s_{ad}\sigma_a)^{-1} \gg \tau_{res}$, d atoms predominantly desorb and collide with the trapped atoms thereby maintaining the thermal equilibrium with the walls. Due to decay processes in the gas and on the walls, n_0 and $\dot{N}_{ev}$ decrease. Due to the smaller $\dot{N}_{ev}$, σ_d will also decrease and reach the point where the first-order recombination

time for a atoms $(K^s_{ad}\sigma_d)^{-1} > \tau_{res}$. At this moment, the gas enters a cross over regime where σ_a is not only determined by a-d recombination but also by diffusion of a atoms. In this regime σ_a gets an opportunity to build up to a value where a-d recombination starts to determine σ_d. At this moment, evaporative cooling of the gas starts. As the gas cools down, $\dot{N}_{ev}$ decreases which also reduces σ_d until σ_a is completely determined by diffusion. The gas has then entered the diffusion limit. As an example, at the observed $T_g = 50\,\mathrm{mK}$ and a typical gas density of $10^{12}\,\mathrm{cm}^{-3}$, the averaged trapped-tail collision rate as derived from Eq. 7.47 is

$$\tau_{wg,1} \simeq 15\,\mathrm{s}. \tag{7.49}$$

For this density, $\sigma_a = 7.5 \times 10^5\,\mathrm{cm}^{-2}$ (see Sect. 7.2.3) which gives a first-order decay time of 130 ms for the d atoms. Since this time is much smaller than the trapped-tail collision rate, the presence of a atoms on the walls will constitute a recombination channel that will evaporatively cool the gas. As opposed to the ordinary and forced evaporative cooling experiments [3, 9] where the evaporative cooling is the result of a triggered recombination or a controlled escape over the trap barrier, in this experiment the gas is evaporatively cooled by a surface recombination mechanism which results from spin relaxational processes in the gas itself. This process takes place automatically for low enough wall temperatures. For $T_w = 200\,\mathrm{mK}$ and the same typical conditions $T_g = 50\,\mathrm{mK}$ and $n_0 = 10^{12}\,\mathrm{cm}^{-3}$, τ_{res} is so small that in the diffusion limit $\sigma_{a,0} \simeq 30\,\mathrm{cm}^{-2}$. This surface density is too small to cause any evaporative cooling.

References

[1] A. Lagendijk, I.F. Silvera, and B.J. Verhaar, Phys. Rev. B **33**, 626 (1986).

[2] H.T.C. Stoof, J.M.V.A. Koelman, and B.J. Verhaar, Phys. Rev. B **38**, 4688 (1988).

[3] O.J. Luiten, H.G.C. Werij, I.D. Setija, M.W. Reynolds, T.W. Hijmans, and J.T.M. Walraven, Phys. Rev. Lett. **70**, 544 (1993).

[4] O.J. Luiten, Ph. D. thesis, University of Amsterdam (1993).

[5] R. van Roijen, J.J. Berkhout, S. Jaakkola, and J.T.M. Walraven, Phys. Rev. Lett. **61**, 931 (1988).

[6] R. van Roijen, Ph. D. thesis, University of Amsterdam (1989).

[7] A.F.G. Wyatt, Phys. Rev. Lett. **69**, 1785 (1992).

[8] W.N. Hardy, M.D. Hürlimann, and R.W. Cline, Jap. J. Appl. Phys. **26**, Suppl. 26-3, 2065 (1987).

[9] J.M. Doyle, J.C. Sandberg, I.A. Yu, C.L. Cesar, D. Kleppner, and T.J. Greytak, Phys. Rev. Lett. **67**, 603 (1991).

[10] J.J. Berkhout, E.J. Wolters, R. van Roijen and J.T.M. Walraven, Phys. Rev. Lett. **57**, 2387 (1986).

[11] R. Sprik, J.T.M. Walraven, and I.F. Silvera, Phys. Rev. B **32**, 5668 (1985).

[12] M. Morrow and A.J. Berlinsky, Can. J. Phys. **61**, 1042 (1983).

[13] I.F. Silvera and J.T.M. Walraven, Prog. Low Temp. Phys. **X**, 139 (1986).

[14] M.W. Reynolds, I. Shinkoda, W.N. Hardy, A.J. Berlinsky, F. Bridges, and B.W. Statt, Phys. Rev. B **31**, 7503 (1985).

[15] B.W. Statt, Phys. Rev. B **25**, 6035 (1982).

[16] R.M.C. Ahn, J.P.H.W. v.d. Eijnde, C.J. Reuver, B.J. Verhaar, and I.F. Silvera, Phys. Rev. B **26**, 452 (1982).

[17] A.J. Berlinsky, W.N. Hardy, and B.W. Statt, Phys. Rev. B **35**, 4831 (1987).

[18] B.W. Statt, A.J. Berlinsky, and W.N. Hardy, Phys. Rev. B **31**, 3169 (1985).

[19] M. Mertig, E.Tjukanov, A.Ya. Katunin, S.A. Vasilyev, and S. Jaakkola, in *Proceedings of the 20th International Conference on Low Temperature Physics*, Physica B **194-196**, 439-440 (1994).

[20] D.S. Zimmerman and A.J. Berlinsky, Can. J. Phys. **62**, 590 (1984).

Samenvatting

In dit proefschrift beschrijf ik de eerste optische koelexperimenten die gedaan zijn aan magnetisch ingevangen waterstof (H). Twee verschillende optische koelmanieren zijn hierbij gebruikt: Doppler koeling en licht-geïnduceerd afdampen. Het is slechts 10 jaren geleden dat Doppler koeling voor het eerst gebruikt werd om een verzameling deeltjes af te koelen. Sinds die eerste Doppler koelexperimenten heeft het scala aan optische koelmethodes een enorme vlucht genomen en is men ook steeds in staat geweest lagere temperaturen te halen. Het is daarom des te verrassender dat de Doppler koelexperimenten aan atomair waterstof een aantal nieuwe aspecten aan het licht hebben gebracht die een wezenlijke bijdrage vormen voor het begrip van Dopplerkoeling. Licht-geïnduceerd afdampen (of ook LIE, van het Engelse "light-induced evaporation") is een nieuwe optische koelmethode die door onze groep ontwikkeld is. Met deze optische koelmethode hebben we een temperatuur weten te halen van 3 mK. Theoretische berekeningen laten echter zien dat veel lagere temperaturen haalbaar zijn.

Om de beide koelmethodes op hun waarde te schatten, is het echter noodzakelijk eerst wat meer van magnetisch opgesloten waterstof te weten. Een waterstofatoom kan zijn electronspin 'op' of 'neer' hebben (enigszins te vergelijken met een staafmagneetje met de 'noord' naar boven gericht of de 'zuid' naar boven). Door die atomen met hun electronspin 'op' in een magnetisch veldminimum te plaatsen, zijn deze deeltjes in een krachtenveld ingevangen (vergelijkbaar met knikkers in een kuil) zonder dat ze in contact staan met wanden. Dit verhoogt de stabiliteit van H met ordes van grootte. Aparte H-atomen willen graag recombineren tot moleculair H_2 hetgeen voornamelijk aan oppervlakken plaatsvindt. Door de grotere stabiliteit van magnetisch ingevangen atomair waterstof kan het gas op langere tijdschalen bestudeerd worden en kunnen verschillende technieken toegepast worden om het gas nog verder af te koelen. De reden dat men H steeds verder wil afkoelen wordt gegeven door de verwachting dat bij een bepaalde overgangstemperatuur (afhankelijk van de dichtheid) het gas macroscopische quantum effecten zal vertonen. Bij deze fase-overgang, de Bose-Einstein condensatie, zullen alle atomen de laagst-energetische quantumtoestand bevolken (of wat onzorgvuldig gezegd: ze

zullen zich identiek gedragen). Het is in de natuurkunde onderhand een algemeen geaccepteerd feit dat deze fase-overgang aan de basis staat van verschijnselen als supergeleiding van bepaalde metalen en superfluïditeit (stromen zonder wrijving) van vloeibaar helium. Door de sterke interactie tussen de deeltjes, is het in deze systemen echter moeilijk een goede beschrijving van deze verschijnselen te geven. De waterstofatomen in een gas hebben een erg zwakke wisselwerking waardoor dit een ideaal systeem zou zijn de Bose-Einstein condensatie (BEC) in zijn meest pure vorm waar te nemen.

De condities waaronder H magnetisch ingevangen wordt onderscheiden het van andere gassen die tot nu toe optisch gekoeld zijn als, natrium, cesium en rubidium. Om te voorkomen dat H meteen op alle oppervlakken neerslaat en recombineert zodra het gecreëerd is, worden alle oppervlakken bedekt met een laagje vloeibaar helium. Helium heeft de laagste bindingsenergie voor H, hetgeen tot gevolg heeft dat geadsorbeerde deeltjes weer makkelijk ontsnappen en de oppervlaktedichtheid laag is. De recombinatiesnelheid aan het oppervlak zal dan ook laag zijn. Deze vloeibare heliumfilm heeft echter wel tot gevolg dat alle metingen bij temperaturen lager dan 1 Kelvin moeten worden uitgevoerd. H wordt geproduceerd in een microgolfontlading bij een temperatuur van ongeveer 700 mK. Deze atomen worden dan door het magnetische veld naar het celvolume gedreven waar ze eerst met de vloeibare heliumfilm op de wanden thermaliseren tot 80 mK alvorens ze magnetisch worden ingevangen. Deze methode van het vullen van de val is uniek voor waterstof en heeft tot gevolg dat hoge dichtheden kunnen worden bereikt. Veel hoger dan tot nu toe in gassen van natrium of cesium bereikt is. Bij deze dichtheden is het gas meestal optisch dicht (al het licht dat op het ingevangen gaswolkje valt wordt geabsorbeerd). Wandloze opsluiting van H resulteert dus in een grotere stabiliteit, maar brengt meteen de moeilijkheid met zich mee dat metingen aan dit opgesloten waterstof ook contactloos moeten gebeuren. Je kunt immers geen thermometer in het gas plaatsen. Hier biedt absorptie spectroscopie uitkomst. Door de atomen te bestralen met licht dat resonant is met de overgang naar het eerste aangeslagen niveau (de Lyman-α overgang) kan locaal informatie over het gas verkregen worden. De piekhoogte van een absorptie spectrum levert informatie over de dichtheid (immers, hoe dichter het gas, hoe sterker de absorptie). Als het gas warmer is zullen meer deeltjes in hogere magneetvelden komen waar de resonantie frequentie sterker verschoven is t.g.v. het Zeemaneffect. De verbreding van een absorptielijn is daarmee een maat voor de temperatuur van het gas. In werkelijkheid komt er wel ietsje meer bij kijken voor een gemeten spectrum kan worden omgezet in een waarde voor dichtheid en temperatuur (hoofdstuk 4 behandelt de voortplanting van licht door een gas van spingepolariseerde waterstofatomen en hoe de eigenschappen van

het gas het absorptiespectrum beïnvloeden). Baanbrekend werk op dit gebied is verricht door mijn voorganger, Jom Luiten, die in het kader van zijn promotie-onderzoek voor het eerst Lyman-α spectroscopie gebruikte om het opgesloten waterstofgas te bestuderen.

Voor het doen van resonant optische experimenten aan H is licht nodig dat resonant is met de Lyman-α overgang ($1S \rightarrow 2P$). Dit Lyman-α licht heeft een golflengte van 121.56 nm en wordt geabsorbeerd in bijna alle materialen en lucht. Het zal duidelijk zijn dat het werken met dit licht geen sinecure is. Om dit licht te genereren met voldoende intensiteit en nauwbandig genoeg om Doppler koeling mee uit te voeren, is een zeer uitgebreide optische opstelling nodig. Beginnend met zeer nauwbandig licht met een golflengte van 729 nm wordt, d.m.v. pulsversterkers en tweede-harmonische generatie, nauwbandig gepulst licht van 365 nm geproduceerd. Een zeer kleine fractie van dit licht wordt d.m.v. derde-harmonische generatie in een gasmengsel van krypton en argon omgezet in Lyman-α licht (de experimentele opstelling om dit licht te genereren wordt beschreven in hoofdstuk 3). Het gepulste karakter van dit licht heeft tot gevolg dat het atoom relatief zelden een photon absorbeert. Minder vaak in elk geval dan wanneer je het in een intense continue bundel zou plaatsen zoals wordt gedaan bij natrium en cesium. De snelheid waarmee de atomen onderling botsen en thermisch evenwicht bereiken is veel groter dan de snelheid waarmee de atomen photonen absorberen. Deze situatie van thermisch evenwicht is uniek voor waterstof en maakt het mogelijk licht-geïnduceerd afdampen als koelmethode te gebruiken en de optische koelprocessen op relatief eenvoudige wijze te modelleren (de thermodynamische eigenschappen van een magnetisch opgesloten gas in thermisch evenwicht worden behandeld in hoofdstuk 2).

Doppler koeling is gebaseerd op de preferentiële absorptie van photonen door atomen die op het licht af komen. Door het Doppler effect zullen deze atomen het licht met een iets grotere frequentie zien dan de atomen die stilstaan of van het licht af bewegen (vergelijk dit met een toeterende trein die je bij een spoorwegovergang passeert). Door de atomen nu te bestralen met licht met een net iets lagere frequentie dan de resonantie frequentie van een atoom in rust, zullen overwegend die atomen aangeslagen worden met een snelheid op het licht af. Deze zullen door de absorptie van een photon worden afgeremd. Bij spontane emissie van het photon zal de snelheidsverandering van het atoom, gemiddeld over alle hoeken van emissie, nul zijn, zodat netto de kinetische energie van het atoom verminderd is en daarmee de temperatuur van het gas verlaagd is. Als zodanig is het verschijnsel tamelijk eenvoudig. De theorie voor het Doppler koelen van een homogeen, thermisch gas is begin jaren '80 ontwikkeld en niet lang daarna experimenteel geverifieerd. In een inhomogeen magnetisch veld worden zaken wat lastiger. Door het Zeeman effect

is de resonantie frequentie van een atoom plaatsafhankelijk geworden. De deeltjes in rust die resonant zijn met het inkomende licht bevinden zich in schillen van constant magnetisch veld rond het veldminimum. Deeltjes buiten deze resonante schil hebbben een hogere resonantie frequentie en zullen dus door de absorptie van een photon voornamelijk worden gekoeld. Deeltjes binnen deze schil zullen voornamelijk worden opgewarmd. De keuze van laserfrequentie zal dus bepalen of er meer deeltjes worden gekoeld of opgewarmd. In het optisch dunne geval (dan wordt een kleine fractie van het licht geabsorbeerd terwijl het zich door het gas voortplant) blijkt optimale koeling op te treden wanneer je de laser ongeveer afstemt op de resonantiefrequentie in het veldminimum. In het optisch dichte geval zal het licht net iets voor de resonante schil volledig geabsorbeerd worden en dus precies door die deeltjes waar het in koeling resulteert. De deeltjes binnen in de schil, die in het optisch dunne geval zouden worden opgewarmd, zijn dan a.h.w. van het licht afgeschermd. De frequentie waar de Doppler koelsnelheid optimaal is, is daarmee afhankelijk van de dichtheid geworden. Dit effect is uniek voor waterstof en is in een aantal evolutiemetingen duidelijk waargenomen (in hoofdstuk 5 wordt Doppler koeling uitvoerig behandeld).

In LIE is de koeling op een ander mechanisme gebaseerd. De energie van deeltjes in een gas in thermisch evenwicht is verdeeld volgens een Boltzmanndistributie (alle energieën komen hierin voor; de meeste deeltjes hebben een energie die evenredig is met de temperatuur van het gas; deeltjes met een veel hogere energie komen ook wel voor, maar het aantal van deze deeltjes neemt exponentieel af met energie). Door nu de deeltjes te verwijderen met een energie veel groter dan de gemiddelde energie, verlaag je de gemiddelde energie en daarmee de temperatuur van het gas. Het verschil met Doppler koelen is dus dat je nu niet de afzonderlijke deeltjes aanpakt, maar de statistisch gemiddelde energie verandert door de energieverdelingsfunctie te beïnvloeden. Dit hebben we gedaan door licht in te stralen dat resonant is met de overgangsfrequentie van deeltjes die zich aan de randen van het gaswolkje en dus in een sterk magnetisch veld bevinden. Deze deeltje hebben een hoge energie. Het bijzondere van de overgang die we aanslaan, is dat bij verval het atoom een grote kans heeft te vervallen naar de toestand waar het een electronspin 'neer' heeft. Als dit gebeurt, wordt het deeltje niet meer gevangen gehouden door het magnetische veld, maar wordt het juist uitgestoten. In het optisch dunne geval werkt deze koelmethode prima totdat het gas zo koud is dat alle deeltjes in het centrum van de val zitten en bijna dezelfde resonantiefrequentie hebben. In deze limiet, is de gemiddelde energie van de deeltjes die verwijdert worden gelijk aan de gemiddelde energie van het gas. Het koelmechanisme is nu gestopt en er worden alleen deeltjes verwijderd. Voor waterstof ligt deze limiet bij ongeveer 3 mK. Voor het bereiken van lagere

temperaturen, moet de dichtheid worden verhoogd. In het optisch dichte geval, zal het licht aan de randen van het gaswolkje geabsorbeerd worden. In dit gebied hebben de deeltjes een hoge energie en zal LIE in koeling resulteren. Helaas, zit ook hier een limiet aan. Een kleine fractie van de aangeslagen atomen vervalt naar dezelfde electronspin 'op' toestand en zorgt voor een opwarming. Wanneer deze opwarming gelijk is aan de koeling t.g.v. LIE, is de koellimiet bereikt en zal het gas alleen deeltjes verliezen. In hoofdstuk 6, waarin LIE behandeld wordt, laat ik zien dat door dit opwarmmechanisme, de condities voor BEC nooit kunnen worden gehaald met LIE.

Hoofdstuk 7 bevat een studie van de stabiliteit van het opgesloten waterstofgas en een model om te verklaren waarom het opgesloten waterstofgas na het vullen koelt naar een temperatuur lager dan de wandtemperatuur. Dit is opvallend omdat je verwacht dat na het vullen het gas gethermaliseerd is met de wanden. Een optisch koelmechanisme kan niet de oorzaak zijn aangezien het effect ook optreedt in afwezigheid van laserlicht. In het gepresenteerde model, laat ik zien dat het gas wordt gekoeld door normaal afdampen. Hierbij worden de deeltjes met genoeg energie om de wanden van de cel te halen (waar het magnetische veld het hoogst is) verwijderd door recombinatie met deeltjes die op de wand geadsorbeerd zitten.

Nawoord

Het welslagen van een natuurkundig experiment, en zeker een experiment als het optisch koelen van atomair waterstof, is afhankelijk van de goede samenwerking van een hele groep mensen. Een aantal wilde ik aan het einde van dit proefschrift toch met name noemen.

Mijn promotor, Jook Walraven, wilde ik danken voor het mogelijk maken een fantastisch experiment vanaf het prille begin tot aan het glorieuze einde mee te maken. Mijn co-promotor, Tom Hijmans, heeft, ondanks zijn wat magere "definitie", met zijn scherpe inzichten altijd een verhelderende en verrijkende bijdrage aan het onderzoek geleverd. The discussions with postdoc Meritt Reynolds have been among the most inspiring moments of my promotion. Thank you very much, Meritt, for all your major and minor contributions. Mijn collega-promovendus, Jom Luiten, was gedurende bijna 6 jaren mijn "partner in crime". Ik ben blij dat we onze samenwerking middels de wekelijkse sessies in de "Flevo-dojo" hebben kunnen voortzetten. Met postdoc Henry Werij heb ik menig spectrum gemeten en gefit. Dankzij vele lange gesprekken en zijn niet aflatende enthousiasme, zijn de nachtelijke meetsessies in een zucht voorbijgevlogen. Zonder de technische ondersteuning van Otto Höpfner en Joost Overtoom was dit experiment niet mogelijk geweest. Otto, samen met Jom heb je een uitzonderlijk productieve experimenteercel gebouwd. Joost, dankzij jouw inspanningen zal in de nabije toekomst het Kosterlitz-Thouless experiment worden uitgevoerd. Ik hoop dat je ons dan ook technisch zal bijstaan, als je nevenactiviteiten als rijwielreparateur annex barkeeper je dan nog voldoende tijd laten. Studenten Frederieke Noordman, Ingrid Zevenbergen en Tycho Sonnemans wilde ik danken voor de bijdrage die zij aan de experimenten geleverd hebben. Een persoonlijk woord van dank wilde ik toch nog richten aan Tycho die verantwoordelijk is geweest voor een belangrijk deel van het ontwerp voor het Kosterlitz-Thouless experiment. Ik wens je nog veel succes met je promotie en hoop dat je geen gasmengpanelen meer hoeft te bouwen. Mijn voorgangers Jaap Berkhout en Raymond van Roijen wilde ik danken voor de inwijding in de geheimen van mengkoelers en magnetische vallen. Mijn opvolgers, Pepijn Pinkse en Allard Mosk, wilde ik veel succes wensen met het vervolgonderzoek. Pepijn, ik hoop dat jouw experiment minstens net zo vruchtbaar

zal zijn als het mijne. Allard, ik hoop dat het jou gegeven mag zijn de kolkende vortexstromen te temmen tot stille wateren. Donald van der Veeken en Jan Michels wilde ik danken voor de prachtige computersimulaties die zij hebben uitgevoerd.

In de loop der jaren hebben een flink aantal mensen ervoor gezorgd dat de sfeer in de groep "Spectroscopie der Verdichte Materie" uiteen kon lopen van kinderlijk humoristisch tot wetenschappelijk stimulerend: Ad Lagendijk, Rudolf Sprik, Theo Nieuwenhuizen, Gerard Wegdam, Meint van Albada, Wim Koops, Bert Holsbeeke, Martin van Exter, Martin van der Mark, Mick Baggen, Pedro de Vries, Martine de Maziëre, Hilde Fleurent, Rogier Groeneveld, Ron Kroon, Johannes de Boer, Peter den Outer, Rik Kop, Mark van Rossum, Mark Kroon, Kees Mastenbroek, Maurice van Hoften en Boris Nieuwenhuis (en iedereen die ik vergeten ben). Met warme gevoelens denk ik terug aan de a.i.o.-nights en de chill-out parties in het "Cooldown Café".

In de eerste jaren van mijn promotie-onderzoek hebben Johan Soede, Fred van Anrooy, Rob Verbruggen, Jan Dekker en Wim Schuijlenburg met erg veel geduld mijn technische ondersteuning verzorgd. Voor hun bijdrage aan alle experimenten (technisch en electronisch) wilde ik verder nog danken: Johan van de Ridder, Derk Bouhuijs, Rene Witte, Ton Jongeneelen, Theo van Lieshout, Edwin Baay, Flip de Leeuw, Piet Sannes, Jan Mulder, Ton Riemersma, Hugo Schlatter, Bert Zwart en Eddy Inoeng. Zonder de probleemloze toevoer van vloeibare stikstof en helium van Nico Jonker, Herman Pothoven en Gordon Reiziger was dit allemaal niet mogelijk geweest. Voor administratieve en huishoudelijke zaken kon ik altijd terecht bij Jenny Batson, Ineke Baay, Friedje Witzenhausen, Mariet Bos, Willem Mattens en Klaas van Paasschen.

Tot slot gaat mijn dankbaarheid uit naar alle vrienden die de afgelopen jaren met me hebben meegeleefd, in het bijzonder naar Frank van Ommeren, Into Goudsmit, Eleni Sakonidou en Willem Vos die mij moed inspraken op de moeilijke ogenblikken en de blijdschap met me deelden op de vreugdevolle ogenblikken. De laatste regels van dit nawoord zouden nooit verschenen zijn zonder de onvoorwaardelijke steun die ik van mijn ouders gekregen heb in al mijn beslissingen. Deze heeft dan geresulteerd in het tweede proefschrift in de familie. Grootvader ben ik in elk geval in het aantal bladzijden voorbijgestreefd.